

Study on Single-shot Ultrafast Burst Imaging
Utilizing Frequency-to-time Encoding
of an Ultrashort Laser Pulse

February 2020

SUZUKI, Takakazu

A Thesis for the Degree of Ph.D. in Engineering

Study on Single-shot Ultrafast Burst Imaging
Utilizing Frequency-to-time Encoding
of an Ultrashort Laser Pulse

February 2020

Graduate School of Science and Technology
Keio University

SUZUKI, Takakazu



Keio University

Graduate School of Science and Technology
School of Integrated Design Engineering

**Study on Single-shot Ultrafast Burst Imaging Utilizing
Frequency-to-time Encoding of an Ultrashort Laser Pulse**

by

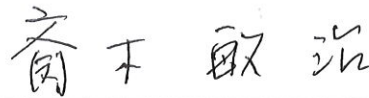
Suzuki, Takakazu

A THESIS SUBMITTED
IN PARTIAL FULFILLMENT OF
THE REQUIREMENTS FOR THE DEGREE
Doctor of Philosophy

APPROVED, THESIS COMMITTEE:



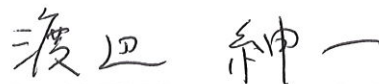
Kannari, Fumihiko



Saiki, Toshiharu



Tanabe, Takasumi



Watanabe, Shinichi



Nelson, Keith A.

Thesis Abstract

Single-shot ultrafast imaging is expected to pave a way to measure transient phenomena in femtoseconds to nanoseconds domain in real-time. Among them, a frequency-to-time encoding of Sequentially Timed All-optical Mapping Photography (STAMP) is the only method capable of direct 2D-burst imaging with both high temporal and spatial resolution on a single-shot basis. However, to realize diverse applications of STAMP, there are requirements to solve the problem of freedom in the number of snapshots and expansion of the time window to the nanoseconds regime.

This study aims to reveal various ultrafast nonrepetitive phenomena in real-time by developing and applying the modified version of STAMP utilizing Spectral Filtering (SF-STAMP). The first half of this thesis focuses on the establishment of a comprehensive SF-STAMP methodology with a simple but widely applicable to single-shot imaging. The second half addresses the single-shot measurements of photo- and THz-induced irreversible ultrafast phase transition that can be observed for the first time by virtue of SF-STAMP's notable features of a single shot and ps-temporal and μm -spatial resolution. Moreover, a real-time *in-situ* measurement application has been demonstrated by combining a conventional high-speed camera and SF-STAMP. These results highlight that the STAMP method has advantages over other single-shot ultrafast imaging methods.

Chapter 1 outlines the background and purpose of this study.

Chapter 2 describes the fundamentals of the ultrafast laser used in this study, the principle of SF-STAMP, scaling to 25 burst frames, and an extension approach to the nanoseconds time window with spectrally sweeping burst delayed pulses.

Chapter 3 addresses a single-shot measurement of THz-driven irreversible phase transition in multilayer MoTe_2 by observing transient reflectivity change of a chirped probe by SF-STAMP, together with 1D-optical streak imaging (1D-OSI) spectroscopy. Insights of THz-induced phase transition dynamics are summarized.

In Chapter 4, the real-time application of SF-STAMP combining with a kHz high-speed camera is demonstrated. Real-time *in-situ* measurement of laser processing evaluates the precursor process of each pulse and its effect on femtosecond laser processing of glass under multiple pulses accumulated conditions with sub-nanosecond time resolution using a chirp pulse probe or spectrally sweeping burst probes.

Chapter 5 discusses the outlook for the future applications of SF-STAMP, especially laser processing and THz wave region.

In Chapter 6, the experimental results and knowledge obtained in each chapter are summarized.

List of Abbreviations

1D	One-Dimensional
2D	Two-Dimensional
A2T	Angle-to-Time
AR	Anti-Reflection
BBO	β -Barium Borate (β -BaB ₂ O ₄)
BPF	Band-Pass Filter
BS	Beam Splitter
CCD	Charge-Coupled Device
CL	Cylindrical Lens
CMOS	Complementary Metal-Oxide-Semiconductor
CPA	Chirped Pulse Amplification
CUP	Compressed Ultrafast Photography
CW	Continuous Wave
DECP	Displacive Excitation of Coherent Phonons
DFT	Dispersive Fourier Transform
DOE	Diffractive Optical Element
DM	Dichroic Mirror
DMD	Digital Micromirror Device
EO	Electro-Optic
F2T	Frequency-to-Time
FACED	Free-space Angular-Chirp-Enhanced Delay
FDT	Fourier Domain Tomography
FES	Field Enhancement Structure
FFT	Fast Fourier Transform
FIR	Far-Infrared
FOV	Field of View
fps	frame per second
FRAME	Frequency Recognition Algorithm for Multiple Exposures
FTOP	Femtosecond Time-resolved Optical Polarimetry
FTL	Fourier Transform Limited
FWM	Four-Wave Mixing

GaP	Gallium Phosphide
GD	Group Delay
GDD	Group Delay Dispersion
GST	Ge ₂ Sb ₂ Te ₅
HCF	Hollow-Core Fiber
HR	High Reflectivity
HS	High-Speed
HWP	Half-Wave Plate
IMI	Impact Ionization
ISRS	Impulsive Stimulated Raman Scattering
KLM	Kerr Lens Mode-locking
LASER	Light Amplification by Stimulated Emission of Radiation
LD	Laser Diode
LIF	Light-in-Flight
LIPSS	Laser-Induced Periodic Surface Structure
LNO	Lithium Niobate (LiNbO ₃)
LSFL	Low Spatial Frequency LIPSS
MCP	Micro-Channel Plate
MIR	Mid-Infrared
MUSIC	Multiplexed Structured Image Capture
NA	Numerical Aperture
NIR	Near-Infrared
OSI	Optical Streak Imaging
PBS	Polarizing Beam Splitter
PD	Photo Detector
PF	Poole-Frenkel
S2T	Space-to-Time
sCMOS	Scientific CMOS
SE	Spectral Encoding
SF2T	Spatial Frequency-to-Time
SF-STAMP	Sequentially Timed All-optical Mapping Photography utilizing Spectral Filtering
SFG	Sum Frequency Generation
SHG	Second Harmonic Generation

SMD	Spatial Mapping Device
SMT	Spectrally Multiplexed Tomography
SPM	Self-Phase Modulation
SRS	Stimulated Raman Scattering
SS	Single-Shot
STAMP	Sequentially Timed All-optical Mapping Photography
STEAM	Serial Time-Encoded Amplified Microscopy
STRIPED FISH	Spatially and Temporally Resolved Intensity and Phase Evaluation Device: Full Information from a Single Hologram
SW	Shock Wave
THPM	Time-resolved Holographic Polarization Microscopy
THz	Terahertz
TMD	Temporal Mapping Device
TMDs	Transition Metal Dichalcogenides
TOD	Third-Order Dispersion
ZnTe	Zinc Telluride

Contents

STUDY ON SINGLE-SHOT ULTRAFAST BURST IMAGING UTILIZING FREQUENCY-TO-TIME ENCODING OF AN ULTRASHORT LASER PULSE

THESIS ABSTRACT	I
LIST OF ABBREVIATIONS	II
CONTENTS.....	V
LIST OF FIGURES	VIII
CHAPTER 1 INTRODUCTION	1
1.1 ULTRAFAST IMAGING	3
1.1.1 History and basic concept of high-speed imaging	4
1.1.2 Time-resolved pump/probe method	5
1.1.3 Streak camera	6
1.2 SINGLE-SHOT ULTRAFAST 2D-IMAGING TECHNIQUES	8
1.2.1 Category of image acquisition in single shot.....	8
1.2.2 Consecutive 2D-imaging.....	8
1.2.2.1 Time-stretch imaging	9
1.2.2.2 Two-dimensional Streak camera	11
1.2.3 Burst 2D-imaging	12
1.2.3.1 Space- (spatial frequency-) to-time encoding	12
1.2.3.2 Angle-to-time encoding.....	14
1.2.3.3 Frequency-to-time encoding	14
1.3 OBJECTIVE OF THIS THESIS	17
1.4 STRUCTURE OF THIS THESIS.....	18
CHAPTER 2 FUNDAMENTALS OF ULTRAFAST LASER, AND DEVELOPMENT AND IMPROVEMENTS OF SF-STAMP	19
2.1 FUNDAMENTALS OF ULTRAFAST LASERS	19
2.1.1 History of ultrafast lasers	19
2.1.2 Mode-locking Ti:sapphire femtosecond laser	20
2.1.3 Phase characterization of ultrashort laser pulse	25
2.1.4 Amplified femtosecond laser system by chirped pulse amplification (CPA)	29

2.2 DEVELOPMENT OF STAMP UTILIZING SPECTRAL FILTERING (SF-STAMP).....	35
2.2.1 Fundamentals of optical imaging system.....	36
2.2.2 STAMP utilizing spectral filtering (SF-STAMP).....	39
2.2.3 Principle of SF-STAMP.....	40
2.2.3.1 Temporal resolution of SF-STAMP.....	44
2.2.3.2 Spatial resolution of SF-STAMP.....	46
2.2.3.3 Proof-of-principle demonstration of the 5-frame SF-STAMP.....	47
2.3 IMPROVEMENTS OF SF-STAMP.....	55
2.3.1 Scaling of the number of burst-frames to 25 frames in SF-STAMP.....	55
2.3.1.1 Single-shot experiments by SF-STAMP with the 25-beam generating DOE.....	58
2.3.2 Extension of the observation time window to nanoseconds in SF-STAMP.....	66
2.3.2.1 Spectrally sweeping burst delay probe pulse train.....	67
2.4 MULTISPECTRAL IMAGING.....	74
CHAPTER 3 SINGLE-SHOT MEASUREMENT OF A THZ-DRIVEN IRREVERSIBLE PHASE	
TRANSITION	75
3.1 BACKGROUND.....	76
3.2 METHODS.....	77
3.3 OBSERVATION OF THZ-INDUCED IRREVERSIBLE PHASE TRANSITION IN TWO-DIMENSIONAL MoTe ₂	84
3.3.1 Experiment.....	84
3.3.2 Results.....	86
3.4 SUMMARY.....	97
CHAPTER 4 REAL-TIME <i>IN-SITU</i> MEASUREMENT OF LASER PROCESSING	98
4.1 BACKGROUND.....	98
4.2 METHODS.....	99
4.3 REAL-TIME OBSERVATION OF MULTIPLE FEMTOSECOND LASER PROCESSING WITH A SUB-NANOSECOND	
TEMPORAL RESOLUTION.....	101
4.3.1 Experiment.....	101
4.3.2 Results.....	104
4.3.2.1 Picosecond region with a frequency-chirped pulse.....	104
4.3.2.2 Sub-nanosecond region with spectrally sweeping burst pulses.....	108
4.4 SUMMARY.....	110

CHAPTER 5	OUTLOOK FOR FUTURE APPLICATION OF SF-STAMP	111
5.1	STAMP APPLICATION FOR LASER PROCESSING	111
5.2	STAMP IN THZ WAVE REGION	112
CHAPTER 6	CONCLUSION	114
REFERENCES		116
LIST OF PUBLICATIONS		138
JOURNAL PAPERS (RELATED TO THIS THESIS).....		138
OTHER JOURNAL PAPERS.....		138
INTERNATIONAL CONFERENCES		139
DOMESTIC CONFERENCES		142
OTHERS		144
ACKNOWLEDGEMENTS		146

List of Figures

Figure 1.1 The time scales in various ultrafast and high-speed imaging techniques.....	3
Figure 1.2 Schematic of a pump/probe method.....	6
Figure 1.3 (a) Operating principle of the Streak tube, (b) Operation timing at time of sweep (quoted from [123]).....	7
Figure 1.4 Schematic of Serial Time-Encoded Amplified Microscopy (STEAM) (Figure reproduced with permission from [57]: doi:10.1038/nature07980 © 2009 NPG).....	10
Figure 1.5 Schematic setup of Compressed Ultrafast Photography (CUP) (Figure reproduced with permission from [63]: doi:10.1038/nature14005 © 2014 NPG).....	11
Figure 1.6 Schematic of Sequentially Timed All-optical Mapping Photography (STAMP) (Figure reproduced with permission from [58]: doi:10.1038/nphoton.2014.163 © 2014 NPG).....	15
Figure 1.7 Schematic structure of this thesis.....	18
Figure 2.1 Schematic of Kerr lens mode-locking (KLM).....	21
Figure 2.2 Schematic of a typical Ti:sapphire laser using Kerr lens mode-locking.....	22
Figure 2.3 Schematic of mode-locking in wavelength components.....	23
Figure 2.4 Relationship in laser pulses between time and frequency domain.....	25
Figure 2.5 Affection of linearly frequency-chirped pulses.....	29
Figure 2.6 (a) Schematic of Chirped Pulse Amplification (CPA); (b) Schematic of the CPA system used in the experiments other than Chapter 3.....	30
Figure 2.7 Schematic of a Martinez-type stretcher.....	31
Figure 2.8 Schematic of an Offner-type stretcher.....	32
Figure 2.9 Schematic of a regenerative amplifier.....	33
Figure 2.10 Schematic of a pulse compressor with a diffraction grating pair.....	34
Figure 2.11 Schematic of optical Fourier transform with lens.....	36
Figure 2.12 Schematic of optical Fourier transform in $4f$ -optical imaging system.....	38
Figure 2.13 Schematic setup of SF-STAMP snapshot multispectral imaging system: diffractive optical element (DOE) and band-pass filter (BPF).....	39
Figure 2.14 Schematic of spatially and spectrally resolving by a DOE and a BPF.....	41
Figure 2.15 Side view image of spatially and spectrally resolving by a DOE and a BPF.....	42
Figure 2.16 Schematic setup of SF-STAMP multispectral imaging system.....	42
Figure 2.17 Comparison of the mechanism of 2D-burst imaging in the original STAMP and SF-STAMP.....	43

Figure 2.18 Relationship of spectral and time widths of SF-STAMP	44
Figure 2.19 Simulation of STAMP's performance; exposure time and frame interval as a function of the spectral width (quoted from [220]).....	46
Figure 2.20 Schematic setup of the single-shot pump/probe measurement with SF-STAMP	47
Figure 2.21 Diagram of the synchronization system with the optical chopper	48
Figure 2.22 Proof-of-principle experimental setup of SF-STAMP (BS: beam splitter, HCF: hollow-core fiber filled with Ar-gas, DOE: diffractive optical element, BPF: band-pass filter)...	49
Figure 2.23 (a) Wavelength-multiplexed image (from 792 to 807 nm) and (b) wavelength-multiplexed image's spectral properties.	50
Figure 2.24 Spectral properties of five image frames at different BPF rotation angles.....	50
Figure 2.25 Experimental setup of microscopic SF-STAMP system for observation of ultrafast laser ablation dynamics. To select only a probe pulse, we used a polarization analyzer after the object lens.	51
Figure 2.26 Measured single-shot SF-STAMP images of air breakdown generation within a time window of 9.2 ps. Exposure time of each frame was 1.1 ps. The dotted line shows the air-glass surface. Air breakdown was generated by an FTL laser pulse. Probe pulse was partially absorbed by air breakdown and thus attenuated (from 0 ps). A dark filament of laser-excited electrons close to the glass surface was also captured from 4.6 ps. Each image has 740×480 pixels. To avoid capturing the scattering light of a pump pulse whose spectral range was 830~770 nm, we used a probe pulse's spectral range of 770~750 nm. Scale bar represents 50 μm.	52
Figure 2.27 Measured single-shot SF-STAMP images of generation of a plasma filament in time window of 9.2 ps. Exposure time of each frame was 1.1 ps. In this case, pump pulse was focused into glass from left side. Dotted line shows air-glass surface. Scale bar represents 50 μm.....	53
Figure 2.28 Measured single-shot SF-STAMP images of plasma filament generation in time window of 2.8 ps. In this case, Exposure time and frame interval of snapshots were 527 and 700 fs. Pump pulse was focused into the glass from the left side. Focused position was 100 μm from the air-glass surface. Scale bar represents 50 μm.....	53
Figure 2.29 (a) Design of 25-beam-generating DOE (800-nm wavelength), (b) arrangement of a 25-beam-generating DOE and a BPF to spatially and spectrally resolve the image, and (c) spectral property of a broadband probe pulse and location of 25-BPF selectable bands in the spectrum.	56
Figure 2.30 25-multispectral images captured by the SF-STAMP system.	57
Figure 2.31 Microscopic images (a) at object plane, (b) at image plane of the 25-frame SF-STAMP	

system.....	57
Figure 2.32 Measured single-shot images of a plasma filament generation inside glass in a time window of 5.6 ps: with the exposure time and frame interval of 0.52 ps and 0.23 ps.....	58
Figure 2.33 Optical property (a) n , (b) k , and (c) α of the amorphous, rocksalt, and hexagonal phases of Ge ₂ Sb ₂ Te ₅ (quoted from [230]).....	59
Figure 2.34 Microscopic image of GST sample and its structure.....	60
Figure 2.35 Experimental setup of ultrafast crystalline-to-amorphous phase transition in GST.	60
Figure 2.36 Measured images of crystalline-to-amorphous phase transition in GST by the 5-frame SF-STAMP (single-shot time window of 1.1 ps). Exposure time and frame interval of snapshots were 465 fs and 287 fs. Scale bar represents 50 μm	61
Figure 2.37 Measured images of crystalline-to-amorphous phase transition in GST by the 25-frame SF-STAMP (single-shot time window of 3.2 ps). Exposure time and frame interval of snapshots were 465 fs and 133 fs. Scale bar represents 50 μm	62
Figure 2.38 Simulation of SF-STAMP's temporal performance; exposure time and frame interval: (a) as a function of bandwidth (dispersion amount of 0.082 ps/nm) and (b) as a function of the amount of dispersion: ($\Delta\lambda_{\text{BPF}}$ of 2.2 nm and $\Delta\lambda_{\text{DOE}}$ of 1.66 nm).	64
Figure 2.39 Simulation of SF-STAMP's temporal performance with $\Delta\lambda_{\text{BPF}}$ of 2.2 nm and $\Delta\lambda_{\text{DOE}}$ of 3.3 nm; exposure time and frame interval as a function of the amount of dispersion: (a) center wavelength of 800 nm and (b) center wavelength of 400 nm.	64
Figure 2.40 Schematic of Free-space Angular-Chirp-Enhanced Delay (FACED) (Figure reproduced with permission from [144]: doi:10.1038/lisa.2016.196 © 2017 NPG).....	67
Figure 2.41 (a) Schematic setup of the spectrally sweeping delayed pulses generation by a 4f-FACED system, (b) spectrum of amplified Ti:Sapphire laser pulse and spectra of spectrally sweeping pulses generated by the 4f-FACED.	70
Figure 2.42 (a) Experimental setup of the combination of a SF-STAMP and spectrally sweeping burst pulses, (b) Multispectral image captured by the 25-frame SF-STAMP using spectrally sweeping burst pulses.....	71
Figure 2.43 Experimental setup of single-shot ultrafast burst imaging with a sub-ns.....	72
Figure 2.44 Measured single-shot image of shock wave evolution on glass by SF-STAMP with 300-ps interval spectrally sweeping FACED pulses. Scale bar represents 50 μm	73
Figure 2.45 Measured single-shot image of growth process of laser induced ablation plume on glass by SF-STAMP with 100-ps interval spectrally sweeping FACED pulses. Scale bar represents 100 μm	73

Figure 3.1 Experimental setup of 2D-burst imaging by SF-STAMP.....	78
Figure 3.2 Schematic setup of 1D-consecutive optical streak imaging (OSI).....	79
Figure 3.3 Experimental setup of 1D-consecutive optical streak imaging (OSI).....	80
Figure 3.4 THz field and spectrum characteristics. (a) The incident free-space single-cycle THz pulses have a maximum 410 kV/cm electric field. (b) THz spectrum is centered at 0.8 THz.	81
Figure 3.5 Temporal and spectral characterization of chirped probe pulses. (a) Experimental setup of chirped EO sampling with a spectrometer. For chirped EO sampling with 4-ps and 400-ps probes, we used a 30- μm LNO slab and a 200- μm ZnTe crystal, respectively. (b) Chirped probe spectrum and its Gaussian fit. The probe spectrum has a bandwidth (full width at half maximum) around 24 nm and can be fitted by a Gaussian function: $e\lambda - 79022 \times 102$. (c) 4-ps chirped probe spectra with THz off (black curve) and on (red curve). The difference between probe spectra with THz on and off is given by the orange curve. The THz-shape signal near 795 nm is THz-induced electro-optical (EO) signal in a thin lithium niobate slab (30 μm) and was used to determine the THz arrival time within the probe window. (d) The black curve shows the 400-ps chirped probe spectrum. Three bottom curves (yellow, orange and red curves) show the THz EO signal measured with a 200- μm ZnTe crystal with different THz arrival time in a 200-ps negative chirp probe window. By changing the optical path length of the probe beam, the THz EO signal moves across the probe spectra, which are shown in the yellow, orange and red curves and were used to determine the THz arrival time.....	83
Figure 3.6 Measurements of irreversible THz-driven phase transition dynamics in multilayer MoTe_2 by multiple single-shot spectroscopy. Schematics of multilayer MoTe_2 on THz metamaterial structure with a single THz pulse excitation and single-shot microscopic probes, including 2D-burst imaging of sequentially timed all-optical mapping photography utilizing spectral filtering (SF-STAMP), one-dimensional optical streak imaging (1D-OSI) and oscilloscope readout. By probing the sample with a chirped laser pulse and analyzing the reflected pulse with a spatial mapping device and a charge-coupled device (CCD), SF-STAMP and 1D-OSI can capture the irreversible phase transition with a 500-fs to 500-ps time window and 100-fs to 10-ps temporal resolution. The oscilloscope readout method with a fast photoreceiver can resolve the dynamics up to a millisecond observation time window with a 200-ps temporal resolution by using a CW laser light and detecting the reflected light intensity.	85
Figure 3.7 Single-shot multispectral temporal snapshots of before a THz pulse irradiation, with a THz pulse, after irradiation measured by SF-STAMP. A THz pulse intensity was 410 kV/cm.....	87
Figure 3.8 Temporal snapshots of transient reflectivity change in MoTe_2 by a THz pulse irradiation. To	

visualize the dynamics in these snapshots, we normalized the spectral intensity with that measured before the THz-pump excitation. The time window of the negative chirped 20-nm bandwidth (770~730 nm) probe pulse was 228 ps. An exposure time and the frame interval of the snapshots were 35.3 ps and 25 ps, respectively. The scale bar represents 2 μm . The diameter of circles occupied 550 pixels..... 88

Figure 3.9 Single-shot 1D-optical streak images of before a THz pulse irradiation, with a THz pulse, after irradiation measured by 1D-OSI. A THz pulse intensity was 410 kV/cm. The scale bar represents 2 μm 89

Figure 3.10 A few hundreds of picoseconds dynamics of THz-driven irreversible phase transition in multilayer MoTe_2 . (a) Optical image of before THz pumping (left) and SF-STAMP burst images of multilayer MoTe_2 after single THz pulse irradiation at 410 kV/cm (right). The temporal snapshot of STAMP images cover from -25 ps to 250 ps with a frame interval of 25 ps. A distinct reflection drop occurs uniformly at the MoTe_2 within the gap after the THz irradiation and stabilizes around 100 ps after THz excitation. (b) 1D-OSI data of multilayer MoTe_2 after a single THz pulse. The inset shows the optical image of the sample used for 1D-OSI measurement. We first observed a THz-pulse shaped reflectivity change around time-zero, which is followed by a fast reflection drop. At around 30-40 ps after THz excitation, we observed a reflection plateau, which lasts for around 20-25 ps before it drops again and stabilizes at a lower reflectivity level within the 200-ps observation window. After 1 sec., a small reflectivity recovery is observed. In both 2D and 1D case, probe pulses were stretched by negative chirp via grating pair compressor. Thus, in this configuration, the left-hand side of the horizontal axis is the shorter wavelength component. To visualize the reflectivity change, we normalized the spectral intensity of single-shot data with that of the only probe information measured before the THz pump pulse excitation. 91

Figure 3.11 Irreversible phase transition dynamics with a 50-ps observation window. (a) The inset shows the optical image of the multilayer MoTe_2 sample for the 50-ps single-shot dynamics measurement. At around zero delay position, a THz-shaped reflectivity change is observed. Due to a shorter duration of chirped probe, the temporal resolution in this measurement is around 1 ps, which enabled us to observe coherent oscillations after the THz excitation. At around 32-ps delay, the reflection plateau is also observed. (b) Fast Fourier transform (FFT) of time-domain data with three consecutive time windows. Three consecutive time windows (8.5-20 ps, 20-31.5 ps, and 31.5-43 ps) have the same size and identical FFT conditions, thus the FFT intensity in three plots can be reliably compared. The FFT of time window from 20-31.5 ps clearly shows two peaks at

0.39 THz and 1.26 THz, which is close to reported interlayer breathing and shear mode of multilayer MoTe₂, respectively. Those two interlayer oscillations harden at earlier delays (8.5-20 ps) and completely disappear at the reflection plateau region (31.5-43 ps). (c) The oscillations correspond to the interlayer breathing mode and interlayer shear mode of multilayer MoTe₂.93

Figure 3.12 Slow (>ns) and ultrafast (<5 ps) dynamics of the THz-driven irreversible phase transition.

(a) The inset shows the optical image of the MoTe₂ sample. The black curve shows the reflectivity change dynamics with a 4-ns observation window. The red curve shows the instrumental response measured with a 35-fs ultrashort pulse. The reflectivity drop is slightly slower than the instrumental response, which means the actual reflection dynamics is in a similar level of the instrumental response at 200 ps. (b) The reflectivity change shows a step-function-like response at time zero with a 90- μ s observation window, followed by an exponential reflectivity recovery process with a time constant of 0.96 μ s. The reflectivity starts to drop exponentially with a time constant of 10.6 μ s in the middle of the recovery process. The inset shows the exponential fitting of the two slow dynamics. (c) SF-STAMP burst images show ultrafast dynamics with 4-ps window. The reflectivity drop only happens at the left and right edge of the sample, as well as the edges between the gold substrate and the sample. Since the reflectivity change does not emerge in the middle of the gap in the initial process after THz irradiation, the 4-ps ultrafast 2D-dynamics with a fine spatial resolution cannot be obtained by 1D-OSI measurements and can only be captured by SF-STAMP method.96

Figure 4.1 (a) SF-STAMP snapshot multispectral imaging system composed of a diffractive optical element (DOE) and a bandpass filter (BPF); (b) Concept of real-time consecutive 1 kHz ultrafast 2D-burst imaging by the combination of SF-STAMP system and a 1000-fps high-speed camera. 100

Figure 4.2 Experimental setup of real-time observation of pulse-by-pulse femtosecond laser processing with consecutive 1 kHz ultrafast 2D-burst imaging. 101

Figure 4.3 Generation of spectrally sweeping burst pulses by the 4f-FACED system. 102

Figure 4.4 Frame result of HS-camera with 25 frequency-time encoded SF-STAMP snapshots, which captured dynamic images of femtosecond laser-induced air plasma generation. 7th snapshot position is delay zero time. Time window of this 40-nm bandwidth (770~730 nm) probe pulse was 11.6 ps. Exposure time and frame interval of snapshots were 937 and 481 fs. Circles represent burst frames trimmed in **Figure 4.5(b)**. 105

Figure 4.5 (a) Schematic of single-shot measurement of femtosecond laser processing of glass with frequency-chirped laser pulse probe. With a 1000-fps HS-camera, we observed each pump laser

shot; (b) Measured pulse-by-pulse single-shot burst images of time evolution of laser ablation on glass and laser-induced air plasma by SF-STAMP with a 12-ps chirped probe (175×130 pixels). Horizontal column corresponds to ultrafast single-shot snapshot with seven frames (center wavelength of 761.6, 759.9, 758.3, 756.6, 753.3, 750, and 743.3 nm). Exposure time of each frame was 937 fs. Vertical column corresponds to HS-camera frames. Number in vertical column is cumulative pump pulses. Scale bar represents $50 \mu\text{m}$ 107

Figure 4.6 (a) Schematic of single-shot measurement of femtosecond laser pulse ablation of glass with spectrally sweeping burst probe laser pulses. With 1000-fps HS-camera, we observed each laser ablation shot. Shockwaves (SWs) generated by laser-induced plasma (SW_{Air}) and by ablation plume (SW_{Plume}) are indicated on images; (b) Measured pulse-by-pulse single-shot burst images of laser ablation and shock-wave evolution on glass by SF-STAMP with 300-ps interval spectrally sweeping pulses (220×150 pixels). Horizontal column corresponds to ultrafast single-shot snapshot with six frames (center wavelengths of 810, 805, 800, 795, 790, and 785 nm). Vertical column corresponds to HS-camera shots. Number in vertical direction is equivalent to number of cumulative pump pulses. Scale bar represents $50 \mu\text{m}$ 109

Figure 5.1 Results of 2D-EO chirped sampling obtained by SF-STAMP 113

Chapter 1

Introduction

Since Maiman succeeded in the first LASER (Light Amplification by Stimulated Emission of Radiation) oscillation in 1960 [1], laser technologies have contributed to various developments of science and technology. Sixty years after the emergence of laser, laser has become an indispensable fundamental technology in our technological era. In particular, since the advent of femtosecond lasers [2,3], and even the chirped pulse amplification (CPA) [4] (the 2018 Nobel Prize in Physics), the progress of optical science conducted by femtosecond technology has been remarkable. Based on the specific features of ultrafast, broad bandwidth, and high-intensity, ultrashort lasers have addressed a variety of research fields, such as ultrafast spectroscopy, high-speed communication, precision measurement using optical frequency combs, nonlinear optics, high-intensity physics, THz wave generation, and laser processing. Thus, femtosecond lasers have become essential tools in research fields such as physics, chemistry, biology, medicine, and optical communications.

For the visualization of ultrafast phenomena in two-dimensional (2D) image—i.e., the (x, y) spatial information—the femtosecond (10^{-15} s, fs) and picosecond (10^{-12} s, ps) time duration of ultrashort lasers is a compelling strobe light that stops or “freezes” the motion of the moment. Time-resolving techniques by repeatedly scanning the ultrashort strobe (probe) pulse [5–17] can capture ultrafast phenomena faster than nanoseconds (10^{-9} s, ns), which could not be realized with conventional 2D-imaging sensors of charge-coupled devices (CCDs) and complementary metal-oxide-semiconductor (CMOS) due to fundamental limitations in their electrical or mechanical operation [18]. These time-resolved images reconstruct temporal snapshots of transient events. However, it is impossible to capture a phenomenon with difficult-to-reproduce; or a phenomenon that occurs only once, such as ultrafast photochemical reaction [19], optical rogue waves [20–22], plasma physics [23], phase transition [24–30], shock-wave propagation and materials damage in laser processing [17,31–33], or biomedical applications [34].

For elucidation of the ultrafast irreversible phenomena with a single-shot basis, many efforts have been carried out, including measurements without spatial imaging or spectral resolution and measurements with either one-dimensional (1D) spatial imaging or spectral resolution [19,26,35–54]. Single-shot ultrafast 2D-imaging, which obtains the (x, y, t) data cube in one event, has been of much interest, and various methods have been proposed over the last 10 years [55–98]. In the category of single-shot optical imaging, a frequency-to-time encoding technique known as “Sequentially Timed All-optical Mapping Photography (STAMP),” invented by Nakagawa *et al.* in 2014 [58,59], is a highly promising technology. The salient

features of STAMP are the feasibility of both high-temporal (~femtosecond order) and -spatial (~micrometer order) resolution and direct burst imaging ability without post-processing or image reconstruction.

In STAMP, transient phenomena are stamped on each wavelength component of a linear frequency-chirped laser pulse probe. Thus, the spatially separated 2D-multispectral images correspond to the ultrafast temporal snapshot at each of the short observation time windows. In this way, temporal resolution variable burst imaging according to the chirped pulse width can be realized. The number of spectral images is equivalent to the possible number of time sequences in a single laser pulse. However, to fulfill the separation of different spectral images simultaneously, it demands a unique periscope-array structure that limits the total number of frames in the original STAMP to six. Additionally, the time window thus far ranges from the femtoseconds to the picoseconds regime with a chirped laser probe.

For the diverse applications of STAMP to single-shot ultrafast 2D-imaging, there are requirements to solve the problem of freedom in the number of snapshots and expansion of the time window to nanoseconds regime that has been unachieved by both conventional high-speed and cutting-edge ultrafast imaging technique.

In this study, first, to overcome the original STAMP restriction, we simplified the setup and increased the number of burst frames up to 25 by developing a STAMP-utilizing Spectral Filtering (SF-STAMP) [60–62]. Also, an extension approach to the nanoseconds time window with spectrally sweeping burst pulses has been demonstrated. Detailed descriptions are in Chapter 2.

Second, employing the SF-STAMP revealed photo- and THz-induced irreversible ultrafast phase transition processes of $\text{Ge}_2\text{Sb}_2\text{Te}_5$ and MoTe_2 , respectively. These 2D-snapshot results can be measured for the first time by SF-STAMP's powerful features of a single shot and ps-temporal and μm -spatial resolution, suggesting that the frequency-to-time encoding of STAMP has advantages over other single-shot ultrafast imaging methods. Detailed descriptions are in Chapters 2 and 3.

Third, as a real-time *in-situ* measurement application in laser processing, a conventional high-speed camera and SF-STAMP are combined. Since the temporal resolution of the STAMP method is irrelevant to the imaging sensor, by introducing a high-speed camera as a detector in STAMP, we can obtain real-time consecutive ultrafast 2D-burst images in accordance with the frame rate of the high-speed camera and STAMP's ultrafast temporal resolutions. Single-shot burst images of pulse-by-pulse femtosecond laser ablation of glass driven by a 1-kHz femtosecond laser are captured by a chirped probe pulse and used for the femtosecond to picosecond regime; and by spectrally sweeping burst pulses, are used for the sub-nanosecond regime. Detailed descriptions are in Chapter 4.

First, however, I review the ultrafast imaging techniques including the history of high-speed imaging, time-resolved pump/probe method, and 1D-streak camera in Chapter 1. I then introduce previous research on the single-shot ultrafast imaging that is the main subject of this research. Finally, the objective and structure of this thesis are described.

1.1 Ultrafast imaging

In this section, previous research related to ultrafast imaging is reviewed. Here, I define the difference between “ultrafast” and “high-speed” imaging. In this thesis, ultrafast imaging means that the frame rate of image sequences is above 5 Mfps (frame per second, or Hz), which corresponds to an adjacent frame interval that is faster than 200 ns. In general, high-speed imaging means 100 fps or higher. An exposure time (shutter speed) is also an indicator of high-speed or ultrafast imaging. **Figure 1.1** shows the time scales in different ultrafast and high-speed imaging techniques.

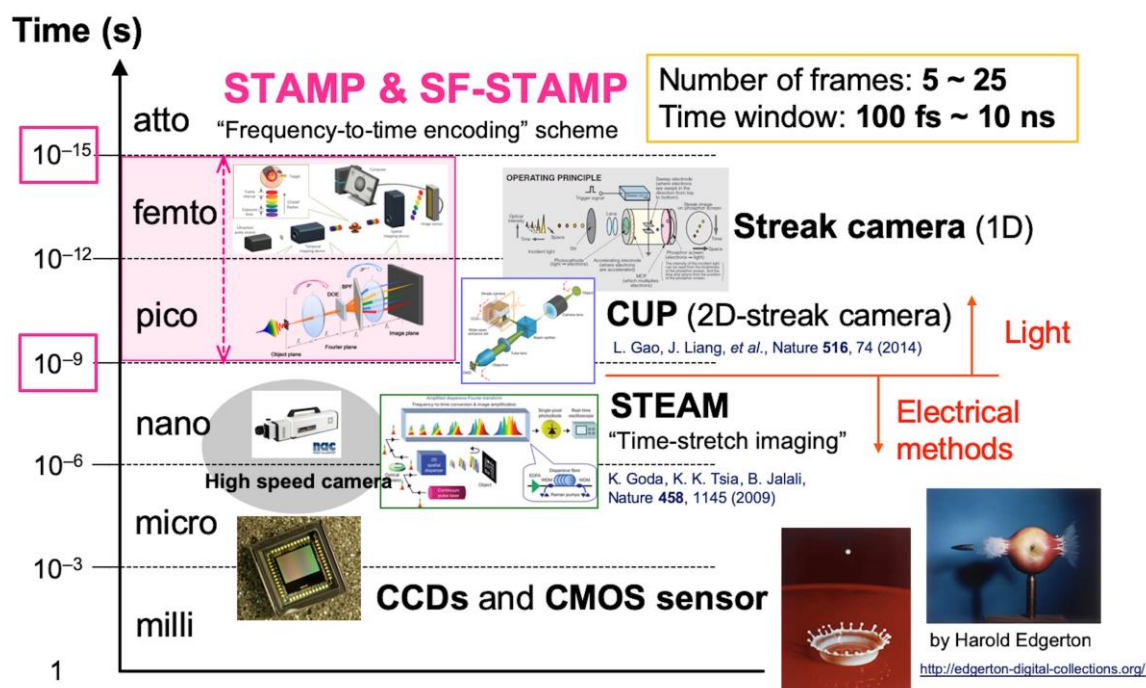


Figure 1.1 The time scales in various ultrafast and high-speed imaging techniques

1.1.1 History and basic concept of high-speed imaging

To obtain a blur-free image of transient phenomena in various areas, including physics, chemistry, biology, medicine, and industry, freezing a moment by high-speed optical imaging is an essential technique. The history of high-speed imaging has progressed in the direction of increasing the frame rate and shortening the exposure time. From the 19th century, when film cameras appeared, obtaining high-speed phenomena has been the subject of public interest. A representative example of the success in capturing high-speed phenomena are “The Horse in Motion” (photographed by Muybridge in 1878), and a shockwave was generated by a bullet that exceeded the speed of sound photographed by Mach in 1887. In 1931, Edgerton of the Massachusetts Institute of Technology (MIT) invented the strobe camera that used a flash lamp, which made it possible to record momentary events that could not be directly captured by the human eye, such as the milk drop coronet [99]. Since then, the frame rate has been improved by mechanically increasing the rotation speed of the film.

Until the 1970s, however, significant improvements had not been achieved for the utilization of charge-coupled devices (CCDs) and a complementary metal-oxide-semiconductor (CMOS). This semiconductor technology made for high-speed imaging faster than 100 kfps (below 10 microseconds) possible. However, CCD or CMOS cameras are not fast enough to reach the sub-nanosecond regime due to the electrical limitations of the memory speed and reading speed to the chip. Even in high-speed cameras, there is also a trade-off between light sensitivity and readout speed [18]. Eventually, in the 1980s, ultrafast imaging at a frame rate of 1 Tfps (sub-picosecond region) was realized with a streak camera using an optoelectronic streak tube, albeit limited in 1D spatial or spectral information.

On the other hand, from the viewpoint of exposure time, an ultrashort laser pulse is fascinating for strobe light in both high brightness and short exposure time. Therefore, a time-resolved measurement that utilizes ultrashort laser pulses, such as a pump/probe method, has been widely used. The pump/probe technique falls short for capturing non-repetitive or random events owing to its requirement for repetitive measurements, albeit providing time-resolved images of ultrafast events.

In 2009, an exotic optical time-stretch imaging method [100] that circumvented traditional limitations in high-speed imaging was invented by Goda, Tsia, and Jalali at the University of California, Los Angeles (UCLA). Serial Time-Encoded Amplified Microscopy (STEAM) [57] has overcome the imaging speed of such conventional 2D-imaging sensors as CCD and CMOS cameras and opened a window onto ultrafast 2D-consecutive imaging in the nanosecond regime. STEAM is a method of all-optical 2D-consecutive imaging using a mode-locked femtosecond laser and a single-pixel photodiode, whose real-time imaging were at a frame interval of 163 ns (a frame rate of 6.1 Mfps) and an exposure time of 440 ps. Image acquisition takes place at a 2D-optical-frequency Fourier plane of each laser pulse, and the imaging frame

rate is defined by the femtosecond laser repetition rate. Now this time-stretch technique has been widely used in spectroscopy and bioimaging [101–103]. Details of the time-stretch method are described in the latter part of Chapter 1.

Moreover, in 2014, Nakagawa *et al.* realized a single-shot 2D-burst motion-picture camera of Sequentially Timed All-optical Mapping Photography (STAMP) [58] with a frequency-chirped laser pulse. To the best of our knowledge, STAMP is thus far the best burst camera for capturing ultrafast events with a sub-picosecond temporal resolution. STAMP demonstrated burst image acquisition with equally short frame intervals of 229 fs (4.4 Tfps) and high pixel resolution (450×450 pixels).

Obviously, the advent of all-optical ultrafast imaging methods of STEAM and STAMP has boosted the research fields on ultrafast imaging both single-shot and time-resolved schemes in the last decade. Of course, imaging sensors and detection schemes have greatly improved with recent technologies [104–108], and the temporal resolution has reached the sub-nanosecond region [109], but optical approaches still have a lot of usages for ultrafast imaging applications in practical ways.

1.1.2 Time-resolved pump/probe method

There are various types of time-resolved spectroscopy; among them, the pump/probe method is widely used. In ultrafast spectroscopy, sub-picosecond temporal resolution is required, and ultrashort laser pulse probes are utilized. For example, observation of coherent phonons in solid materials [110,111]. Furthermore, using attosecond (10^{-18} s, as) lasers, extremely fast phenomena in the attosecond range have also been reported [112,113]. In addition, by employing the wavelength band of X-ray, near-infrared (NIR), mid-infrared (MIR) [114], far-infrared (FIR) [115], and Terahertz (THz), ultrafast spectroscopy outside of the visible range is also conducted. Same as 1D-spectroscopy, the time-resolved pump/probe 2D-imaging technique [5–7] provides ultrafast snapshots at different delay times. However, it falls short for imaging of difficult-to-reproduce events. **Figure 1.2** illustrates the schematic of a pump/probe method. The laser pulse is divided into two pulses: a pump (excitation) and a probe (strobe) pulse. The pump pulse-induced transient changes are measured with the probe pulse. By moving the delay stage, repetitive measurements of the different timing make time-resolved information.

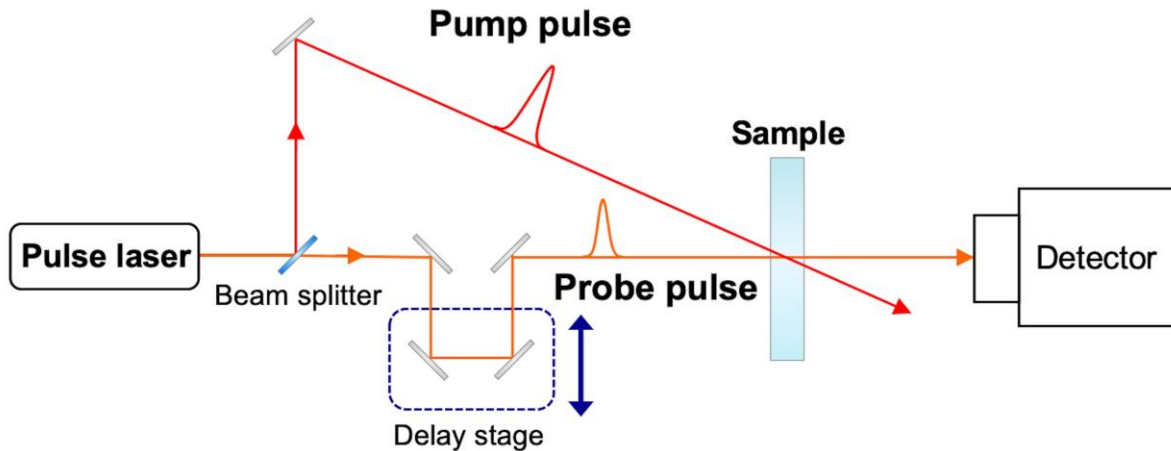


Figure 1.2 Schematic of a pump/probe method

1.1.3 Streak camera

Before 1960, when the laser was invented, the boundary of the temporal resolution in optical science was the nanosecond. The advent of the picosecond-pulse Nd-glass lasers in 1966 [116] achieved into the picosecond time resolution. However, the fastest time resolution of the photodiode at that time was 100 ps [117], so direct measurement of ps pulse duration by an oscilloscope was impossible. Therefore, as an indirect measurement method, the autocorrelation method [118,119], or the optical Kerr gate method [120–122], was used. Finally, the streak camera [123] made a direct measurement of the picosecond regime possible.

Figure 1.3(a) shows the operating principle of the streak camera. The measuring light passes through a slit (typically 10–50 μm wide) and the imaging optics (lenses) form a line image on the photocathode of the streak tube. At this position, 4-optical pulses, which vary slightly in terms of both time and space, and which have different optical intensities, are input through the slit and arrive at the photocathode. The incident light to the photocathode is converted into a number of electrons proportional to the intensity of the light; thus, these four optical pulses are converted sequentially into electrons. They then go through a pair of accelerating electrodes, where they are accelerated and blasted against a phosphor screen.

As the generated electrons pass between a pair of sweep electrodes, high voltage is applied to the sweep electrodes at a timing synchronized to the incident light (**Figure 1.3(b)**). This operation initiates a high-speed sweep (the electrons are swept from top to bottom). During the high-speed sweep, the electrons, which arrive at slightly different times, are deflected in slightly different angles in the perpendicular direction and enter the micro-channel plate (MCP). The electrons are multiplied several thousands of times

at the MCP, after which they impact against the phosphor screen, where the electrons are converted again into the light. On the phosphor screen, the phosphor image corresponding to the optical pulse which was the earliest to arrive is placed in the uppermost position, with the other images being arranged in sequential order from top to bottom, that is, the vertical direction on the phosphor screen works as the time axis. Also, the brightness of the various phosphor images is proportional to the intensity of the individual incident optical pulses. The position in the horizontal direction of the phosphor image corresponds to the horizontal location of the incident light. In this way, the streak camera can convert changes in the temporal and spatial light intensity of measuring light into an image of the brightness distribution on the phosphor screen. Thus, in the finally obtained 2D-image, an ultrafast event's spatial information is contained in the horizontal axis while the temporal information is contained in the vertical axis. i.e., the 1D-space-time data set of the (x, t) is measured.

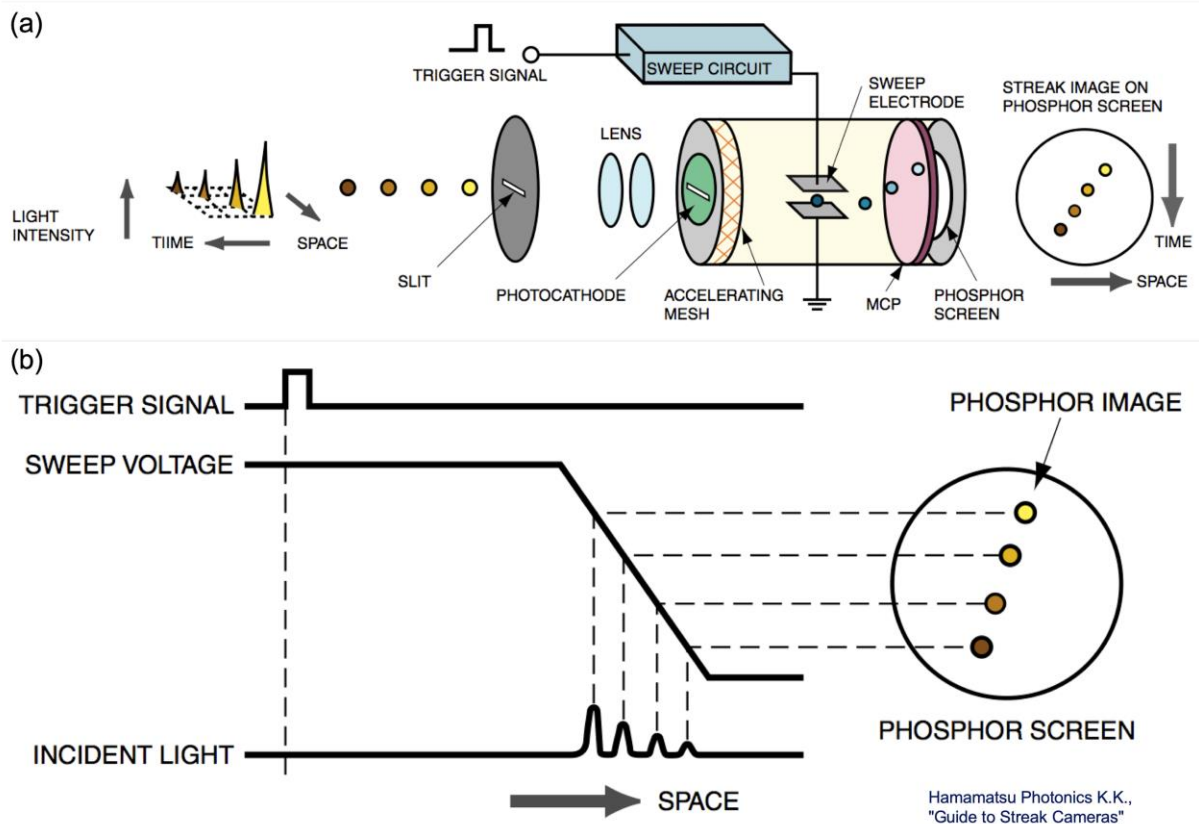


Figure 1.3 (a) Operating principle of the Streak tube, (b) Operation timing at time of sweep (quoted from [123])

As described aforementioned, a streak camera serves a 1D-ultrafast imaging device. Currently, a commercialized streak camera reaches the time resolution of up to 100 fs [124] although its narrow entrance slit limits the imaging field of view (FOV) to the line shape.

However, acquiring a 2D-time sequence image of (x, y, t) with a streak camera needs scans in the y -direction of that is perpendicular to its entrance slit (x -direction). This requirement imposes the severe constraints on the applicable objects; the event itself must be repetitive at each scanning position. Thus, streak cameras with multiple scanning cannot address irreversible phenomena. The single-shot 2D-streak camera methods are described in the latter part of this chapter (see 1.2.2.2).

1.2 Single-shot ultrafast 2D-imaging techniques

As reviewed the ultrafast imaging with time-resolved methods, though the reconstructed temporal snapshots have a fine temporal resolution, the object for ultrafast measurements are restricted to only reversible phenomena. To address the real-time imaging of non-repeatable event in an ultrafast time scale, a variety of single-shot ultrafast optical imaging techniques have been developed in the last 10 years [55–98]. The progress of ultrafast laser technologies [125,126], the performance improvement of ultrafast detectors [104–108], and the advent of new computational schemes in imaging, such as compressed sensing [108,127,128] and single-pixel imaging [129,130], have also encouraged the development of single-shot ultrafast imaging fields [56].

1.2.1 Category of image acquisition in single shot

According to the illumination requirement, single-shot ultrafast optical imaging can be categorized into active detection and passive detection. “Active detection” means that ultrafast phenomena are captured with illumination probe. Thus, the specially designed probe pulses are key elements in the active detection. However, the nature of active detection excludes the detection ability of luminescence. On the other hand, “passive detection” means ultrafast 2D-image detection with receive-only detectors, such as a Streak camera, and ultrafast imaging sensors. As for the number of frames in single-shot imaging, we can also differentiate the consecutive mode and the burst mode. In the rest of this section, the representative single-shot methods of both consecutive and burst mode are described.

1.2.2 Consecutive 2D-imaging

With single-shot 2D-consecutive imaging, video graphical images, that is, ultrafast movies are obtained. In general, passive detection methods are categorized into the consecutive mode, though commercialized high-speed framing cameras, such as Ultranaac Tau (Nac Image Technology, Inc.) with 1 Gfps (frame interval of 1 ns) work in burst mode, detecting 12-image sequences in total [131]. As with passive detection,

the time-stretch technique with active detection provides a consecutive image flow. Here, two representative single-shot consecutive techniques—Serial Time-Encoded Amplified Microscopy (STEAM) [57] and Compressed Ultrafast Photography (CUP) [63]—are explained.

1.2.2.1 Time-stretch imaging

The optical time-stretch method [100–103,132–140] achieves 2D-consecutive image acquisition at a frame rate of 10 Mfps to 1 Gfps by overcoming technical and fundamental limitations in conventional imaging sensors. Goda, Tsia, and Jalali originally demonstrated a STEAM camera in 2009 [57]. Image acquisition takes place at a 2D-optical-frequency Fourier plane of each laser pulse with a 2D-spectral shower.

The 2D-spectral pattern is generated by a 2D-spatial disperser that consists of a pair of orthogonally oriented spatial dispersers (a virtually imaged phased array (VIPA) and diffraction grating). The spatial information of the target is encoded to the frequency component. Then, the spectrum information is converted to a time signal by the dispersive Fourier transform (DFT) properties of light in both spatial and temporal domains. Finally, utilizing a single photodiode and a fast oscilloscope, instead of a CCD camera enables high-speed detecting in real-time. Therefore, STEAM utilizes space-to-frequency and frequency-to-time encoding. In the consecutive time-stretching imaging, a frame rate and an exposure time are determined by a repetition rate of the probe laser pulse and a pulse duration, respectively. By virtue of its affinity with optical signal processing, time-stretch imaging can be combined with various optical techniques such as amplification, nonlinear processing, and compressive sensing [135]. In this sense, optical time-stretch imaging is a powerful ultrafast real-time imaging scheme in the nanoseconds to microsecond regime, albeit lack of detection ability of fluorescence imaging.

For high-speed fluorescence imaging, radiofrequency versions of optical time-stretch imaging, such as fluorescence imaging by radiofrequency-tagged emission (FIRE) [141] have been demonstrated [142,143]. In this case, spatial profile of the fluorescence signal is encoded into its radiofrequency spectrum.

A time-stretch approach outside of optical fiber was recently reported [144–147]. This free-space angular-chirp-enhanced delay (FACED) [144,148,149] realized the visible wavelength time-stretch laser scanning imaging for the first time.

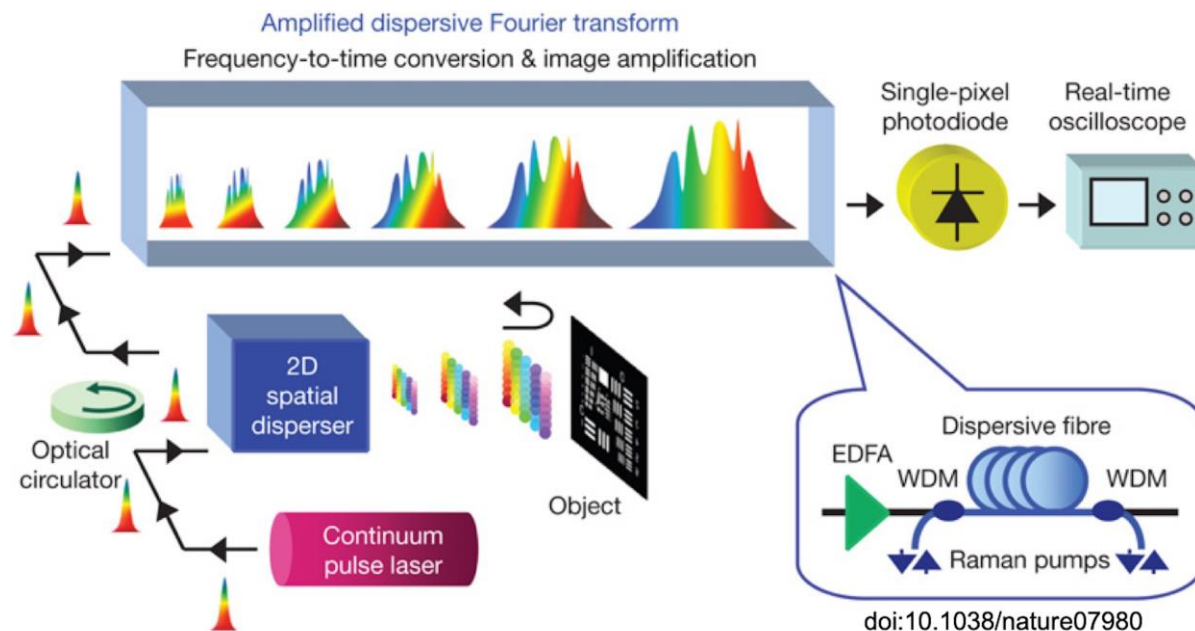


Figure 1.4 Schematic of Serial Time-Encoded Amplified Microscopy (STEAM)

(Figure reproduced with permission from [57]: doi:10.1038/nature07980 © 2009 NPG)

Figure 1.4 shows the schematic setup of the optical time-stretch imaging by STEAM. The STEAM camera maps a 2D-image into a serial time-domain waveform in every repetitive pulse train. A broadband pulse from the mode-locked femtosecond pulse laser first enters the 2D-spatial disperser that maps the spectrum component into 2D-spectral probes. The 2D-probes are incident onto the object. The object is illuminated by different frequency components of the 2D-probes and the spatial information of the object is encoded to the spectrum showers. The reflected 2D-probes then return to the spatial disperser and recombine into one pulse; in this process, space-to-time encoding is achieved. Next, the pulse enters the amplified DFT to map the spectrum of the image-encoded pulse into a temporal waveform and to optically amplify it before detecting it with a single-pixel photodiode and an oscilloscope. By virtue of DFT, the optically amplified spatial profile, which is encoded into the frequency components, appears as a modulated waveform in the time domain. Finally, a 2D-profile is constructed by sorting back the 1D-time information. In the first demonstration of STEAM, real-time consecutive ultrafast imaging with a frame interval of 163 ns (a frame rate of 6.1 Mfps), and an exposure time of 440 ps was realized.

1.2.2.2 Two-dimensional Streak camera

As mentioned in the Streak camera section (1.1.3), an obtained ultrafast sequence by a Streak camera [123], which transforms the temporal profile of an incident light into a spatial profile on an image sensor, is limited in 1D-spatial information, albeit with a sub-picosecond temporal resolution. 2D-image acquisition methods by a Streak camera with down-sampling 2D-spatial profile to 1D-spatial information have been demonstrated. The 2D-image is reconstructed from the space-encoded 1D-streak images. For spatial information down-sampling schemes, image sampling with pinhole array [150–152], tilted lenslet array [75], time-unwarping [153], and time-folding [86] have been proposed. However, these 2D-Streak cameras suffer from the number of frames or single-shot detection.

To overcome this problem and to realize a single-shot consecutive 2D-Streak camera without employing any mechanical or optical scanning mechanism, Gao, Liang¹, *et al.* invented the method of Compressed Ultrafast Photography (CUP) [63] in 2014.

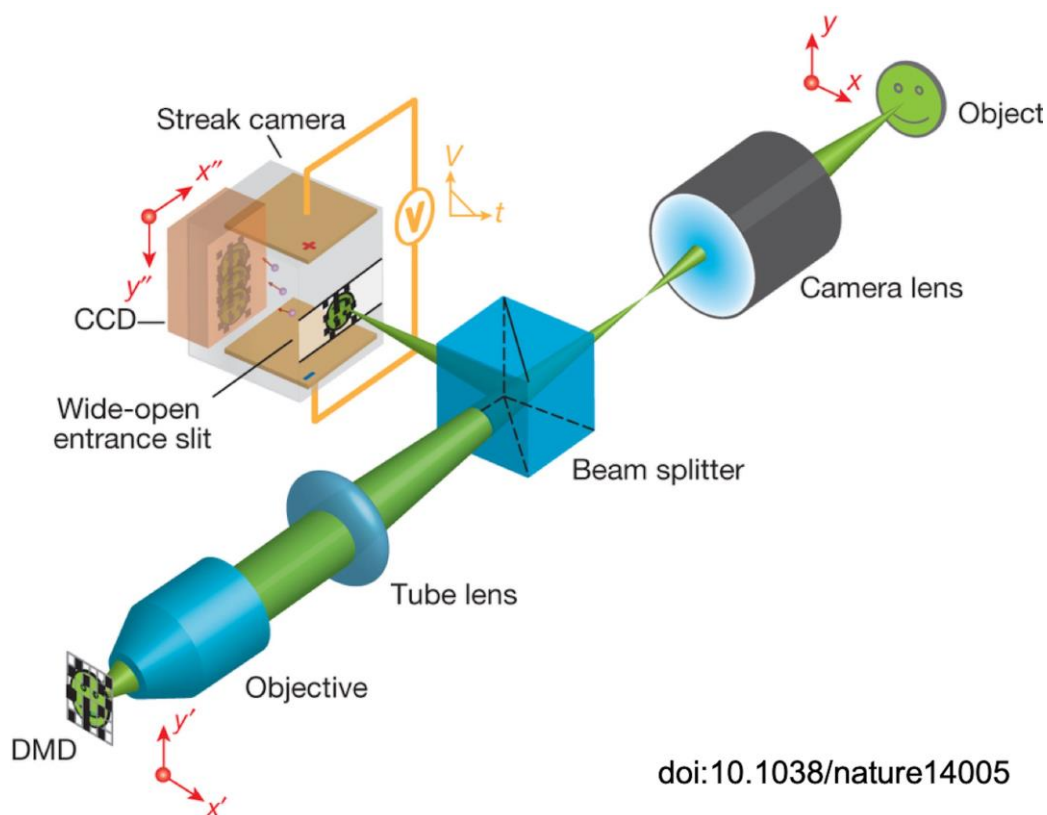


Figure 1.5 Schematic setup of Compressed Ultrafast Photography (CUP)

(Figure reproduced with permission from [63]: doi:10.1038/nature14005 © 2014 NPG)

¹ These authors contributed equally to the work.

Figure 1.5 depicts a schematic of the 2D-Streak camera by CUP. In CUP, an input image is encoded with a pseudo-random binary pattern by a digital micromirror device (DMD) as the spatial encoding module, and then temporally dispersed along a spatial axis using a Streak camera. With compressed sensing algorithms, the 2D-temporal snapshots are reconstructed. The frame rate of the reconstructed video in CUP is determined by v/d , where v is the temporal shearing velocity of the streak camera, and d is the pixel size of the internal CCD along the temporal shearing direction. The prominent advantage of CUP deriving from the receive-only passive detection is the imaging ability of a variety of ultrafast luminescent phenomena with a single-shot basis. So far, the CUP-based single-shot ultrafast imaging [63–69] has demonstrated imaging speed up to 10 Tfps (frame interval of 100 fs) with an exposure time of 580 fs and 350 frames. Each frame was occupied with 450×150 pixels [67]. However, the problem of low spatial resolution (The original CUP resolution was ~ 0.36 line pairs per mm [63].) compared to other single-shot ultrafast imaging methods still remains, and there is space for improvement of image reconstruction.

1.2.3 Burst 2D-imaging

Single-shot 2D-burst imaging method is categorized to active detection and divided into three different operation schemes in probe variations: space-to-time (S2T) and spatial frequency-to-time (SF2T), angle-to-time (A2T), and frequency-to-time (F2T) encoding. In general, the possible number of frames in burst operation is the same as number of active probes.

1.2.3.1 Space- (spatial frequency-) to-time encoding

In this subsection, single-shot 2D-burst imaging methods with space-to-time (S2T) encoding and spatial frequency-to-time (SF2T) encoding are described.

The S2T encoding method constructs temporal 2D-snapshots with spatially and temporally different probe pulses. Thus, a different spatial position has different time information. To generate spatio-temporal discrete pulses, the echelon is typically used with a method such as femtosecond time-resolved optical polarimetry (FTOP) [71,77,85]. However, the number of frames and the imaging FOV are a tradeoff in the S2T. The time-resolved technique of light-in-flight (LIF) [154–157] is also a kind of S2T method. Recently, single-shot LIF-holography [74] was reported, but the constraint of the number of frames and FOV is the same as the S2T. Due to the space requirement in the S2T, imaging configurations of FTOP and LIF methods only permit non-colinear trajectory. To overcome this limitation in image acquisition, spatial mapping methods after a sample position with copropagating probe pulses have been demonstrated [80,81].

A framing camera with burst probes is another S2T. In this case, burst probes propagate in line and work as an ultrafast illumination strobe source with conventional MHz high-speed framing cameras [84,90]. Also, single-shot detections with in-line burst probes by multiple image sensors have been reported [85,92,96]. However, these approaches suffer from the freedom of scaling in the number of frames, the number of burst frames in a framing camera (typically up to 16 frames), or the number of image sensors (typically ~5 sensors).

On the other hand, the SF2T encoding utilizes collinear illumination probes with different spatial carrier frequencies. This approach can support both intensity and phase information of an imaging target with one imaging sensor; the image-encoded probes are spatially superimposed on a detector. In the reconstruction process, temporal information tagged with each probe pulse is separated at the spatial frequency domain, then 2D temporal snapshots are retrieved. In 2017, an SF2T encoding technique using intensity modulation in probe pulses referred to as “Frequency Recognition Algorithm for Multiple Exposures (FRAME)” was developed by Ehn *et al.* [70].

In FRAME, various carrier frequencies are attached to probes using sinusoidal intensity modulation by a Ronchi grating with a different orientation. The different angle sinusoidal patterns preserve the temporal information of a transient scene and are separated in the spatial frequency domain. In image reconstruction, first, the acquired superposed image is Fourier transformed. Temporal 2D-image information carried by each carrier frequency probe is separated in the spatial frequency domain. Then, the amplitude images of each carrier frequency are recovered by filtering, shifting, and inverse Fourier transforming of the isolated data in the spatial frequency domain. This procedure is the same as image retrieve of digital holography. In this case, minimum exposure time is dictated by only the laser pulse duration, so an attosecond-laser pulse may further increase video rates. A passive detection technique using this type of multiplexed structured image capture (MUSIC) has also been proposed [88]. However, to increase the probe pulses, different optical path branches are needed; thus, suffering from scaling in the number of frames, albeit the capability of high temporal resolution.

Another type of SF2T encoding methodology is the spatial frequency division multiplexing holography, such as the time-resolved holographic polarization microscopy (THPM) [78], single-shot sequential holographic imaging (SSSHI) [94], and time and spatial-frequency multiplexing (TSFM) microscopy [97]. In this sequential scheme, transient image captured probes are recoded to the interference fringes via off-axis reference pulses. The time information encoded hologram is then reconstructed with the same procedure as the aforementioned Fourier transform procedure. The SF2T hologram leverages both phase and amplitude images. However, the complexity of the experimental setup precludes scaling feasibility in increasing the number of burst frames.

1.2.3.2 Angle-to-time encoding

The angle-to-time (A2T) encoding method utilizes the different angle information. Each probe pulse with a different angle records an image of the transient events simultaneously. As the A2T methods, the direct imaging result [73] and several reconstructed methods such as spectrally multiplexed tomography (SMT) [72], Fourier domain tomography (FDT) [76], phase retrieval photography with coherent diffraction imaging (CDI) [93], and time-resolved imaging by multiplexed ptychography (TIMP) [82,83,89] have been reported. These tomographic or ptychographic approaches can reconstruct more than 30 frames in a single shot. However, the A2T method suffers from the spatial and temporal resolutions.

1.2.3.3 Frequency-to-time encoding

Frequency-to-time (F2T) encoding method is the technique used in Sequentially Timed All-optical Mapping Photography (STAMP) [58]. The F2T method utilizes frequency (wavelength) components of a chirped laser pulse as time-encoding probes. Note that the adaptation of frequency and time is not only limited to a chirped pulse; for example, a discrete pulse train with different wavelengths also works, such as FACED pulses [144,158] or multi-wavelength pulses generated by chromatic aberration of time lens [159]. After probing the transient scene, a 2D-image at a different time is stamped on each spectral information. To detect the multispectral 2D-information separately, dispersive optical elements or snapshot multispectral imaging systems are used. Finally, 2D-temporal snapshots of (x, y, t) are directly obtained without image reconstruction. Recently, some STAMP like F2T methods have also been reported [79,91,95,98]. Meanwhile, employing an imaging spectrometer as a detection side of the F2T enables single-shot ultrafast consecutive 1D-optical streak imaging (OSI) spectroscopy [35]. A detailed description of 1D-OSI is in Chapter 3.

Here, the single-shot F2T encoding 2D-burst imaging of STAMP [58] is introduced. STAMP was invented by Nakagawa *et al.* in 2014 to realize ultrafast single-shot all-optical imaging with a femtosecond mode-lock laser that is faster than STEAM. STAMP employs a linear frequency-chirped laser pulse as a strobe probe and adapts wavelength dispersion to the group delay time (i.e., converting the wavelength to the time axis by the F2T). Then different wavelength daughter pulses in which 2D-image information is encoded are spatially mapped on a CCD camera such that the captured images are snapshots of the target. In this way, STAMP works as a single-shot 2D-burst camera with sub-picosecond temporal resolution.

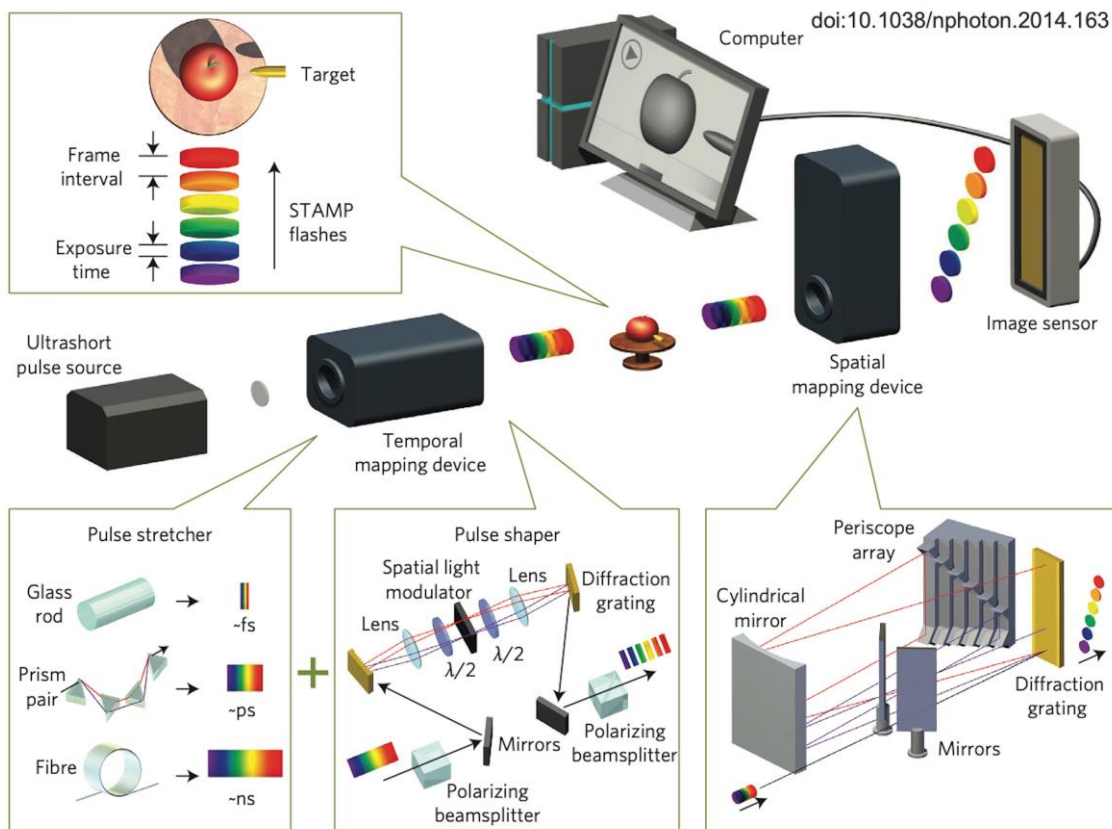


Figure 1.6 Schematic of Sequentially Timed All-optical Mapping Photography (STAMP)

(Figure reproduced with permission from [58]: doi:10.1038/nphoton.2014.163 © 2014 NPG)

Figure 1.6 shows a schematic of the STAMP. The basic concept of STAMP is to capture the ultrafast transient phenomena with a frequency-chirped pulse. This is achieved by two processes: temporal mapping device (TMD) and spatial mapping device (SMD). First, a femtosecond pulse passes through a TMD composed from a pulse stretcher and a $4f$ -pulse shaper. Depending on specific experimental requirements, the pulse stretcher uses different dispersing elements to stretch the chirped pulse duration. The pulse shaper then filters different frequency components of the chirped probe, generating spectrally sweeping burst probe pulses. In the case of the original STAMP, 6-burst pulses probe the transient event. After the target, these transmitted probes pass through an SMD, which uses a diffraction grating and imaging optics to separate multispectral images in space. Finally, the time-encoded spectral images are directly recorded in different areas on an imaging sensor simultaneously. To the best of our knowledge, STAMP is thus far the world's fastest burst camera for capturing ultrafast events with a sub-picosecond temporal resolution. STAMP demonstrates burst image acquisition with equally short frame intervals of 229 fs (4.4 Tfps) and high pixel resolution (450×450 pixels). Therefore, STAMP is a compelling 2D-direct imaging method with both high temporal and spatial resolution on a single-shot scheme.

In STAMP, the snapshot of spectral images measured by a linearly frequency-chirped laser pulse corresponds to the temporal snapshot. Therefore, the combination of a snapshot multispectral imaging system and the F2T encoding performs a STAMP. Spectral shapers with a periscope array [160] or with slice mirrors [161] have been reported for the STAMP application.

However, the number of unique periscopes used in the original STAMP scheme limited the total number of frames to six. Also, the time window ranges from femtoseconds to picoseconds regime so far. For the diverse applications of STAMP to single-shot ultrafast imaging, there are requirements to solve the problem of freedom in the number of snapshots and expansion of the time window to nanoseconds regime unachieved by both conventional high-speed and cutting-edge ultrafast imaging technique.

1.3 Objective of this Thesis

As reviewed in the ultrafast imaging techniques so far, single-shot ultrafast imaging circumvents the limitation in conventional high-speed cameras temporal resolutions and is expected to pave a way to measure transient phenomena in the femtoseconds to nanoseconds domain in real time. Obtained basic knowledge by single-shot 2D-snapshot will bring many insights into physics, chemistry, and the medical sciences. Excellent reproducible events can be measured by a widely used time-resolved pump/probe method; but difficult-to-reproduce phenomena such as irreversible phase transition in crystal chemistry, in-vivo scattering effects, laser-induced shock waves, and laser chaos are not suitable for repetitive measurement due to poor precision reproducibility. If the fluctuation of the excitation pump laser output is sensitive to measurements, the time-resolved method will cause an error, albeit with the highly reproducible phenomenon. Among the single-shot methods, a frequency-to-time encoding of STAMP is the only method capable of direct 2D-burst imaging with both high temporal and spatial resolution on a single-shot basis. This single-shot approach leverages an observation window ranging from sub-picoseconds to nanoseconds, which is impossible to access by the conventional ways. Thus, STAMP is a highly attractive imaging technique that addresses observations of ultrafast irreversible phenomena. However, for the diverse applications of a STAMP method to single-shot ultrafast imaging, there are requirements to solve the problem of freedom in the number of snapshots and expansion of the time window to nanoseconds regime.

This study aims to reveal various ultrafast nonrepetitive phenomena in real-time by developing and applying the modified version of STAMP utilizing Spectral Filtering (SF-STAMP) for single-shot measurement. The first half of this thesis focuses on the establishment of a comprehensive SF-STAMP methodology with a simple but widely applicable to single-shot ultrafast 2D-burst imaging. First, to realize the freedom of scaling simplicity, the development and improvements of the 25-frame snapshot SF-STAMP multispectral imaging system have been achieved. Then, to expand a time window for nanoseconds regime, spectrally sweeping burst probes with a ~ 100 -ps interval generated by a $4f$ -FACED system have been applied to the SF-STAMP scheme.

The second half of this thesis addresses the single-shot measurements of photo- and THz-induced irreversible ultrafast phase transition processes in $\text{Ge}_2\text{Sb}_2\text{Te}_5$ and MoTe_2 , respectively, that can be observed for the first time by virtue of SF-STAMP's notable features of a single shot and ps-temporal and μm -spatial resolution. Moreover, a real-time *in-situ* measurement application in multiple femtosecond laser pulses processing has been demonstrated by combining a conventional high-speed camera and SF-STAMP. These results highlight that the frequency-to-time encoding of STAMP has advantages over other single-shot ultrafast imaging methods.

1.4 Structure of this Thesis

This thesis consists of six chapters. The schematic structure is shown in **Figure 1.7**. Chapter 2 describes the fundamentals of the ultrafast laser used in this study, the principle of the ultrafast 2D-burst imaging scheme of sequentially timed all-optical mapping photography utilizing spectral filtering (SF-STAMP), SF-STAMP's scaling to 25 frames, and an extension approach to the nanoseconds time window with spectrally sweeping burst pulses. Chapter 3 addresses a single-shot measurement of THz-driven irreversible phase transition in multilayer MoTe₂ by observing transient reflectivity change of a chirped probe by SF-STAMP, together with 1D-optical streak imaging (1D-OSI) spectroscopy; we observed the disappearance of the initial phase and discovered a metastable phase during the irreversible phase transition around 30-40 ps after a THz pulse excitation, and insights of THz-induced phase transition dynamics are summarized. In Chapter 4, the real-time application of SF-STAMP combining with a kHz high-speed camera is demonstrated; real-time *in-situ* measurement of laser processing evaluates the precursor process of each pulse and its effect on femtosecond laser processing of glass under multiple pulses accumulated conditions with sub-nanosecond time resolution using a chirp pulse probe or spectrally sweeping burst probes. Chapter 5 discusses the outlook for the future applications of SF-STAMP, especially laser processing and THz wave region. In Chapter 6, the experimental results and knowledge obtained in each chapter are summarized, and I conclude this thesis.

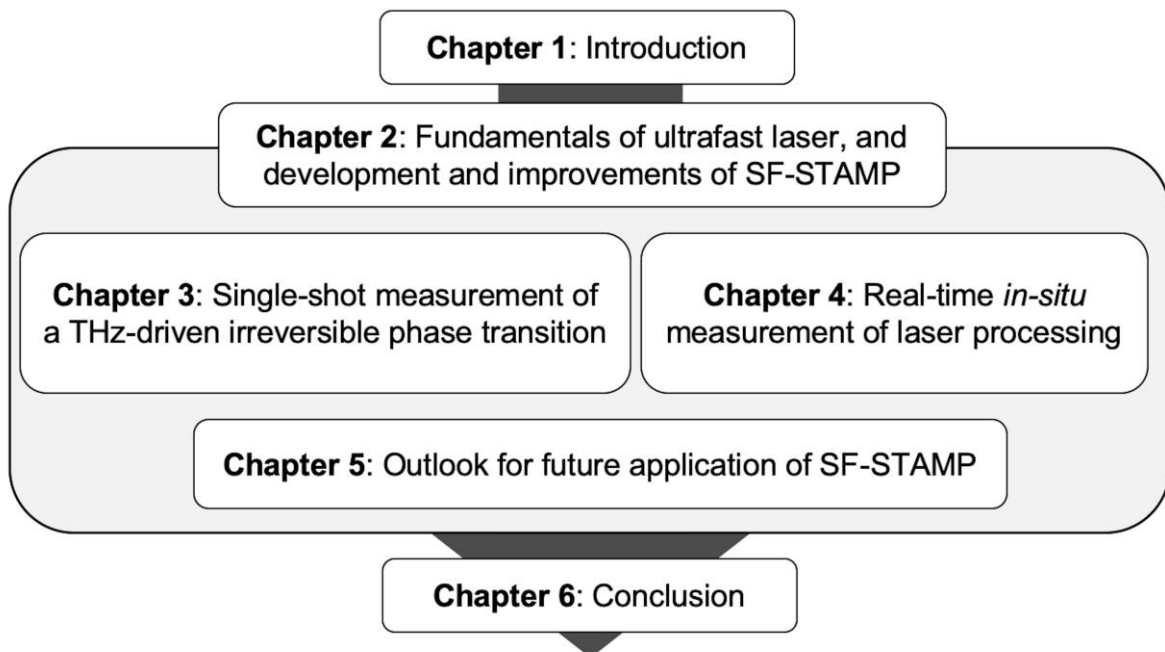


Figure 1.7 Schematic structure of this thesis

Chapter 2

Fundamentals of ultrafast laser, and development and improvements of SF-STAMP

Chapter 2 describes the fundamentals of the ultrafast laser used in this study, the principle of the ultrafast 2D-burst imaging scheme of sequentially timed all-optical mapping photography utilizing spectral filtering (SF-STAMP), SF-STAMP's scaling to 25 frames, and an extension approach to the nanoseconds time window with spectrally sweeping burst pulses.

2.1 Fundamentals of ultrafast lasers

In this section, the theory necessary for performing single-shot ultrafast 2D-burst imaging using a linear frequency-chirped pulse is described. The development and improvements of STAMP utilizing spectral filtering (SF-STAMP) are described in the latter parts of this chapter.

First, the generation and phase characteristics of the ultrashort laser pulse, and the influence of dispersion on the ultrashort laser pulse are explained. Next, the light source used in this study, the femtosecond laser amplification system by chirped pulse amplifier (CPA), is described.

2.1.1 History of ultrafast lasers

When "LASER" (Light Amplification by Stimulated Emission of Radiation) was born, it was not amplification of light but that of microwaves; hence, it was called "MASER" (Microwave Amplification by Stimulated Emission of Radiation). Here, the history from MASER to the birth of LASER is briefly reviewed. The maser begins when Einstein published the theory on stimulated emission in 1917. Later, Weber published the theory of masers in 1952, and Gordon, Zeiger, and Townes (at Columbia University) succeeded in the world's first maser oscillation in 1954 [162,163]. Based on this, the development of the maser in the near-infrared and visible range (wavelength ranging from 380 to 780 nm) was performed, and in 1958, Schawlow and Townes (at Bell Telephone Laboratories) published the theory of optical maser [164]. In 1960, Maiman (at Hughes Research Laboratories) realized the world's first LASER oscillation (wavelength of 694.3 nm) using a ruby medium [1,165]. The oscillation of the ruby laser animated the laser research and the competition for laser oscillation began in various wavelength bands. The He-Ne laser (wavelength of 632.8 nm) was developed in 1961 by Javan et al. at Bell Telephone

2. Fundamentals of ultrafast laser, and development and improvements of SF-STAMP

Laboratories [166], and the semiconductor laser was developed in 1962 by Hall et al. at General Electric Research Laboratory [167]. In the same year, GE's Holonyak et al. succeeded in semiconductor laser oscillation in the visible region [168]. In 1964, Patel of Bell Laboratories demonstrated the CO₂ laser (wavelengths of 9.4 μm and 10.6 μm) [169], and Geusic *et al.* (at Bell Laboratories) did the Nd: YAG laser (wavelength of 1064 nm) [170]. In 1966, IBM's Sorokin and Lankard developed organic dye lasers [171], and excimer lasers in the ultraviolet region [172] were invented by Basov *et al.* at Lebedev Physical Institute in 1970. These contributions brought the 1964 Nobel Prize in Physics to Townes and Basov, and the 1981 Nobel Prize in Physics to Schawlow.

On the other hand, research on pursuing a short laser pulse was also conducted eagerly. The Maiman's flashlamp-pumped ruby laser also had a pulse oscillation of about 100 ns. In 1964, using Q-switch technology, a pulse duration of 30 ns was obtained [173]. Passive mode-locking, which plays a vital role in today's short-pulse lasers, was already realized with a ruby laser in 1965 [174]. A pulse width of 0.37 ps was achieved with an Nd³⁺-doped glass laser in 1966 [116], reached to the sub-picosecond regime. In order to realize the femtosecond region, in addition to passive mode-locking [117,175,176], a gain medium with a broadband spectrum indicated by the uncertainty principle between pulse-width (Δt) and spectral width ($\Delta\omega$) given by Equation (2.1) is also required.

$$\Delta t \Delta\omega \geq K \text{ (Constant)} \quad (2.1)$$

In 1974, the CW passive mode-locking of the dye laser produced a pulse width of 0.7 ps, a repetition rate of 100 kHz, and a peak intensity of ~kW [177]. An ultrashort laser pulse of 90 fs was obtained by Fork et al. at Bell Telephone Laboratories in 1981 [178]. This made the femtosecond laser a reality. However, the dye laser was unstable due to liquid jet fluctuations and other factors, even though it has a wide gain of 10 to 50 nm which was suitable for obtaining a short pulse.

Therefore, a solid-state laser represented by the Ti:sapphire laser [2], which is almost synonymous with the femtosecond laser, has appeared. In 1991, Spence et al. (at University of St. Andrews) proposed the Kerr lens mode-locking (KLM) of Ti:sapphire laser, and realized a pulse width of 60 fs [3,179].

2.1.2 Mode-locking Ti:sapphire femtosecond laser

As seen in the previous section, the Ti:sapphire mode-locking laser [180] popularized the femtosecond laser. The reason why Ti:sapphire crystals are widely used instead of dye lasers is a wide gain medium with high thermal conductivity, saturation intensity, and optical damage threshold. Besides, it is possible to obtain an ultrashort laser pulse of several tens of fs stably by using CW mode-locking. Moreover, the Ti:sapphire

crystal has an absorption maximum near the wavelength of 510 nm, so the second harmonic of commercial lasers of Nd: YLF (center wavelength of 1047 nm) and Nd: YAG (center wavelength of 1064 nm) can be employed as a pump light source. In recent years, Ti:sapphire lasers pumped by high power laser diodes (LDs) have also appeared [181–184].

In general, Kerr lens mode-locking (KLM) is widely used in Ti:sapphire lasers. KLM is realized by the function of a saturable absorber by changing the focusing state of the laser beam derived from the optical Kerr effect inside a laser cavity. **Figure 2.1** shows a schematic of KLM.

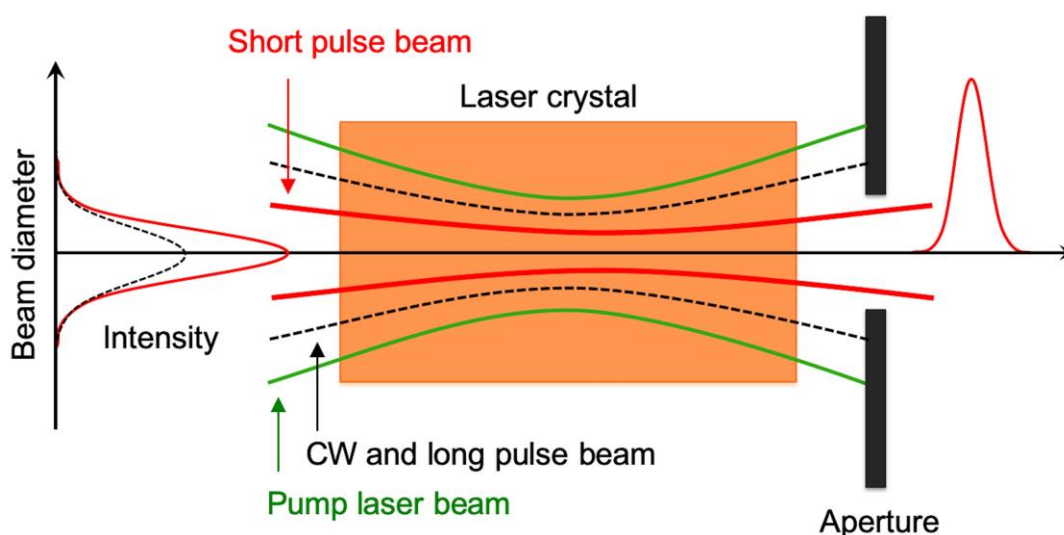


Figure 2.1 Schematic of Kerr lens mode-locking (KLM)

When the instantaneous intensity of the laser light oscillating inside the crystal becomes sufficiently large, the nonlinear refractive index change of the laser medium occurs due to the optical Kerr effect, and a refractive index distribution of a convex lens is generated so that the laser pulse is self-focused. At the same time, an optical nonlinear effect of self-phase modulation (SPM) occurs, and the spectrum becomes broadened. As a result, the distribution of spatial mode inside the oscillator changes; the shorter the pulse and the higher the peak intensity, the smaller the loss at the aperture (circular aperture); and the optical pulse itself performs as an ultrafast shutter. Therefore, the laser crystal equivalently functions as a saturable absorber, and the shorter the pulse, the larger the gain obtained by reciprocating the cavity. A broad-spectrum by SPM is also achieved. By repeating this process, the shortening of the pulse progresses, and the passive mode-locking is realized.

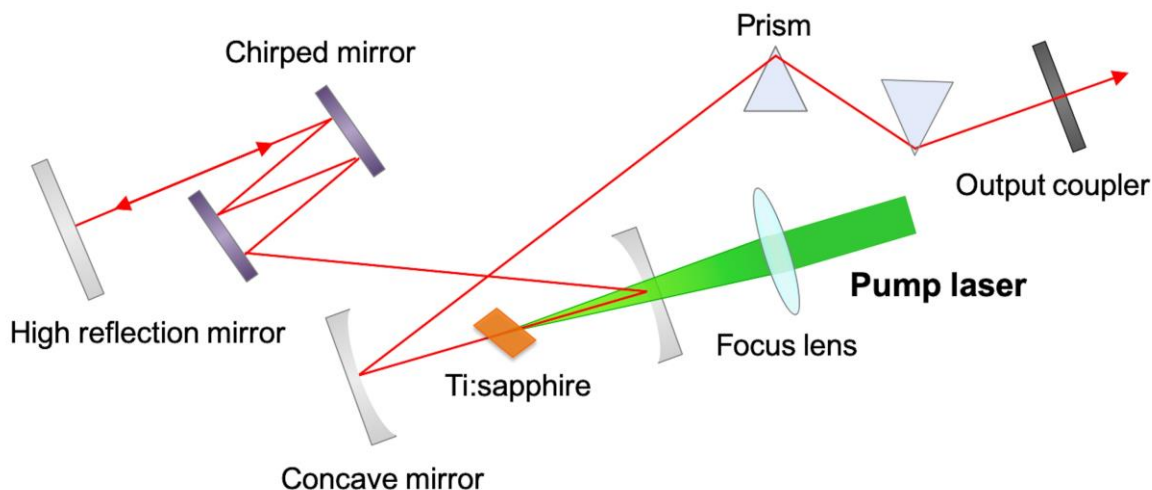


Figure 2.2 Schematic of a typical Ti:sapphire laser using Kerr lens mode-locking

A typical configuration of a Ti:sapphire laser cavity with KLM is shown in **Figure 2.2**. Inside the cavity, a concave mirror pair is placed across a Ti:sapphire crystal. When the laser pulse propagates through the crystal, the pulse width is stretched due to material dispersion. For this reason, dispersion compensation mirrors (chirp mirror) consisting of the dielectric multilayer, or a prism pair compressor, are used as dispersion compensation elements. Consequently, the short pulse duration is maintained, and KLM is realized by the optical Kerr effect.

From the viewpoint of wavelength components, as shown in **Figure 2.3**, an ultrashort laser pulse is strengthened at the position where peaks of each wavelength are aligned by superimposing several waves of different wavelengths so that all wavelength (spectral) components are in phase at a certain timing. It is generated by canceling at other positions. Therefore, ultrashort laser pulses such as femtosecond lasers have a broad spectrum, unlike typical CW laser light with a narrow spectrum. Each frequency component over a wide spectrum is called a longitudinal mode, and regulating the relative phase between longitudinal modes is called mode-locking.

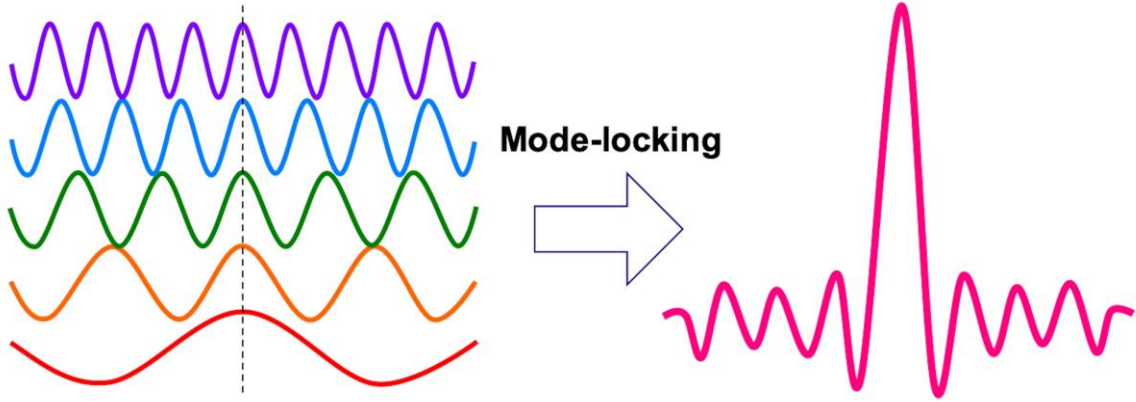


Figure 2.3 Schematic of mode-locking in wavelength components

Next, the synthesis of the ultrashort laser pulses is interpreted mathematically. The complex amplitude of the optical electric field over multiple modes of $E(t)$ is given by Equation (2.2):

$$E(t) = \sum_{q=-(N-1)/2}^{(N-1)/2} E_q e^{-j\{(\omega_0+q\Delta\omega)t + \phi_q\}} \quad (2.2)$$

Here, N is the number of all oscillation modes, $\Delta\omega$ is the longitudinal mode interval, ω_0 is the angular frequency of center (0th) longitudinal mode, E_q is the field amplitude of the q -th mode, and ϕ_q is the initial phase.

When the relative phases between longitudinal modes are regulated by mode-locking, the initial phase becomes $\phi_q = 0$ and the electric field of laser oscillation can be described as follows (for simplicity, the amplitude of the electric field in all modes is $E_q = E_0$):

$$\begin{aligned} E(t) &= \sum_{q=-(N-1)/2}^{(N-1)/2} E_0 e^{-j(\omega_0+q\Delta\omega)t} \\ &= E_0 e^{-j\omega_0 t} \sum_{q=-(N-1)/2}^{(N-1)/2} (e^{-j\Delta\omega t})^q \\ &= E_0 e^{-j\omega_0 t} (e^{-j\Delta\omega t})^{-\frac{N-1}{2}} \cdot \frac{1 - (e^{-j\Delta\omega t})^N}{1 - e^{-j\Delta\omega t}} \\ &= E_0 e^{-j\omega_0 t} e^{j\frac{(N-1)\Delta\omega}{2}t} \cdot \frac{e^{j\frac{\Delta\omega}{2}t} - e^{-j\frac{(2N-1)\Delta\omega}{2}t}}{e^{j\frac{\Delta\omega}{2}t} - e^{-j\frac{\Delta\omega}{2}t}} \end{aligned}$$

2. Fundamentals of ultrafast laser, and development and improvements of SF-STAMP

$$\begin{aligned}
 &= E_0 e^{-j\omega_0 t} \cdot \frac{e^{j\frac{N\Delta\omega}{2}t} - e^{-j\frac{N\Delta\omega}{2}t}}{e^{j\frac{\Delta\omega}{2}t} - e^{-j\frac{\Delta\omega}{2}t}} \\
 &= E_0 \cdot \frac{\sin\left(N\frac{\Delta\omega}{2}t\right)}{\sin\left(\frac{\Delta\omega}{2}t\right)} \cdot e^{-j\omega_0 t} \tag{2.3}
 \end{aligned}$$

At a period of $T = 2\pi/\Delta\omega$, a point where the denominator in Equation (2.3) becomes zero appears, and a pulse train is generated. The peak amplitude at that time is N times the amplitude of one mode.

The time width of each pulse (Δt) is $1/N$ of the period T , so it is given by Equation (2.4):

$$\Delta t = \frac{T}{N} = \frac{2\pi}{N\Delta\omega} = \frac{2\pi}{N(2\pi\delta\nu)} = \frac{1}{N\delta\nu} = \frac{1}{\Delta\nu} \tag{2.4}$$

Here, $\Delta\nu$ is the frequency interval between longitudinal modes. Thus, the standard uncertainty relationship by Fourier transform is valid between the pulse width Δt and the whole spectral width $\Delta\nu$.

$$\Delta t \Delta\nu = K \text{ (Constant determined by the shape of a pulse)} \tag{2.5}$$

Therefore, ultrashort pulses can be obtained by mode-locking in a broadband spectrum where many longitudinal modes exist (see **Figure 2.4**).

The frequency interval between longitudinal modes in a laser cavity ($\delta\nu$) can be described as follows,

$$\delta\nu = \frac{c}{2L} \tag{2.6}$$

where, L is the length of the cavity and c is the speed of light in a vacuum.

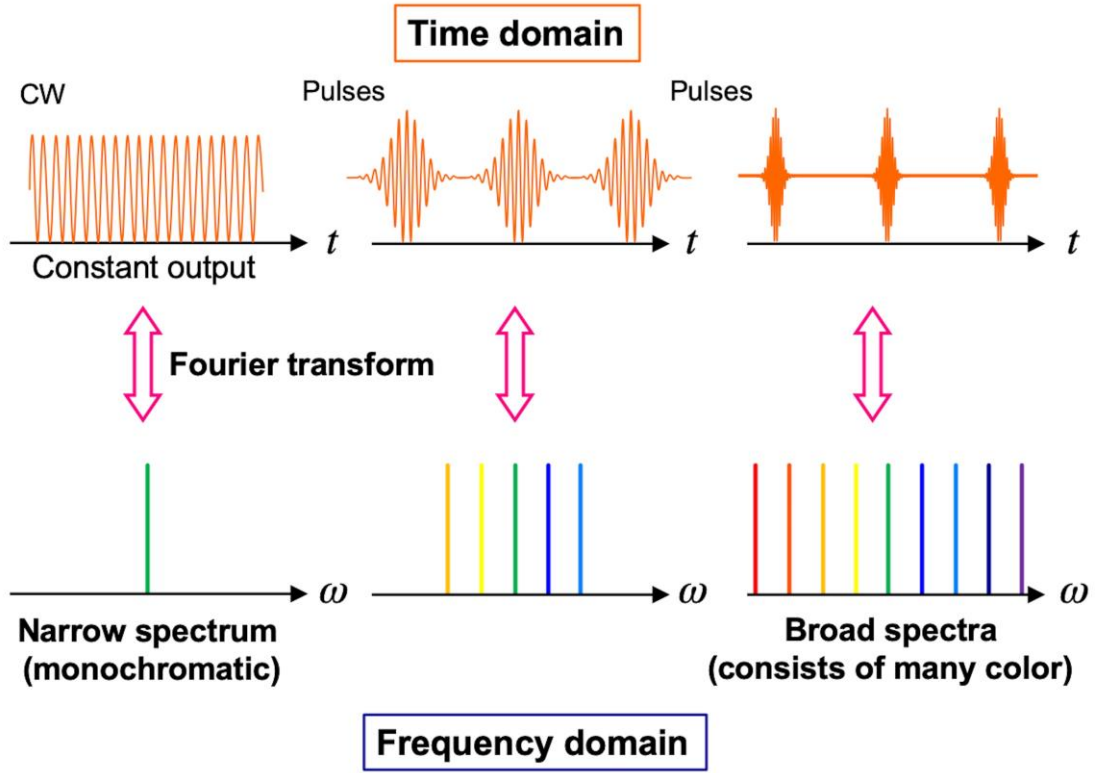


Figure 2.4 Relationship in laser pulses between time and frequency domain

2.1.3 Phase characterization of ultrashort laser pulse

The following fundamentals and description are based on some textbooks and references of ultrafast optics [185–187].

The complex amplitude of the electric field of a laser pulse in free-space $E(t)$ is given by Equation (2.7):

$$E(t) = A(t)e^{j\theta(t)} \quad (2.7)$$

Here, $A(t)$ is the time-dependent amplitude and $\theta(t)$ is the time-dependent phase. $\{A(t)\}^2$ represents the time-dependent light intensity and corresponds to the envelope of the time waveform of the observed pulse.

The time-dependent phase $\theta(t)$ can be described as Equation (2.8) with the center angular frequency of ω_0 , the time-dependent phase of $\varphi(t)$, and the absolute phase of θ_0 :

$$\theta(t) = \varphi(t) - \omega_0 t + \theta_0 \quad (2.8)$$

By changing these parameters, ultrashort laser pulses have various phase characteristics and various aspects.

For broadband pulses such as femtosecond laser pulses, in addition to the description in the time domain, the description in the frequency domain is also important in terms of understanding the dispersion

2. Fundamentals of ultrafast laser, and development and improvements of SF-STAMP

characteristics and controlling the laser pulse. The complex amplitude of the electric field of a laser pulse $E(t)$ can be expressed as a combination of Fourier frequency components:

$$E(t) = \frac{1}{\sqrt{2\pi}} \int_{-\infty}^{\infty} F(\omega) e^{-j\omega t} d\omega \quad (2.9)$$

Here, $F(\omega)$ is the Fourier frequency components and can be described as Equation (2.10) with the spectral amplitude of $B(\omega)$ and the spectral phase of $\phi(\omega)$:

$$F(\omega) = B(\omega) e^{-j\phi(\omega)} \quad (2.10)$$

$$= \frac{1}{\sqrt{2\pi}} \int_{-\infty}^{\infty} E(t) e^{j\omega t} dt \quad (2.11)$$

As can be seen from Equations (2.9) to (2.11), once the pair of the amplitude $A(t)$ and phase $\theta(t)$ is determined, the set of the spectral amplitude $B(\omega)$ and spectral phase $\phi(\omega)$ is uniquely determined, and vice versa. When $\phi(\omega)$ is constant—that is, when the spectral phase of the laser pulse is aligned over all frequency components (mode-locking)—the pulse width becomes the shortest; this is called the Fourier transform limited (FTL) pulse. At this time, the equality of the uncertainty relation between the pulse width Δt and the frequency width $\Delta\nu$ ($= \Delta\omega/2\pi$) holds.

$$\Delta t \Delta\nu \geq K \text{ (Constant)} \quad (2.12)$$

Also, by modulating the spectral phase $\phi(\omega)$, the temporal waveform of the pulse can be shaped.

Next, the dispersion effect, in which the spectral phase $\phi(\omega)$ of the laser pulse changes depending on the frequency, is explained. The main causes of dispersion are the material dispersion in which the refractive index of the substance changes with the frequency of light, and the structural dispersion derived from the structure of a waveguide or other element. In the following, we consider the dispersion effect in a linear optical system (without optical loss and nonlinear optical effects).

When the phase arises due to passage through a bulk dispersion medium of length L , we can write

$$\phi(\omega) = -\beta(\omega)L \quad (2.13)$$

where $\beta(\omega)$ is the propagation constant in the medium.

2. Fundamentals of ultrafast laser, and development and improvements of SF-STAMP

The Taylor series expansion of the spectral phase $\phi(\omega)$ and $\beta(\omega)$ around the central angular frequency ω_0 are commonly as follows:

$$\begin{aligned}\phi(\omega) &= \phi_0 + \frac{d\phi}{d\omega}(\omega - \omega_0) + \frac{1}{2} \frac{d^2\phi}{d\omega^2}(\omega - \omega_0)^2 + \frac{1}{6} \frac{d^3\phi}{d\omega^3}(\omega - \omega_0)^3 + \dots \\ &= \phi_0 + \phi_1(\omega - \omega_0) + \frac{1}{2} \phi_2(\omega - \omega_0)^2 + \frac{1}{6} \phi_3(\omega - \omega_0)^3 + \dots\end{aligned}\quad (2.14)$$

$$\begin{aligned}\beta(\omega) &= \beta_0 + \frac{d\beta}{d\omega}(\omega - \omega_0) + \frac{1}{2} \frac{d^2\beta}{d\omega^2}(\omega - \omega_0)^2 + \frac{1}{6} \frac{d^3\beta}{d\omega^3}(\omega - \omega_0)^3 + \dots \\ &= \beta_0 + \beta_1(\omega - \omega_0) + \frac{1}{2} \beta_2(\omega - \omega_0)^2 + \frac{1}{6} \beta_3(\omega - \omega_0)^3 + \dots\end{aligned}\quad (2.15)$$

The coefficient of β_1 ($= d\beta/d\omega$) in the second term on the right side of Equation (2.15) is an amount that gives the delay time to the laser pulse and is called group delay (GD) or first-order dispersion. The part of $\beta(\omega)$ that is not linear in angular frequency ($\omega = 2\pi c/\lambda$) is called dispersion. The β_2 ($= d^2\beta/d\omega^2$) term contributes a quadratic spectral phase variation, which leads to a linear variation in delay with frequency. This second-order dispersion or group delay dispersion (GDD) imparts a linear chirp to the output pulse. The β_3 ($= d^3\beta/d\omega^3$) term contributes a cubic spectral phase leading to a quadratic variation in delay with frequency. This third-order dispersion (TOD) results in an asymmetric pulse distortion in temporal waveform with an oscillatory structure. These GDD and TOD terms are sufficient to describe femtosecond pulse propagation in most dispersive media in most circumstances. However, in some very critical applications, such as sub-10-fs laser design and chirped-pulse amplifiers (CPAs) for very short pulses, additional higher-order terms must also be retained.

Here, the effect of second-order dispersion (linear chirp) on the time waveform of the laser pulse is considered. Assuming a Gaussian FTL pulse as the incident light, the electric field of the laser pulse in the time domain $E_{in}(t)$ can be expressed by Equation (2.16):

$$E_{in}(t) = A_0 e^{-\alpha t^2} e^{-j\omega_0 t} \quad (2.16)$$

The pulse width (full width at half maximum) Δt and the spectral width $\Delta\omega$ of a Gaussian pulse are as follows:

$$\Delta t = \sqrt{\frac{2\ln 2}{\alpha}} \quad (2.17)$$

$$\Delta\omega = \frac{4\ln 2}{\Delta t} \quad (2.18)$$

2. Fundamentals of ultrafast laser, and development and improvements of SF-STAMP

When this laser pulse propagates through the dispersive medium and a linear chirp ($\phi_2 = -\beta_2$) is attached, the electric field of the output pulse $E_{\text{out}}(t)$ becomes as follows:

$$E_{\text{out}}(t) = \frac{A_0}{2\sqrt{\alpha\pi}} \int_{-\infty}^{\infty} \exp\left\{-\frac{(\omega - \omega_0)^2}{4\alpha}\right\} \exp\left\{-j\frac{\phi_2}{2}(\omega - \omega_0)^2\right\} e^{-j\omega t} d\omega \quad (2.19)$$

$$\propto \exp\left\{-\frac{\alpha}{1 + 4\alpha^2 \phi_2^2} t^2\right\} \exp\left\{-j\left(\frac{2\alpha^2 \phi_2}{1 + 4\alpha^2 \phi_2^2} t^2 - \omega_0 t\right)\right\} \quad (2.20)$$

This shows that the linear chirp (GDD) alters the spectral phase, and consequently, the amplitude shape changes and the pulse width stretches in the time domain. From Equation (2.20), regardless of whether the

GDD is positive or negative, the pulse width is expanded to $\sqrt{1 + 4\alpha^2 \phi_2^2}$ times of the incident pulse, since the complex amplitude of the output pulse changes $\alpha \rightarrow \frac{\alpha}{1 + 4\alpha^2 \phi_2^2}$.

Here, the instantaneous angular frequency of $\omega(t)$ can be described as Equation (2.21):

$$\omega(t) = -\frac{d\theta(t)}{dt} \quad (2.21)$$

$$\begin{aligned} &= -\frac{d}{dt}\left(\frac{2\alpha^2 \phi_2}{1 + 4\alpha^2 \phi_2^2} t^2 - \omega_0 t\right) = \omega_0 - \frac{4\alpha^2 \phi_2}{1 + 4\alpha^2 \phi_2^2} t \\ &= \omega_0 + \frac{4\alpha^2 \beta_2}{1 + 4\alpha^2 \beta_2^2} t \end{aligned} \quad (2.22)$$

Thus, in normal dispersion ($\beta_2 > 0$), the instantaneous angular frequency becomes a positive chirp that increases linearly with time, and in the case of anomalous dispersion ($\beta_2 < 0$), it becomes a negative chirp in which the frequency decreases linearly with time. **Figure 2.5** depicts the affection of linearly frequency-chirped pulses. In a positive chirp pulse, the long-wavelength component propagates faster than the short-wavelength, whereas in the negative chirp, the short-wavelength delivers faster than the long-wavelength component.

In general, to evaluate the property of ultrashort laser pulses, pulse measurement techniques [188] of autocorrelation [189–191], spectral interferometry (SI) [192], spatial-spectral interferometry (SSI) [193,194], Frequency-Resolved Optical Gating (FROG) [195–197], and Spectral Phase Interferometry for Direct Electric-field Reconstruction (SPIDER) [198,199] are widely used.

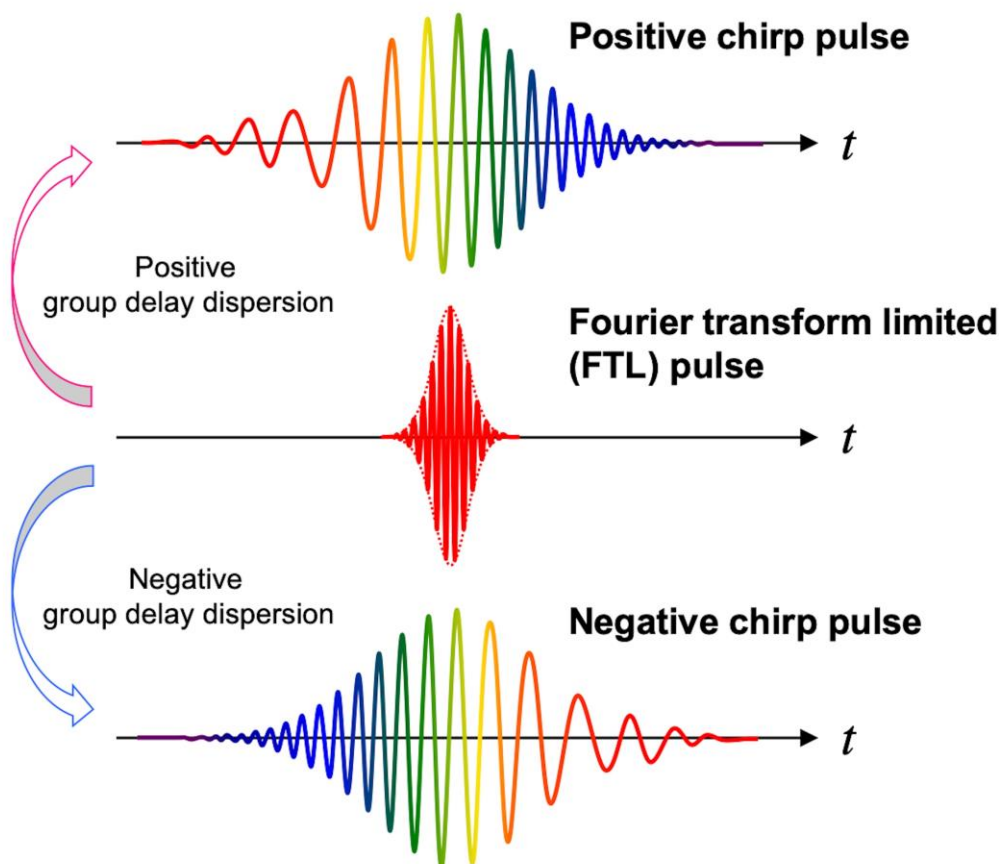


Figure 2.5 Affection of linearly frequency-chirped pulses

2.1.4 Amplified femtosecond laser system by chirped pulse amplification (CPA)

The femtosecond laser after the oscillator has pulse energy of several nJ, and its intensity is not enough for diverse applications other than mere optical measurement. Hence, in order to utilize the femtosecond laser as a light source for nonlinear phenomena such as supercontinuum generation, molecular control, and laser processing, amplification technology is required. However, only amplifying the intensity of the pulse may cause damage to the optical elements and gain medium inside the amplifier; and may degrade the spatial quality of the beam, such as self-focusing due to nonlinear optical effects. Therefore, the chirped pulse amplification (CPA) [4,200] was demonstrated for the first time by Strickland and Mourou at the University of Rochester in 1985. Now, the CPA technique has been widely utilized, and their contributions deserved the 2018 Nobel Prize in Physics. CPA is a method to obtain high pulse energy ultrashort laser pulses by three steps: expanding the pulse duration of ultrashort light pulses, amplifying energy, and compressing the pulse width again as shown in **Figure 2.6**.

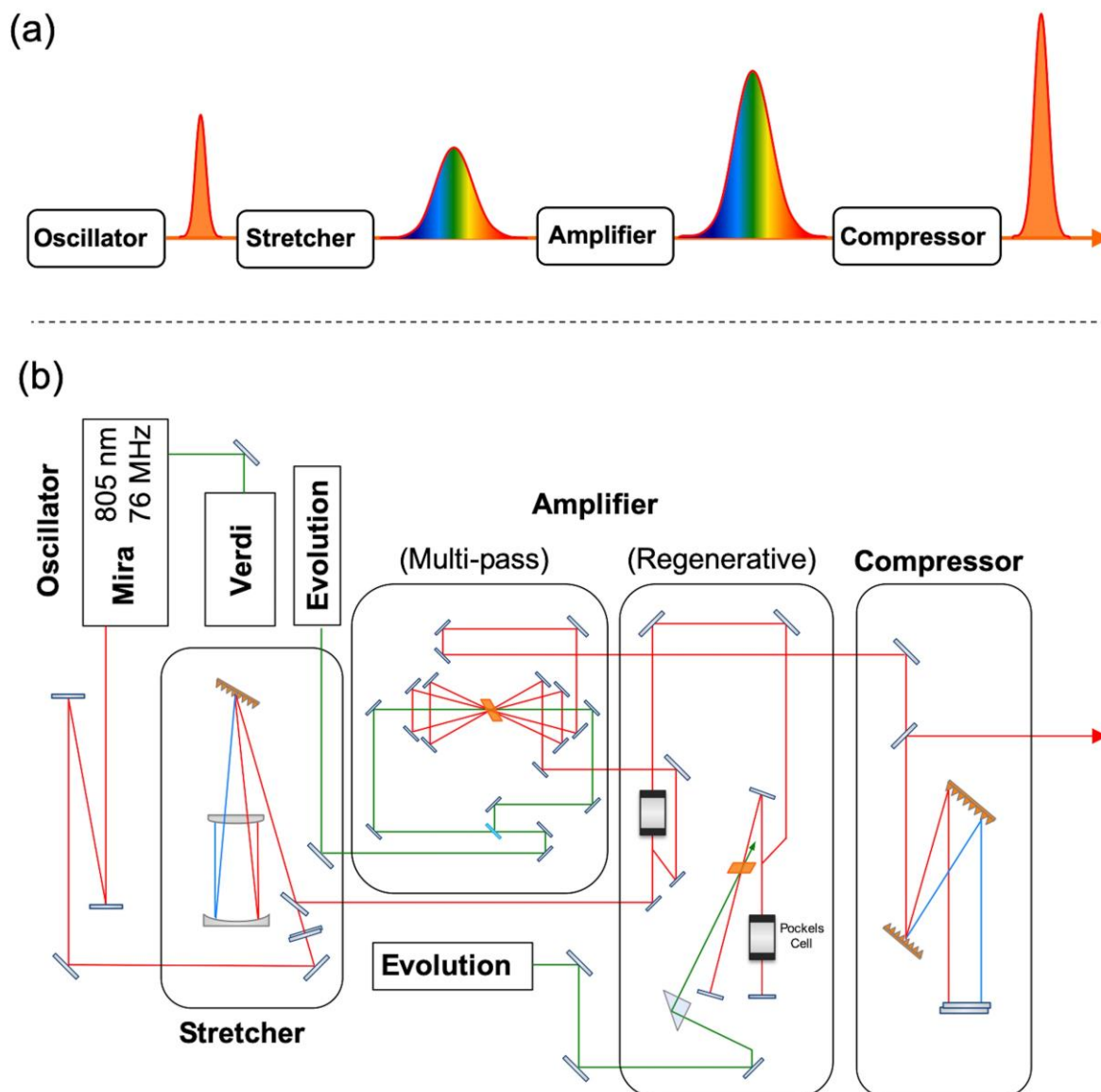


Figure 2.6 (a) Schematic of Chirped Pulse Amplification (CPA); (b) Schematic of the CPA system used in the experiments other than Chapter 3.

Next, the essential three steps in the CPA—that is, pulse stretcher, amplifier, and pulse compressor—are described.

Pulse stretcher

As explained in the previous section, the pulse width of the ultrashort pulse stretches when a linear chirp is added. First, let us consider a diffraction grating that is commonly used as a dispersive element. In the diffraction grating, if the groove pitch of the diffraction grating is d , the incident angle is θ_i , the diffraction angle is θ_d , and the diffraction order is m , the diffracted light is expressed by the following equation:

$$d(\sin \theta_i \pm \sin \theta_d) = m\lambda \tag{2.23}$$

Usually, first-order diffracted light with the highest diffraction efficiency is used. When a broadband pulse is an incident on the diffraction grating, the diffraction angle varies with each wavelength. Therefore, the optical path length is different for each wavelength, and dispersion is given to the optical pulse.

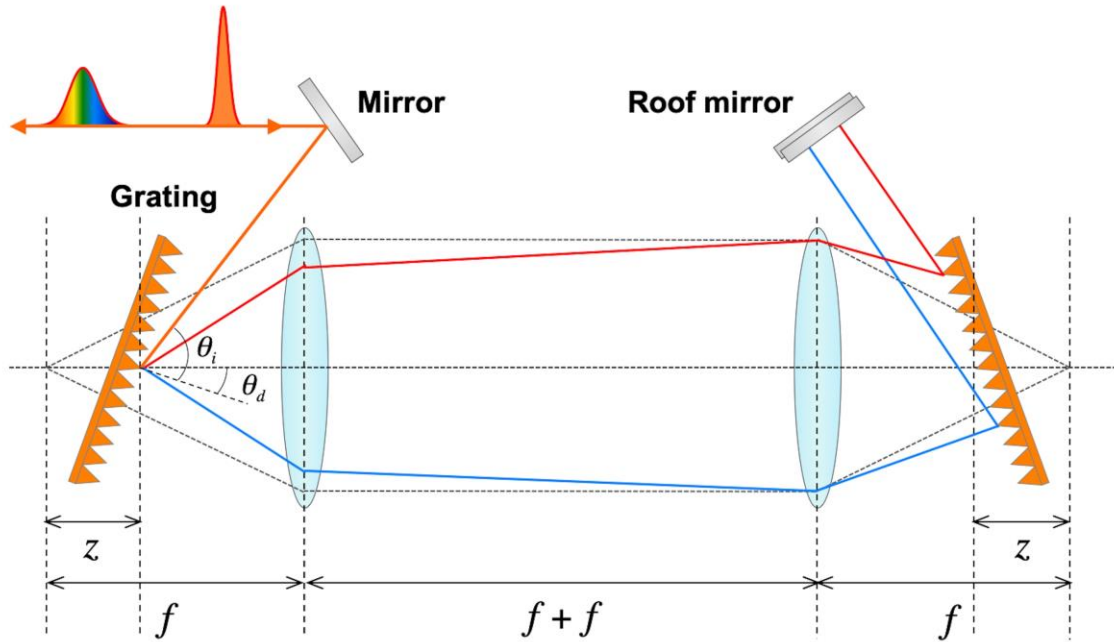


Figure 2.7 Schematic of a Martinez-type stretcher

Using this mechanism, in 1987, Martinez proposed a pulse stretcher using a diffraction grating [201] (hereafter the Martinez-type stretcher). The configuration of the Martinez-type stretcher is shown in **Figure 2.7**. The laser pulse dispersed by the first diffraction grating passes through the lens and enters the second diffraction grating at an angle equal to the diffraction angle. As a result, the spatially dispersed beam becomes parallel light. Then, the spatial dispersion is removed by folding the same optical path with a plane mirror. At this time, the amount of dispersion can be adjusted by the distance z from the focal position of the lens (focal length of f).

The optical path length for the angular frequency component ω in this process $L_{\text{Martinez}}(\omega)$ is

$$L_{\text{Martinez}}(\omega) = 2z \cos \theta_d(\omega_0) \left[\frac{1}{\cos \theta_d(\omega)} + \cos\{\theta_i - \theta_d(\omega)\} \right] \quad (2.24)$$

where the center frequency is ω_0 , and can be obtained from the distance (z) and the incident angle (θ_i).

On the other hand, the Martinez-type stretcher uses a lens, which causes higher-order dispersion and aberration. To remedy this problem, the Barty-type stretcher using a cylindrical mirror [202] and the Offner-type using concave and convex mirrors [203,204] have been proposed.

The following describes the Offner-type stretcher that employed in the CPA system used in the experiments all but Chapter 3. **Figure 2.8** shows the configuration of the Offner-type stretcher.

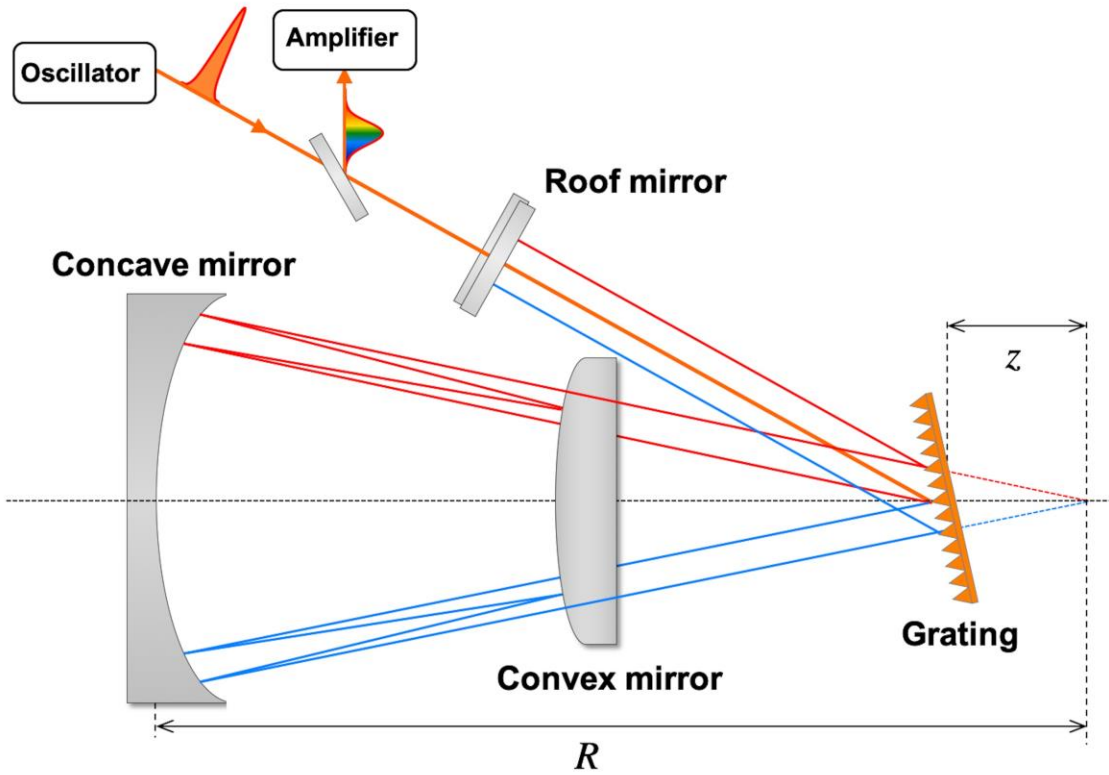


Figure 2.8 Schematic of an Offner-type stretcher

In the Offner-type stretcher, a concave mirror and a convex mirror are placed at the center with a curvature radius of 2:1, and the optical pulse can be stretched without aberration. Also, there is an advantage of the easy usage of single diffraction grating. When the curvature radius of the convex mirror is R , the distance from the concentric center to the diffraction grating is z , and the groove pitch of the diffraction grating is d , the spectral phase of the Offner-type stretcher $\phi_{\text{Offner}}(\omega)$ is given by Equation (2.25):

$$\phi_{\text{Offner}}(\omega) = \frac{\omega}{c} \left[5R - \frac{1 + \{1 + \cos(\theta_i - \theta_d(\omega))\}}{\cos \theta_d(\omega)} \right] + \frac{2\pi z}{d} \tan \theta_d(\omega) \quad (2.25)$$

Since there is a relationship between group delay $\tau(\omega)$ and path length $L(\omega)$ [205],

$$\frac{\partial \phi(\omega)}{\partial \omega} = \tau(\omega) = \frac{L(\omega)}{c} \quad (2.26)$$

$$= \frac{d\phi}{d\omega}(\omega_0) + \frac{d^2\phi}{d\omega^2}(\omega - \omega_0) + \frac{1}{2} \frac{d^3\phi}{d\omega^3}(\omega - \omega_0)^2 + \dots \quad (2.27)$$

the path length $L(\omega)$ and the dispersion of each order $d^n\phi/d\omega^n$ can be obtained.

Amplifier

The seed laser pulse whose time width is elongated by the pulse stretcher is subsequently amplified using the gain medium, such as a Ti:sapphire crystal. As amplifiers, regenerative amplifier [206] and multipath amplifier [207,208] are commonly used. **Figure 2.9** shows the schematic setup of a regenerative amplifier.

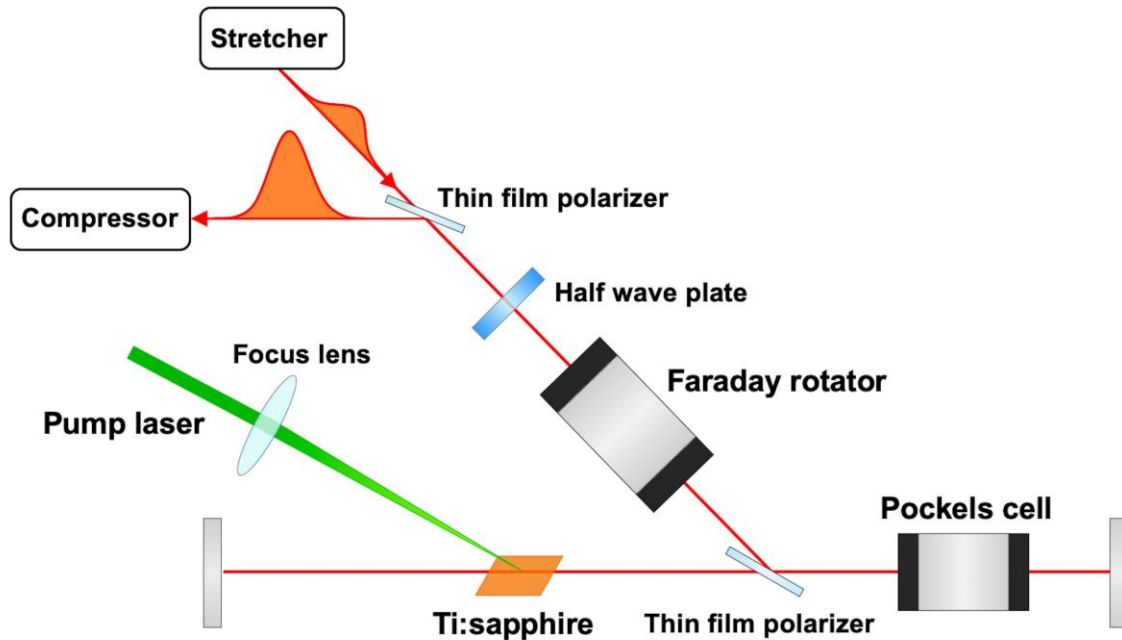


Figure 2.9 Schematic of a regenerative amplifier

A regenerative amplifier has a configuration in which a gain medium is placed in a laser cavity, including an optical switch using a Pockels cell that is an electro-optic element and a Faraday rotator that is a magneto-optic element. Stretched seed pulses are amplified in the cavity, and the repetition rate is reduced from MHz to kHz order. In this round trip inside the cavity, laser pulses with high beam quality are obtained, but the gain of one path is small due to energy loss in the Pockels cell, and the number of round trips must be increased. Therefore, the effect of dispersion and spectral narrowing due to dispersive elements such as Pockels cells, thin-film polarizers, and gain media, affects the spectral shape and phase of the amplified laser pulse. For further amplification, a multipath amplifier is also utilized.

Pulse compressor

A pulse compressor using a diffraction grating pair [209] was devised by Treacy in 1969. **Figure 2.10** illustrates the schematics of a grating pair compressor.

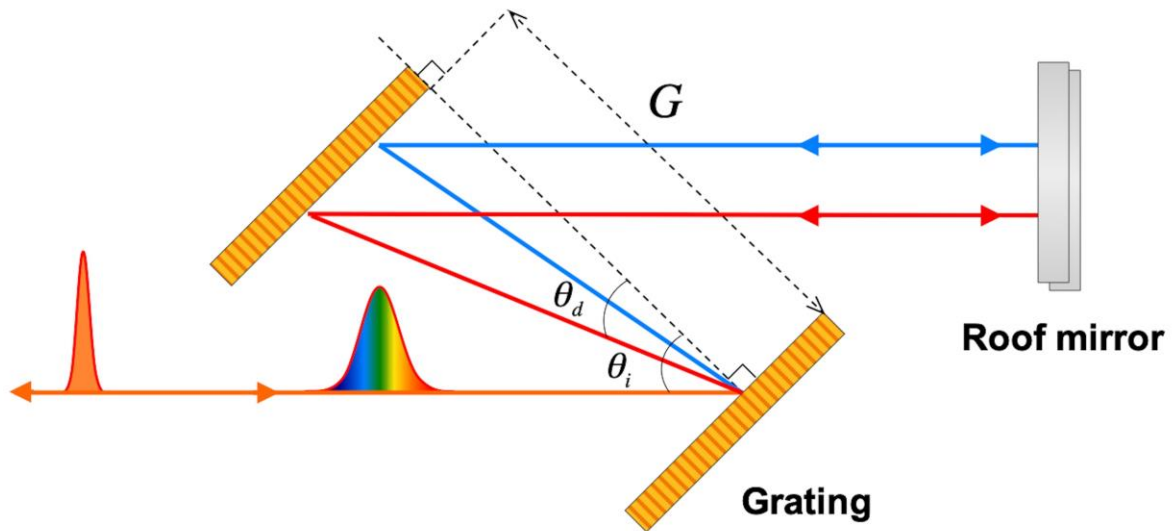


Figure 2.10 Schematic of a pulse compressor with a diffraction grating pair

The input beam is incident on the first grating at angle θ_i . The diffracted angle θ_d is a function of frequency, and the pulse front after diffraction from the first grating is tilted. After diffracting from the second grating, all the output rays are again parallel to the input beam and independent of frequency, and there is no longer any angular dispersion or pulse tilt. The distance between diffraction gratings arranged in parallel is denoted G . The pitch of the grating is d .

In this situation, first-order dispersion (GD), second-order dispersion (GDD), and third-order dispersion (TOD) are expressed as follows:

$$\frac{d\phi}{d\omega} = \frac{G\{1 + \cos(\theta_i - \theta_d)\}}{c \cos \theta_d} \quad (2.28)$$

$$\frac{d^2\phi}{d\omega^2} = \frac{\lambda^3}{2\pi c^2} \frac{G}{d^2 \cos^3 \theta_d} \quad (2.29)$$

$$\frac{d^3\phi}{d\omega^3} = -\frac{3\lambda}{2\pi c} \left(1 + \frac{\lambda \sin \theta_d}{d \cos^2 \theta_d}\right) \frac{d^2\phi}{d\omega^2} \quad (2.30)$$

Equation (2.29) shows that a parallel diffraction pair can provide a tunable amount of anomalous dispersion. This device can be used to compensate for material dispersion by adjusting the grating separation. For positively chirped input pulses, the grating pair can be used to compress these pulses to the FTL. For FTL-input pulses, passage through the grating pair leads to a negative chirp on the output pulse. Equation (2.30) shows that a grating pairs compressor cannot simultaneously compensate for both second- and third-order material dispersion; although the second-order dispersions can be made to cancel, the third-order dispersions will add.

2.2 Development of STAMP utilizing spectral filtering (SF-STAMP)

As aforementioned in Chapter 1, Sequentially Timed All-optical Mapping Photography (STAMP) [58] is a powerful single-shot ultrafast imaging method, thanks to these salient features: the feasibility of both high temporal (\sim femtosecond order) and spatial (\sim micrometer order) resolution, and the ability of direct 2D-burst imaging without post-processing of image reconstruction. In the STAMP scheme, the snapshot of spectral images measured by a linearly frequency-chirped laser pulse corresponds to the temporal snapshot. Therefore, the combination of a snapshot multispectral imaging system and the frequency-to-time encoding performs a single-shot burst image acquisition.

In the original STAMP, a unique periscope-array structure in the spatial mapping device (SMD) [58] achieved the spatial separation of different multispectral images [160]. In principle, STAMP's total number of frames can be increased, but six multispectral images are the current limitation. In fact, it is not easy to manufacture a periscope-array that can manage larger spectral components. The utilization of slice mirrors as a spectral shaper in SMD [161] has been reported for the STAMP application, but this approach still suffers from the complex mechanical design and realization. To realize various applications of STAMP to single-shot ultrafast imaging, there are demands to solve the problem of freedom in the number of snapshots and expansion of the time window to nanoseconds regime unachieved by both conventional high-speed and cutting-edge ultrafast imaging technique.

In this section, after introducing fundamentals of optical imaging system, the principle and details of STAMP utilizing spectral filtering (SF-STAMP) [60,61] are described.

2.2.1 Fundamentals of optical imaging system

Here, theories of optical imaging required for 2D-imaging are explained.

Optical Fourier transform

A lens is the most important optical element for optical experiments, and the greatest advantage of using a lens is that it forms a Fraunhofer diffraction, which is originally formed sufficiently far from the aperture at the focal plane of the lens.

In the Fraunhofer diffraction region, the amplitude distribution on the aperture plane $u_1(\xi, \eta)$ and the amplitude distribution on the screen $u_2(x, y)$ are connected with the Fourier transform, as shown in Equation (2.31), where z is the distance between the aperture and the screen.

$$u_2(x, y) = \iint_{-\infty}^{\infty} u_1(\xi, \eta) e^{-jk\frac{x\xi+y\eta}{z}} d\xi d\eta \quad (2.31)$$

Therefore, optically Fourier transforming the beam is possible by using a lens.

Next, let us mathematically interpret that the object placed on the front focal plane of the lens with focal length f is Fourier transformed to the rear focal plane. As shown in **Figure 2.11**, the coordinates of the front focal plane (Object plane) where the object is placed are (ξ, η) , the coordinates of the lens position are (x_1, y_1) , and the coordinates of the rear focal plane (Fourier plane) are (x, y) .

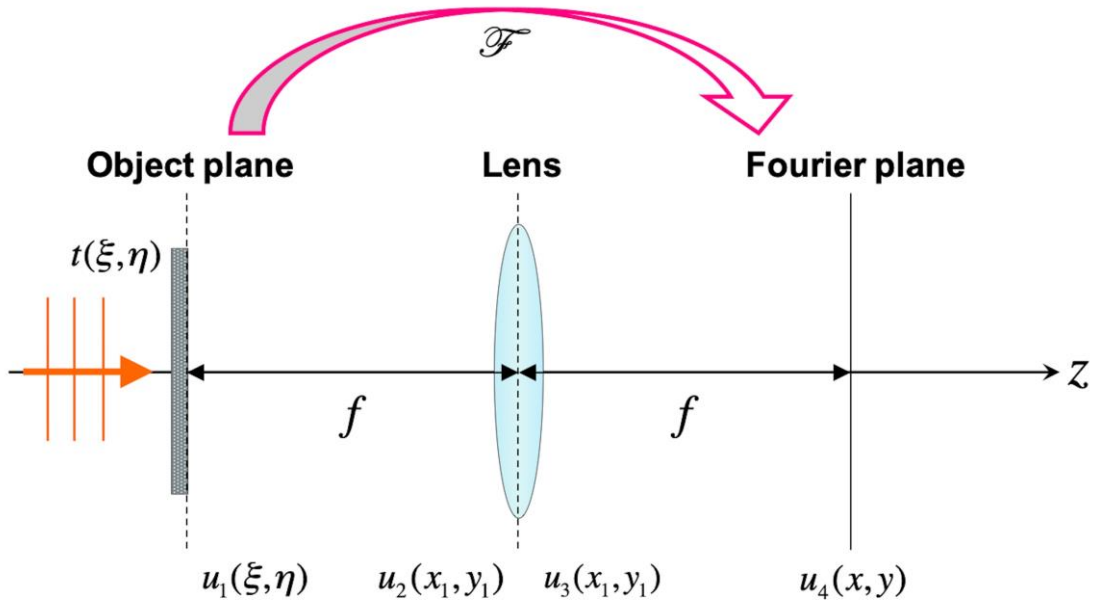


Figure 2.11 Schematic of optical Fourier transform with lens

2. Fundamentals of ultrafast laser, and development and improvements of SF-STAMP

Here, assuming that a plane wave of amplitude A is incident on the object, the amplitude distribution immediately after the object is $u_1(\xi, \eta)$, the amplitude distribution just before the lens is $u_2(x_1, y_1)$, just after the lens is $u_3(x_1, y_1)$, and the amplitude distribution on the Fourier plane is $u_4(x, y)$. The amplitude distribution immediately after the object is $u_1(\xi, \eta)$, and is expressed by

$$u_1(\xi, \eta) = At(\xi, \eta) \quad (2.32)$$

with the amplitude transmittance distribution of an object $t(\xi, \eta)$. Since this propagates by the distance f to the lens, the amplitude distribution immediately before the lens $u_2(x_1, y_1)$ using the Fresnel diffraction formula becomes

$$u_2(x_1, y_1) = \iint_{-\infty}^{\infty} u_1(\xi, \eta) e^{j\frac{k}{2f}\{(x_1-\xi)^2+(y_1-\eta)^2\}} d\xi d\eta \quad (2.33)$$

Then, multiplying this by the transmittance of the lens $t_{\text{lens}}(x_1, y_1)$, the amplitude distribution immediately after the lens $u_3(x_1, y_1)$ is expressed as

$$u_3(x_1, y_1) = t_{\text{lens}}(x_1, y_1) \cdot u_2(x_1, y_1) \quad (2.34)$$

Since this propagates by the distance f to the Fourier plane, the amplitude distribution on the Fourier plane $u_4(x, y)$ using the Fresnel diffraction formula again becomes

$$u_4(x, y) = \iint_{-\infty}^{\infty} u_3(x_1, y_1) e^{j\frac{k}{2f}\{(x-x_1)^2+(y-y_1)^2\}} dx_1 dy_1 \quad (2.35)$$

Plugging Equations (2.32) to (2.34) into Equation (2.35),

$$u_4(x, y) = A \iint_{-\infty}^{\infty} t(\xi, \eta) \left[\iint_{-\infty}^{\infty} e^{j\frac{k}{2f}\{(x_1-x-\xi)^2+(y_1-y-\eta)^2\}} dx_1 dy_1 \right] e^{-j\frac{k}{f}(x\xi+y\eta)} d\xi d\eta \quad (2.36)$$

$$\begin{aligned} &= A' \iint_{-\infty}^{\infty} t(\xi, \eta) e^{-j\frac{k}{f}(x\xi+y\eta)} d\xi d\eta \\ &= A' \iint_{-\infty}^{\infty} t(\xi, \eta) e^{-j2\pi(\frac{x}{\lambda f}\xi + \frac{y}{\lambda f}\eta)} d\xi d\eta \\ &= A' \iint_{-\infty}^{\infty} t(\xi, \eta) e^{-j2\pi(v_x\xi + v_y\eta)} d\xi d\eta \end{aligned} \quad (2.37)$$

$$= \mathcal{F}\{t(\xi, \eta)\} \quad (2.38)$$

the amplitude distribution on the Fourier plane $u_4(x, y)$ becomes Equation (2.38), where the constants that are not related to the coordinates are collectively A' , and the spatial frequencies set as $v_x = x/\lambda f$, $v_y = y/\lambda f$. As

can be seen from Equation (2.37), $u_4(x, y)$ is the Fourier transform of the transmittance of the object $t(\xi, \eta)$ ($\mathcal{F}\{\}$ is an operator representing the Fourier transform).

4f-optical imaging system

Here, the image formation in the 4f-optical imaging system using two lenses is explained. **Figure 2.12** illustrates the schematic of optical Fourier transform in 4f-optical imaging system.

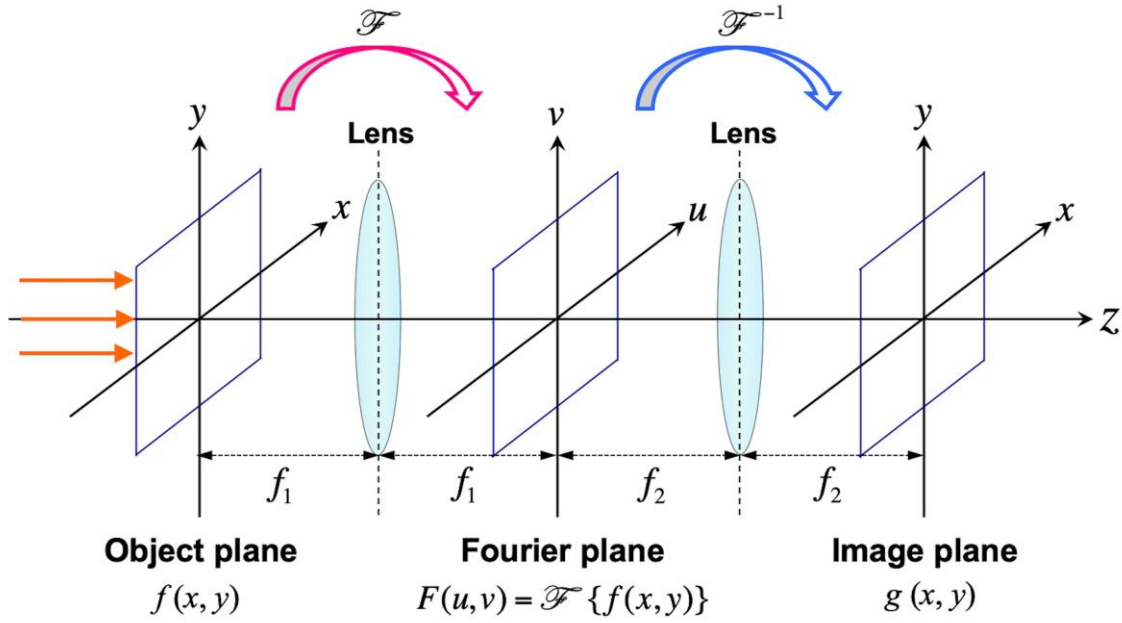


Figure 2.12 Schematic of optical Fourier transform in 4f-optical imaging system

The input beam is optically Fourier-transformed and inverse-Fourier-transformed by passing through the lens twice. In other words, the first lens (focal length of f_1) converts the 2D-spatial information on the object plane $f(x, y)$ into the 2D-spatial frequency information on the Fourier plane $F(u, v)$.

$$F(u, v) = \iint_{-\infty}^{\infty} f(x, y) e^{-j2\pi(ux+vy)} dx dy \quad (2.39)$$

$$= \mathcal{F}\{f(x, y)\} \quad (2.40)$$

If the spatial frequency filter on the Fourier plane is $H(u, v)$, the frequency response function transferred from the Fourier plane $G(u, v)$ becomes

$$G(u, v) = F(u, v) \cdot H(u, v) \quad (2.41)$$

2. Fundamentals of ultrafast laser, and development and improvements of SF-STAMP

After that, the inverse Fourier transform of $G(u, v)$ is performed by the second lens (focal length of f_2), and a 2D-image $g(x, y)$ is formed on the Image plane at the distance $2f_2$. The $g(x, y)$ is expressed as follows by using the convolution theorem (* represents convolution integral):

$$g(x, y) = \mathcal{F}^{-1}\{F(u, v) \cdot H(u, v)\} \quad (2.42)$$

$$= f(x, y) * h(x, y) \quad (2.43)$$

$$= \iint_{-\infty}^{\infty} f(\xi, \eta) h(x - \xi, y - \eta) d\xi d\eta \quad (2.44)$$

Note that in the case of $H(u, v) = 1$ — that is, when filtering is not performed on the Fourier plane — $g(x, y) = f(x, y)$ is valid. From the above, 2D-information on the object plane can be conveyed to the image plane by using the $4f$ -optical imaging system. However, the transferred imaged is rotated 180° .

2.2.2 STAMP utilizing spectral filtering (SF-STAMP)

STAMP utilizing Spectral Filtering (SF-STAMP) [60,61] is a modified simpler single-shot ultrafast 2D-burst imaging method realized by combination of STAMP and a scheme of the spatially spectrum resolving idea of the Spatially and Temporally Resolved Intensity and Phase Evaluation Device: Full Information from a Single Hologram (STRIPED FISH) [196,210–214], which is superb for single-shot measurements of ultrashort laser pulses in both space and time using wavelength-multiplexed digital holography.

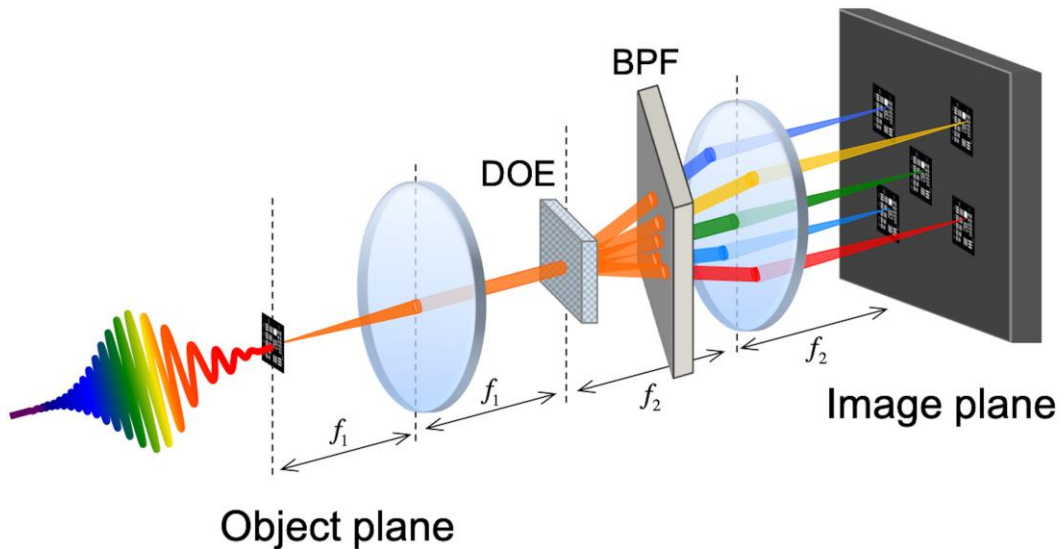


Figure 2.13 Schematic setup of SF-STAMP snapshot multispectral imaging system: diffractive optical element (DOE) and band-pass filter (BPF)

In the SF-STAMP snapshot multispectral imaging system shown in **Figure 2.13**, a diffractive optical element (DOE) duplicates spatially resolved replicas of the probe pulse. These replicas are incident to a tilted bandpass filter (BPF), which selects different narrow-band wavelengths depending on the angle of incidents. Thus, the image at the object plane is spectrally and spatially resolved, and then relayed to the image plane by the $4f$ -optical imaging system. The possible number of frames in SF-STAMP is equivalent to the number of replicas from a DOE. The detailed descriptions of the principle and improvements of SF-STAMP are provided in the rest of this chapter.

2.2.3 Principle of SF-STAMP

To realize a flexible increase in the STAMP camera's total number of frames, another approach for realizing spectral separation in free space is needed. One method that inspired us for this purpose is the Spatially and Temporally Resolved Intensity and Phase Evaluation Device: Full Information from a Single Hologram (STRIPED FISH) [210–215], which is excellent for single-shot measurements of ultrashort laser pulses in both space and time using wavelength-multiplexed digital holography. STRIPED FISH, which employs a simple and compact setup that consists of a diffractive optical element (DOE) and a band-pass filter (BPF), measures spatially and temporally resolved wavelength-multiplexed interferograms of signal and reference laser beams (40 multispectral interferograms can be obtained with a single pulse [212]). Reconstructing them creates a complete 3D spatio-temporal map of the intensity and the phase of an ultrashort laser pulse $E(x, y, t)$ in a single shot. Instead of conventional spatio-temporal measurement methods [194,216,217], where only 2D-information is simultaneously measured, STRIPED FISH can simultaneously obtain complete 3D-information and is applicable to measurements of spatio-temporally complex pulses, such as high-intensity pulses after amplifiers and low repetition rate pulses.

In this sub-section, we propose and experimentally demonstrate a simpler single-shot ultrafast 2D-burst imaging method by applying the STRIPED FISH method to STAMP. This method, which we call STAMP utilizing Spectral Filtering (SF-STAMP), consists of a $4f$ -optical imaging system with a DOE and a BPF for spatially resolving the optical spectrum and generating snapshot multispectral images.

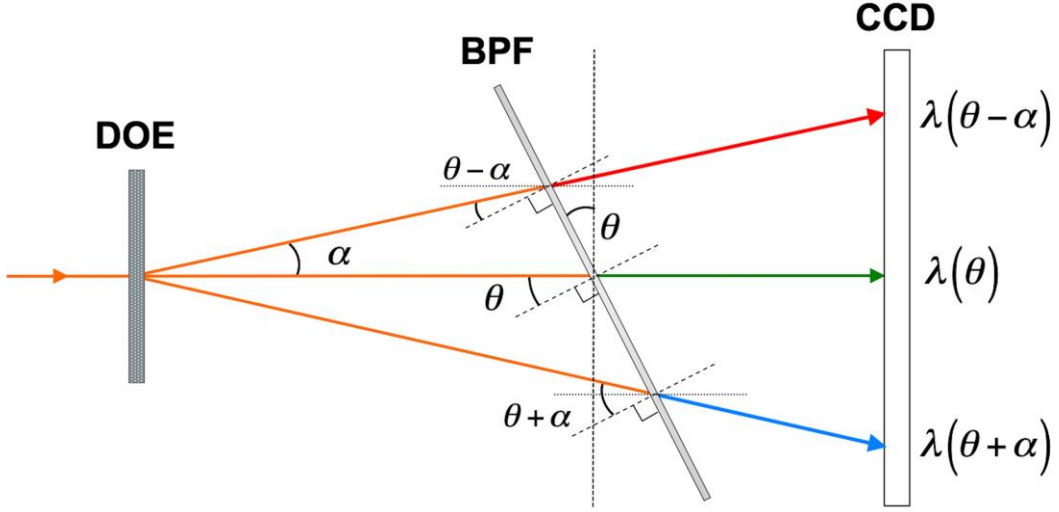


Figure 2.14 Schematic of spatially and spectrally resolving by a DOE and a BPF

Figure 2.14 shows the concept of spatially and temporally resolving of wavelengths by a DOE and a BPF. First, an incident beam to the DOE is transformed into an array beam and propagates with a diffraction angle (α). In other words, a DOE's incident beam is duplicated to plural array beams and spatially resolved. Therefore, the number of DOE's generating array beams determines SF-STAMP's possible number of frames. Next, the array beams replicated by the DOE are selected by the BPF, and each array beam becomes a different narrowband beam. The transmitted wavelength of $\lambda(\theta)$ depends on the angle of incident into the BPF (θ) [211,218] and is given by

$$\lambda(\theta) = \lambda_0 \left(1 - \frac{\theta^2}{2n_{\text{eff}}^2} \right) \quad (2.45)$$

where λ_0 is the center wavelength of the BPF and n_{eff} is the effective refractive index. By tilting the BPF, since the incident angle of the array beams is changed, the transmission wavelength is varied.

As shown in **Figure 2.14**, since the angles of both edges of the array beams incident to the BPF, which is tilted by angle θ , shift to $\theta - \alpha$ and $\theta + \alpha$, we can filter out long-wavelength $\lambda(\theta - \alpha)$ and short-wavelength $\lambda(\theta + \alpha)$ from the broadband light. The FWHM of a BPF (typically ~ 2 nm) determines the transmitted bandwidth, and according to the tilted angle, the bandwidth becomes wider. In experimental practice, however, an incident beam has a slightly different angle component, the spectrum in a narrow-wavelength resolved image is not exactly monolithic but swept along with the horizontal axis.

Rotating the DOE around the beam propagating axis rotates the array beam as shown in **Figure 2.15**. Thus, a combination of a DOE and a BPF can choose and adjust a different wavelength between the long-wavelength edge and the short-wavelength edge from the array beam. Note that after adjusting the rotation position of the DOE, no further angle tuning is needed.

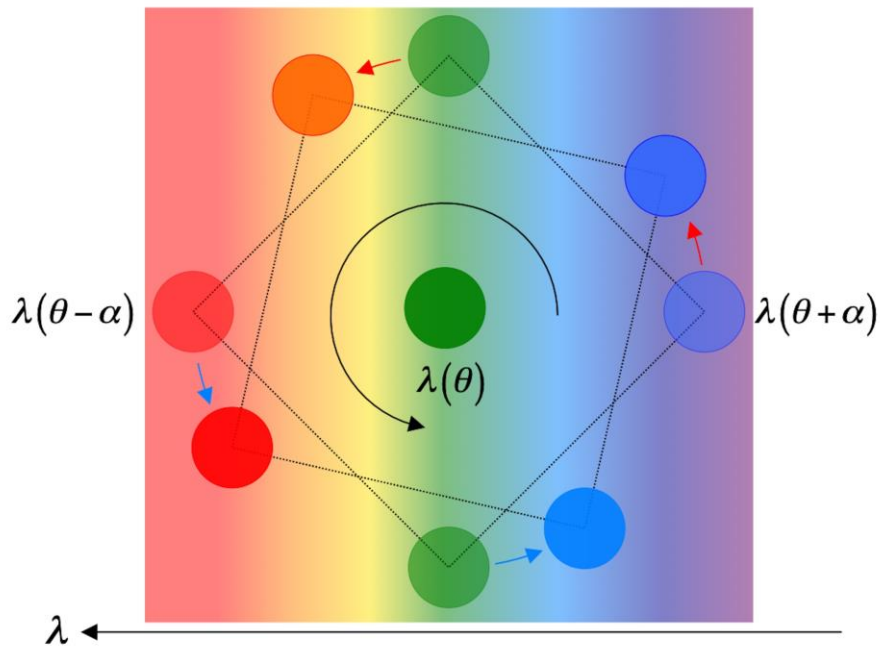


Figure 2.15 Side view image of spatially and spectrally resolving by a DOE and a BPF

If we use a linearly frequency-chirped laser pulse as a probe strobe light, this spectral filtering procedure is equivalent to STAMP's temporal mapping device (daughter pulses are generated by a $4f$ -pulse shaper). In this process, we can not only temporally but also spatially resolve the different wavelength components of a chirped pulse.

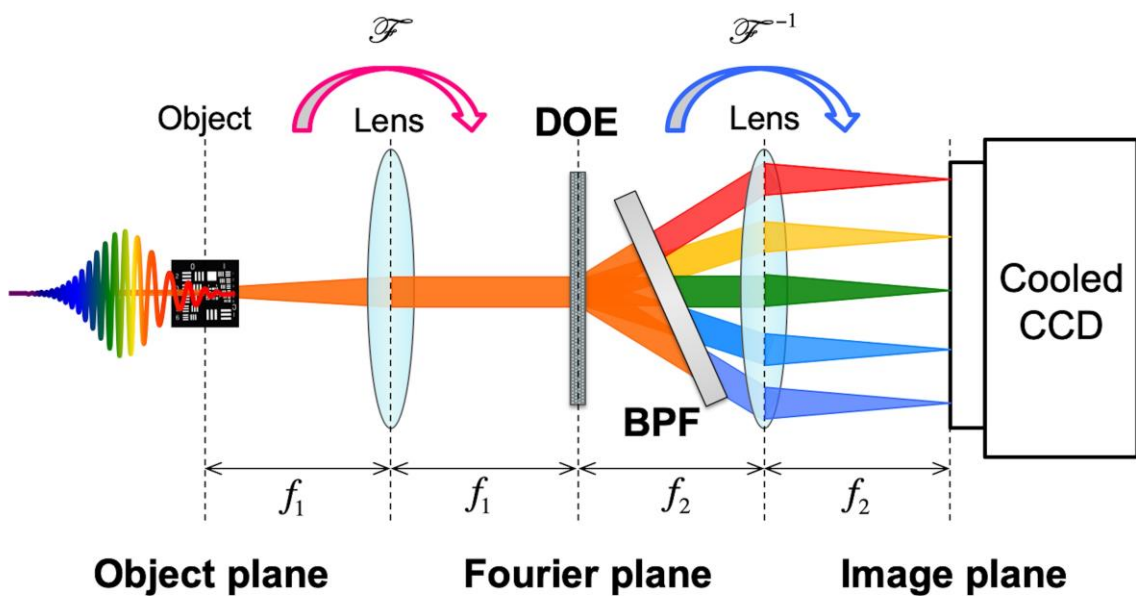


Figure 2.16 Schematic setup of SF-STAMP multispectral imaging system

Figure 2.16 shows a schematic setup of an SF-STAMP multispectral imaging system, which is a $4f$ configuration with a DOE and a BPF. Similar to STRIPED FISH, holographic interference measurements produce an advantage; not only amplitude images but also phase images are obtained. Due to the low resolution of a hologram measured with image sensors, using the analog optical Fourier transform has superior resolution to measure the amplitude images. If we only capture the intensity images, no reference beam for the holography is necessary for the SF-STAMP system, and thus its optical layout is simpler than that of STRIPED FISH. In principle, when applying an optical system commonly used in phase contrast microscopy, we can capture fast dynamics in the refractive index change of materials with SF-STAMP.

The probe beam is optically Fourier transformed by the first lens (f_1), and then the beam is duplicated to plural array beams by the DOE. The tilted BPF spectrally resolves the diffracted array beams depending on their incident beam angles. The spectrally filtered beams are optically inverse Fourier transformed by the second lens (f_2), and 2D-multispectral images are simultaneously generated on the image plane of a 2D-imaging sensor (in our case, a cooled CCD camera). When using a linearly frequency-chirped pulse, the spectral image corresponds to a snapshot at an ultrashort observation time slot in the chirped probe pulse.

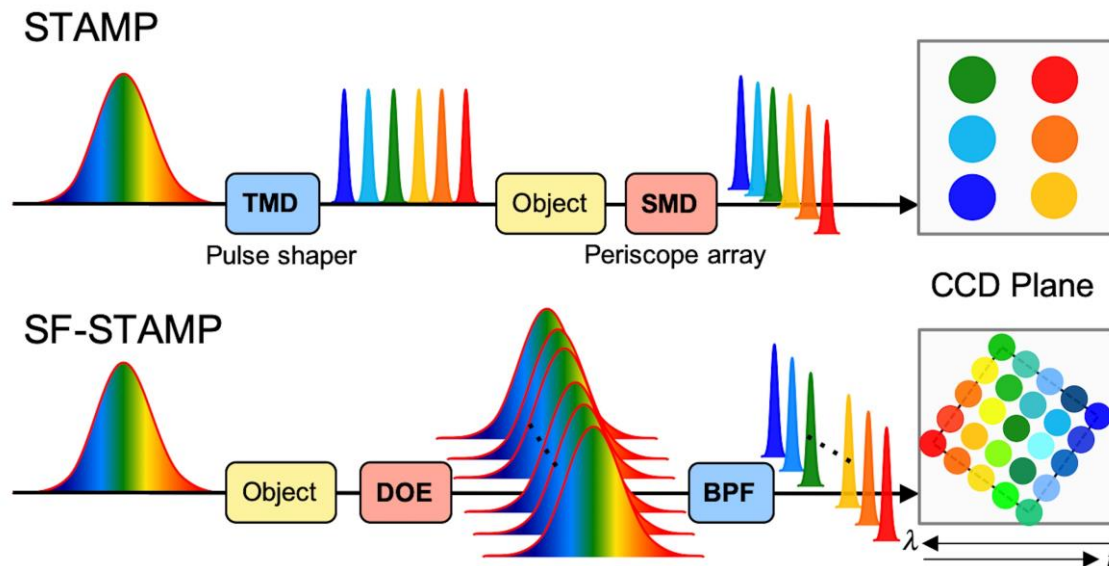


Figure 2.17 Comparison of the mechanism of 2D-burst imaging in the original STAMP and SF-STAMP (TMD: Time Mapping Device, SMD: Spatially Mapping Device)

Here, we summarize the differences between the temporal and spatial mapping processes in STAMP and SF-STAMP as shown in **Figure 2.17**. In STAMP, chirp pulse is shaped into ultrashort optical pulse trains arranged sequentially by wavelength with a temporal mapping device (TMD), exposed to Object, and then spatially mapped with a spatial mapping device (SMD) to form 2D-multispectral images on a CCD. On the

other hand, SF-STAMP abandoned the pulse shaper in TMD. Consequently, instead of using several temporally discrete probe pulses, SF-STAMP uses a single frequency-chirped pulse to probe the transient event. A DOE generates spatially resolved replicas of the transmitted probe pulse. These duplicates were incident to a tilted BPF, which selected different narrowband wavelengths according to the angle of incident. Since the number of frames in SF-STAMP is determined by a beam-generating DOE, increasing them is easy. Therefore, the SF-STAMP system is simpler and more flexible than the original STAMP. Also, the wavelength band can be easily made variable by adjusting the spectral range of a BPF [219].

However, since the beam replication and spectral filtering is performed, the light utilization efficiency of a probe pulse is reduced compared to the original STAMP method using the periscope-array. Since both STAMP and SF-STAMP are active detection schemes and require a chirped-pulse probe, unlike passive methods such as Compressed Ultrafast Photography (CUP) [63], ultrafast single-shot imaging of self-luminous phenomena such as fluorescence is not possible.

2.2.3.1 Temporal resolution of SF-STAMP

Similar to STAMP's temporal resolution [220], the temporal resolution of SF-STAMP can be designed to match a user's required condition. The relationship of the spectral and time widths of SF-STAMP is shown in **Figure 2.18**.

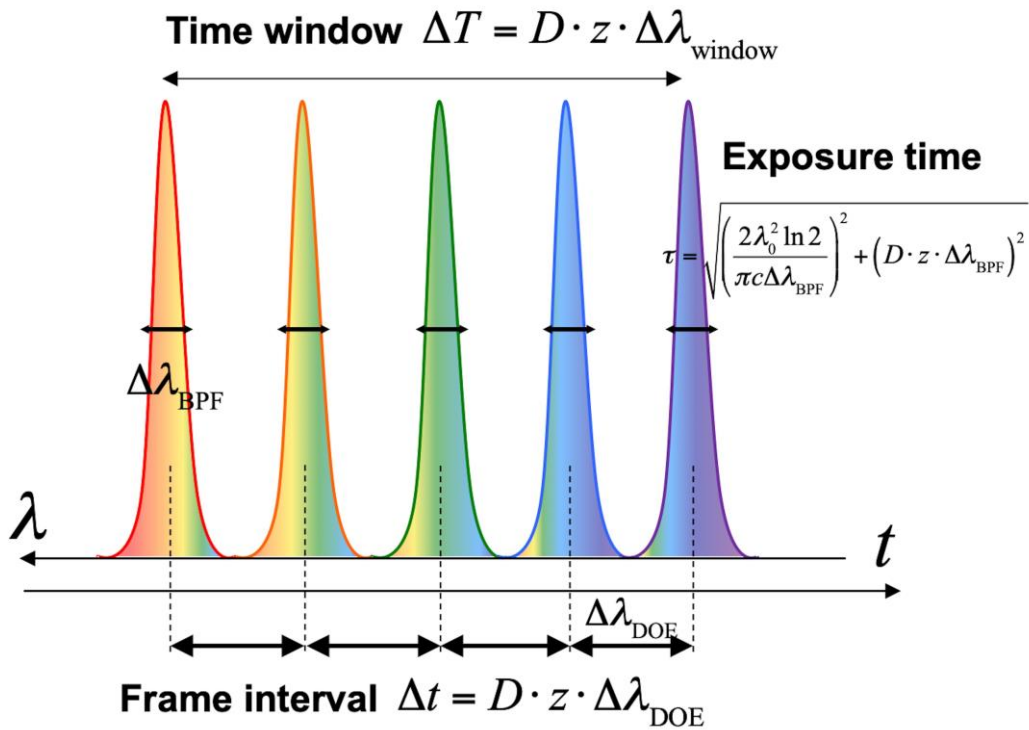


Figure 2.18 Relationship of spectral and time widths of SF-STAMP

2. Fundamentals of ultrafast laser, and development and improvements of SF-STAMP

The time window for observations (ΔT) is given by Equation (2.46):

$$\Delta T = D \cdot z \cdot \Delta\lambda_{\text{window}} \quad (2.46)$$

Here, D (ps/km·nm) is the dispersion parameter, z (km) is the length of the dispersive elements, and $\Delta\lambda_{\text{window}}$ is the entire observation bandwidth selected by the BPF. For a tilted single BPF, the $\Delta\lambda_{\text{window}}$ can be described as follows:

$$\Delta\lambda_{\text{window}} = \lambda(\theta - \alpha) - \lambda(\theta + \alpha) \quad (2.47)$$

From Equation (2.46), we can set the observation time window by either tuning the amount of dispersion added to the probe pulse ($D \cdot z$) (ps/ nm), or by changing the bandwidth of the BPF's selected spectrum ($\Delta\lambda_{\text{window}}$). The exposure time of each wavelength image (τ) is given by Equation (2.48) and the frame interval (Δt) is given by Equation (2.49):

$$\tau = \sqrt{\left(\frac{2\lambda_0^2 \ln 2}{\pi c \Delta\lambda_{\text{BPF}}}\right)^2 + (D \cdot z \cdot \Delta\lambda_{\text{BPF}})^2} \quad (2.48)$$

$$\Delta t = D \cdot z \cdot \Delta\lambda_{\text{DOE}} \quad (2.49)$$

Here, $\Delta\lambda_{\text{BPF}}$ is the spectral bandwidth (FWHM) of a BPF, $\Delta\lambda_{\text{DOE}}$ is the neighboring spectral differences (note that it is not necessarily constant over all of the entire frames and is varied by a DOE-BPF arrangement.), λ_0 is the center wavelength of the laser pulse from the optical source, and c is the speed of light in a vacuum.

Equation (2.48) indicates that the temporal resolution of each frame shot increases as the spectral width of the BPF narrows with the second term; however, if the spectral width is too narrow, the exposure time increases due to the relation of the Fourier transform with the first term. **Figure 2.19** shows this relationship [220]. Therefore, the optimum BPF spectral width to minimize the temporal resolution exists.

In experiments, however, the optimum exposure time is not always feasible due to available BPF specifications. In some cases, the duration of exposure time comes to be longer than a frame interval. In the below experiments, the details of actual temporal resolutions and optimum situation cases will be described.

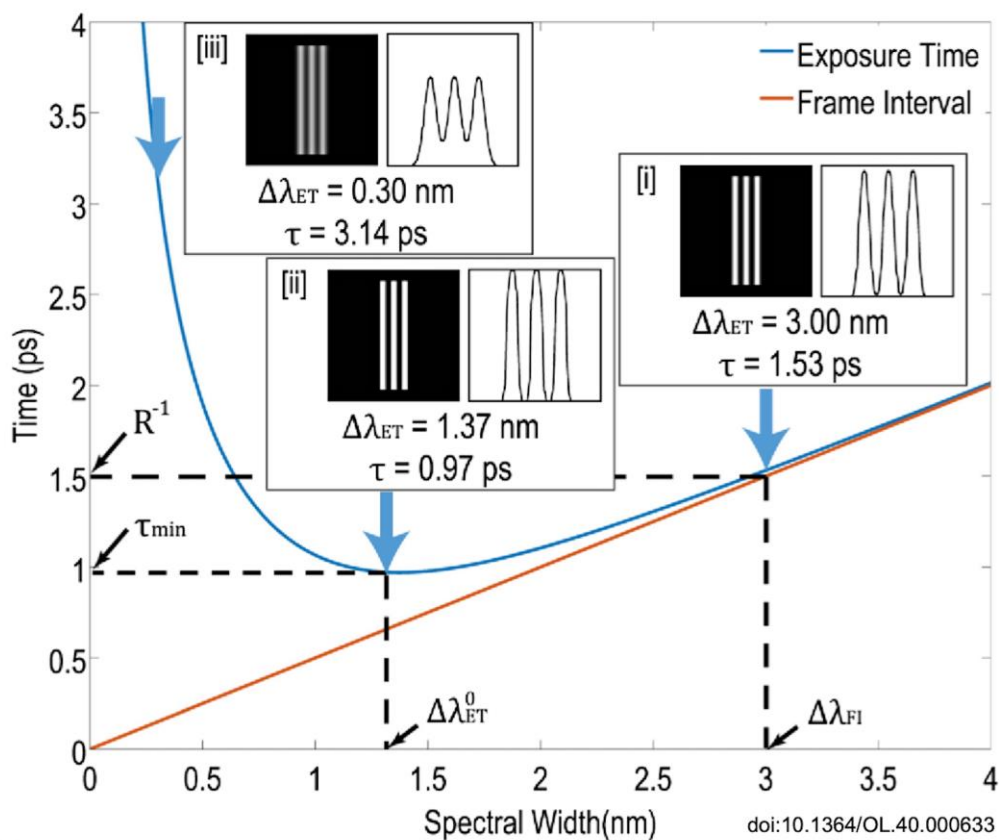


Figure 2.19 Simulation of STAMP's performance; exposure time and frame interval as a function of the spectral width (quoted from [220])

2.2.3.2 Spatial resolution of SF-STAMP

The spatial resolution of an SF-STAMP is determined by the resolution of the image sensor and the optical system. Since the SF-STAMP optical system is based on the $4f$ -imaging optical system, it can be combined with other imaging methods, such as a microscopic optical system, by relaying the image. In the experiments below, a microscopic optical system was used for the observation of ultrafast phenomena. Thus, the spatial resolution of SF-STAMP is limited by the numerical aperture of the objective lens just like conventional microscopy. The details of actual spatial resolutions are described in each experimental part below. A combination of a transmission microscopic system, the absorption of probe light can be measured as an amplitude image of shadowgraph, so that a phenomenon with an absorption change can be observed (Chapters 2 and 4). With a reflection type microscopy, transient refractivity change also can be measured (Chapter 3). In addition, by using a phase-contrast microscopic system, the phase difference, such as the refractive index, can be converted into an amplitude image, so it is possible to measure a phase object that cannot be observed with a simple shadowgraph.

2.2.3.3 Proof-of-principle demonstration of the 5-frame SF-STAMP

Here, the proof-of-principle experiments of the 5-frame SF-STAMP are described.

Single-shot pump/probe experiment

In general, the pump/probe method is a time-resolved measurement technique in which the optical path lengths of pump and probe light are repeatedly scanned and measured. Notably, since the STAMP method employs a frequency chirp pulse as a probe light, no scanning of the delay path is needed. Thus, a single-shot pump/probe measurement is possible.

Figure 2.20 shows a schematic setup of the single-shot pump/probe experiment with SF-STAMP. The light source was a mode-locked Ti:sapphire laser (Coherent, Mira) with chirped pulse amplification (CPA). The average energy was 1 mJ at a repetition rate of 1 kHz with a pulse width of 50 fs (FWHM). The amplified femtosecond laser pulse was split into a pump pulse and a probe pulse. In the probe pulse arm, to broaden the bandwidth, the probe pulse was focused into the Ar-gas filled hollow-core fiber (HCF) (126- μm core diameter). In the HCF, a broadband pulse (650–900 nm) was generated by self-phase modulation (SPM) and four-wave mixing. To stretch the pulse duration, the broadband pulse was passed through optical glass rods (such as N-SF11 and BK7). Then the frequency-chirped pulse utilized a frequency-to-time encoding probe of an SF-STAMP scheme. For a single-shot measurement, we employed an optical chopper (the repetition rate was reduced to 35.7 Hz) and a mechanical shutter to select one pulse. The repetition reduction process is shown in **Figure 2.21**. The single-shot experiments described later are based on this methodology.

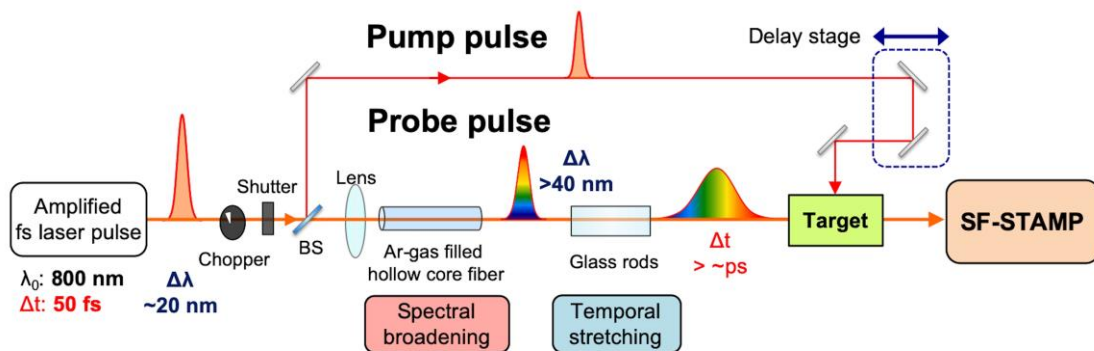


Figure 2.20 Schematic setup of the single-shot pump/probe measurement with SF-STAMP

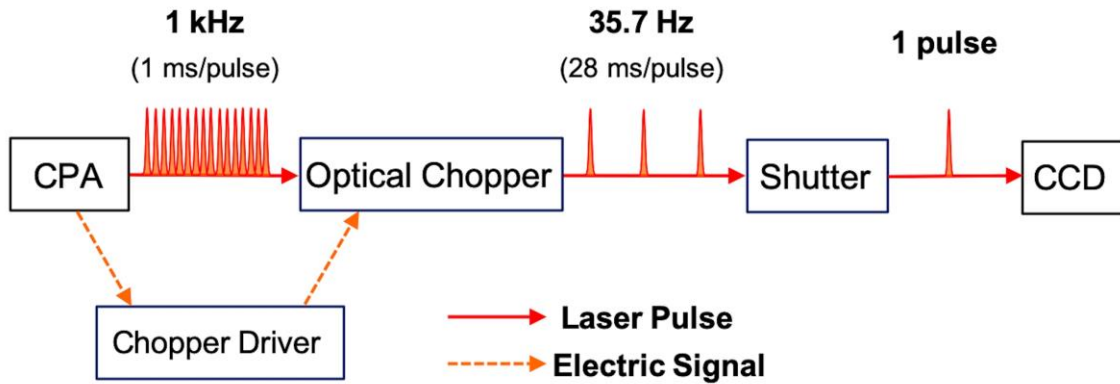


Figure 2.21 Diagram of the synchronization system with the optical chopper

Experimental setup of the 5-frame SF-STAMP

The entire setup of the proof-of-principle experiments is shown in **Figure 2.22**. In this experiment, the light source was a mode-locked Ti:sapphire laser (Coherent, Mira) after chirped-pulse amplification (CPA) with an 800-nm center wavelength and a 20-nm bandwidth (FWHM). The pulse width was 50 fs (FWHM), the repetition rate was 1 kHz, and the average pulse energy was 340 μJ . The amplified laser beam was focused into an Ar-gas filled hollow-core fiber (HCF) (400-mm long, 126- μm diameter) by an $f = 400$ mm lens. In the HCF, a broadband pulse (>200 nm) was generated by self-phase modulation (SPM). To add the linear frequency chirp and stretch the pulse width to ~ 40 ps, the broadband pulse was passed through optical glass rods (N-SF10 and BK7) and used as a probe pulse. The dispersion parameters of these glass rods at 800 nm were measured separately using spectral interferometry as $D_{\text{N-SF10}} = -468.9$ ps/km \cdot nm and $D_{\text{BK7}} = -149$ ps/km \cdot nm, which agreed well with those provided by the material suppliers. The chirp induced during nonlinear spectral broadening in the HCF was also measured by SPIDER as 400 fs², which is much smaller than that of these glass rods. As a pump pulse for inducing laser ablation, a Fourier transformed limited (FTL) pulse after the CPA was split before the HCF. For a single-shot measurement, we employed an optical chopper (the repetition rate was reduced to 35.7 Hz) and a shutter and chose one pulse.

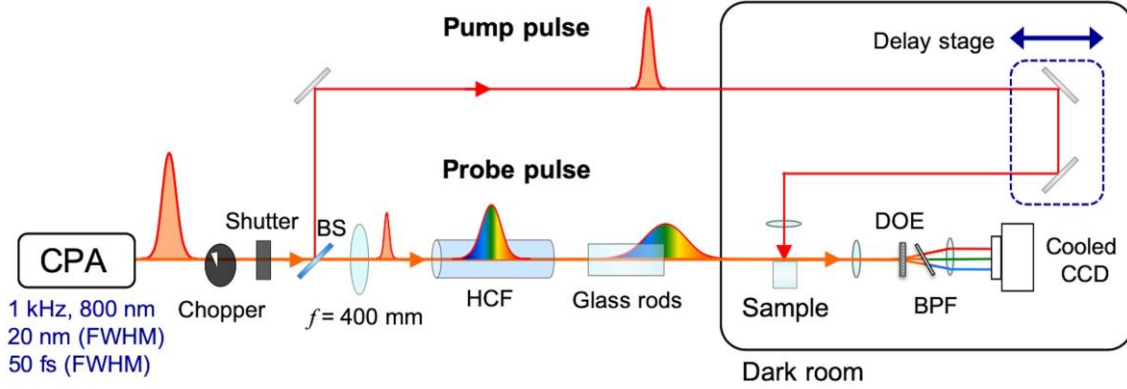


Figure 2.22 Proof-of-principle experimental setup of SF-STAMP (BS: beam splitter, HCF: hollow-core fiber filled with Ar-gas, DOE: diffractive optical element, BPF: band-pass filter)

In the SF-STAMP system, a linearly frequency-chirped pulse (probe pulse), including the sample's information, passed the first Fourier lens ($f_1 = 75$ mm) and a DOE (HOLOEYE, DE 225), which generates 2×2 beams and has a diffraction angle (α) of $\sim 5.1^\circ$. Since a non-diffracted beam (0^{th} order) is also available, the number of frames in SF-STAMP is five in total with this DOE. The transmittance of each 1^{st} diffracted array beam and the 0^{th} diffraction is $\sim 10\%$ and 14% , respectively. Then the diffracted array beams passed a BPF (IRIDIAN, ZX000167), which has a center wavelength of 830 nm, a spectral bandwidth of 2.2 nm (FWHM), and a transmittance of $>90\%$, and which were spectrally resolved. Finally, by a second Fourier lens ($f_2 = 75$ mm), each of five different wavelength images was imaged on different positions of a cooled CCD sensor. In this experiment, all the lenses we used were achromatic. The electrically cooled CCD camera (BITRAN, BS-42N) had 2048×2048 pixels (each pixel size was 7.4×7.4 μm), and the size of the CCD plane was 15.16×15.16 mm. Quantum efficiency was $>10\%$ at 800 nm.

We obtained a snapshot multispectral image that contains five different wavelength images when a USAF test target was on the object plane of the SF-STAMP system. The wavelength-multiplexed image and its spectral properties (from 792 to 807 nm) are shown in **Figure 2.23(a)** and **Figure 2.23(b)**. In this setup, each wavelength image was well separated within the entire spectral bandwidth selected by a tilted BPF $\Delta\lambda_{\text{window}}$ of 20 nm and occupied 450×450 pixels. Within this bandwidth, each image's resolution was almost the same. No image aberration is visible in **Figure 2.23(a)**. By rotating and tilting the BPF, the incident angle of the array beams was changed, and the transmission wavelength was varied. This SF-STAMP system arrangement can produce five shots of wavelength-multiplexed images within 730 to 830 nm (limited by the BPF's spectral selection range). Each shot has five different wavelength images ($\Delta\lambda_{\text{DOE}} = 5$ nm) with single-shot bandwidths $\Delta\lambda_{\text{BPF}}$ of 2.2 nm. The spectral properties selected by 5-shot images at

2. Fundamentals of ultrafast laser, and development and improvements of SF-STAMP

various BPF rotating angles are shown in **Figure 2.24**. For larger rotating angles ($\sim 30^\circ$), the transmitted wavelength's bandwidth begins to increase, and we can select the wavelength by rotating the BPF up to $\sim 50^\circ$.

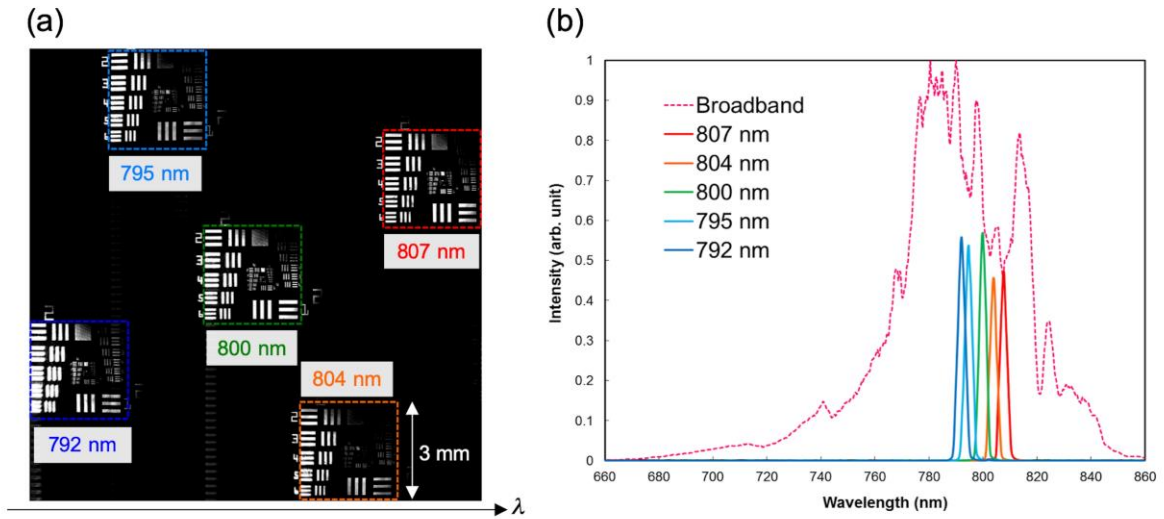


Figure 2.23 (a) Wavelength-multiplexed image (from 792 to 807 nm) and (b) wavelength-multiplexed image's spectral properties.

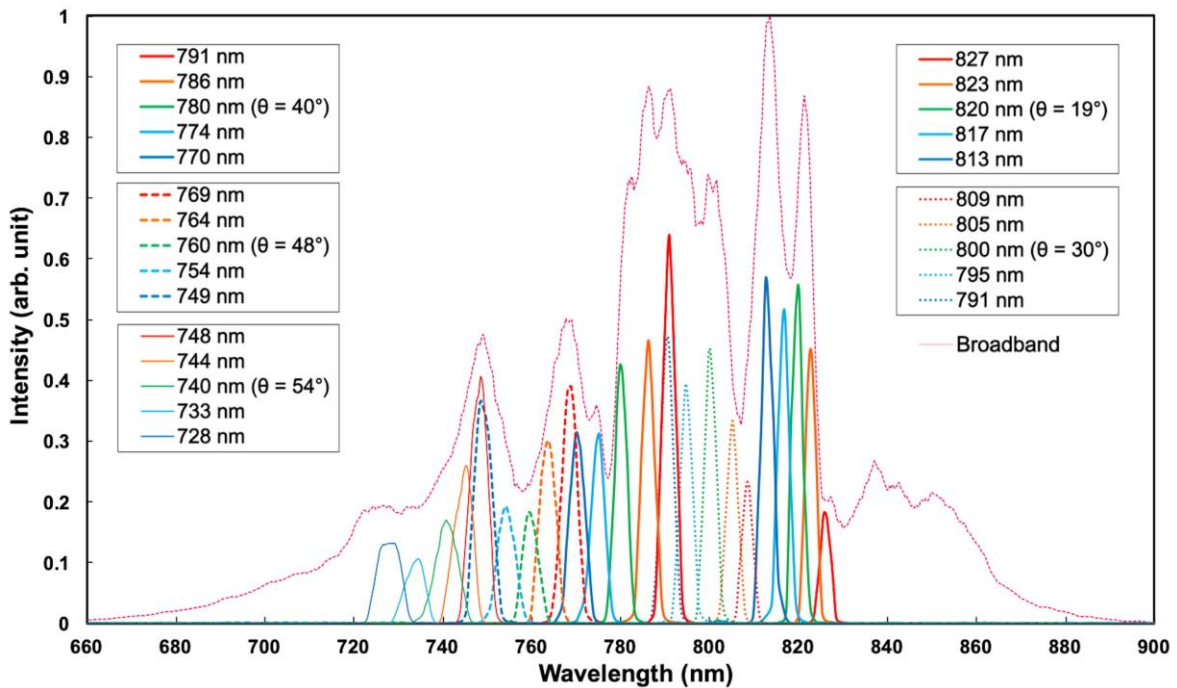


Figure 2.24 Spectral properties of five image frames at different BPF rotation angles

Observation of ultrafast phenomena using SF-STAMP

As an experimental demonstration of SF-STAMP, we monitored the ultrafast dynamics of a laser ablation. We used a thin glass (50- μm thick, Nippon Electric Glass, Green Glass [OA-10G]) and ablated the surface by a focusing an FTL pump laser pulse (30 μJ , 50 fs [FWHM]). By propagating through glass rods (N-SF10 and BK7 whose propagating lengths are 700 and 900 mm, respectively), we added a total dispersion of $D \cdot z = 0.46$ ps/nm to a broadband probe pulse. The time window of single-shot measurements corresponded to 9.2 ps ($\Delta\lambda_{\text{window}} = 20$ nm, $\Delta\lambda_{\text{DOE}} = 5$ nm, $\Delta\lambda_{\text{BPF}} = 2.2$ nm). For imaging the dynamics of a laser ablation, we made a microscopic imaging system (**Figure 2.25**) with an $f = 30$ -mm condenser lens and an objective lens ($\times 20$, $NA = 0.40$, Olympus, LMPLFLN20X). Thus, the minimum spatial resolution of the experiment determined by the diffraction limit was $800 \text{ nm}/2NA = 1 \mu\text{m}$ (Abbe's diffraction limit). Then, the enlarged image was relayed to the object plane of the SF-STAMP system. The polarization analyzer was used for selecting only a polarization of the probe pulse, because the pump and probe pulse were orthogonally polarized to each other.

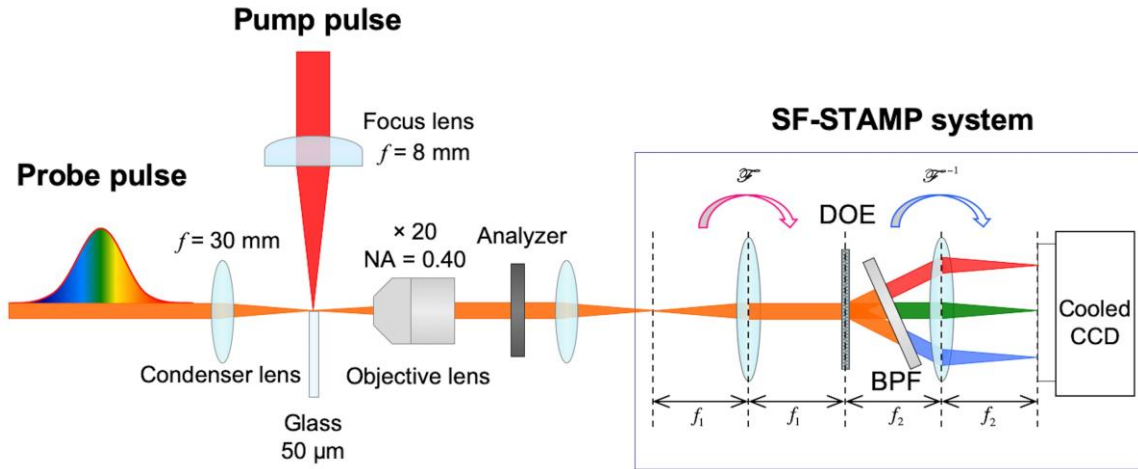


Figure 2.25 Experimental setup of microscopic SF-STAMP system for observation of ultrafast laser ablation dynamics. To select only a probe pulse, we used a polarization analyzer after the object lens.

Figure 2.26 shows 5-frame images of the moment when a femtosecond laser induced-air breakdown was generated in a single shot. In this setup, the time window was 9.2 ps, each image's exposure time was 1.1 ps, and the frame interval was 2.3 ps (corresponding to frame rates of 0.43 Tfps). Each wavelength image occupied 740×480 pixels. All the images were trimmed and subtracted from the image obtained before ablation, and their brightness was adjusted to compensate for the intensity variation among the probe

2. Fundamentals of ultrafast laser, and development and improvements of SF-STAMP

spectra. In a single-shot observation time window, an air breakdown was generated by an FTL laser pulse that was focused at 50 μm above the glass surface with a spherical lens ($f = 8 \text{ mm}$, $NA = 0.6$).

When the intense femtosecond laser pulse is propagating through the air, a plasma channel is formed due to the laser-induced air breakdown; this can instantaneously change the local refractive index [221–224]. The electrons and atoms in the ionized plasma reach the target surface and are reflected backward. Simultaneously, the free electrons on the target surface absorbed the laser energy and are emitted from the target surface by photoelectric and thermionic effects on a femtosecond to tens-of-picoseconds time scale. We adjusted the delay time between the pump and probe pulses by searching for the instance when an air breakdown occurred within a single probe-shot (spectral range of 770~750 nm); and we determined the delay time $t = 0$, since an air breakdown is generated by the electric field of the femtosecond laser pulse [223]. From $t = 0$, the probe pulse was partially absorbed by electrons produced in the air breakdown and thus attenuated [221].

In the present setup, we monitored the change in the probe amplitude (i.e., the shadow-graphic image); when converting the setup to be sensitive to refractive index changes such as a phase-contrast microscope, we will be able to find a clearer initiation of the air breakdown. We also confirmed that no air breakdown takes place in the spectral range longer than 770 nm. An air breakdown clearly appeared, and a filamentation close to the glass surface was also captured after 4.6 ps. The Rayleigh length of focusing was 18 μm . Two black spots, observed after 4.6-ps frames, are probably intense plasma spots generated at plasma channeling near the beam waist. The plasma formation will reflect the spatial beam quality of the incident pump laser pulse and also the spatiotemporal dynamics of the laser beam propagation in the channel.

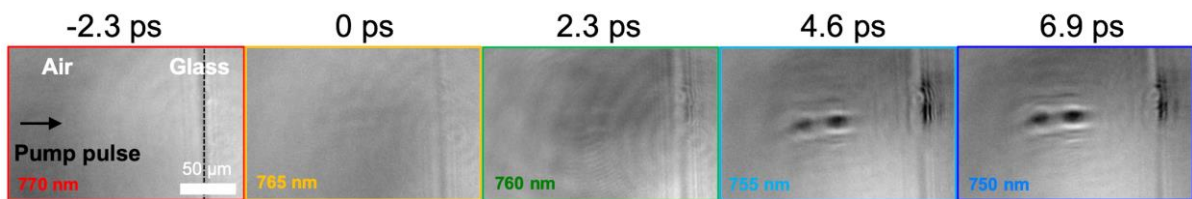


Figure 2.26 Measured single-shot SF-STAMP images of air breakdown generation within a time window of 9.2 ps. Exposure time of each frame was 1.1 ps. The dotted line shows the air-glass surface. Air breakdown was generated by an FTL laser pulse. Probe pulse was partially absorbed by air breakdown and thus attenuated (from 0 ps). A dark filament of laser-excited electrons close to the glass surface was also captured from 4.6 ps. Each image has 740×480 pixels. To avoid capturing the scattering light of a pump pulse whose spectral range was 830~770 nm, we used a probe pulse’s spectral range of 770~750 nm. Scale bar represents 50 μm .

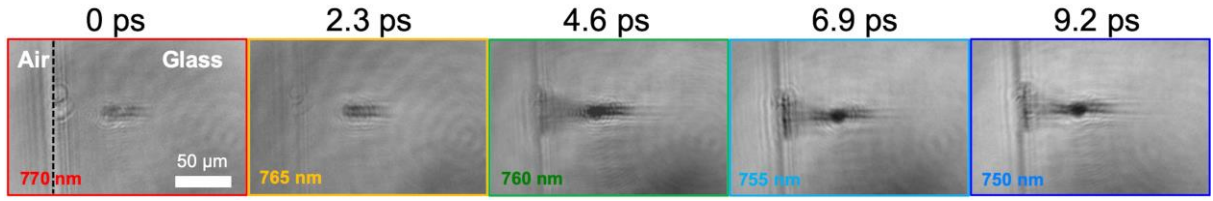


Figure 2.27 Measured single-shot SF-STAMP images of generation of a plasma filament in time window of 9.2 ps. Exposure time of each frame was 1.1 ps. In this case, pump pulse was focused into glass from left side. Dotted line shows air-glass surface. Scale bar represents 50 μm .

Figure 2.27 shows the moment results when an FTL laser pulse was focused into the glass. The laser pulse was focused at 50 μm into the glass from the surface. A dielectric breakdown and laser-induced plasma are visible. The dark area near the glass surface corresponds to the high density of the electrons in the plasma state. This observation is consistent with previous reports [221].

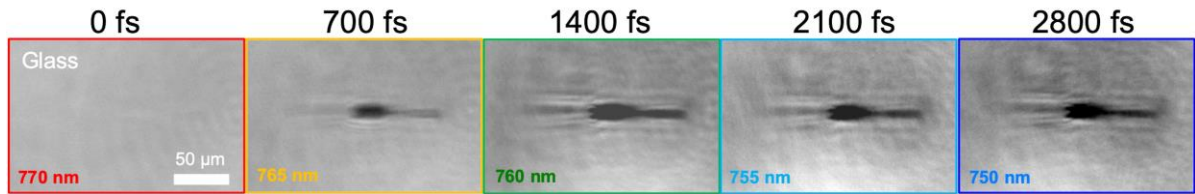


Figure 2.28 Measured single-shot SF-STAMP images of plasma filament generation in time window of 2.8 ps. In this case, Exposure time and frame interval of snapshots were 527 and 700 fs. Pump pulse was focused into the glass from the left side. Focused position was 100 μm from the air-glass surface. Scale bar represents 50 μm .

The results of a different time window of SF-STAMP are shown in **Figure 2.28**. In this case, we changed the total dispersion to $D \cdot z = 0.14$ ps/nm. The time window was reduced to 2.8 ps, each image's exposure time was 527 fs, and the frame interval was 700 fs (corresponding to frame rates of 1.43 Tfps). Therefore, SF-STAMP can capture different time scales. An FTL laser pulse was also focused into the glass, but to a little deeper position than that of **Figure 2.27**.

In this setup (using the same DOE and BPF), from Equations (2.48) and (2.49), the minimum frame interval of 477 fs can be achieved at $D \cdot z = 0.0953$ ps/nm. In this limit, the exposure time is equal to the frame interval. On the other hand, in a case with longer frame intervals, since the exposure time will not be longer than the frame interval, the frame interval can simply be selected by the second-order dispersion added to stretch the probe laser pulse. When the available probe laser pulse bandwidth is limited, the longest observation time window is determined by the highest linear chirp rate. We might be able to use a

2. Fundamentals of ultrafast laser, and development and improvements of SF-STAMP

multi-pass grating pulse stretcher or a single-mode fiber to realize higher chirp rates. However, when intense femtosecond laser pulses are launched into a single-mode fiber (a multi-mode fiber is not applicable due to mode dispersion), the laser propagation always causes Stimulated Raman Scattering, which degrades the frequency-time relation in the probe pulse. We can use moderate second-order dispersion obtainable by material dispersion of the long glass rods to stretch the probe laser pulse up to ~ 100 ps, when we use probe pulses with a much broader spectrum, such as the supercontinuum pulse used in our experiment.

In principle, STAMP schemes suffer from a disadvantage of measuring the scattering light or emission, which does not obey the relationship between the delay time and the instantaneous frequency in a linearly chirped-probe pulse. This defect can be removed when we use a pump pulse with a different wavelength from a probe pulse. When light emission is generated, such as fluorescence in the same wavelength band of a probe laser pulse, that light will also overlap to motion pictures. Therefore, the probe pulse's wavelength must be properly selected. In this experiment, we used a pump pulse that had a spectral range of 830~770 nm. To avoid capturing the scattering light of a pump pulse, we used a probe pulse's spectral range of 770~750 nm.

Summary of this section

We proposed and experimentally demonstrated a more straightforward all-optical ultrafast 2D-burst imaging method of STAMP utilizing spectral filtering (SF-STAMP), the temporal resolution of which is defined by the duration of a frequency-chirped probe pulse. This kind of phenomenon in the femtosecond-to-picosecond timescale has previously only been observed by the pump/probe imaging in which a sample is replaced in every measurement. This demonstration highlights the single-shot utility of STAMP's movie-shooting capability. In principle, by controlling the amount of dispersion that is added to the flash pulse, we can choose an observation time scale from sub-picoseconds ($\sim 10^{-13}$ s) to sub-nanoseconds ($\sim 10^{-10}$ s). The number of possible frames is determined by the number of array beams duplicated from a DOE, and the number of multispectral images and the spectral bandwidth that a BPF can select in a single shot can be increased using a larger CCD image sensor and another DOE with a larger diffraction angle and many array beams.

2.3 Improvements of SF-STAMP

The 5-frame SF-STAMP system has successfully shown a proof-of-principle demonstration of 2D-burst imaging so far. The total number of frames was limited to five because of the 2×2 beams that were generated by the DOE. In principle, in the same condition of this experiment (chirped-broadband light source, band-pass filter, and Fourier lenses), by using a CCD camera with a larger image plane and another DOE with a larger diffraction angle and many array beams, the spectral bandwidth in a single-shot can be broadened to ~ 50 nm and the possible number of frames will be ~ 30 .

In this section, SF-STAMP's scaling to 25 frames, and an extension approach to the nanoseconds time window with spectrally sweeping burst pulses are described.

2.3.1 Scaling of the number of burst-frames to 25 frames in SF-STAMP

To increase the number of frames in an SF-STAMP system, we used a specially designed 25-beam-generating DOE (HOLOEYE) that generates 5×5 dot beams with a full diffraction angle (2α) of 25.6° at a wavelength of 800 nm (**Figure 2.29(a)**). The first and second Fourier lenses in the SF-STAMP system have a focal length of $f_1 = f_2 = 50$ mm. The combination of DOE and BPF (IRIDIAN, ZX000167, a center wavelength of 830 nm and bandwidth [FWHM] of 2.2 nm) determines the entire observation bandwidth of ~ 40 nm that ranges from 825 to 785 nm. **Figure 2.29(b)** shows the DOE and BPF layout for spatially and spectrally resolving the image. The spectrum location of the 25-BPF selectable bands in the probe laser is indicated in **Figure 2.29(c)**. In the 5-frames SF-STAMP case, we used a DOE (HOLOEYE, DE 225) with a full diffraction angle of $\sim 10^\circ$, the same BPF, and a 20-nm bandwidth. Since an imaging sensor with a large detecting area is required for capturing 25 images, we used an electrically cooled CCD camera (BITRAN, BU-55LN) that has 4872×3248 pixels (each pixel size is 7.4×7.4 μm) and a CCD plane size of 36.1×24.0 mm. Quantum efficiency was $>10\%$ at 800 nm.

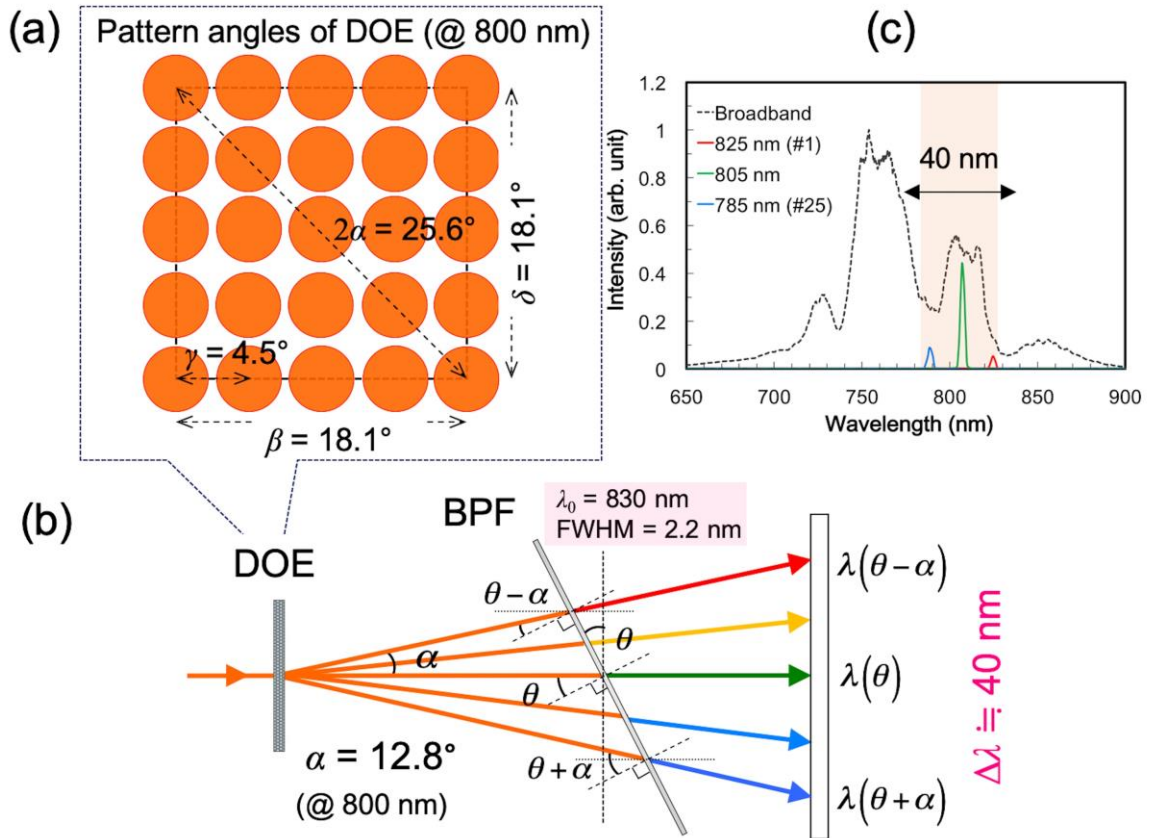


Figure 2.29 (a) Design of 25-beam-generating DOE (800-nm wavelength), (b) arrangement of a 25-beam-generating DOE and a BPF to spatially and spectrally resolve the image, and (c) spectral property of a broadband probe pulse and location of 25-BPF selectable bands in the spectrum.

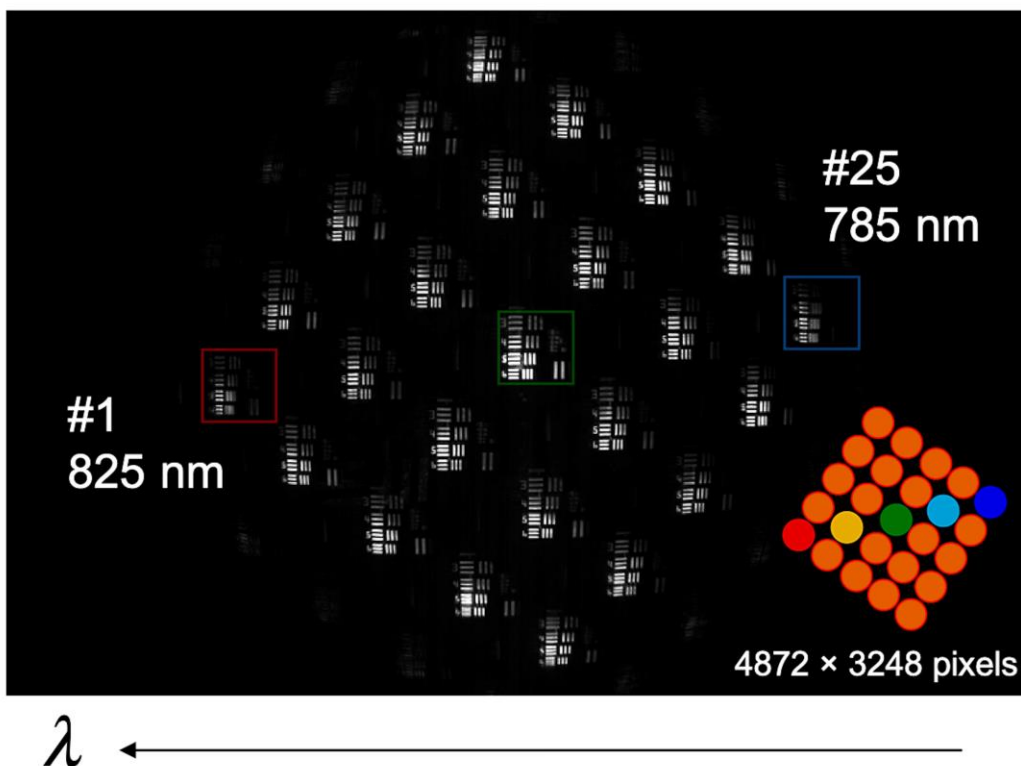


Figure 2.30 25-multispectral images captured by the SF-STAMP system.

We examined the imaging performance for 25-multispectral images by placing a USAF-1951 test target on the object plane of the SF-STAMP system, and the captured image is shown in **Figure 2.30**. Each spectral image occupied 450×450 pixels. **Figure 2.31** also shows a microscopic image of the test target obtained with a combination of a 20 times microscopic system ($NA = 0.40$, OLYMPUS, LMPLFLN20 \times) and the 25-frame SF-STAMP. The spatial resolution was the same as the 5-frame SF-STAMP experiment case in 2.2.3.

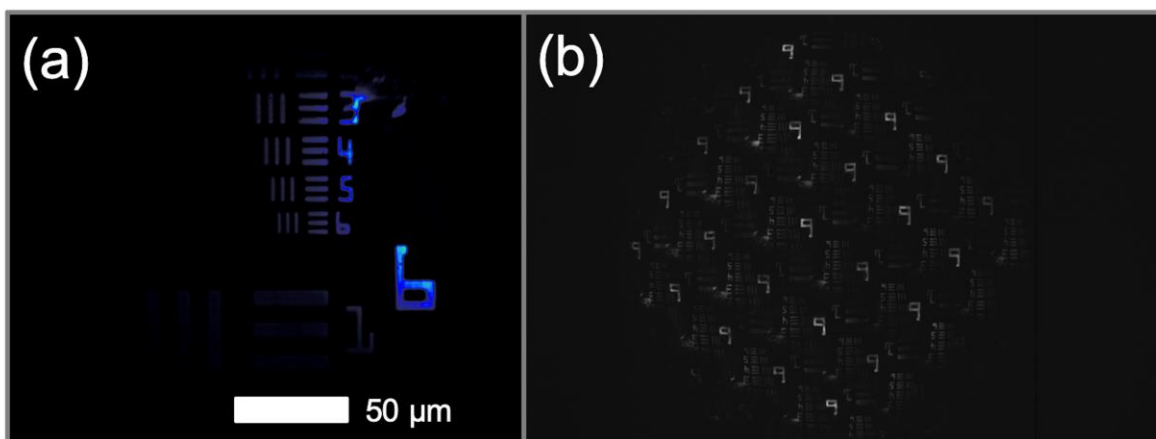


Figure 2.31 Microscopic images (a) at object plane, (b) at image plane of the 25-frame SF-STAMP system

2.3.1.1 Single-shot experiments by SF-STAMP with the 25-beam generating DOE

In this section, the details of single-shot experiments conducted with the 25-frame SF-STAMP system are described. The improved SF-STAMP has observed ultrafast transient phenomena; a femtosecond laser-induced plasma phenomenon in glass and the crystalline-to-amorphous phase transition of $\text{Ge}_2\text{Sb}_2\text{Te}_5$ that excited by a femtosecond laser pulse [61].

Single-shot observation of a femtosecond laser-induced plasma phenomenon in glass

Combining a microscopic imaging system and the 25-frame SF-STAMP system, we successfully captured the ultrafast dynamics of a femtosecond laser-induced plasma inside glass. The experimental setup was the same as the 5-frame SF-STAMP case (**Figure 2.25**). The changes in the refractive index inside the glass induced by a femtosecond laser are shown in **Figure 2.32**. A dielectric breakdown and a laser-induced plasma are visible in single-shot 25 frames. In this case, the total dispersion of 0.14 ps/nm was added on the broadband probe pulse. The spectral bandwidth was 40 nm (from 825 nm to 785 nm) such that the observation time window was 5.6 ps. In frame #5, a dielectric breakdown appeared at the center of the image. In frames #7–9, the change of intensity gradually increased. From frame #11, this dark region grew to shape of a plasma filament. In frame #25, the dark spot was clearly observed. The averaged frame interval was 0.23 ps (corresponding to frame rates of 4.35 Tfps) and the exposure time was 0.52 ps.

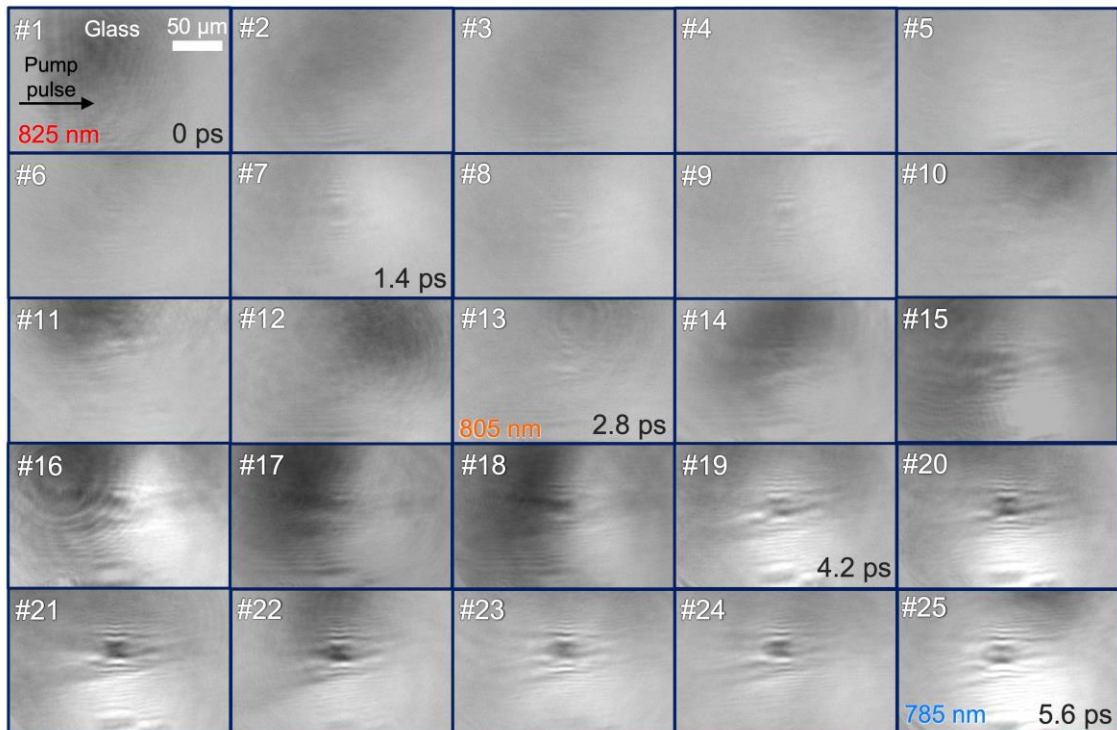
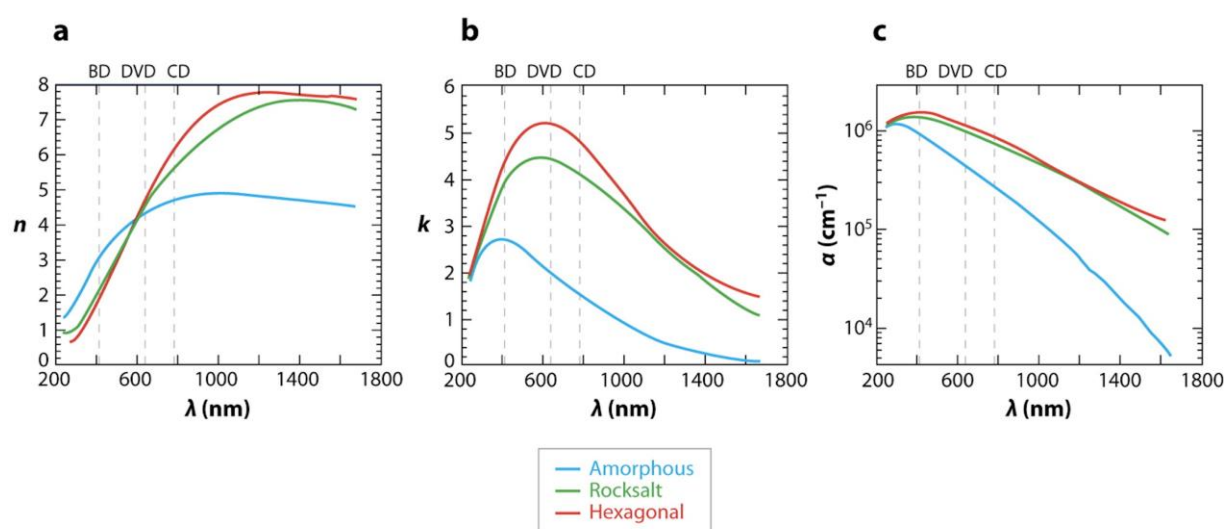


Figure 2.32 Measured single-shot images of a plasma filament generation inside glass in a time window of 5.6 ps: with the exposure time and frame interval of 0.52 ps and 0.23 ps

Single-shot observation of ultrafast photo-induced phase transition in $\text{Ge}_2\text{Sb}_2\text{Te}_5$ (GST)

Next, a femtosecond laser-induced crystalline-to-amorphous phase transition of $\text{Ge}_2\text{Sb}_2\text{Te}_5$ (GST) was captured with a single-shot 2D-imaging basis for the first time. The optical properties in the crystalline and amorphous phases of GST (refractive index n , extinction coefficient k , absorption coefficient $\alpha = 4\pi k/\lambda$) are shown in **Figure 2.33**. The complex refractive index ($N = n + ik$) differs significantly between the two-phase states. Therefore, GST has higher reflectivity, lower transmittance, and higher absorption in the crystalline state than in the amorphous phase. On the other hand, in the amorphous phase, the reflectance is low, the transmittance is high, and the absorption is small. Thus, GSTs can repeat phase changes between the crystalline and amorphous phases. These difference in optical properties are utilized as a material for rewritable optical memories such as digital versatile discs (DVDs) [24]. In optical recording systems, reversible phase changes between crystalline and amorphous phases are induced by irradiating the focused nanosecond laser pulses or continuous-wave (CW) laser output by transient temperature ramping.

On the other hand, in recent years, ultrafast crystalline-to-amorphous phase transition induced by femtosecond laser pulses by a non-thermal process, which occurs in the sub-picosecond time regime, has often been reported [25,26,28,53,225–229]. In their measurements, time-resolved methods with X-ray and electron diffraction, and single-shot spectroscopy were employed. However, no results have been reported with 2D-image measurements for this ultrafast phase transition in a single-shot measurement scheme.



AR Raoux S. 2009.
Annu. Rev. Mater. Res. 39:25–48

doi:10.1146/annurev-matsci-082908-145405

Figure 2.33 Optical property (a) n , (b) k , and (c) α of the amorphous, rocksalt, and hexagonal phases of $\text{Ge}_2\text{Sb}_2\text{Te}_5$ (quoted from [230])

2. Fundamentals of ultrafast laser, and development and improvements of SF-STAMP

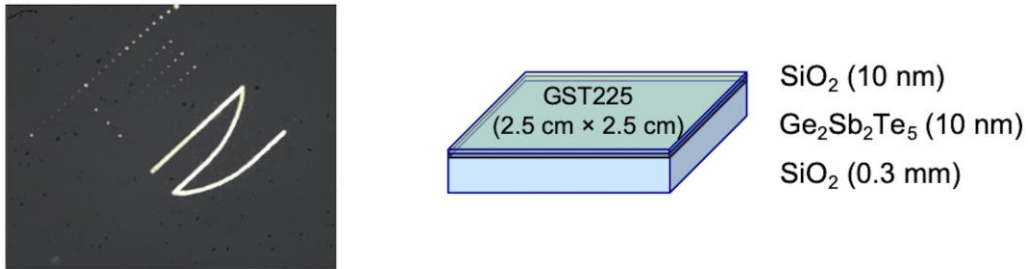


Figure 2.34 Microscopic image of GST sample and its structure

Figure 2.34 shows the GST sample, which was composed of a 0.3-mm-thick glass substrate, a 10-nm-thick GST film layer, and a 10-nm-thick SiO₂ protective coat. The pump laser fluence that is required to cause a permanent amorphous phase change is ~ 10 mJ/cm², and thus the pump pulse was focused on the GST sample from the opposite direction of the probe pulse by using a $\times 20$ objective lens ($NA = 0.40$, OLYMPUS, LMPLFLN20 \times).

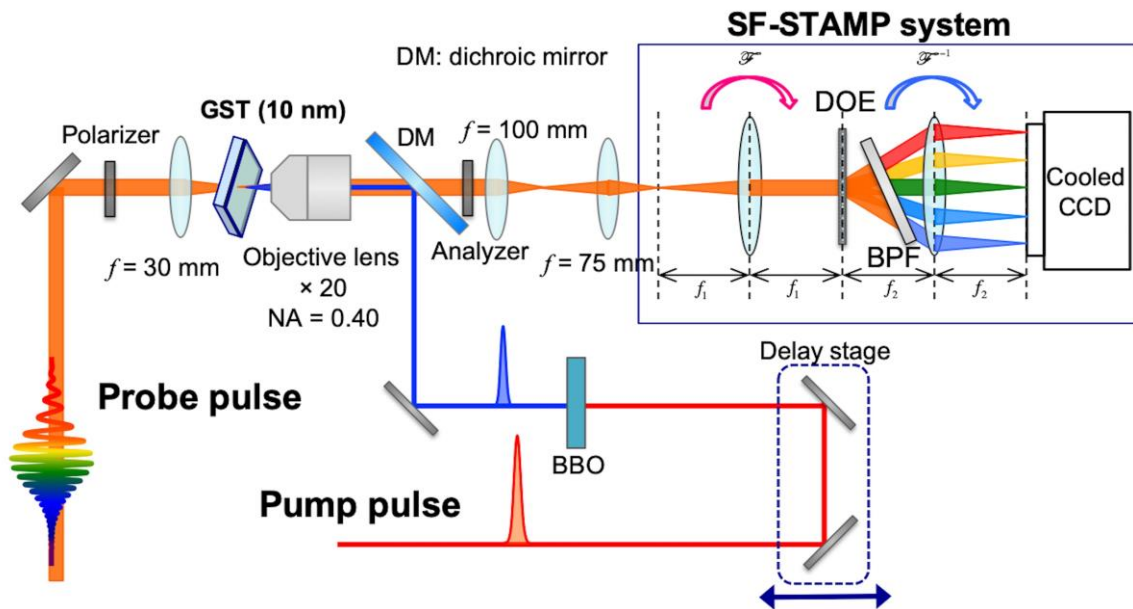


Figure 2.35 Experimental setup of ultrafast crystalline-to-amorphous phase transition in GST.

The entire experimental setup is shown in **Figure 2.35**. The light source was a mode-locked Ti:sapphire laser (Coherent, Mira) with chirped pulse amplification (CPA). The average energy was 1 mJ at a repetition rate of 1 kHz with a pulse width of 50 fs (FWHM). The amplified laser pulse (800 nm) was split into a pump pulse, which initiates the phase transform of the GST film, and a probe pulse. To avoid crosstalk

2. Fundamentals of ultrafast laser, and development and improvements of SF-STAMP

between the spectra of the scattered pump and probe pulses, we converted the pump pulse to the second harmonic (400 nm) with a BBO nonlinear crystal. Moreover, the polarizations of the pulses were also adjusted to be orthogonal to each other. In the probe pulse branch, to broaden the bandwidth over 40 nm, the probe pulse was focused into the Ar-gas filled hollow-core fiber (HCF) (126- μm core diameter). In the HCF, a broadband pulse (650–900 nm) was generated by self-phase modulation (SPM) and four-wave mixing. To stretch the pulse width, the broadband pulse was passed thorough optical glass rods (N-SF11 and BK7, each of which has dispersion parameters at 800 nm of -551.8 ps/nm \cdot km and -131.4 ps/nm \cdot km). The entire material dispersion of $D\cdot z$ is 0.082 ps/nm. In the 25-frame SF-STAMP system, where $\Delta\lambda_{\text{BPF}} = 2.2$ nm, $\Delta\lambda_{\text{DOE}} = 1.7$ nm (on average), and $\lambda_0 = 805$ nm; thus the averaged values of exposure time (τ) and the frame interval (Δt) were 465 fs and 133 fs, respectively.

To observe the GST phase transition, we only detected the intensity change of the transmitted probe laser. We constructed a transmission microscopic optical system and relayed an enlarged image to the SF-STAMP system. The intensity of a probe pulse was set lower than the threshold at which no phase change occurs by the probe itself. The glass plate with a GST sample was placed slightly inclined to avoid being affected by the influence of stray light due to reflection from the GST sample layers. For a single-shot measurement, we employed an optical chopper and a shutter to select one pulse.

We achieved the temporal overlap between the pump and chirped probe pulses in two steps. First, at the sample position, we placed a BBO crystal and generated sum-frequency with the Fourier transform limited pump pulse (800 nm in this case) and the chirped probe pulse. The wavelength of the sum-frequency pulse was measured by varying the relative delay between the two pulses and calibrating the position of the delay stage. We confirmed that the measured chirp rate agreed well with that estimated from the material dispersion of the glass rods. Next, we set the GST sample and converted the pump pulse to a frequency-doubled (400 nm) pump pulse. The optical path length of the BBO nonlinear crystal was compensated by the delay stage.

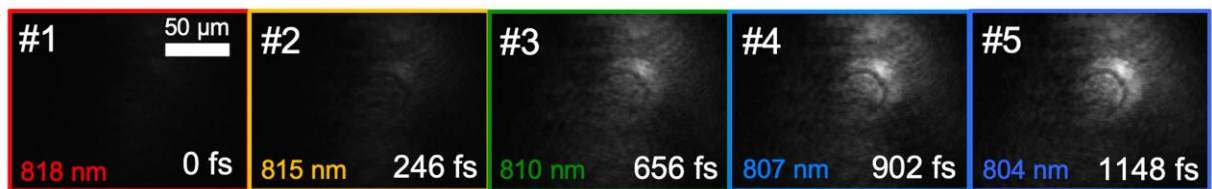


Figure 2.36 Measured images of crystalline-to-amorphous phase transition in GST by the 5-frame SF-STAMP (single-shot time window of 1.1 ps). Exposure time and frame interval of snapshots were 465 fs and 287 fs. Scale bar represents 50 μm .

Figure 2.36 shows the result of an ultrafast crystalline-to-amorphous phase transition of GST induced by a 400-nm femtosecond laser excitation with a 5-frame SF-STAMP setup. In this setup, we added the total dispersion of 0.082 ps/nm on the probe pulse. In the 5-frame measurement, the spectral bandwidth in a single-shot was 20 nm (from 818 to 804 nm), and the observation time window was 1.1 ps. The specific time for each frame is determined by the center wavelength of the BPF and the linear chirp rate of the probe laser pulse. The average frame intervals were 287 fs corresponding to frame rates of 1.23 Tfps.

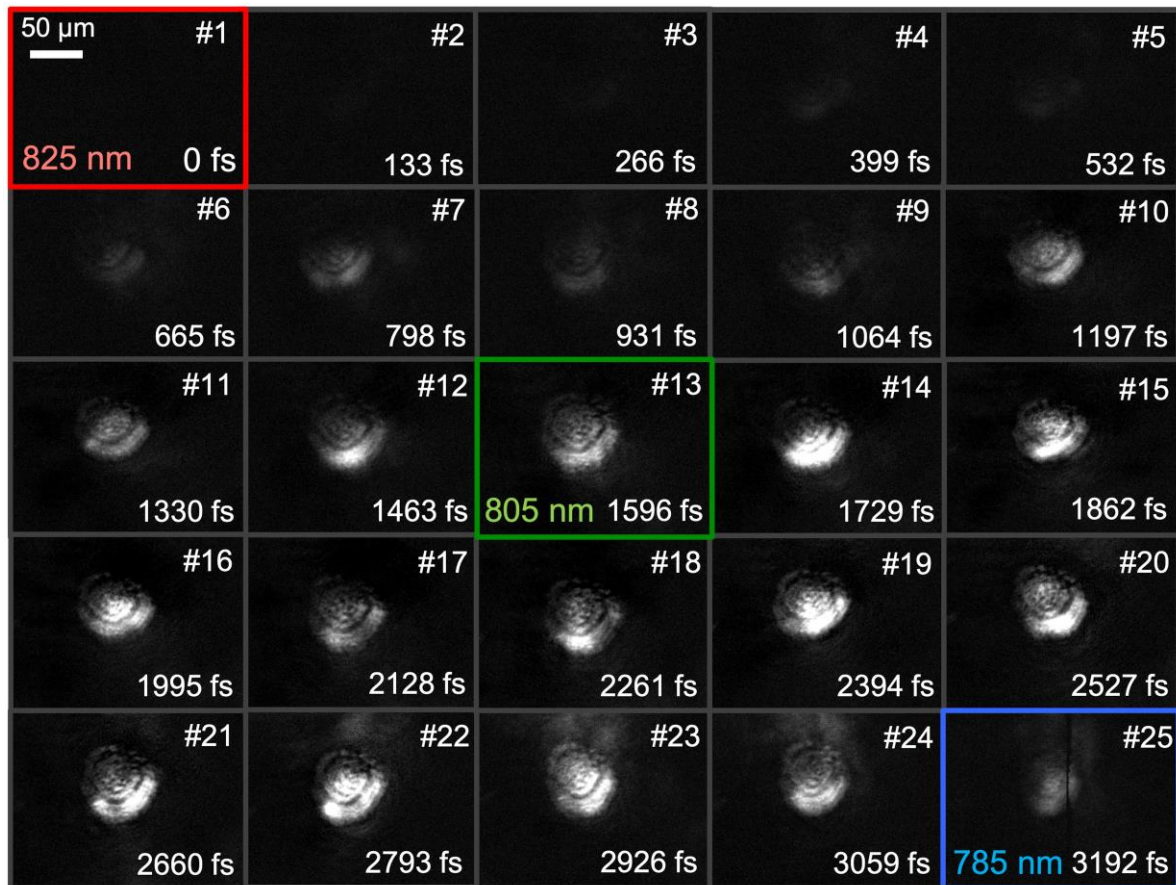


Figure 2.37 Measured images of crystalline-to-amorphous phase transition in GST by the 25-frame SF-STAMP (single-shot time window of 3.2 ps). Exposure time and frame interval of snapshots were 465 fs and 133 fs. Scale bar represents 50 μm .

The result of the 25-frame SF-STAMP measurement is shown in **Figure 2.37**. The single-shot time window was 3.2 ps, corresponding to 40-nm bandwidths, and the average frame intervals were 133 fs (corresponding to frame rates of 7.52 Tfps). In both cases in **Figure 2.36** and **Figure 2.37**, the average exposure time at each frame was 465 fs. Each wavelength image occupied 400 \times 300 pixels. All the images were trimmed, and the intensity differences were taken from the image obtained before the pump

2. Fundamentals of ultrafast laser, and development and improvements of SF-STAMP

irradiation, and their brightness was adjusted to compensate for the intensity variation among the probe spectra. Since we can ignore the dependence of GST's optical transmittance on wavelength in the probe bandwidth of 40 nm [231], no further correction was made for each frame image.

As shown in **Figure 2.36** and **Figure 2.37**, on the irradiation area of the pump laser pulse, the GST film showed higher transmittance of the probe laser beam and a bright amorphous mark appeared at ~250 fs after the pump laser irradiation. The minimum transmittance change detectable with the electrically cooled CCD camera was ~3% in our setup. The gradual change in the probe laser transmission up to ~660 fs was well shown in **Figure 2.37**, which was not resolved in the 5-frame shot in **Figure 2.36**. These single-shot measurement results agree with the phase transition time scale reported in previous research [25,26,228]. The interference fringes in the pictures were caused by the pump pulse's diffraction at the edge of the objective lens. The amorphized marks did not change after 798 fs and still exhibited the interference fringe. In comparison with this amorphized area, the surrounding crystalline areas kept high reflectance. Therefore, we confirmed that the spatial intensity distribution of the pump laser pulse is clearly coincident with the phase change pattern; the phase-change domain does not spatially spread to the surrounding area. In the theory, which has widely been accepted, the laser-induced nonthermal amorphization is initiated from Ge-atom displacements from octahedral to tetrahedral sites [26]. Therefore, the amorphized domain is defined by the pump pulse's irradiation area, and even the interference pattern is transferred to amorphization. Our 2D-burst result is the first observation of such a fast-phase transition induced by a femtosecond laser pulse on a single event basis.

Optimum temporal resolution

In the experiment of the crystalline-to-amorphous phase transition in GST, the amount of dispersion was 0.082 ps/nm and $\Delta\lambda_{\text{BPF}} = 2.2$ nm. Thus, the exposure time of each frame was 465 fs. Compared to the much amount of dispersion cases such as the experiment in 2.2.3.3, exposure time is longer than the adjacent frame interval. Even though the temporal resolution was not the ideal case, a burst time sequence of SF-STAMP multispectral images reflected transient transmittance change.

Here, the optimum temporal resolution is discussed. Based on Equations (2.48) and (2.49), the simulation results of exposure time (τ) and frame interval (Δt) are shown in **Figure 2.38**. In **Figure 2.38(a)**, these temporal performances were expressed as a function of bandwidths, where the amount of dispersion was fixed at 0.082 ps/nm and center wavelength was 800 nm. From this relationship, the minimum exposure time in this case ($D \cdot z = 0.082$ ps/nm) was 395 fs when $\Delta\lambda_{\text{BPF}}$ of 3.4 nm was adapted. On the other hand, the function of amounts of dispersion ($\Delta\lambda_{\text{BPF}}$ of 2.2 nm and $\Delta\lambda_{\text{DOE}}$ of 1.66 nm) is shown in **Figure 2.38(b)**. In this situation (same as **Figure 2.37**), however, exposure time always longer than frame interval.

2. Fundamentals of ultrafast laser, and development and improvements of SF-STAMP

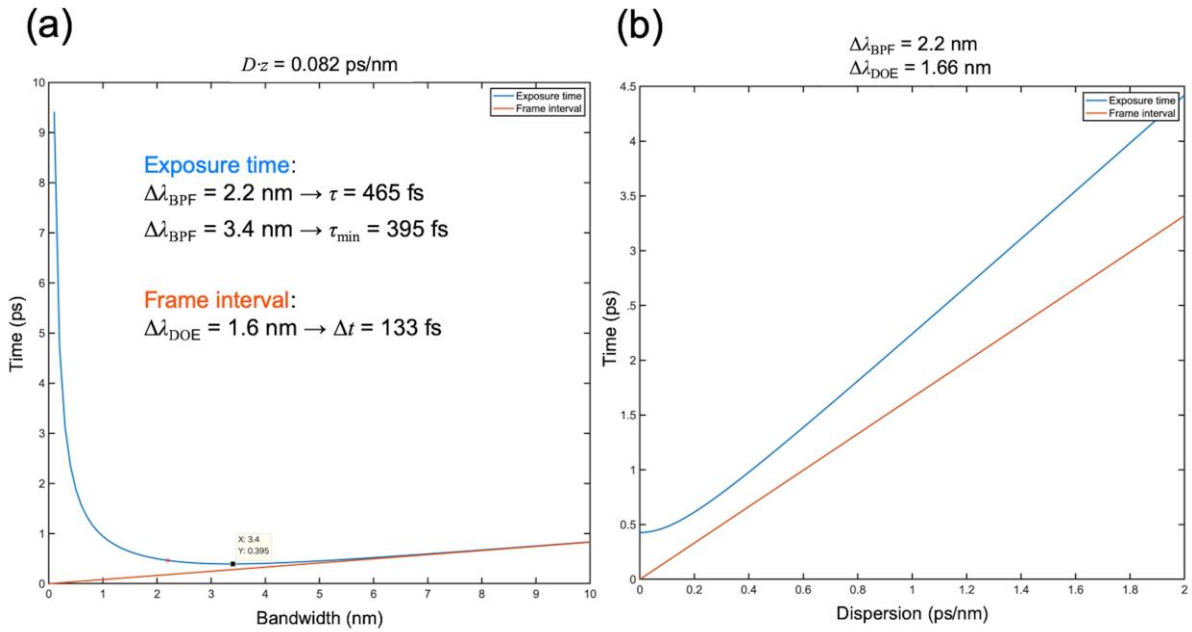


Figure 2.38 Simulation of SF-STAMP's temporal performance; exposure time and frame interval: (a) as a function of bandwidth (dispersion amount of 0.082 ps/nm) and (b) as a function of the amount of dispersion: ($\Delta\lambda_{\text{BPF}}$ of 2.2 nm and $\Delta\lambda_{\text{DOE}}$ of 1.66 nm).

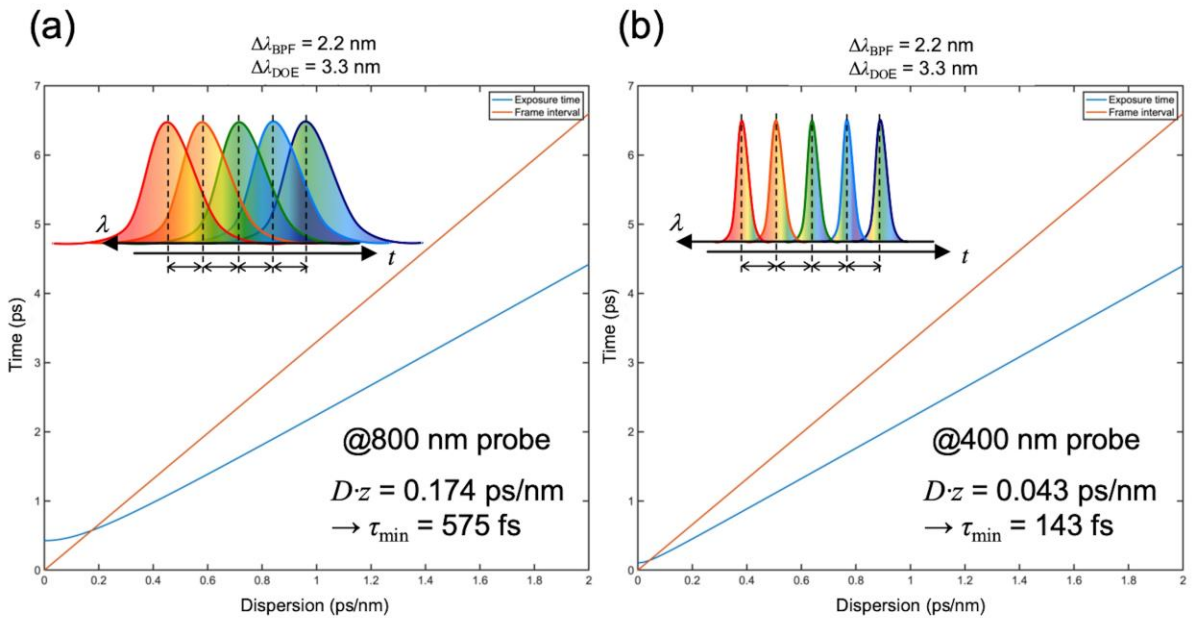


Figure 2.39 Simulation of SF-STAMP's temporal performance with $\Delta\lambda_{\text{BPF}}$ of 2.2 nm and $\Delta\lambda_{\text{DOE}}$ of 3.3 nm; exposure time and frame interval as a function of the amount of dispersion: (a) center wavelength of 800 nm and (b) center wavelength of 400 nm.

2. Fundamentals of ultrafast laser, and development and improvements of SF-STAMP

Meanwhile, the simulation results of exposure time and frame interval as a function of amounts of dispersion ($\Delta\lambda_{\text{BPF}}$ of 2.2 nm and $\Delta\lambda_{\text{DOE}}$ of 3.3 nm) are shown in **Figure 2.39**. The situation of frame intervals here is equivalent to **Figure 2.36** and every other frame in **Figure 2.37**. **Figure 2.39(a)** suggests that when the center wavelength is 800 nm, exposure time and frame interval overlap at the dispersion of 0.174 ps/nm. Thus, the minimum exposure time in this fixed BPF and DOE relation case was 575 fs. To realize much faster temporal resolution in this constraint, a 400-nm probe is useful. As shown in **Figure 2.39(b)**, when employing center wavelength of 400 nm, exposure time and frame interval overlap at the dispersion of 0.043 ps/nm, and the minimum exposure time comes to 143 fs. Therefore, a shorter wavelength probe will contribute to high temporal resolution in STAMP.

Summary of this section

The initial SF-STAMP system has been modified, the probe laser bandwidth expanded from 20 nm to ~40 nm, and the number of burst frames successfully increased from 5 to 25. As the 25-frame SF-STAMP single-shot ultrafast imaging demonstrations, a femtosecond laser-induced plasma phenomenon in glass and an ultrafast photo-induced phase transition in $\text{Ge}_2\text{Sb}_2\text{Te}_5$ (GST) were captured. The optimum temporal resolution of SF-STAMP was also discussed in the GST experiment case.

2.3.2 Extension of the observation time window to nanoseconds in SF-STAMP

So far, the SF-STAMP has achieved 25 burst images over several tens of picoseconds with sub-picosecond temporal resolution. However, the extension of the observation time window into the nanosecond region has not been achieved. Around nanosecond time range that the conventional high-speed camera cannot reach, many interesting fast phenomena exist, such as interaction with shockwaves. Thus, the time window in SF-STAMP must be extended to the sub-nanosecond region.

In SF-STAMP, as expressed by Equation (2.46), the observation time window of a chirped-pulse probe is determined by either tuning the amount of dispersion ($D \cdot z$) (ps/nm) or changing the bandwidth of the BPF's selected spectrum ($\Delta\lambda_{\text{window}}$). Thus, there are two possible extension scenarios by dispersion dose or broadband spectrum usage. When extending it to nanoseconds with an optical fiber dispersion, in addition to second-order dispersion, such nonlinear optical phenomena as stimulated Raman scattering (SRS), self-phase modulation (SPM), and four-wave mixing (FWM) take place during the pulse propagation, which degrades the relationship between the instantaneous frequency and the time; while a much broadband pulse approach, such as an octave-spanning supercontinuum pulse generated by a rare-gas-filled hollow-core fiber, can be stretched to a few hundred picoseconds with a reasonable length of dispersive materials. However, in this case, chromatic distortion with such a broadband light in an imaging optics degrades the image quality. Even worse, a broadband pulse cannot apply to a wavelength-dependent object. Hence, extending the time window into nanoseconds with a chirped probe is not straightforward.

On the other hand, when applying a unique optical setup that can generate delayed pulses with different wavelength [159], or such dispersive optics as the free-space angular-chirp-enhanced delay (FACED) [144,148], wavelength sweeping discrete burst pulses can even be generated for pulses with a narrower spectrum. The FACED was initially developed as a method to stretch pulse durations into nanoseconds with a narrow spectrum for ultrafast time-stretching laser scanning microscopy. Since FACED performs a time-stretch in free space, we can obtain stretched pulses without significant optical loss or undesirable nonlinear effects. When using a $4f$ -system based on an angular disperser that returns all the pulses with different center wavelengths into the same axis again, these delayed burst pulses with different center wavelengths can implement to a probe laser pulse train for SF-STAMP. Since their number of burst pulses and the pulse interval can alter, the entire train length can reach nanoseconds.

In this subsection, the principle of FACED is introduced, then the details and results of the spectrally sweeping burst probes generation $4f$ -FACED system that is combined with a FACED composed of a pair of tilted mirrors and a $4f$ -system. Finally, experimental demonstrations of single-shot 6-burst imaging have been achieved by SF-STAMP with spectrally sweeping probe pulses of a 300-ps interval in a 1.5-ns time window.

2.3.2.1 Spectrally sweeping burst delay probe pulse train

Free-space angular-chirp-enhanced delay (FACED)

FACED was developed by Wu, Xu², *et al.* in 2017 to realize the visible wavelength time-stretch laser scanning [144,148]. A FACED is an optical system that stretches the time width of an input pulse in free space using multiple reflections by misaligned mirror pairs. FACED is different from the conventional time stretching approach using dispersive materials such as optical fiber. The time extension is performed in free space, thus there is little loss, and it is possible to apply the visible range, which has a large loss with optical fibers. **Figure 2.40** shows the configuration of the FACED device.

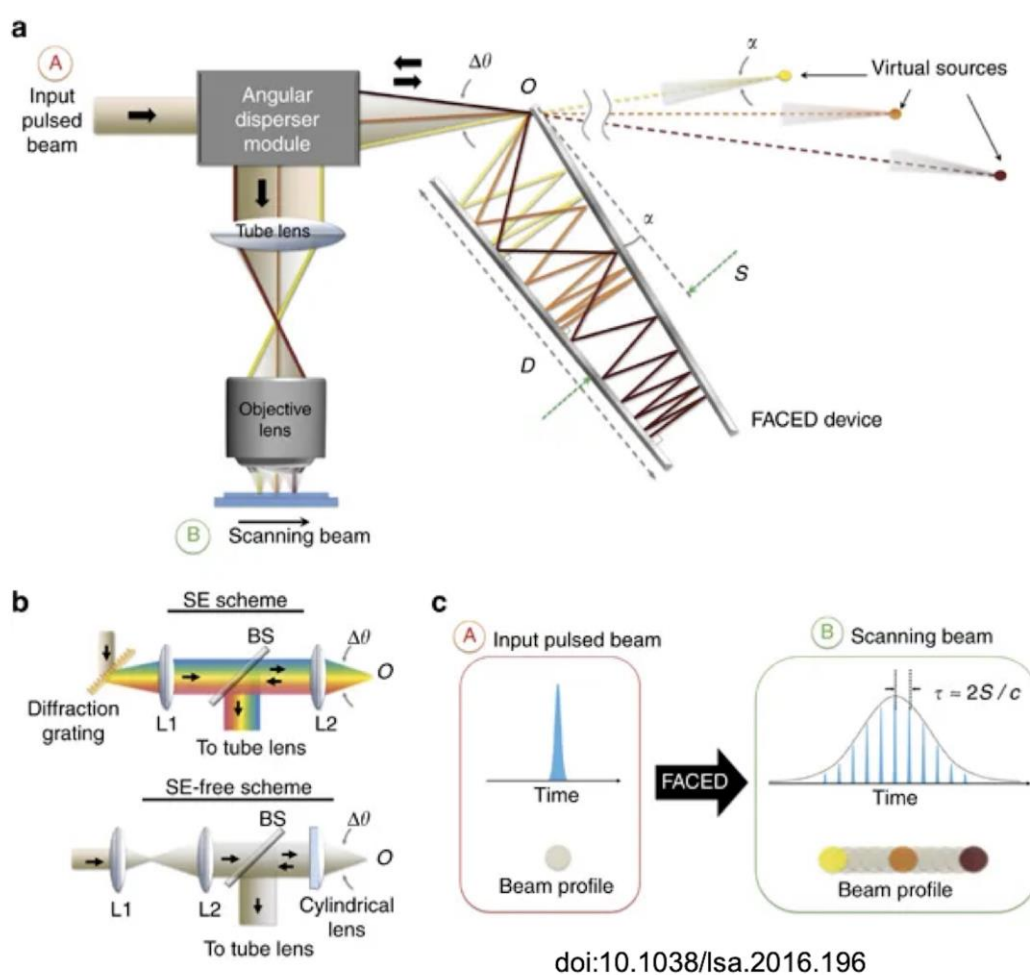


Figure 2.40 Schematic of Free-space Angular-Chirp-Enhanced Delay (FACED)

(Figure reproduced with permission from [144]: doi:10.1038/lisa.2016.196 © 2017 NPG)

² These authors contributed equally to the work.

2. Fundamentals of ultrafast laser, and development and improvements of SF-STAMP

FACED utilizes the minute misalignment angle (α) between a pair of highly reflective plane mirrors (separated by a distance S), which results in a substantial enhancement in the light-path length and, consequently, the pulse stretching in free space within a practically compact setup.

The input light is converged at the entrance to the FACED device (position O in **Figure 2.40**). This is achieved using an optical module consisting of a relay-lens system and an angular disperser, which can be either a diffraction grating (for time-stretch imaging with spectral encoding, called the SE scheme) or simply a focusing cylindrical lens (for time-stretch imaging without spectral encoding, called the SE-free scheme; **Figure 2.40(b)**). In our SF-STAMP application, the SE scheme is employed. The condition with properly misalignment-angle geometry and suitable mirror dimensions produces spatially chirped zig-zag paths possible. This misaligned mirror geometry creates the spatially chirped paths and substantially enhances the temporal delay of each path within the FACED device in free space. In this way, the output pulse is temporally stretched by this angle-dependent delay.

When the input light is a broadband pulse and is angularly dispersed by the diffraction grating in the SE scheme, different frequency components propagate the zig-zag paths, hence, even in the free-space operation, introducing significant wavelength-dependent time delays (that is, GDD) is achievable. In the FACED device, a discrete set of beam paths return exactly along their initial incoming paths after they have reached one of the mirrors at normal incidence. These rays, referred to as cardinal rays, have angles of incidence (θ) and given by Equation (2.50):

$$\theta = k\alpha \quad (k \text{ is an integer}) \quad (2.50)$$

where k is an integer, at the entrance O . Note that the rays that are not cardinal are also back-reflected, albeit not along their original paths. These non-cardinal rays can be regarded as having been emitted from a set of virtual sources, each with a beam divergence angle of α .

Thus, the FACED device can generate an array of time-delayed virtual sources that are automatically aligned in space by the misaligned mirror geometry. By engaging any relay-lens system to sequentially project these virtual sources onto various locations on the sample plane, such that FACED can not only provide pulse stretching in free space, but also an all-optical laser-scanning mechanism for time-stretch imaging [144–147].

The number of FACED pulses (that is, cardinal rays) M is simply proportional to the input cone angle of the converging beam $\Delta\theta$:

$$M = \frac{\Delta\theta}{\alpha} \quad (2.51)$$

2. Fundamentals of ultrafast laser, and development and improvements of SF-STAMP

The temporal delay between any adjacent pulses (τ) can be directly obtained from the difference in their optical paths:

$$\tau = \frac{2S}{c} \quad (2.52)$$

where c is the speed of light and S is mirrors separation length. Therefore, the input light is separated in time into sub-pulses, each of which corresponds to a virtual source (**Figure 2.40(c)**).

The envelope of the burst pulse train is the output stretched pulse. The total time delay across all M FACED pulses, that is, the overall stretched pulse width ΔT_{total} , can be determined by

$$\Delta T_{\text{total}} = \tau M = \frac{2S \Delta\theta}{c \alpha} \quad (2.53)$$

Note that Equations (2.52) and (2.53) are valid when $\Delta\theta$ is small (<100 mrad, relative error $<0.2\%$).

From the above, the number of FACED pulses and the time interval of an adjacent pulse can be arbitrarily tuned by adjusting the angle of the mirror pair (α) and the mirror's separation interval (S). Note that the total time window is physically limited by the horizontal length of the mirror pair.

In the latter part of this section, based on the fundamental concept of FACED, the application of spectrally sweeping burst delayed probes for sub-nanosecond SF-STAMP is described.

Generation of spectrally sweeping delayed pulses with 4f-FACED system

Figure 2.41(a) depicts the schematic setup of the spectrally sweeping delayed pulses generation by a 4f-FACED system. The 4f-FACED system consists of a transmission diffraction grating (1600 lines/mm), two cylindrical lenses with focal lengths of 100 mm (CL1) and 150 mm (CL2), and a pair of slightly tilted, highly reflective dielectric mirrors (200 mm, $>99.5\%$) (HR1, HR2). An input laser pulse is angularly dispersed by the diffraction grating, and converged at the entrance of the mirror pair with different angles of incident depending on the wavelength. Each wavelength component of the input pulse propagates different optical paths between the mirror pair. The beam propagation can be treated as a set of spatially chirped zig-zag paths. Such a beam trajectory substantially enhances the time delays between different paths of the reflected beams, consequently generating multiple FACED pulses with different center wavelengths at a fixed interval [144].

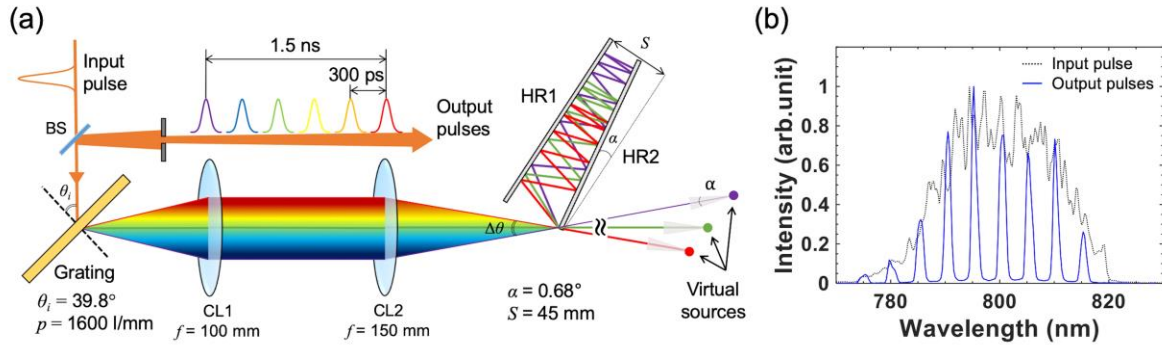


Figure 2.41 (a) Schematic setup of the spectrally sweeping delayed pulses generation by a $4f$ -FACED system, (b) spectrum of amplified Ti:Sapphire laser pulse and spectra of spectrally sweeping pulses generated by the $4f$ -FACED.

In the $4f$ -FACED system, the number of burst pulses can be tunable by changing the angle of the mirror pair (α), and the pulse interval can be adjusted by changing mirror separation length (S). We set angle $\alpha = 0.68^\circ$ and mirror separation $S = 45$ mm to generate six pulses with a 300-ps interval. We confirmed the relationship between wavelength and delay time of those discrete pulses generated from FACED system by sum frequency generation (SFG) with a reference pulse. For the ultrafast 2D-image acquisition by the STAMP scheme, the copropagating probe pulses need to be produced. Thus, we placed a beam splitter (BS) after the $4f$ -FACED system to separate the output burst pulses from the input pulse. These output burst pulses coincide beams emitted at divergence angle α from a set of virtual sources at turning points with cardinal rays that reach one of the mirrors at normal incidence. In each pulse, only the cardinal rays return exactly along their initial light-path, and thus a spatial shear and a temporal delay occur within a single pulse reflected from the FACED. In a single-shot measurement by SF-STAMP, since this temporal delay in a pulse leads to a slight increase in exposure time, we placed a 4-mm slit at 180 mm from the grating to ease these effects at SF-STAMP. **Figure 2.41(b)** shows the spectrum of the input light source (black line) and the output spectrally sweeping burst pulses (blue line).

The light source was a mode-locked Ti:sapphire laser (805 nm, FWHM of 20 nm) with a chirped pulse amplification (CPA). The average pulse energy was 1 mJ with a pulse width of 50 fs (FWHM) at a repetition rate of 1 kHz. Six pulses with 300-ps time intervals were generated with center wavelengths from 785 to 810 nm, and the overall stretched pulse width was expanded to 1.5 ns.

Multi-spectral imaging by combination of SF-STAMP and burst probes

We performed multi-spectral imaging by SF-STAMP using the spectrally sweeping pulses as probe sources. **Figure 2.42(a)** shows its experimental setup. An amplified femtosecond laser pulse entered the $4f$ -FACED

2. Fundamentals of ultrafast laser, and development and improvements of SF-STAMP

system and formed a spectrally sweeping delayed pulse train. These pulses were enlarged by microscope optics using a 20x objective lens ($NA = 0.40$, Olympus LMPLFLN20x) and relayed to the SF-STAMP imaging system composed of a 25-beam generating DOE (HOLOEYE, customized model, which generates 5×5 beams with a full diffraction angle of 25.6°) and a BPF (IRIDIAN, ZX000167, center wavelength of 830 nm and a bandwidth (FWHM) of 2.2 nm). **Figure 2.42(b)** shows the captured multispectral images on the electrically cooled CCD image sensor (BITRAN, BU-55LN, with 4872×3248 pixels, each pixel size is $7.4 \mu\text{m} \times 7.4 \mu\text{m}$). The burst pulses were duplicated to 25 beams, each of which formed images with different wavelengths defined by the BPF. Since the bandwidth of the probe was ~ 20 nm, not all the beams had sufficient spectral intensity to form a clear spectral image in the 25-frame SF-STAMP system. In these multispectral images, some images with a dark slit (for example, a center image indicated by a white dot circle) are observed. These unusable images contain the spectrally adjacent probes with 300-ps temporal separation. Therefore, we chose only six images (indicated by circles with the number) to capture the burst images for the following experimental results.

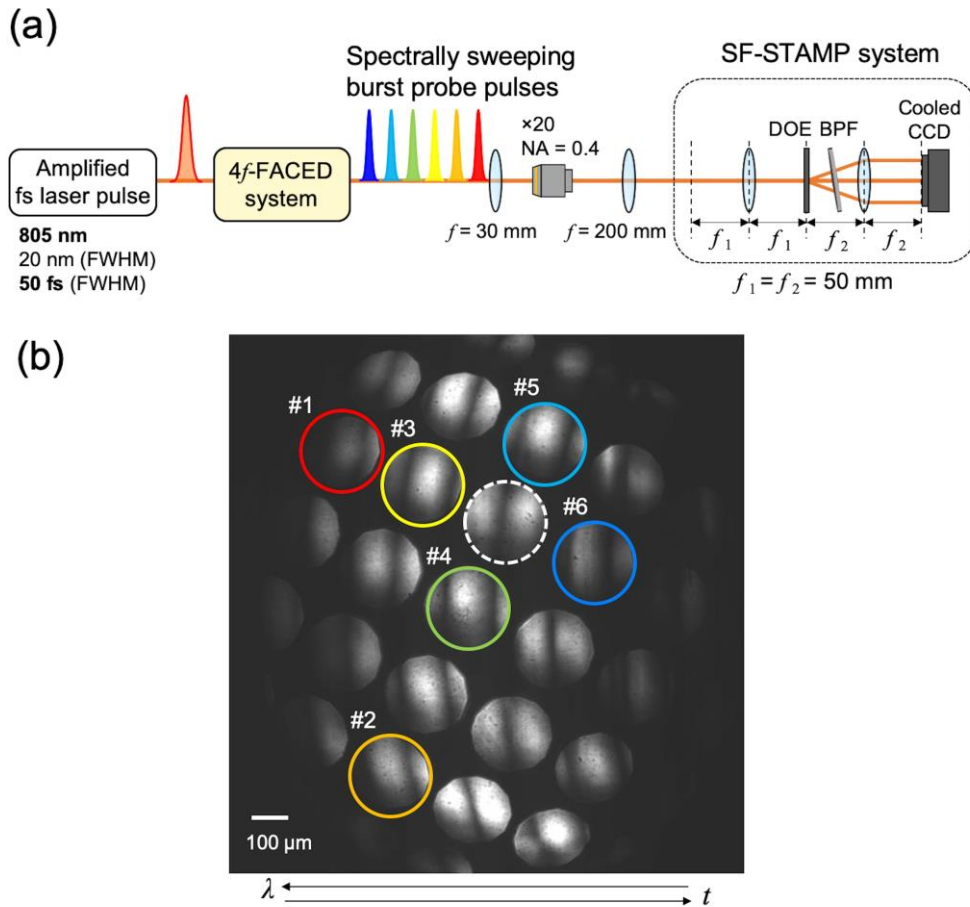


Figure 2.42 (a) Experimental setup of the combination of a SF-STAMP and spectrally sweeping burst pulses, (b) Multispectral image captured by the 25-frame SF-STAMP using spectrally sweeping burst pulses.

Single-shot observation by SF-STAMP with spectrally sweeping delayed pulse train

Next, single-shot observation by SF-STAMP with six spectrally sweeping delayed pulse train was conducted. The entire experimental setup is shown in **Figure 2.43**. The amplified fs-laser pulse was split to a 400-nm pump pulse, which ablated the surface of thin glass film, and an 800-nm probe pulse. The pump pulse was converted to its second harmonic (400 nm) with a β -barium borate (BBO) nonlinear crystal so that we avoid crosstalk between the spectra of the scattered pump and probe pulses. For a single-shot measurement, before splitting pump and probe pulses, we used an optical chopper and a shutter, and pick up one pulse. A 400-nm pump laser pulse with a pulse energy of $\sim 30 \mu\text{J}$ was focused at the surface of a thin glass (50- μm thick, Nippon Electric Glass, Green Glass (OA-10G)) using a spherical lens ($\text{NA} = 0.6$) with a focal length of 8 mm. The focused spot diameter was 1.3 μm . The 800-nm fundamental wavelength pulse transmitted through the BBO crystal was delivered to the 4f-FACED system, and six spectrally sweeping burst pulses were generated and used as sub-nanosecond probes. Ultrafast snapshots of the laser ablation were enlarged and relayed to the SF-STAMP imaging system to capture the six burst snapshots in a single laser shot basis.

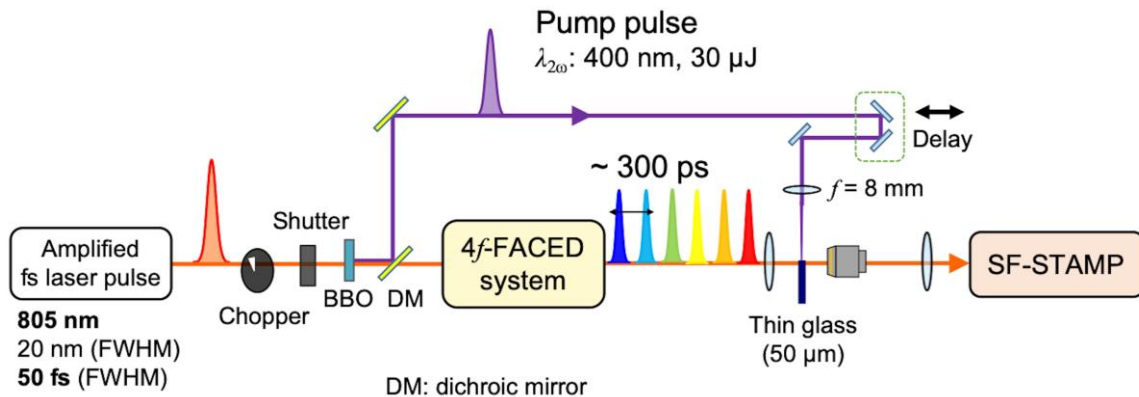


Figure 2.43 Experimental setup of single-shot ultrafast burst imaging with a sub-ns

Figure 2.44 shows the results of the ultrafast imaging of laser ablation on the glass surface. The single-shot entire time window was 1.5 ns, and the average frame interval was 300 ps (corresponding to frame rates of 3.3 Gfps). The average exposure time for each frame was 22 ps. Each wavelength image occupied 220×150 pixels of the CCD sensor. All the images were trimmed, where the pixel intensity of the image was divided by that of the image obtained before the ablation laser irradiation, and the relative intensity among the six images was artificially adjusted to compensate for the intensity variation among the probe spectra. A shock wave and ablation plume clearly grew from the glass surface after the pump pulse

was irradiated and expanded with time, and the expansion of the ablation plume appeared in the third frame. The shock wave started to slightly shrink at the fifth frame.

Figure 2.45 shows the different time-interval results of the ultrafast imaging of laser ablation on the glass surface. In this case, the single-shot entire time window was 400 ps, and the average frame interval was 100 ps ($S = 15$ mm).

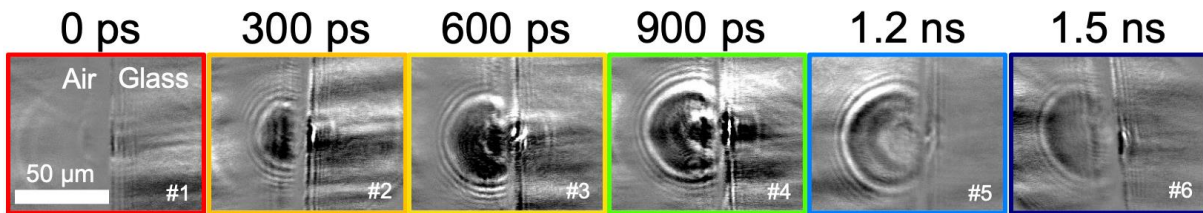


Figure 2.44 Measured single-shot image of shock wave evolution on glass by SF-STAMP with 300-ps interval spectrally sweeping FACED pulses. Scale bar represents 50 μm .

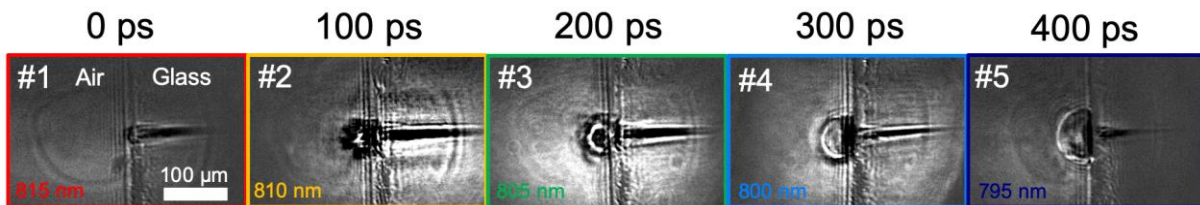


Figure 2.45 Measured single-shot image of growth process of laser induced ablation plume on glass by SF-STAMP with 100-ps interval spectrally sweeping FACED pulses. Scale bar represents 100 μm .

Summary of this section

We demonstrated and extended the time window of the single-shot ultrafast imaging method of SF-STAMP to the nanosecond regime by applying spectrally sweeping burst laser pulses generated from a $4f$ -FACED system. Using spectrally sweeping burst laser pulses with a 25-nm entire bandwidth as the probe laser pulses, we successfully captured 6-burst images of the femtosecond laser ablation process on the glass surface with a 300-ps frame interval in a 1.5-ns time window, and 5-burst images with a 100-ps frame interval in a 400 ps time window.

We limited the maximum number of frames to six by the 25-frame SF-STAMP with FACED burst probes. FACED can extend the time window beyond 5 ns by an incident laser pulse with a 25-nm bandwidth, and the differences in the center wavelength of the adjacent pulses generated by the $4f$ -FACED system were

constant. Meanwhile, the differences in the transmission wavelength of each frame obtained by the DOE and BPF were not exactly linear. In practice, the transmission wavelength within a single image selected by the BPF is distributed along with the horizontal (wavelength) axis. Therefore, it is not straightforward to simultaneously increase both the number of frames (>10 frames) and the time window (> ns) by the SF-STAMP combination approach. Thus, by combining a method of integral field spectroscopy (IFS) that can effectively and efficiently use all the wavelength components, the number of frames and the measurement time window can be increased further with the STAMP scheme.

2.4 Multispectral imaging

As mentioned above, combining a snapshot multispectral imaging system and the frequency-to-time encoding realizes STAMP operation, the SF-STAMP realized this requirement by angle-depended spectral filtering, and it is advantageous that the selected spectrum band can be easily varied by adjusting the incident angles to the BPF. However, the light utilization efficiency of a probe pulse is lower in the SF-STAMP method than that in the original STAMP due to beam duplication and spectral filtering. Thus, to develop a snapshot multispectral imaging system with high-efficiency of the light utilization will pave a way for more diverse STAMP application, such as the combination of polarization microscope with STAMP and THz wave region STAMP. Previous reported snapshot multispectral imaging methods are briefly reviewed in these references [232,233]

Chapter 3

Single-shot measurement of a THz-driven irreversible phase transition

Chapter 3 addresses a single-shot measurement of THz-driven irreversible phase transition in multilayer MoTe₂ by observing transient reflectivity change of a chirped probe by SF-STAMP together with 1D-optical streak imaging (1D-OSI) spectroscopy. We observed the disappearance of the initial phase and discovered a metastable phase during the irreversible phase transition around 30-40 ps after a THz pulse excitation. Insights of THz-induced phase transition dynamics are summarized.

Abstract:

Recent discoveries of a Terahertz (THz)-driven irreversible topological phase transition in two-dimensional (2D)-MoTe₂ demonstrate possibilities of stabilizing a novel transient or metastable quantum phase in equilibrium [234]. However, the irreversible nature of the phase transition precludes conventional repetitive ultrafast spectroscopy in which both excitation and probe pulses perturb and interrogate the sample many times. Here, by stamping the irreversible transient reflectivity change to a frequency-chirped probe laser pulse, we performed both single-shot *in-situ* 2D-burst imaging of sequentially timed all-optical mapping photography utilizing spectral filtering (SF-STAMP) and one-dimensional (1D)-optical streak imaging (OSI) spectroscopy to obtain a few to hundreds of picoseconds dynamics of the irreversible phase transition in MoTe₂. We observed that interlayer phonon oscillations cease at a reflection plateau around 30-40 ps after a single THz pulse excitation, which demonstrates the existence of a metastable phase during the irreversible phase transition and may relate to the theoretically-predicted [235] distorted trigonal prismatic phase (2H*). Further electronic readout of optical reflectivity reveals a non-ultrafast discharging process and explains the long-term THz-induced sample damage in multilayer MoTe₂. This result highlights the complex multi-phase landscapes of quantum materials that can be accessed with THz excitation and provides mechanistic insights for better THz-based polymorph engineering in layered materials.

3.1 Background

The discovery of two-dimensional transition metal dichalcogenides (2D-TMDs) [236,237]—which are semiconductors of the type MX_2 , where M is a transition metal atom (such as Mo or W) and X is a chalcogen atom (such as S, Se or Te) with complex multi-phase landscapes—has expanded our understanding of the stable and metastable states that can exist, opening myriad new possibilities for applications that exploit and switch properties of the novel states [238]. The semiconducting hexagonal (2H) and distorted octahedral metallic phase (1T') in MoTe_2 have attracted considerable attention since their energy difference is rather moderate and the 1T' MoTe_2 is theoretically predicted to be a topological insulator [239]. An irreversible phase transition induced by visible laser irradiation [240] was reported in multilayer 2H MoTe_2 , but follow-up measurements and calculations indicate that the new phase was a compositionally altered Te-metalloid-like phase rather than the 1T' phase [241–243]. A 2H-1T' phase transition in monolayer MoTe_2 has been induced by ionic liquid gating [244], but the 1T' phase is reversed back once the gate is off.

Recent progress in high-field intensity terahertz (THz) pulse generation on the tabletop basis [245–248] has demonstrated the ability to drive quantum materials into novel states that do not exist as equilibrium phases [29,30,249–254]. Furthermore, Shi, Bie³, *et al.* reported a surprising phenomenon [234] that an irreversible 2H-1T phase transition in monolayer and bilayer MoTe_2 can be driven by high-field intensity THz pulses of $\sim\text{MV}/\text{cm}$, which relies on an optical rectification process [247] from an optical pulse and field enhancement structures (FES) of the THz metamaterial [249,255,256]. Although the irreversible nature of the phase transition precludes conventional repetitive pump-probe spectroscopy, they performed a single-shot time-resolved second harmonic generation (SHG) measurement following THz excitation to obtain mechanistic insights into the phase transition and its dynamics. However, their single-shot measurements were conducted by replenishing samples in each shot and have only a small number of data points due to the limitation of the sample availability. Several questions have remained unclear; for example, whether the observed anomalous transient SHG behavior corresponds to any unexplored metastable phases such as distorted trigonal prismatic phase of 2H* [235,257]

Obtaining a more comprehensive time-resolved observation of the far-from-equilibrium dynamics with a single-shot methodology could address unresolved questions. Since the phase transition only happens within a 2- μm FES-THz metamaterial gap at a micron-scale sample, a requirement of microscopic probe rules out single-shot methodologies of space-to-time encoding [39] and angle-to-time encoding [258]. While those two single-shot methodologies with encoding the time information into the spatial domain

³ These authors contributed equally to the work.

3. Single-shot measurement of a THz-driven irreversible phase transition

typically cannot probe dynamics with an observation window up to hundreds of picoseconds due to limited sample sizes, the reported SHG dynamics and picosecond-nature of the THz pulse indicate a slower dynamics than with most optical-excitation experiments [259,260]. Thus, we adopted single-shot methods with frequency-to-time encoding of both one and two-dimensional (1D-, 2D-) imaging with a frequency-chirped laser pulse, which leverages a microscopic resolution probe with a tunable pico-to-sub-nanosecond observation time window to obtain the comprehensive one-shot data. Non-reversible transient reflectivity change is stamped to wavelength components of the probe pulse as time information.

Here, a 2D-burst imaging technique of sequentially timed all-optical mapping photography (STAMP) [58] utilizing spectral filtering: SF-STAMP [60,61] revealed ultrafast structural change with both ps-time resolution and μm -spatial resolution. These features are powerful and vital for dynamical investigations because of a large inhomogeneity in FES of the sample. 1D-spectroscopy of optical streak imaging (OSI) observed the distinct reflection plateau during the 2H-1T's pathway after the THz pulse irradiation. Furthermore, a fast oscilloscope readout method captured damage process at slower timescale.

3.2 Methods

SF-STAMP: single-shot two-dimensional burst imaging with a chirped laser pulse

In this experiment, to realize single-shot measurement with frequency-to-time encoding, we used SF-STAMP [60,61], a modified version of STAMP [58] utilized with spectral filtering. In STAMP, transient phenomena are stamped on each wavelength component of a linearly frequency-chirped laser pulse and then spatially mapped onto an image sensor simultaneously. The spatially separated 2D-multispectral photographs are equivalent to the temporal snapshot at each of the short observation time window. The SF-STAMP $4f$ -imaging system composed of a 25-beam generating diffractive optical element: DOE (HOLOEYE, customized model, which generates 5×5 beams with a full diffraction angle of 25.6° at 800 nm) and a band-pass filter: BPF (Semrock, LL01-808, a center wavelength of 808 nm and a bandwidth (FWHM) of 3.1 nm). The chirped probe beam is divided into array beams by the DOE. The tilted BPF spectrally resolves the diffracted array beams depending on their angle of incidence. Then, the spectrally filtered beams are optically inverse Fourier transformed by the second lens, and the 2D-multispectral images are focused on the image plane. As an image sensor, we employed the scientific sCMOS camera (Andor, Zyla 5.5) with 2560×2160 pixels (each pixel size is $6.5\ \mu\text{m}\times 6.5\ \mu\text{m}$). The image plane size is $16.6\ \text{mm}\times 14.0\ \text{mm}$. Quantum efficiency was $>30\%$ at 800 nm. To visualize the reflectivity change, we normalized the spectral intensity of single-shot data with that of the only probe information measured

3. Single-shot measurement of a THz-driven irreversible phase transition

before the THz pump pulse excitation. This visualization procedure was also done in 1D-OSI. **Figure 3.1** shows the experimental setup of 2D-burst imaging by SF-STAMP.

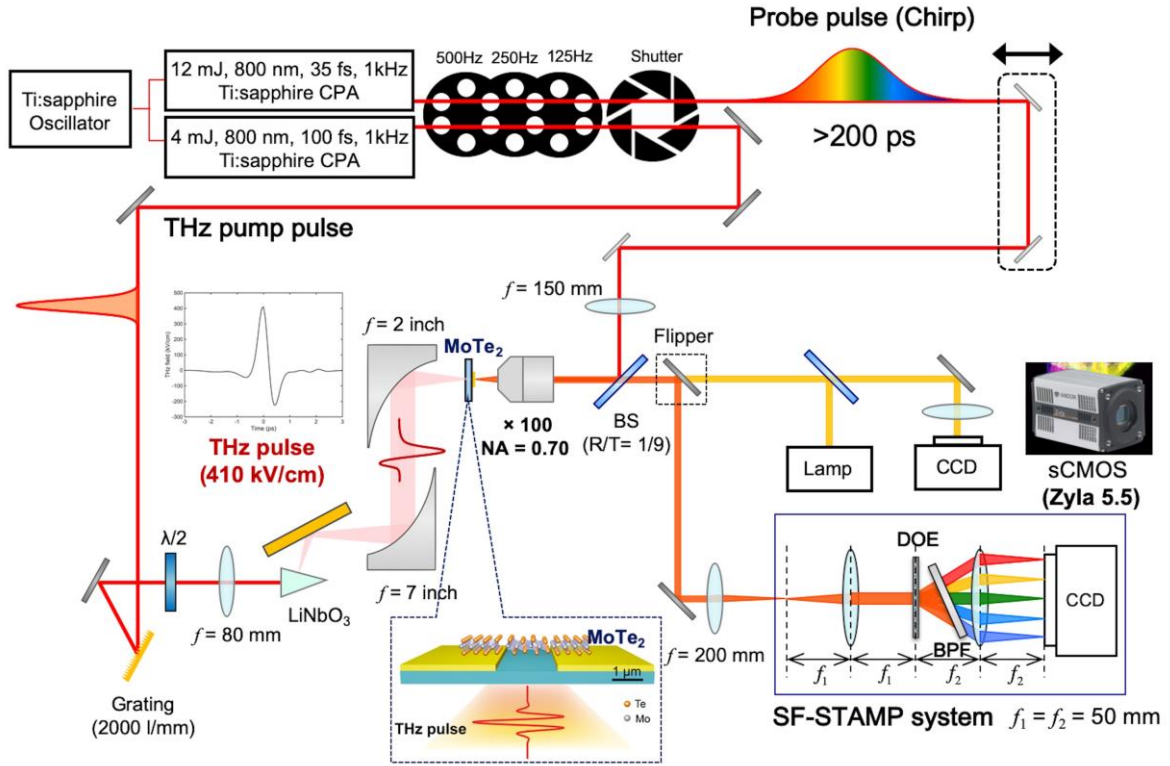


Figure 3.1 Experimental setup of 2D-burst imaging by SF-STAMP.

The outputs from two synchronized chirped pulse amplifiers (CPAs) were down-counted from 1 kHz repetition rate to 125 Hz by using three consecutive choppers. Adjacent pulse intervals of 8 ms allowed enough temporal separation for the shutter to isolate single pulses. The pulse front of one CPA output (100 fs, 4 mJ) was tilted by a grating to achieve phase matching between fundamental 800 nm pulses and generated THz pulses in a Mg: LiNbO₃ crystal [247]. The single-shot probe pulse was from another CPA (35 fs, 12 mJ). Fine control of the pump-probe arrival time was realized by adjusting the probe beam via a translational stage. The 12-mJ pulse from CPA was attenuated to below the damage threshold and used to illuminate the sample with an objective lens ($\times 100$, $NA = 0.70$, Nikon, LU Plan EPI SLWD, MUE30901). Thus, the minimum spatial resolution of the experiment determined by the diffraction limit was $800 \text{ nm}/2NA = 571 \text{ nm}$ (Abbe's diffraction limit). The reflected probe beam was relayed to the SF-STAMP imaging system and divided into plural array beams by the DOE. The tilted BPF spectrally resolved the diffracted array beams depending on their angle of incidence. Then, the spectrally filtered beams were optically inverse Fourier transformed by a lens, and the 2D-multispectral images were focused on a camera. $\lambda/2$: Half-wave plate, BS: beam splitter, DOE: diffractive optical element, BPF: band-pass filter.

1D-OSI: one-dimensional consecutive optical streak imaging spectroscopy with a chirped laser pulse

Based on the chirped pulse electro-optic (EO) sampling method [261,262], we applied frequency-to-time encoding to 1D-spectroscopy of OSI. **Figure 3.2** illustrates a schematic of 1D-OSI. 1D-OSI has consecutive and much higher sampling rates compared with the SF-STAMP method. A cylindrical lens was used to expand the focus point of the chirped probe pulse on the MoTe₂ sample to the line shape, which can suppress detector readout noise and improve the signal-to-noise ratio by averaging the spatial axis information. The reflected probe pulse was spectrally dispersed, and Fourier transformed by a grating (Spectrogon, 1800 line/mm) and a lens. A 1D-streak image with consecutive frequency components is formed on the sCMOS camera (Andor, Zyla 5.5). The vertical axis represents spatial information of the sample, and the wavelength information is encoded to the horizontal axis. **Figure 3.3** shows the experimental setup of 1D-consecutive optical streak imaging (OSI).

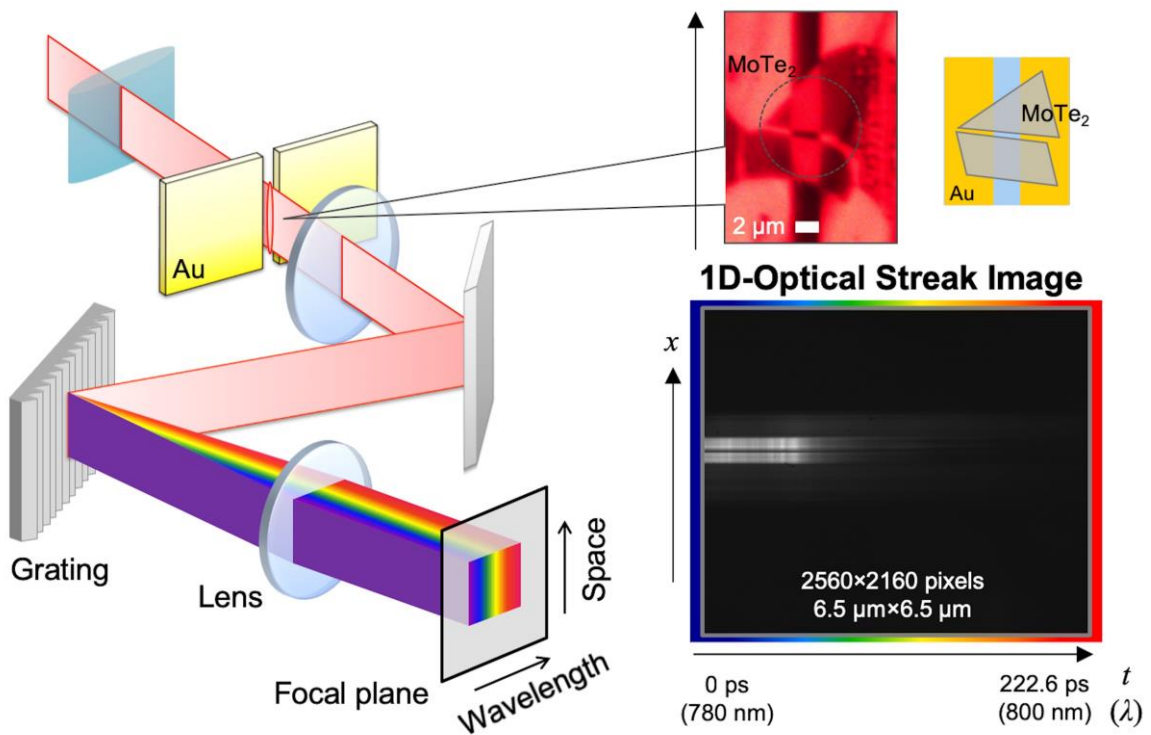


Figure 3.2 Schematic setup of 1D-consecutive optical streak imaging (OSI).

3. Single-shot measurement of a THz-driven irreversible phase transition

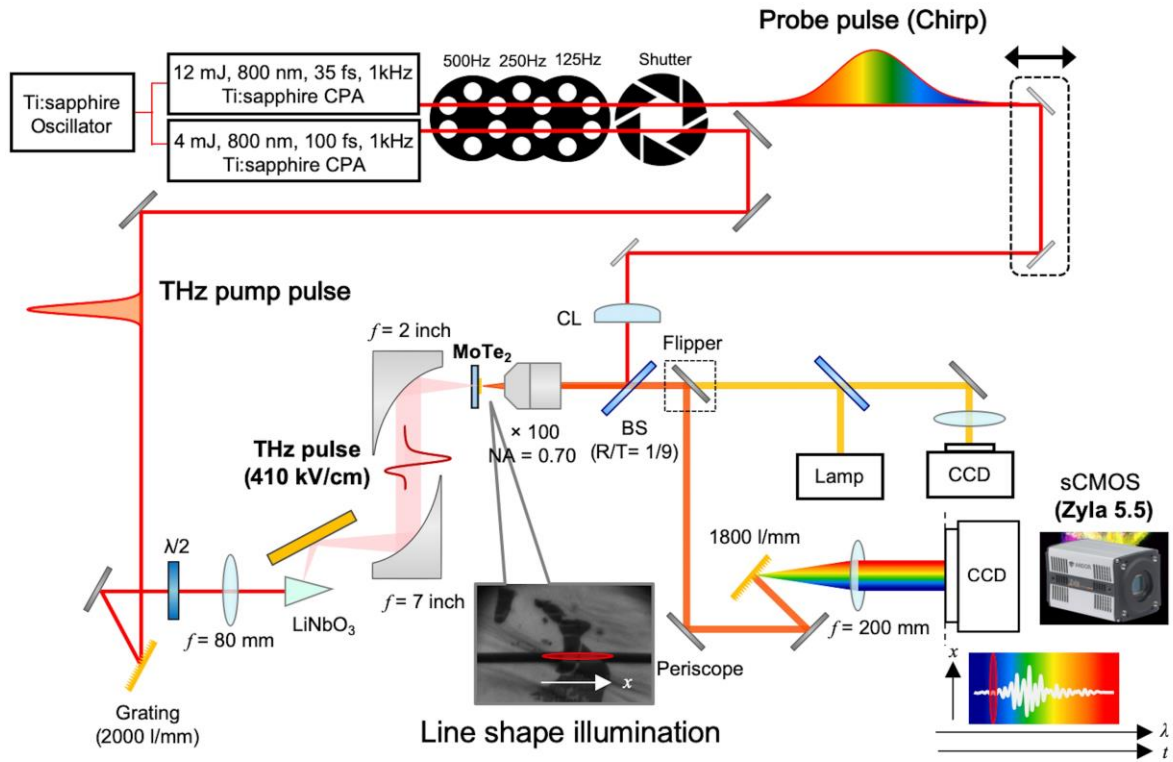


Figure 3.3 Experimental setup of 1D-consecutive optical streak imaging (OSI).

The THz pump arm of the setup is the same as **Figure 3.1**. For the probe arm, a cylindrical lens was used to expand the probe beam and illuminate a line-shape area of the multilayer MoTe₂ sample in the gap with the probe beam, as shown in the inset optical image. The reflection of horizontal line-shape illumination was converted to vertical by the periscope, then spectrally dispersed by a grating, and the 1D-consecutive optical streak images were focused on a camera. In the streak image (x , λ or t), thus, the vertical axis represents spatial information of the sample, and the wavelength information is encoded to the horizontal axis. $\lambda/2$: Half-wave plate; BS: beam splitter; CL: cylindrical lens.

Oscilloscope readout spectroscopy

We encoded the transient reflectivity change into the intensity of a CW laser light at 532 nm (Coherent, Verdi G-series). The reflected laser light is fiber-coupled to 3.5-GHz photoreceiver (New Focus, 1591NF). The electronic signal is collected by a 33-GHz oscilloscope (Tektronix DPO73304D).

High-field THz pulse generation and microscopic single-shot probes

The outputs of two synchronized chirped pulse amplifiers (CPAs; Coherent, Legend Elite Duo) were used for the THz pump arm and the chirped probe pulse arm. Free space high-field THz pulses were generated in

3. Single-shot measurement of a THz-driven irreversible phase transition

Mg:LiNbO₃ crystal by tilting the pulse front to achieve phase matching [247]. By using a two-parabolic-mirror 4f-THz imaging system, the image of the terahertz spot on the sample was focused to around 600 μm in diameter. The incident THz pulse was measured in the time domain EO sampling with a 100- μm thick 110-oriented gallium phosphide (GaP) crystal.

When pumping with 4.5-mJ pulses from a Ti:sapphire CPA (repetition rate of 1 kHz, central wavelength of 800 nm, pulse duration of 100 fs), the maximum electric field of the THz pulses reached 410 kV/cm at the focus with a center frequency of 0.8 THz as shown in **Figure 3.4**. A chirped probe pulse was delivered from another Ti:sapphire CPA (repetition rate of 1 kHz, central wavelength of 800 nm, pulse duration of 40 fs) and its amount of chirp was adjusted by a home-built grating pair stretcher to add negative chirp. The probe pulse (or light) passed through a 100 \times objective lens ($NA = 0.7$) before the sample and was used to image (or relay) the reflected probe beam from the micron-scale MoTe₂ sample to the image sensor (or photodetector). The arrival timing of the counter-propagating THz pump pulse during the chirped probe pulse duration was determined by EO sampling with a 200- μm thick 110-oriented zinc telluride (ZnTe) crystal. All of the measurements were conducted at a single-shot basis at an ambient condition (300 K, 1 atm).

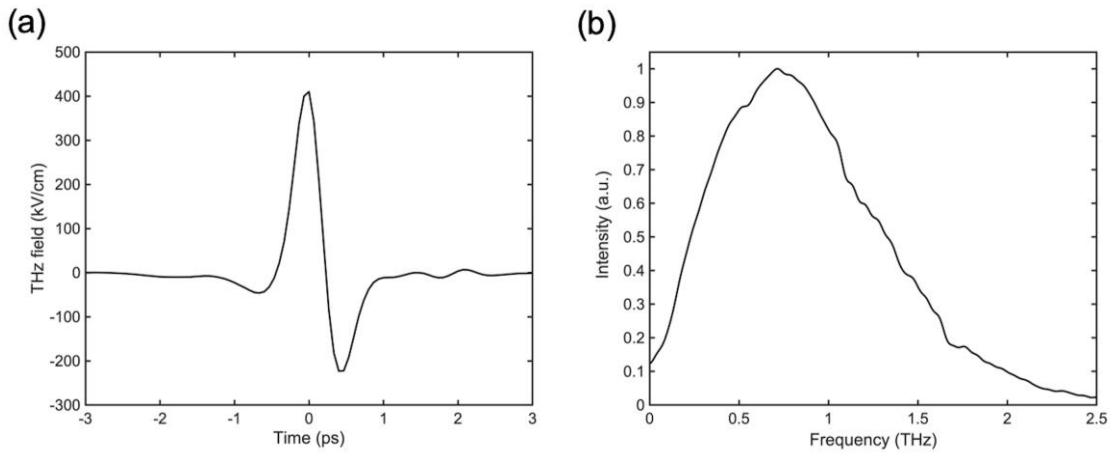


Figure 3.4 THz field and spectrum characteristics. (a) The incident free-space single-cycle THz pulses have a maximum 410 kV/cm electric field. (b) THz spectrum is centered at 0.8 THz.

Temporal and spectral characterization of chirped optical laser pulses

The precise determination of THz arrival time in the chirped probe window is crucial for single-shot measurements with limited number of MoTe₂ samples. Electro-optic (EO) sampling of a co-propagating THz field with a chirped optical pulse has been demonstrated to be a coherent THz detection method with a decent signal level. Here, we used a chirped optical pulse to electro-optically sample a counter-propagating

3. Single-shot measurement of a THz-driven irreversible phase transition

THz field [35]. **Figure 3.5(a)** shows the experimental setup of chirped EO sampling. In this method, the polarization of different wavelength components of the chirped pulse is rotated by a different portion of the THz electric field. The chirped probe spectrum is shown in **Figure 3.5(b)**. As shown in **Figure 3.5(c)**, the modulation of polarization is converted to the amplitude modulation with an optical analyzer (polarizer). For spectral detection, we employed a spectrometer with a spectral resolution of 0.25 nm (Ocean optics, HR4000CG-UV-NIR). The precise determination of THz arrival time in our setup with a counter-propagating geometry is challenging due to the complexity of EO sampling signal, which comes from both front and back sides of the EO crystal. Especially for SF-STAMP measurements with 4-ps window, we used a thin lithium niobate (LNO) slab with a thickness of 30 μm as the EO crystal to minimize possible misinterpretations of EO signal. As shown in **Figure 3.5(c)**, chirped probe scattering from LNO crystal without THz modulation provides moderate background with random polarizations. The THz modulation of probe beam in a thin LNO slab is small compared with the background, so the EO signal is close to linear in field strength. The differential spectrum distribution of the 4-ps chirped probe pulse with and without THz shows a THz-shape EO signal. By calculating the difference of THz and optical path length between MoTe_2 sample and EO crystal, THz arrival time relative to the probe window was determined with an error of around 1 ps.

For measurements with the 200-ps time window, the probe pulse was negatively chirped to around 400 ps from a transform-limited 40-fs pulse, which resulted in a temporal resolution around 4 ps for 1D-OSI. Thus, the THz EO signal is convoluted with a slow instrumental response, which has a smaller signal level compared with the conventional EO method with ultrashort pulse probes and mechanical delays. Here, we sacrificed fine temporal accuracy to have a high THz EO signal by using a thick ZnTe crystal of 200 μm as the EO crystal. As shown in **Figure 3.5(d)**, THz EO signal was obtained within the 400-ps chirped probe window and overwhelmed the noise level of probe laser scattering. Since the temporal resolution of 4 ps is longer than the THz pulse, we were not able to resolve the second lobe of THz pulse, which was resolved in the case of 4-ps chirped probe. The observed second lobe with a smaller amplitude in the THz EO signal is due to a double internal reflection of the THz pulse in the EO crystal. In **Figure 3.5(d)**, three bottom curves (yellow: EO 780 nm; orange: EO 790 nm; and red curves: EO 800 nm) show the THz EO signal measured with a different THz arrival time in a 400-ps negative chirp probe window. By changing the optical path length of the probe beam, the THz EO signal moves across the probe spectra between 780 to 800 nm. In this case, the bandwidth of 20 nm corresponds to the time window of 200 ps for SF-STAMP and 1D-OSI measurements. By adjusting the probe path length, we determined the THz arrival time.

3.3 Observation of THz-induced irreversible phase transition in two-dimensional MoTe₂

3.3.1 Experiment

Figure 3.6 depicts schematics of a single THz pulse excitation on multilayer MoTe₂ and single-shot microscopic probes. Multilayer MoTe₂ samples are exfoliated on the THz-FES, which consists of 100- μm wide parallel gold strips deposited onto fused silica substrates and separated by a 1.8- μm capacitive gap. In our experiment, ~ 0.4 MV/cm free-space THz excitation pulse was used in all of the following three different single-shot measurements and was higher than the phase transition threshold reported in the previous work [234]. The polarization of THz was perpendicular to the gold gap. For the probe branch in SF-STAMP and 1D-OSI measurements, the time-dependent reflectivity change was encoded to a frequency-chirped probe pulse, and the single-shot observation time window was adjusted from several to hundreds of picoseconds by tuning the chirp of the probe pulse. A diffractive optical element (DOE) and a band-pass filter (BPF) were used to spatially separate the frequency-time coupled wavelength components for the SF-STAMP measurement [60,61]. For the 1D-OSI spectroscopy, a grating and a lens were used to Fourier transform the time/frequency variations of the probe pulse intensity into a spatial profile on a CCD sensor [261]. Slow dynamics ranging from nanoseconds to microseconds were captured by encoding time-dependent reflectivity in a continuous-wave (CW) laser and decoding the signal electronically with a fast photodiode detector and oscilloscope.

3. Single-shot measurement of a THz-driven irreversible phase transition

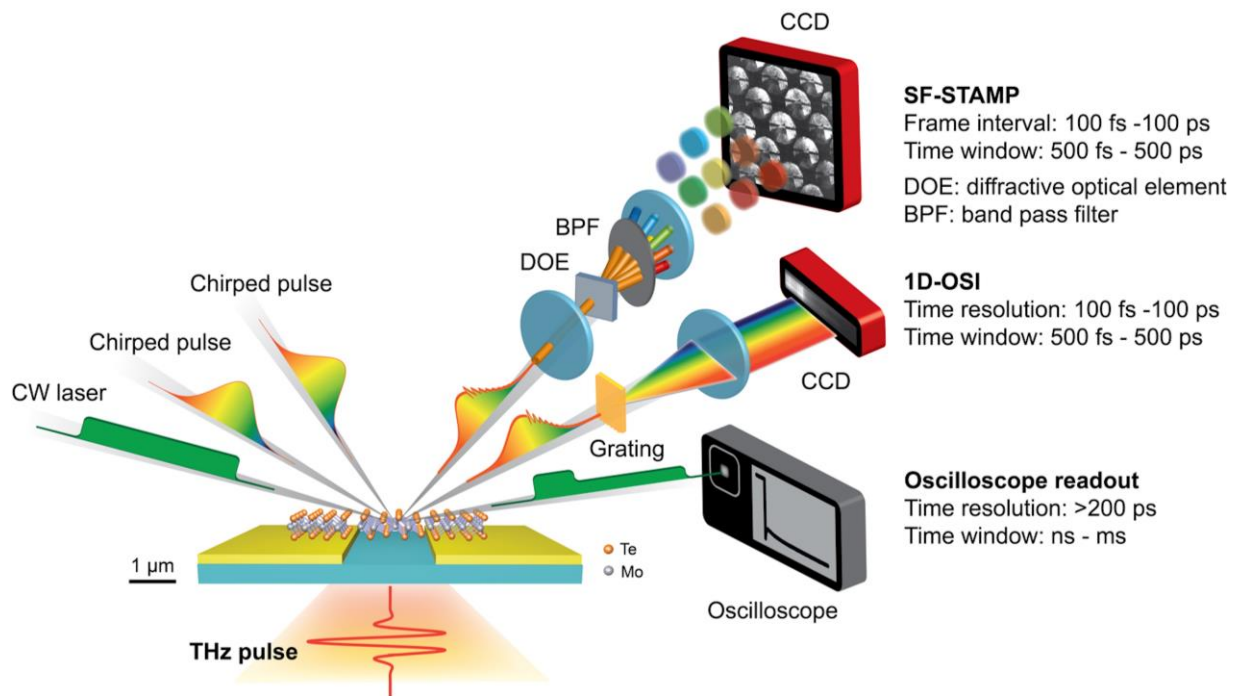


Figure 3.6 Measurements of irreversible THz-driven phase transition dynamics in multilayer MoTe₂ by multiple single-shot spectroscopy. Schematics of multilayer MoTe₂ on THz metamaterial structure with a single THz pulse excitation and single-shot microscopic probes, including 2D-burst imaging of sequentially timed all-optical mapping photography utilizing spectral filtering (SF-STAMP), one-dimensional optical streak imaging (1D-OSI) and oscilloscope readout. By probing the sample with a chirped laser pulse and analyzing the reflected pulse with a spatial mapping device and a charge-coupled device (CCD), SF-STAMP and 1D-OSI can capture the irreversible phase transition with a 500-fs to 500-ps time window and 100-fs to 10-ps temporal resolution. The oscilloscope readout method with a fast photoreceiver can resolve the dynamics up to a millisecond observation time window with a 200-ps temporal resolution by using a CW laser light and detecting the reflected light intensity.

3.3.2 Results

~300-ps observation window

We first conducted single-shot SF-STAMP and 1D-OSI measurements with observation windows of around 300 ps and 200 ps, respectively. **Figure 3.7** shows the single-shot SF-STAMP multispectral temporal snapshots of before a THz pulse irradiation, with a THz pulse, after irradiation. The normalized transient reflectivity change by dividing the before a THz pump irradiation image is shown in **Figure 3.8**. In this SF-STAMP configuration, the circled multispectral temporal snapshots (ranging from 780 nm to 800 nm) with a smaller number (#: 1~9) correspond to the shorter wavelength images, that is, the earlier time snapshot in the SF-STAMP time sequence. The time window of this 20-nm bandwidth negative chirped probe laser pulse was 228 ps (The total amount of dispersion of 11.4 ps/nm). An exposure time and the frame interval of the snapshots were 35.3 ps and 25 ps, respectively. Abbe's diffraction limit was 0.57 μm . The scale bar represents 2 μm .

Figure 3.9 shows the single-shot 1D-OSI results of before a THz pulse irradiation, with a THz pulse, after irradiation. The temporal resolution of 1D-OSI spectroscopy is determined by the following relationship: $\sqrt{\tau_0 \times \tau_{chirp}}$ [52,262]; where τ_0 is the transform-limited duration of the probe pulse and τ_{chirp} is the chirped pulse duration. Both measurements were conducted with a 400-ps negatively chirped pulse stretched from a transform-limited 40-fs pulse, which resulted in a temporal resolution around 4 ps.

3. Single-shot measurement of a THz-driven irreversible phase transition

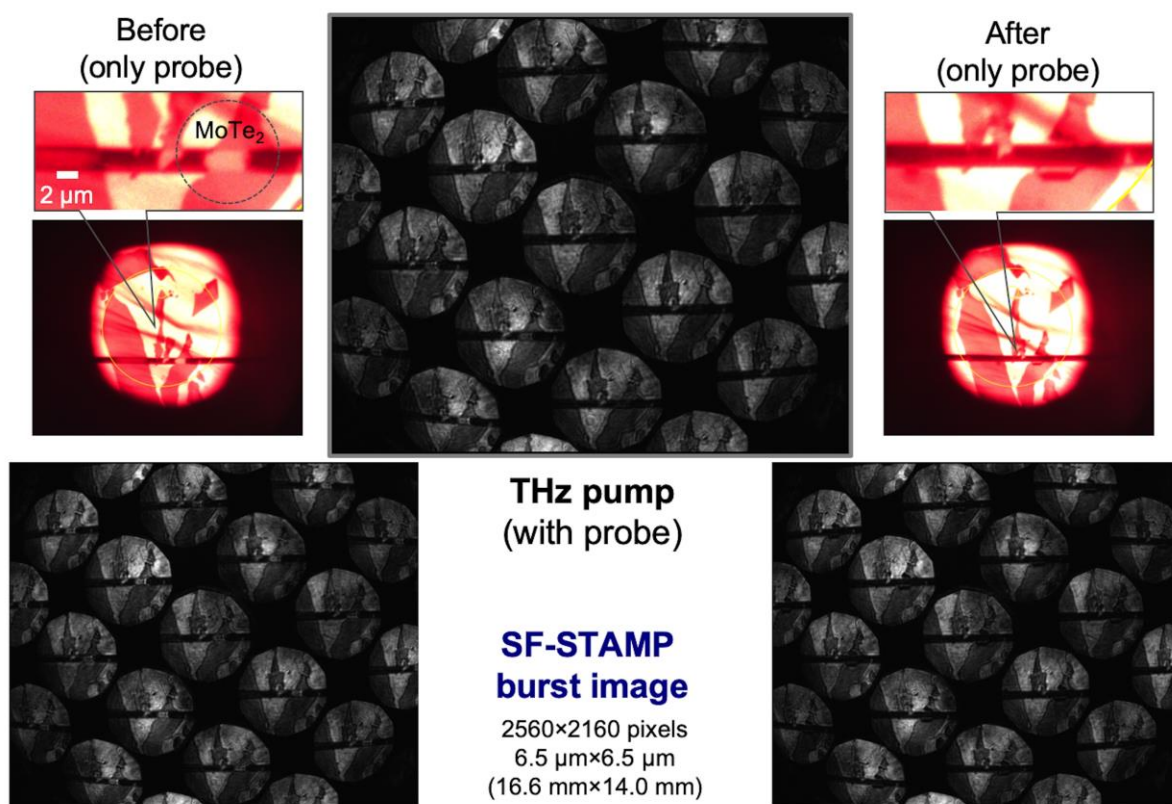


Figure 3.7 Single-shot multispectral temporal snapshots of before a THz pulse irradiation, with a THz pulse, after irradiation measured by SF-STAMP. A THz pulse intensity was 410 kV/cm.

3. Single-shot measurement of a THz-driven irreversible phase transition

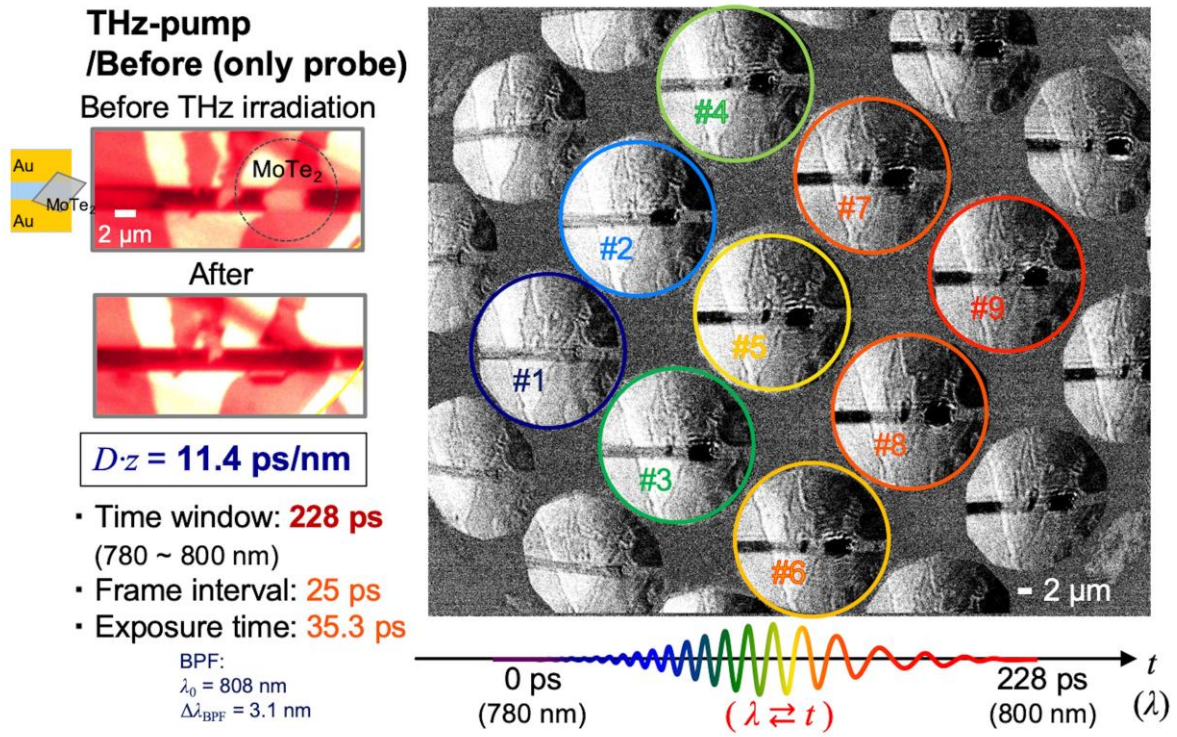


Figure 3.8 Temporal snapshots of transient reflectivity change in MoTe₂ by a THz pulse irradiation. To visualize the dynamics in these snapshots, we normalized the spectral intensity with that measured before the THz-pump excitation. The time window of the negative chirped 20-nm bandwidth (770~730 nm) probe pulse was 228 ps. An exposure time and the frame interval of the snapshots were 35.3 ps and 25 ps, respectively. The scale bar represents 2 μm. The diameter of circles occupied 550 pixels.

3. Single-shot measurement of a THz-driven irreversible phase transition

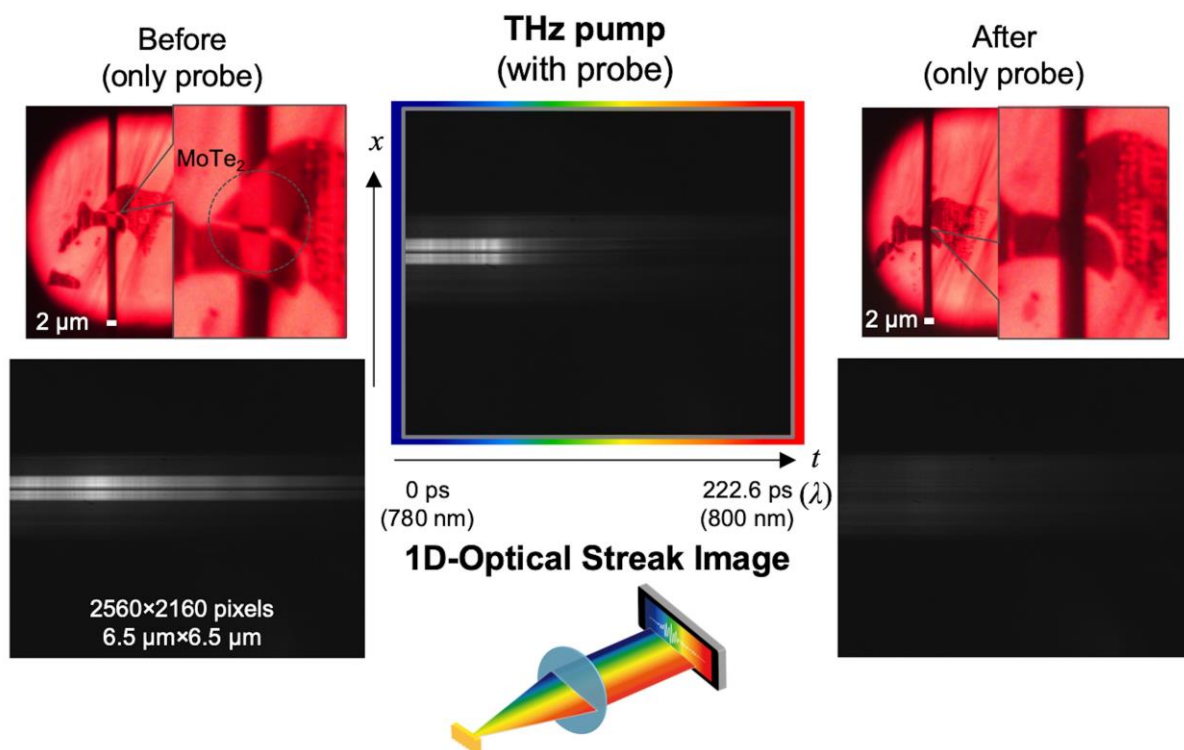


Figure 3.9 Single-shot 1D-optical streak images of before a THz pulse irradiation, with a THz pulse, after irradiation measured by 1D-OSI. A THz pulse intensity was 410 kV/cm. The scale bar represents 2 μm.

3. Single-shot measurement of a THz-driven irreversible phase transition

As shown in the 12-frame snapshot SF-STAMP images (the frame interval of 25 ps) of **Figure 3.10(a)**, the reflectivity of the multilayer MoTe₂ in the gap drops uniformly right after a THz excitation and stabilizes around 100 ps after the THz irradiation. The dynamics are consistent with the 1D-OSI measurements, which has a much higher sampling rate. In **Figure 3.10(b)**, we first observe a THz-shape reflectivity response near the THz arrival time. This response is a coherent interaction with THz electric field. It is convoluted with the 4-ps temporal resolution, which is further confirmed in another 50-ps window 1D-OSI measurement with a higher temporal resolution of around 1 ps, as shown in **Figure 3.11(a)**. Since our probe wavelength region is near 800 nm and close to the B exciton resonance [237,263] of multilayer or few-layer MoTe₂, we ascribe this effect to the THz coherent interactions of exciton states, which has been reported in other types of 2D-TMDs [264].

The reflectivity starts to drop abruptly following the THz-exciton interactions and reaches a reflection plateau around 30-40 ps after THz excitation. This reflection plateau lasts for around 25 ps before the reflectivity drops again to an even lower level and stabilizes there within 200-ps observation window. Compared with the reported single-shot SHG measurement, the reflection plateau emerges at a similar time scale with the emergence of an anomalous SHG behavior, both of which indicate the existence of a metastable phase [235,257] during the irreversible phase transition. After around 1 second, we checked the post-mortem reflectivity with another probe pulse without THz excitation. We noticed that the sample reflectivity recovers slightly, which means there are some non-ultrafast dynamics beyond our 200-ps observation window.

3. Single-shot measurement of a THz-driven irreversible phase transition

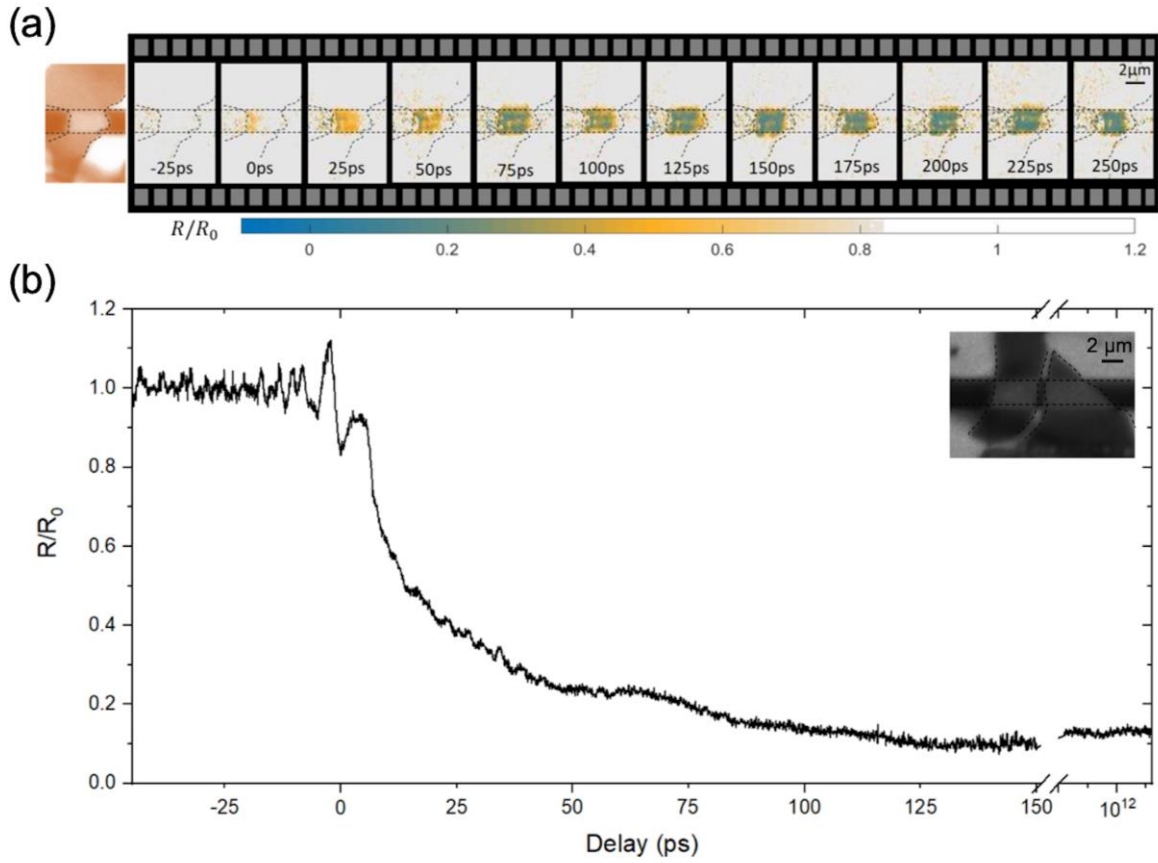


Figure 3.10 A few hundreds of picoseconds dynamics of THz-driven irreversible phase transition in multilayer MoTe₂. (a) Optical image of before THz pumping (left) and SF-STAMP burst images of multilayer MoTe₂ after single THz pulse irradiation at 410 kV/cm (right). The temporal snapshot of STAMP images cover from -25 ps to 250 ps with a frame interval of 25 ps. A distinct reflection drop occurs uniformly at the MoTe₂ within the gap after the THz irradiation and stabilizes around 100 ps after THz excitation. (b) 1D-OSI data of multilayer MoTe₂ after a single THz pulse. The inset shows the optical image of the sample used for 1D-OSI measurement. We first observed a THz-pulse shaped reflectivity change around time-zero, which is followed by a fast reflection drop. At around 30-40 ps after THz excitation, we observed a reflection plateau, which lasts for around 20-25 ps before it drops again and stabilizes at a lower reflectivity level within the 200-ps observation window. After 1 sec., a small reflectivity recovery is observed. In both 2D and 1D case, probe pulses were stretched by negative chirp via grating pair compressor. Thus, in this configuration, the left-hand side of the horizontal axis is the shorter wavelength component. To visualize the reflectivity change, we normalized the spectral intensity of single-shot data with that of the only probe information measured before the THz pump pulse excitation.

3. Single-shot measurement of a THz-driven irreversible phase transition

50-ps observation window

To obtain further details of the reflection plateau region, we performed another 1D-OSI measurement with a smaller time window (~ 50 ps) and higher temporal resolution (~ 1 ps) on a different multilayer MoTe₂ sample, as shown in **Figure 3.11(a)**. Upon the arrival of the THz pulse, we also observed the THz-shape reflectivity change, consistent with the THz-exciton coherent interactions observed in the measurement above. As expected, the THz-shape modulation is much sharper than the above measurement since the temporal resolution in this measurement is higher. In addition to the reflection plateau, we observed two coherent phonon oscillations after THz excitation in **Figure 3.11(b)**. At a delay of around 20-31.5 ps, two oscillations have frequencies at around 0.39 ± 0.04 THz and 1.26 ± 0.04 THz, respectively. These two coherent phonon motions have similar frequencies interlayer breathing and shear modes (**Figure 3.11(c)**) in multilayer MoTe₂ [265]. Most remarkably, both from time-domain (**Figure 3.11(a)**) and frequency-domain data (**Figure 3.11(b)**), we noticed that two interlayer phonon oscillations suddenly cease at the reflection plateau at around 32-ps delay.

Especially from **Figure 3.11(b)**, Fourier transformations are conducted on three consecutive time windows with precisely the same conditions and show an abrupt disappearance of interlayer phonon oscillations at the reflection plateau, which strongly deviates from the exponential phonon decay process. This phenomenon further confirms that MoTe₂ enters a transient metastable phase during the irreversible phase transition. The metastable phase could be the distorted trigonal prismatic phase (2H*) based on the theoretical calculation of MoTe₂ in a highly electronically excited state [235]. We think the disappearance of phonon oscillations is mainly due to the incoherence nature of electronic-excitation-driven phase transition, during which the phonon coherence is no longer maintained. Since our microscopic probe size is around 1.5- μm and close to the gap size, we are essentially probing the sample excited by a THz field with different levels of FES-THz. This spatial inhomogeneity could also contribute to the destruction of phonon coherence.

We also notice that interlayer phonons harden as the probe window moves closer to the THz arrival time. For example, at an earlier delay of around 8.5-20 ps, those oscillation frequencies blue shift to 0.57-0.74 THz and 1.35-1.52 THz. Similar THz-driven interlayer shear oscillation has also been observed in multilayer Td phase WTe₂ [253], during which the interlayer shear phonons also soften at a longer delay but with a much smaller extent.

3. Single-shot measurement of a THz-driven irreversible phase transition

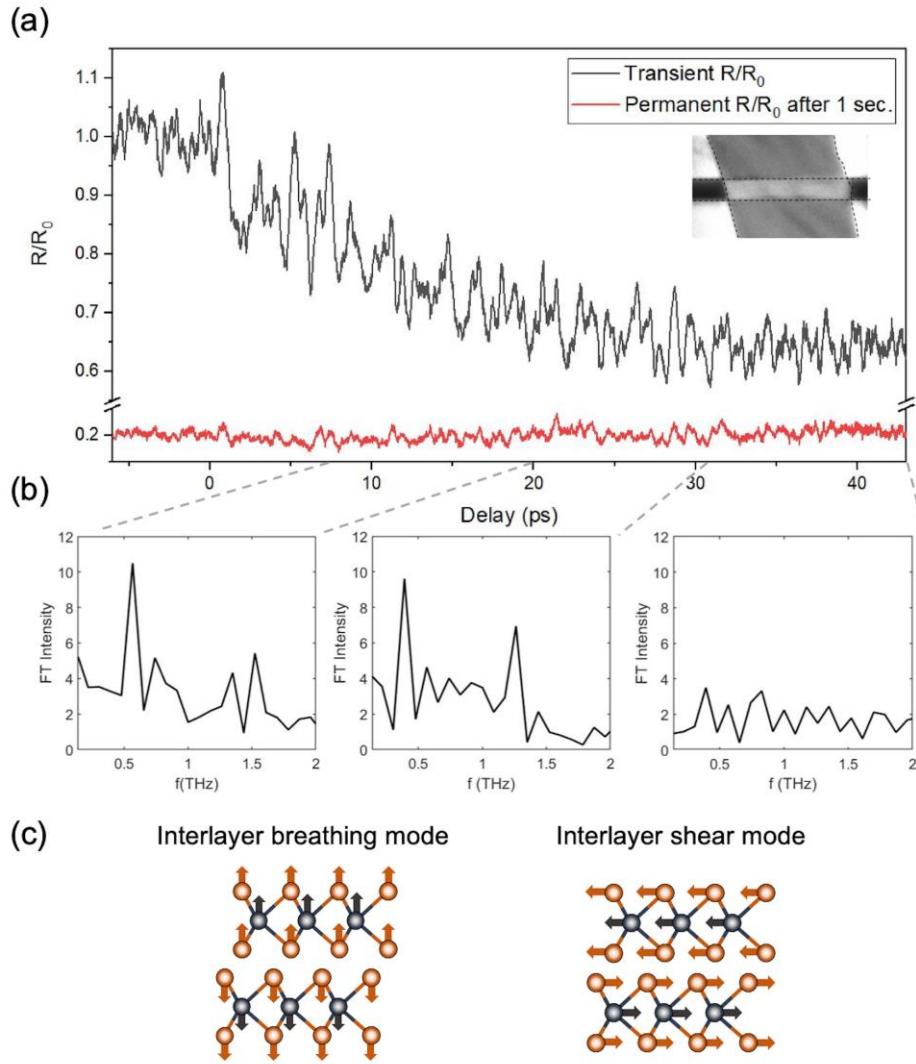


Figure 3.11 Irreversible phase transition dynamics with a 50-ps observation window. (a) The inset shows the optical image of the multilayer MoTe₂ sample for the 50-ps single-shot dynamics measurement. At around zero delay position, a THz-shaped reflectivity change is observed. Due to a shorter duration of chirped probe, the temporal resolution in this measurement is around 1 ps, which enabled us to observe coherent oscillations after the THz excitation. At around 32-ps delay, the reflection plateau is also observed. (b) Fast Fourier transform (FFT) of time-domain data with three consecutive time windows. Three consecutive time windows (8.5-20 ps, 20-31.5 ps, and 31.5-43 ps) have the same size and identical FFT conditions, thus the FFT intensity in three plots can be reliably compared. The FFT of time window from 20-31.5 ps clearly shows two peaks at 0.39 THz and 1.26 THz, which is close to reported interlayer breathing and shear mode of multilayer MoTe₂, respectively. Those two interlayer oscillations harden at earlier delays (8.5-20 ps) and completely disappear at the reflection plateau region (31.5-43 ps). (c) The oscillations correspond to the interlayer breathing mode and interlayer shear mode of multilayer MoTe₂.

Possible driving mechanism for time-dependent interlayer phonon excitations

In materials with symmetric A_1 vibrational modes, ultrafast electronic excitations can suddenly shift the minimum of the potential energy surface of the A_1 mode, giving rise to a coherent vibration of A_1 symmetry about the displaced energy surface minimum. This process is called displacive excitation of coherent phonons (DECP) [111]. We do not think DECP is the driving mechanism since the interlayer shear and breathing modes [265] are not the symmetric A_1 of the multilayer 2H phase MoTe_2 . In addition, coherent phonon oscillations excited via DECP are typically slower than the driving field, while the observed interlayer shear oscillation have a frequency over 1 THz, almost beyond the bandwidth of our THz pulse. The interlayer breathing and shear modes are Raman-active and silent modes in multilayer 2H MoTe_2 , respectively [265]; thus this behavior cannot be explained by resonant field-dipole interactions of IR-active modes. It is theoretically possible that the Raman-active interlayer breathing mode can be driven by impulsive stimulated Raman scattering (ISRS) process.

Since the THz electric field realized so far is much weaker than the optical electric field, ISRS process driven by a THz electric field is much less efficient than an optical excitation. Several optical-pump repetitive experiments have been conducted in multilayer 2H MoTe_2 and no interlayer shear or breathing oscillations were detected [259,266], which indicates that ISRS may not be the driving mechanism for this unusual THz-driven phonon excitations. ISRS process also cannot explain the excitation of silent interlayer shear mode with a frequency almost beyond our THz spectrum.

Recently, a transient charge-current driving mechanism was proposed to explain the observation of interlayer shear oscillations in orthorhombic (Td) phase bulk WTe_2 and MoTe_2 by THz, Mid-infrared (MIR) or optical excitations [253,260]. In this theory, laser irradiation induces electronic transitions between bonding and antibonding states, thus depleting the bond charges, destabilizes the interlayer coupling strength and launches the shear motions. Although Td phase WTe_2 or MoTe_2 are semimetals while 2H phase MoTe_2 is a semiconductor with a 1 eV bandgap, picosecond-nature of THz electric field, especially with a further field enhancement, is much more suitable to induce carrier liberation, multiplication and subsequent transient current in the sample compared with an optical excitation. Thus, we think the highly electronic excitations and subsequent transient currents in multilayer 2H MoTe_2 could weaken the interlayer bonding strength and give rise to interlayer phonon excitations.

As shown in **Figure 3.11(b)**, THz-driven interlayer phonon oscillations were noticed to be time-dependent and softened at a later time after the irradiation of THz pump pulse. A slight phonon softening at a later pump-probe delay was also noticed in the MIR-driven shear oscillations [253] in bulk Td WTe_2 . The observed anharmonicity is opposite to the phonon hardening at a later pump-probe delay

3. Single-shot measurement of a THz-driven irreversible phase transition

observed in Bismuth [267], which may be related to a different lattice potential/electronic anharmonicity and requires further investigations.

Slow (>ns) and ultrafast (<5 ps) dynamics

SF-STAMP and 1D-OSI measurements clearly discover that a transient metastable phase exists during the THz-driven irreversible phase transition in multilayer MoTe₂. In order to gain further mechanistic understandings of the whole phase transition dynamics and reveal the origin of puzzling THz-induced sample degradation observed in the multilayer MoTe₂, we performed another single-shot measurement of slow dynamics with a fast oscilloscope readout method and of ultrafast dynamics with SF-STAMP in a 4-ps window. Employing a fast oscilloscope and photodetector, we were able to capture the reflectivity dynamics up to milliseconds with a temporal resolution around 250 ps (**Figure 3.12(a)**). As expected, the sample reflectivity shows a step-function-like response with a falling time around 300 ps, which is consistent with the 100-ps dynamics observed in the above 1D-OSI measurements. It means that the oscilloscope readout method could not resolve ultrafast phase transition dynamics. With a longer 90- μ s observation window of oscilloscope, we resolved the slow dynamics of reflectivity recovery. As shown in **Figure 3.12(b)**, an exponential recovery is first observed with a time constant around 1 μ s. This timescale is much faster than the carrier recombination time [266] and at a similar level of an RC circuit's time constant, thus we think the recovery dynamics is due to the charge circulating process from MoTe₂ (resistance) to THz metamaterial (capacitor). Although THz-driven Poole-Frenkel (PF) and impact ionization (IMI) effect does not produce a net charge in MoTe₂, a portion of THz-excited carriers can localize at the interface between MoTe₂ and fused silica substrate or gold surface. The reflectivity starts to drop again with a time constant around 10 μ s before the completion of the charge circulating process. We think the slow reflectivity dynamics corresponds to a slow sample degradation due to the current flow and contributes to the emergence of compositionally altered Te-metalloid-like phase, which inhibits the emergence of desired distorted octahedral phase (1T') in multilayer MoTe₂.

The PF and IMI driving mechanism are further confirmed in the SF-STAMP measurement with an ultrafast 4-ps window. We captured 12-frame images with a \sim 300-fs frame interval and \sim 500-fs temporal resolution as shown in **Figure 3.12(c)**. No noticeable reflectivity drop is observed within the 4-ps observation window (\sim 2 ps after the THz arrival) for the sample in the middle of the gap, while the reflectivity drops appreciably at the edge of the MoTe₂ on the gap, including the sample near the gap and the sample edge. This is because the THz local enhancement is much higher at the edge compared to the middle of the gap [255], which could also apply to the edge of a small-band-gap conductive semiconductor. The emergence of reflectivity drop at the sample edge excludes the THz-driven field emission from the

3. Single-shot measurement of a THz-driven irreversible phase transition

gold as the dominant driving force for the phase transition and confirms the PF and IMI driving mechanism.

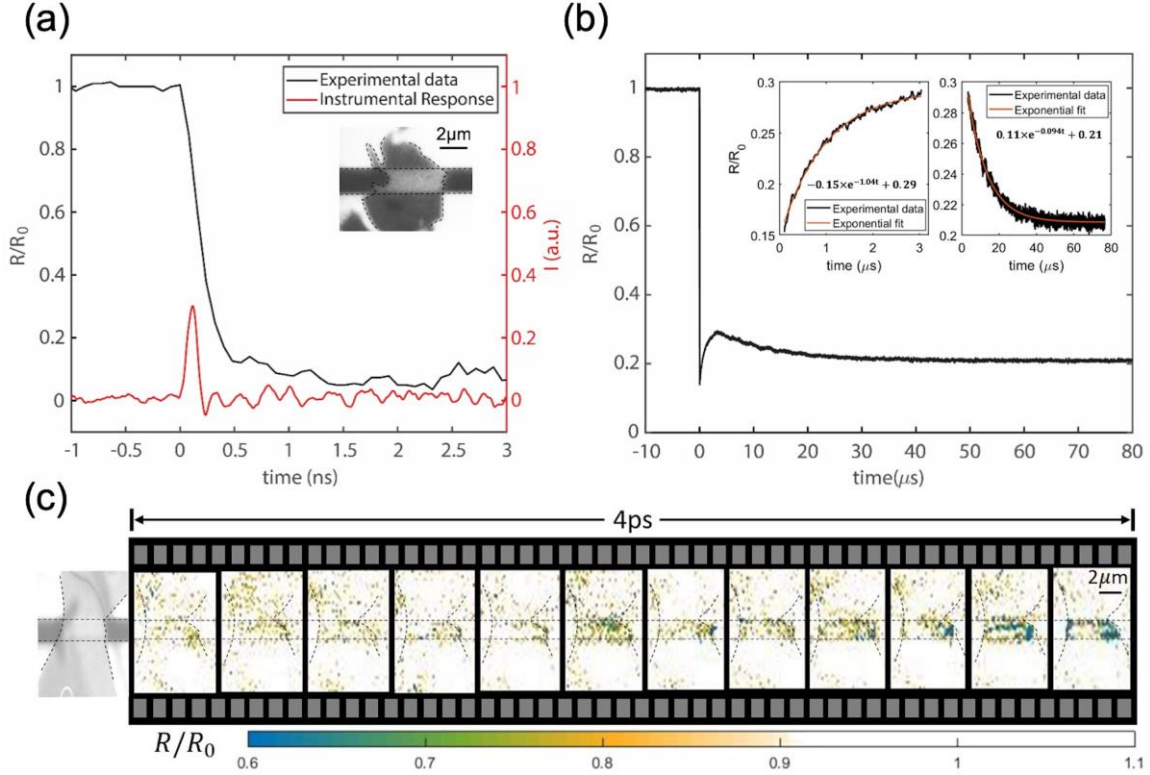


Figure 3.12 Slow ($>ns$) and ultrafast (<5 ps) dynamics of the THz-driven irreversible phase transition. (a) The inset shows the optical image of the MoTe₂ sample. The black curve shows the reflectivity change dynamics with a 4-ns observation window. The red curve shows the instrumental response measured with a 35-fs ultrashort pulse. The reflectivity drop is slightly slower than the instrumental response, which means the actual reflection dynamics is in a similar level of the instrumental response at 200 ps. (b) The reflectivity change shows a step-function-like response at time zero with a 90-μs observation window, followed by an exponential reflectivity recovery process with a time constant of 0.96 μs. The reflectivity starts to drop exponentially with a time constant of 10.6 μs in the middle of the recovery process. The inset shows the exponential fitting of the two slow dynamics. (c) SF-STAMP burst images show ultrafast dynamics with 4-ps window. The reflectivity drop only happens at the left and right edge of the sample, as well as the edges between the gold substrate and the sample. Since the reflectivity change does not emerge in the middle of the gap in the initial process after THz irradiation, the 4-ps ultrafast 2D-dynamics with a fine spatial resolution cannot be obtained by 1D-OSI measurements and can only be captured by SF-STAMP method.

Time constant estimation of the resistor-capacitor (RC) circuit with multilayer MoTe₂ and the THz enhancement structure

The time constant of the RC circuit with 2H multilayer MoTe₂ on a THz field enhancement structure (FES) can be estimated by treating MoTe₂ as a resistor and FES as a capacitor. The resistance of micron-size multilayer MoTe₂ can be estimated by $R = \frac{L}{\sigma S}$, where R is the resistance, σ is the conductivity [268] at the order of $1 \Omega^{-1}\text{cm}^{-1}$, L is the length at $2 \mu\text{m}$, and S is the area of the cross section at the order of 10^{-11}cm^{-2} . So, the resistance is estimated to be at the order of $10^7 \Omega$. The capacitance of THz enhancement structure can be estimated by treating the structure as a parallel plate capacitor, which have a separation distance d at $2 \mu\text{m}$ and a plate area at around $200 \text{nm} \times 1 \text{cm} = 2 \times 10^{-5} \text{cm}^{-2}$. Thus, the capacitance C is at the order of 10^{-2}pF and the time constant ($\tau = RC$) is estimated at the order of 10^{-7}s . After THz-driven irreversible phase transition, the resistance of new 1T' phase is two to three orders magnitude smaller [269] than that of 2H MoTe₂. However, a much greater electric field near the edge of the enhancement structure have been found to induce dramatic sample damages at the edge, which could give rise to a large ohmic contact resistance and jeopardize the actual discharging speed.

3.4 Summary

In conclusion, we comprehensively obtained the irreversible THz-driven phase transition dynamics in multilayer MoTe₂ by three different single-shot schemes of SF-STAMP, 1D-OSI, and oscilloscope readout spectroscopy. Consistent with the time scale of the reported SHG abnormal behavior, we observed interlayer shear, and breathing oscillations suddenly cease at a reflection plateau around 30-40 ps after THz excitation, which demonstrates the existence of a metastable phase during the irreversible phase transition. Oscilloscope readout method reveals slow sample discharging and degradation dynamics, and further SF-STAMP ultrafast measurement confirms the PF and IMI effect as the driving force for the irreversible phase transition. Our results points out the existence of a theoretically predicted metastable phase [235] during the complicated THz-driven irreversible phase transition dynamics in multilayer MoTe₂ and could potentially provide a better device geometry protecting 1T' phase from slow current-induced damage.

Chapter 4

Real-time *in-situ* measurement of laser processing

In Chapter 4, the real-time application of SF-STAMP combining with a kHz high-speed camera is demonstrated. Real-time *in-situ* measurement of laser processing evaluates the precursor process of each pulse and its effect on femtosecond laser processing of glass under multiple pulses accumulated conditions with sub-nanosecond time resolution using a chirp pulse probe or spectrally sweeping burst probes.

Abstract:

Real-time, *in-situ* operation of a single-shot, frequency-time encoding burst imaging method of sequentially timed all-optical mapping photography utilizing spectral filtering (SF-STAMP) is demonstrated by employing a high-speed (HS-) camera with the frame rate of a 1000-fps as a detector. We obtained single-shot burst images of a pulse-by-pulse femtosecond laser ablation of a glass by a chirped probe laser pulse with a 1-2-ps frame interval or by a spectrally sweeping burst laser pulse train with a 300-ps interval. A chirped probe laser pulse observed burst images of plasma generation during the early stage of laser ablation in a glass with a short frame interval. A spectrally sweeping probe laser pulse train also captured burst images of plume and shock-wave generation in air with a 1.5-ns observation time window.

4.1 Background

As described in Chapter 2, the SF-STAMP's observation time window has been extended to sub-ns by utilizing probes of spectrally sweeping burst pulses with a few hundred of picoseconds intervals. By using a chirped probe laser pulse or spectrally sweeping burst probe laser pulses as the need arises in sub-ps or sub-ns time scales, STAMP can circumvent the limitation in the temporal resolution of high-speed (HS-) camera technologies. Since STAMP's temporal resolution is not controlled by imaging sensors, we introduce an HS-camera as a detector in STAMP and obtain real-time consecutive ultrafast 2D-burst images in accordance with the frame rate of the HS-camera.

Applying real-time measurements with a high temporal resolution for femtosecond laser processing [270] provides such rich physics insights as the generation and the propagation of shock waves and clacks [271–273] as well as the formation of a laser-induced periodic surface structure (LIPSS) [274–276] in the time scale of picoseconds to nanoseconds. Previous researches conducted pump-probe, time-resolving schemes

for revealing the dynamics of laser processing; but in most cases, they focused on morphological observations after a single pump pulse irradiation [224]. Recently, time-resolved investigations have been conducted of multiple pulse laser-induced plasma or shockwave generation at silicon [277] or fused silica [278], and the pump-probe measurements were combined with an HS-camera to investigate the dependence of multiple pulse irradiation on the propagation of pressure waves in glass [279]. However, it remains challenging to accurately obtain ultrafast non-reproducible behavior or a series of time sequences at identical processing conditions without optical delay scanning.

In this chapter, we combined SF-STAMP and a 1000-fps HS-camera for laser ablation of glass operated by a 1-kHz femtosecond laser [62]. We aim to use the SF-STAMP technique to collect transient image data in laser ablation processes to increase our understanding of physics in laser processing and to optimize laser parameters with those data analyses. In general laser ablation processes, no thermal accumulation takes place if the repetitive laser pulse interval is longer than a thermal relaxation time of $\sim\mu\text{s}$. Therefore, the observation done for 1-kHz laser ablation in this work does not change from that acquired with a series of observations with a single laser shot using SF-STAMP and a conventional camera. However, since laser ablation processes always require multi-laser pulse shots, we can acquire complete transient image data for a certain number of laser pulses in a shorter time at 1 kHz. Therefore, a real-time, transient image acquisition technique, which combines SF-STAMP and an HS-camera, will be applicable and very useful for high repetitive laser ablation processing. Moreover, when combined with much faster cameras (up to 10^9 frames per second is commercially available [131]), we can simply apply our experimental scheme to higher repetition rate laser pulse processes where thermal accumulation influences the processing performance.

We captured the pulse-by-pulse multiple femtosecond laser ablation processing of glass operated by a 1-kHz femtosecond laser in real-time by a chirped probe laser pulse or by spectrally sweeping burst probe laser pulses with a 300-ps interval. We obtained the burst images of plasma generation during the early stage of laser ablation in a glass with a short frame interval by chirped probe laser pulses. On the other hand, we captured burst images of plume and shock-wave generation in air with a 1.5-ns observation time window by spectrally sweeping probe laser pulses.

4.2 Methods

Figure 4.1(a) depicts the schematic setup of an SF-STAMP snapshot multispectral imaging system with two different probe laser pulses: a frequency-chirped laser pulse probe and spectrally sweeping burst laser pulse probes for femto- to picosecond and pico- to nanosecond regimes. SF-STAMP's spatial resolution is determined by the numerical aperture of the objective lens as in conventional microscopy. We show the

concept of real-time consecutive pulse-by-pulse ultrafast 2D-burst imaging by a combination of an SF-STAMP system and a 1000-fps HS-camera (**Figure 4.1(b)**). In each frame of the HS-camera, we capture single-shot frequency-time encoded burst SF-STAMP's sub-frame images up to 25 (the numbered images in each HS-camera frame).

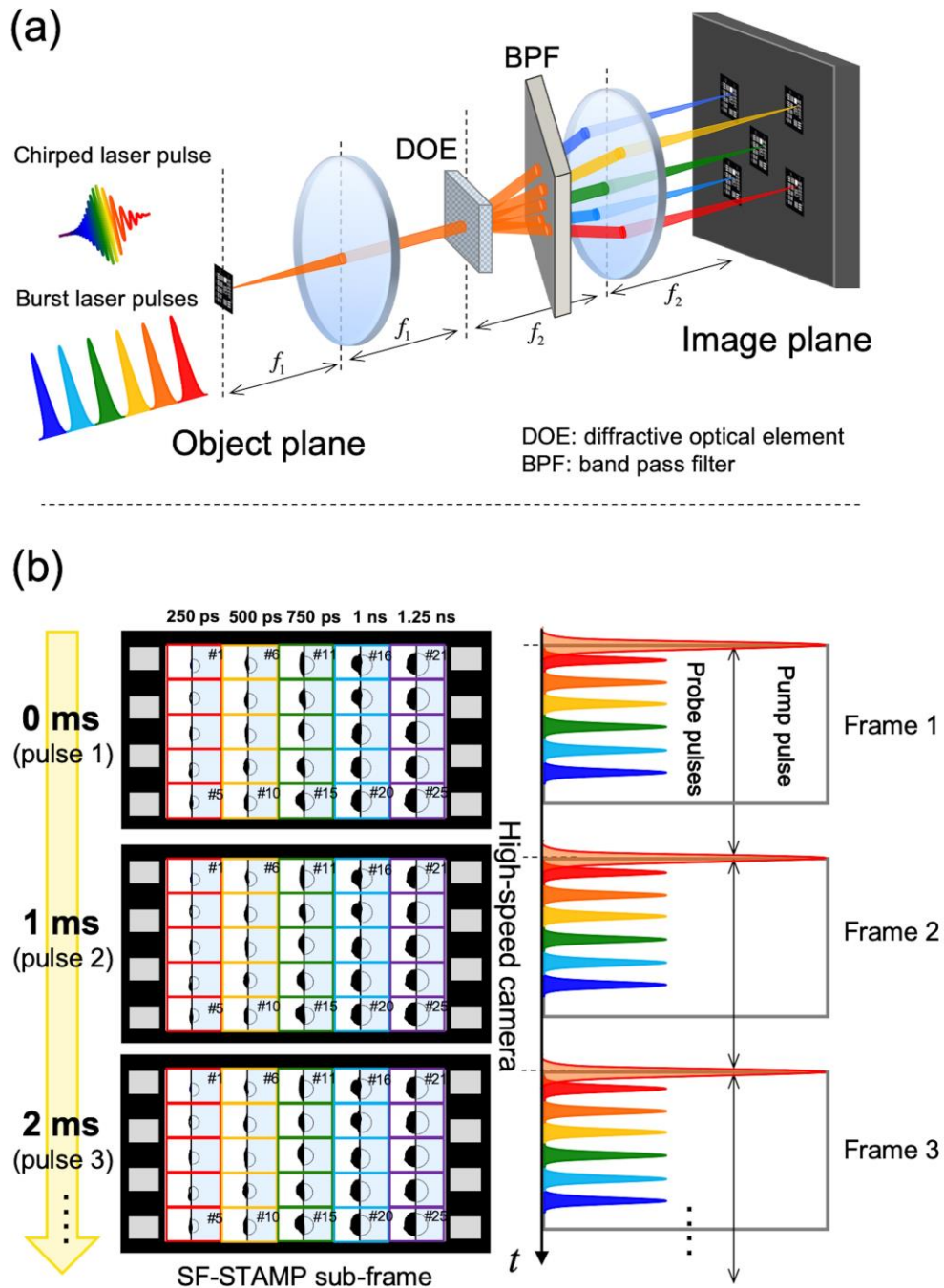


Figure 4.1 (a) SF-STAMP snapshot multispectral imaging system composed of a diffractive optical element (DOE) and a bandpass filter (BPF); (b) Concept of real-time consecutive 1 kHz ultrafast 2D-burst imaging by the combination of SF-STAMP system and a 1000-fps high-speed camera.

4.3 Real-time observation of multiple femtosecond laser processing with a sub-nanosecond temporal resolution

4.3.1 Experiment

The entire experimental setup of the real-time consecutive ultrafast 2D-burst imaging scheme is shown in **Figure 4.2**. The experimental measurements are based on a single-shot pump-probe layout, which is similar to previous works in Chapter 2 [60,61]. Thus, after setting the timing of a pump and a probe pulse, we do not need to scan the delay. In fact, in our previous experiments, we selected a single laser pulse from 1-kHz laser pulses by a mechanical shutter. With the 1000-fps HS-camera, we used all the 1-kHz laser ablation shots. The light source was a mode-locked Ti:sapphire laser (Coherent, Mira) with chirped pulse amplification (CPA) by both regenerative and multi-pass amplifiers. The pulse energy was ~ 1.0 mJ at a 1-kHz repetition rate with a pulse width of 50 fs (FWHM). The amplified laser pulse (800 nm) was split into probe and pump pulses for femtosecond laser ablation processing. For the probe branch, we used a frequency-chirped probe pulse or spectrally sweeping burst pulse probes. When employing a chirped probe pulse for the picosecond time window, the probe pulse was focused into an Ar-gas-filled hollow-core fiber (HCF) (240-mm long, 126- μm diameter) by an $f = 400$ mm lens, and the output beam was collimated using an $f = 500$ mm concave mirror. In the HCF, a 700–900 nm broadband pulse was generated by self-phase modulation (SPM). To stretch the pulse duration to ~ 10 ps, the broadband pulse was passed through optical glass rods of NSF-11 and BK7. (The total amount of dispersion was 0.29 ps/nm). The time window of this 40-nm bandwidth positive chirp probe pulse was stretched to ~ 11.6 ps.

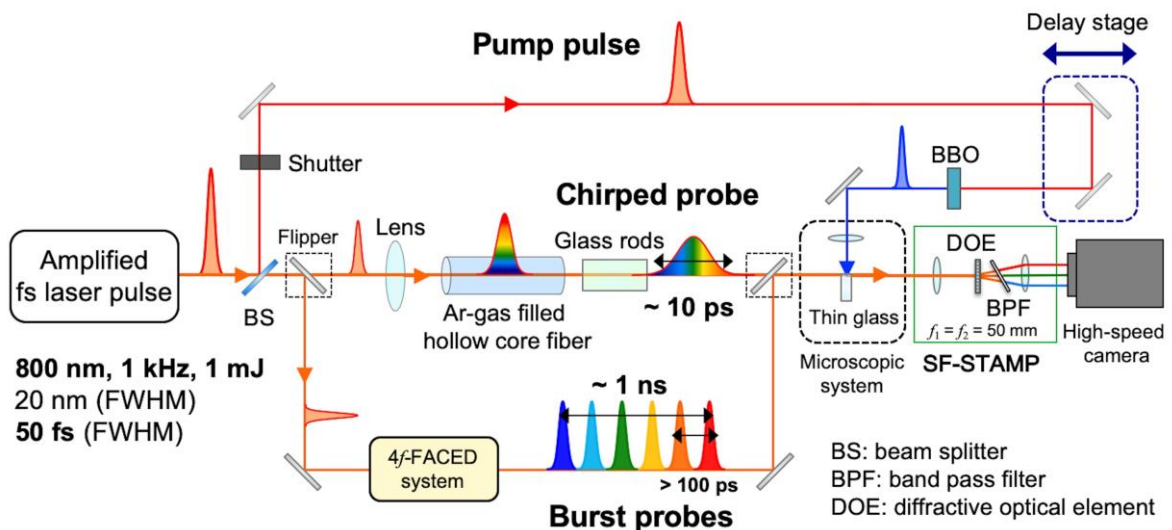


Figure 4.2 Experimental setup of real-time observation of pulse-by-pulse femtosecond laser processing with consecutive 1 kHz ultrafast 2D-burst imaging.

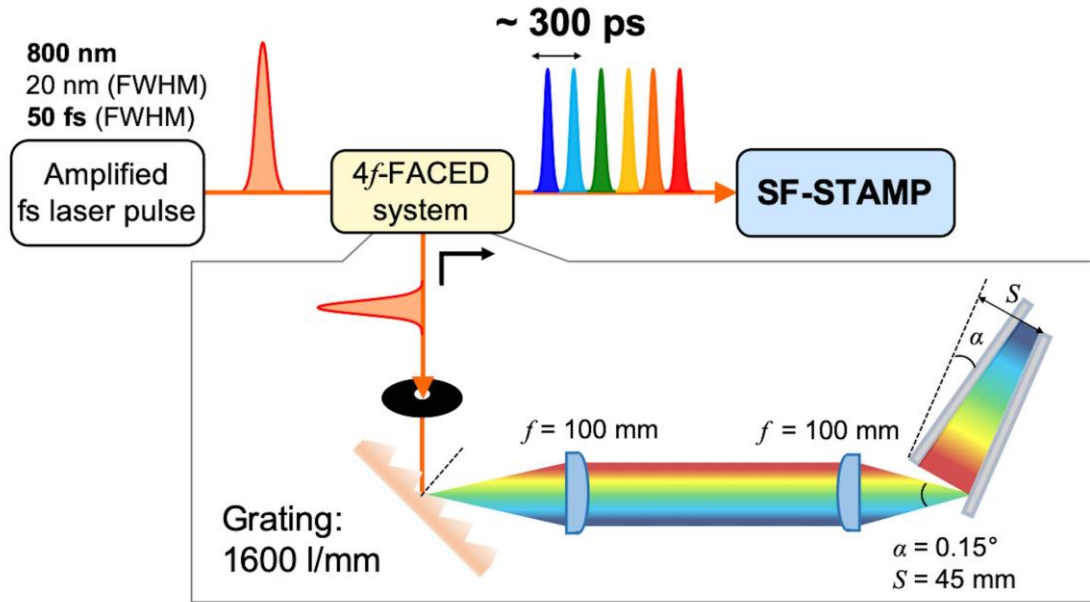


Figure 4.3 Generation of spectrally sweeping burst pulses by the 4f-FACED system.

For achieving a nanosecond observation time window with sub-ns temporal resolutions, we adopted a 4f-FACED system to generate spectrally sweeping burst pulses (**Figure 4.3**). We used 800-nm output pulses from the CPA without spectral broadening by the HCF. An input laser pulse (a 25-nm bandwidth ranging from 785 to 810 nm) was angularly dispersed by diffraction grating (1600 lines/mm) and focused at the entrance of a pair of slightly tilted high reflective dielectric mirrors (200 mm, $R > 99.5\%$) with different incident angles depending on the wavelength by the 4f-system with two cylindrical lenses with 100-mm focal lengths. For fulfilling the requirements of STAMP's probe pulse source, the probe pulses need to propagate collinearly; thus, we placed a beam splitter after the 4f-FACED system to separate the output burst pulse train from the input pulse. Since different frequency components propagate different optical paths and reflect at the mirror, multiple pulses with different center wavelengths are generated at a fixed interval [144]. In the present 4f-FACED system, the number of pulses can be tunable by changing the angle of mirror pair α , and the pulse interval can be adjusted by mirror separation length S . To generate six burst pulses with a 300-ps interval, we determined $\alpha = 0.68^\circ$ and $S = 45$ mm and extended the single-shot time window to ~ 1.5 ns. In a pump pulse optical branch, we employed an electrically controlled mechanical shutter (Thorlabs, SH05 and SC10) and adjusted the trigger timing of the laser ablation. To avoid spectral overlap between the scattered pump and the probe pulses, we converted the pump laser to the second harmonic (400 nm) with a β -barium borate (BBO) nonlinear crystal. The polarizations of the pulses were

4. Real-time *in-situ* measurement of laser processing

also adjusted to be orthogonal. The pump femtosecond laser pulse ($< 85 \mu\text{J}$) was focused to a thin, 50- μm thick, glass sample (Nippon Electric Glass, Green Glass (OA-10G)) by an $f = 8\text{-mm}$ lens.

In an SF-STAMP multispectral imaging system, the probe pulse passed a first Fourier lens ($f = 50 \text{ mm}$) and a diffractive optical element (DOE) (HOLOEYE, customized model), which generates 5×5 beams with a full diffraction angle of 25.6° . Then the diffracted 25 array beams passed a tilted bandpass filter (BPF) (Semrock, LL01-780, a center wavelength of 780 nm and a bandwidth (FWHM) of 3.1 nm for a chirped probe; IRIDIAN, ZX000167, a center wavelength of 830 nm and a bandwidth (FWHM) of 2.2 nm for burst probes) and a second Fourier lens where $f = 50 \text{ mm}$. To observe a small laser processing area, we constructed a microscope system with an $f = 30\text{-mm}$ condenser lens and an objective lens ($\times 20$, $NA = 0.40$, Olympus, LMPLFLN20X). Thus, the minimum spatial resolution of the experiment determined by the diffraction limit was $800 \text{ nm}/2NA = 1 \mu\text{m}$ (Abbe's diffraction limit). All the lenses were achromatic. The enlarged shadowgraph image of the thin glass sample was relayed to the SF-STAMP system and separated into multispectral images. We employed a 1000-fps HS-camera (Nac Image Technology Inc., MEMRECAM HX-7s) as a high-speed imaging sensor that has 2048×1920 pixels; each pixel was $11 \mu\text{m} \times 11 \mu\text{m}$. Note that the HS-camera achieves fast acquisition capability by a larger pixel size than conventional CCD cameras. However, the spatial resolution remains limited by the diffraction limit determined by the microscope optics in our setup. With the HS-camera, we can store more than 5000 frames; this combination of a kHz frame-rate camera and ultrafast time scale single-shot burst technique enables *in-situ* measurements of laser processing with high temporal resolution up to 5000 pulses. In our STAMP experiment, we attenuated the probe laser pulse to $\sim 100 \text{ nJ}$ to avoid influencing the laser processing. When using a chirped probe laser pulse, we used a laser pulse that was spectrally broadened by a rare-gas filled HCF. Therefore, the laser intensity at the unit bandwidth became lower ($\sim 0.5 \text{ nJ/nm}$) than that of a spectrally sweeping pulse train ($\sim 4 \text{ nJ/nm}$) generated by 4f-FACED.

4.3.2 Results

4.3.2.1 Picosecond region with a frequency-chirped pulse

Figure 4.4 shows one typical frame captured by the HS-camera with 25 frequency-time encoded SF-STAMP multispectral images, which captured the burst images of femtosecond laser-induced air plasma generation. The pump laser energy was $\sim 80 \mu\text{J}$. In this configuration, the observation wavelength of the chirped probe laser pulse ranged from 730 to 770 nm. The images with a smaller number (#: 1~25) correspond to longer wavelength images, which are from an earlier time snapshot in the SF-STAMP time sequence. To visualize the shadowgraph in these snapshots, we normalized the spectral intensity with that measured before the pump laser excitation to compensate for the variation in the spectral power at each wavelength component filtered by the BPF. When the probe laser pulse temporally overlaps with the pump laser pulse, the laser-induced plasma channel in air is distinct in the shadowgraph image. In **Figure 4.4**, #7 snapshot captured the air plasma. We set this snapshot to a zero delay ($t = 0$). Since the air plasma generation timing moves as the delay-path of pump laser pulse changes, we determined the probing time window length by monitoring the plasma generation timing. Consequently, the time window of this 40-nm bandwidth positive chirped probe laser pulse was 11.6 ps where the optical delay length of 3.48 mm. The exposure time and the frame interval of the snapshots were 937 and 481 fs.

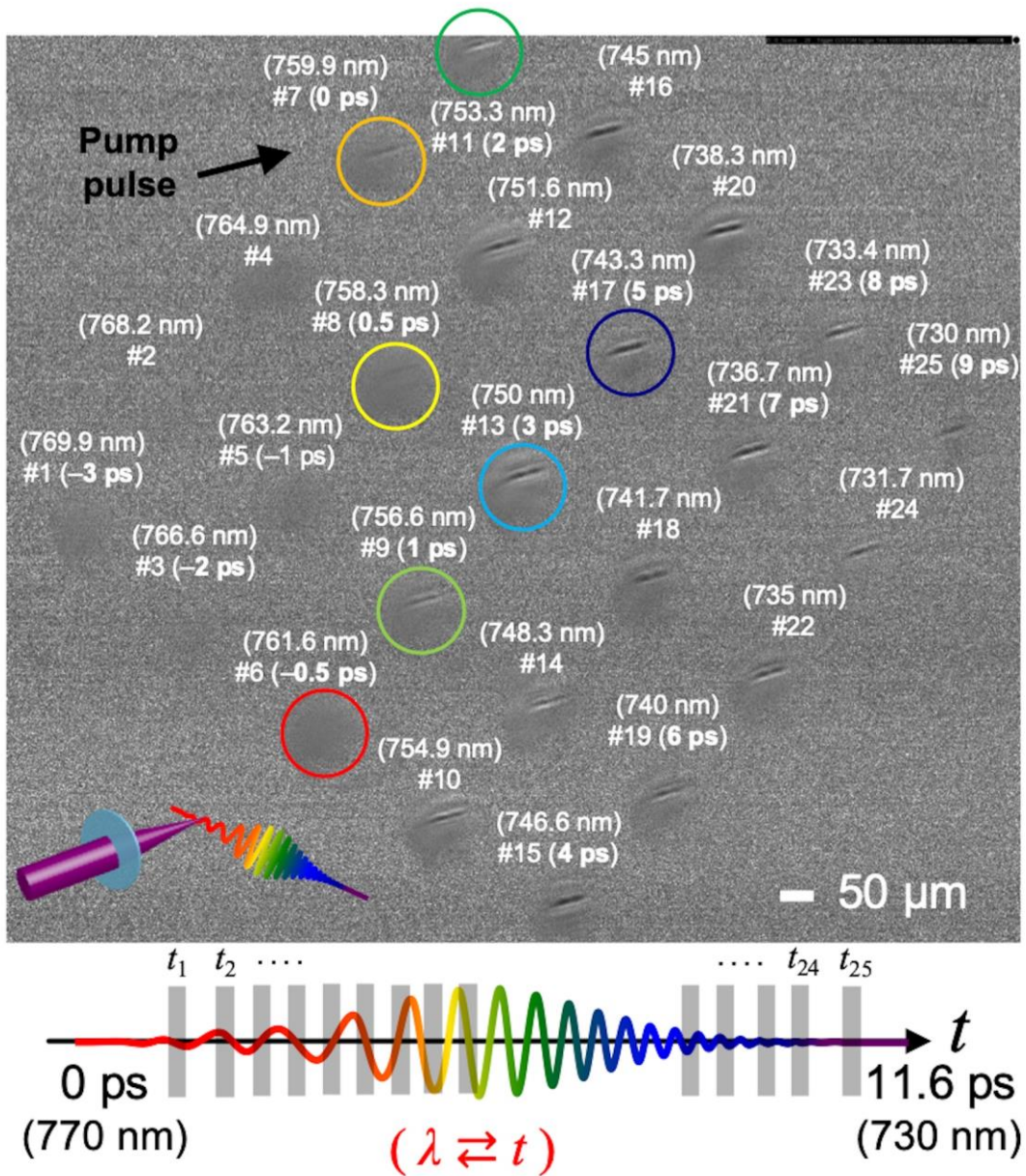


Figure 4.4 Frame result of HS-camera with 25 frequency-time encoded SF-STAMP snapshots, which captured dynamic images of femtosecond laser-induced air plasma generation. 7th snapshot position is delay zero time. Time window of this 40-nm bandwidth (770~730 nm) probe pulse was 11.6 ps. Exposure time and frame interval of snapshots were 937 and 481 fs. Circles represent burst frames trimmed in **Figure 4.5(b)**.

Next we measured the picosecond-scale dynamics of the multiple laser pulse ablation of a glass with a chirped laser probe pulse at every 1-kHz ablation laser shot (**Figure 4.5(a)**). The pulse energy of the 400-nm femtosecond ablation laser pulse was $\sim 30 \mu\text{J}$. The processing laser pulse was focused slightly inside the bulk. A 12-ps chirped probe laser pulse tracked shot-by-shot burst snapshot images of the temporal evolution of the laser ablation on the glass and laser-induced air plasma generation. Out of 25 multispectral snapshots in each ablation laser pulse irradiation, seven frames (center wavelengths of 761.6, 759.9, 758.3, 756.6, 753.3, 750, and 743.3 nm) were trimmed and arranged with the order of time in the horizontal columns of **Figure 4.5(b)**. Each spectral image occupied 175×130 pixels on the HS-camera. The scale bar represents $50 \mu\text{m}$. **Figure 4.5(b)** shows the precursor process of laser ablation from pre-irradiation (-0.5 ps: 1st column) into 5 ps (7th column) after the femtosecond laser irradiation. The images at $t = 0$ were set in the 2nd column. The vertical columns correspond to the HS-camera frames of the 1st, 2nd, 10th, 50th, 100th, and 200th ablation laser pulse shots. At the 1st pulse laser ablation, laser-induced air plasma was generated ~ 2 ps after the pump pulse arrived. After the 2nd shot, the glass surface was ablated, and the shapes of the post-mortem area inside the glass were captured in the first column. At the 2nd pulse laser ablation, similar to the previous reports on multiple laser pulse ablation [277,278] where the material morphology generated by prior pulses interacted with subsequent laser pulses and reshaped the effective spatial laser intensity distribution inside the material, we observed the enhancement of laser-induced air plasma formation (**Figure 4.5(b#2_1ps)**). The distinct air plasma is visible in **Figure 4.5(b#2_1ps)**, but it did not appear in the 1st shot in **Figure 4.5(b#1_1ps)**. Since the 1st pulse altered the glass surface to a crater-like shape, the laser beam was partially reflected and induced laser refocusing during the 2nd pulse irradiation. Effects induced by the multiple pulse irradiation were also confirmed in the sub-nanosecond measurement (following the description in 4.3.2.2). When the glass surface laser ablation generated a deep hole beyond the effective laser pulse penetration depth at around 100 pulses, no significant further ablation plume was visible after 100 pulses. Thus, #200 pulse images were almost the same as those of the #100 pulse, and the processing depth became saturated. Only the air breakdown outside the glass was visible in these shots.

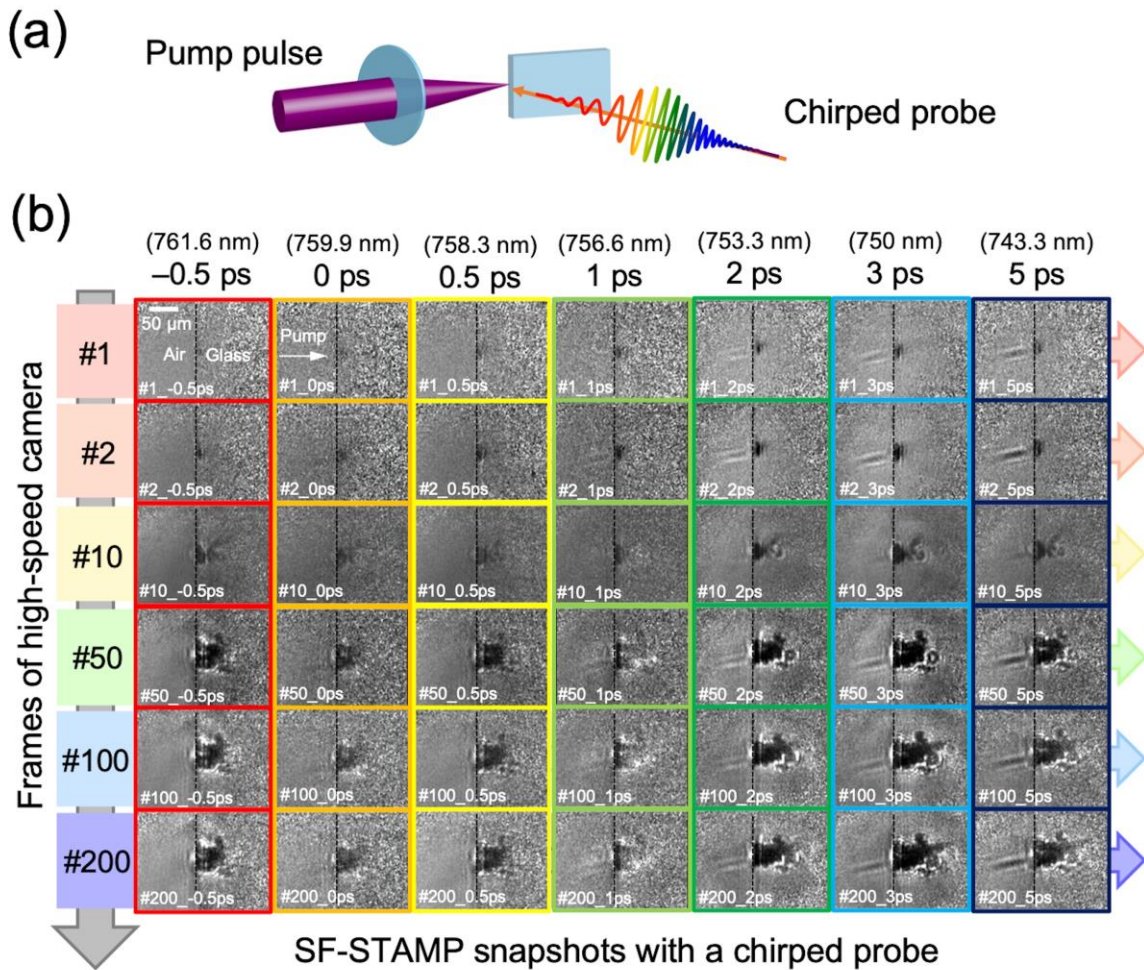


Figure 4.5 (a) Schematic of single-shot measurement of femtosecond laser processing of glass with frequency-chirped laser pulse probe. With a 1000-fps HS-camera, we observed each pump laser shot; (b) Measured pulse-by-pulse single-shot burst images of time evolution of laser ablation on glass and laser-induced air plasma by SF-STAMP with a 12-ps chirped probe (175×130 pixels). Horizontal column corresponds to ultrafast single-shot snapshot with seven frames (center wavelength of 761.6, 759.9, 758.3, 756.6, 753.3, 750, and 743.3 nm). Exposure time of each frame was 937 fs. Vertical column corresponds to HS-camera frames. Number in vertical column is cumulative pump pulses. Scale bar represents 50 μm.

4.3.2.2 Sub-nanosecond region with spectrally sweeping burst pulses

We also obtained burst images with a nanosecond time window using six spectrally sweeping burst probe pulses (center wavelengths of 810, 805, 800, 795, 790, and 785 nm) that were generated with 4f-FACED (**Figure 4.6(a)**). Since we used a fraction of the direct laser output from the amplifier without supercontinuum generation, the probe laser intensity at the unit bandwidth was higher than that of the chirped laser pulse used for the measurements in **Figure 4.5**. Therefore, burst images were captured with an improved SNR. The processing laser pulse was focused at the surface. We measured the slower dynamics around the nanosecond at a sub-ns time resolution, which conventional high-speed cameras cannot realize. **Figure 4.6(b)** shows the shot-by-shot burst snapshot images of the laser ablation and the shock-wave evolution on the glass probed by a laser pulse train that consisted of six pulses with a 300-ps interval (1.5-ns time window). The average exposure time of each frame was 21.8 ps. In **Figure 4.6(b)**, the horizontal columns correspond to single shot ultrafast burst images captured by SF-STAMP. The vertical columns correspond to the HS-camera images of the 1st, 2nd, 10th, 50th, 100th, and 500th laser ablation shots. Each snapshot occupied 220×150 pixels of the HS-camera. The scale bar represents 50 μm . The pulse energy of the 400-nm femtosecond pump laser was $\sim 30 \mu\text{J}$. In the sub-nanosecond scale dynamics, the effects of multiple pulse ablation were measured between the 1st and 2nd pulses. Comparing **Figure 4.6 (b#1_1.2ns)** with **Figure 4.6(b#2_1.2ns)**, the interaction between the shockwaves (SWs) generated from the laser-induced plasma and laser ablation is different. Since the air plasma generation timing differs at the 1st and 2nd laser ablation due to the above reflection and the refocusing effects of the ablation laser beam by the modified glass surface, the SW generation timing from the laser-induced air plasma also shifts and leads to different interactions with SW generated at the surface ablation. The SW interaction lasts until the glass surface is volumetrically ablated. Since no ablation plume exploded to the air after the 10th pulse, the SW interactions disappeared. After the 50th pulse, the laser-induced air plasma outside the glass disappeared before 300 ps; only progressive etching took place. The ablated hole shape in the glass that appeared at the first frame is different in **Figure 4.5** and **Figure 4.6** due to a slightly different focusing position.

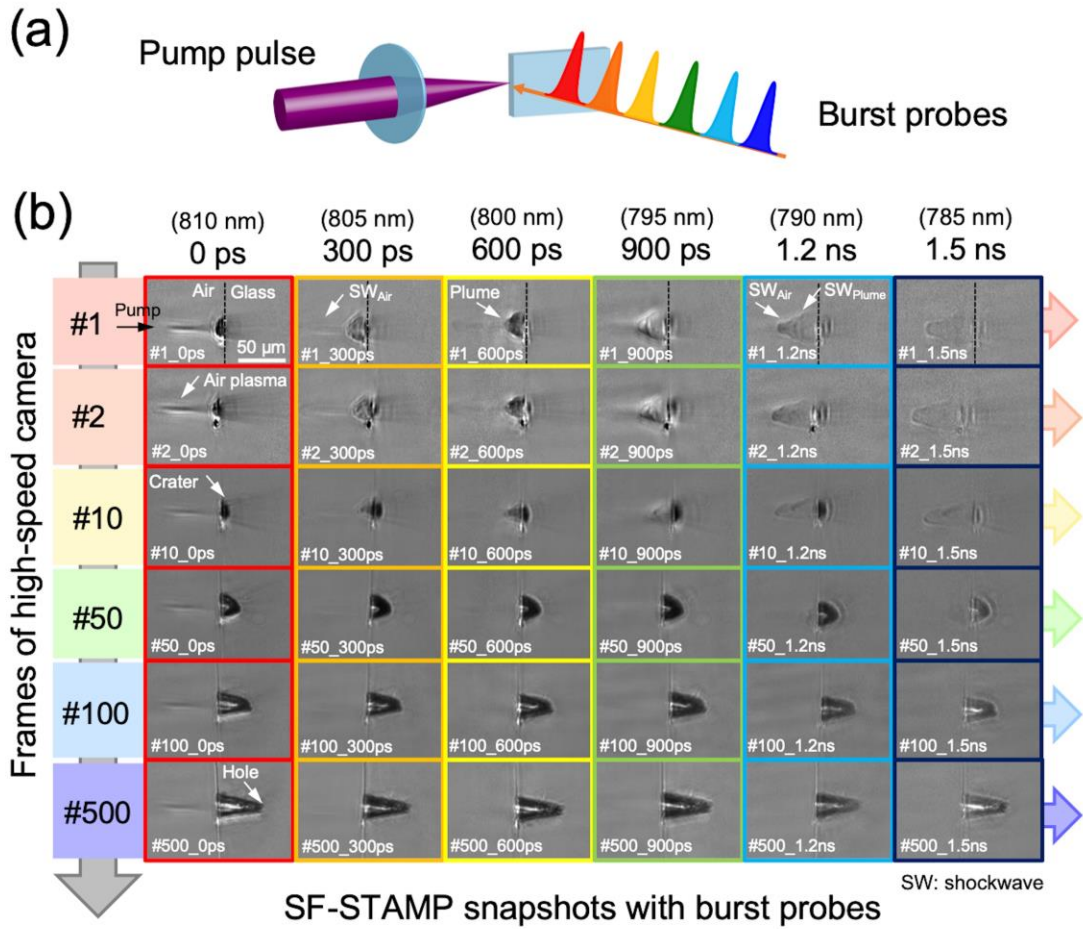


Figure 4.6 (a) Schematic of single-shot measurement of femtosecond laser pulse ablation of glass with spectrally sweeping burst probe laser pulses. With 1000-fps HS-camera, we observed each laser ablation shot. Shockwaves (SWs) generated by laser-induced plasma (SW_{Air}) and by ablation plume (SW_{Plume}) are indicated on images; (b) Measured pulse-by-pulse single-shot burst images of laser ablation and shock-wave evolution on glass by SF-STAMP with 300-ps interval spectrally sweeping pulses (220×150 pixels). Horizontal column corresponds to ultrafast single-shot snapshot with six frames (center wavelengths of 810, 805, 800, 795, 790, and 785 nm). Vertical column corresponds to HS-camera shots. Number in vertical direction is equivalent to number of cumulative pump pulses. Scale bar represents 50 μm.

4.4 Summary

We combined the single-shot ultrafast 2D-burst imaging technique of SF-STAMP and a 1000-fps HS-camera to achieve real-time monitoring of pulse-by-pulse femtosecond laser pulse ablation with sub-nanosecond temporal resolution. Frequency-chirped probe pulses can achieve sub-picosecond to tens of picosecond time window measurements. By adopting the spectrally sweeping burst pulses generated by the 4*f*-FACED system, the time window in a single-shot measurement can be extended to the sub-nanosecond regime. Such *in-situ* ultrafast imaging methods are attractive and suitable for collecting transient data in irreversible ultrafast phenomena to increase our understanding of the ultrafast physics in interactions between laser pulses and such procedures as ablation. For future applications, for example, we will measure the direct observation of LSFL (low spatial frequency LIPSS) formations [280–282], THz-induced LIPSS [283], and the real-time measurement of high-repetition-rate (MHz to GHz) burst laser processing under heat accumulation [284–289]. For kHz to MHz-burst laser processing, the combination of an Mfps-camera and STAMP can track real-time images with STAMP's sub-frame resolution.

Chapter 5

Outlook for future application of SF-STAMP

Chapter 5 discusses current limitations in SF-STAMP and the outlook for the future applications of SF-STAMP, especially laser processing and THz wave region.

SF-STAMP has addressed several ultrafast irreversible phenomena in Chapters 2, 3, and 4. However, as mentioned, the low efficiency of light utilization is an inherent limitation in an SF-STAMP system. Thus, a combination of function microscopic optical systems, such as phase contrast or polarizing imaging, suffers from implementation on the condition of a weak light intensity probe case. The combination of an SF-STAMP and spectrally sweeping burst probes generated by a $4f$ -FACED has demonstrated a few hundreds of picoseconds interval single-shot. Due to the nature of spectral filtering by an angle-dependent BPF, however, full utilization of multispectral images with time-encoding is difficult to implement. Therefore, another snapshot multispectral imaging approach with high-light efficiency without an angle-dependent spectral filtering scheme will realize a more functional STAMP. In this light efficiency improved scenario, combination with polarization spectroscopy or imaging will be applied, benefiting us ultrafast polarization information.

5.1 STAMP application for laser processing

As demonstrated in Chapter 4, real-time *in-situ* pulse-by-pulse ultrafast 2D-burst imaging with sub-nanosecond temporal resolution can be performed with a STAMP and a high-speed camera. These *in-situ* ultrafast imaging methods are attractive and suitable for imaging laser ablation processing. For future applications, for example, direct observation of LSFL (low spatial frequency LIPSS) formations [280–282] or THz-induced LIPSS [283], and real-time measurement of high-repetition-rate (MHz to GHz) burst laser processing under heat accumulation [284–289] would be measured. For kHz to MHz-burst laser processing, the combination of an Mfps-camera and STAMP can track real-time images with a STAMP's ultrafast temporal resolution.

On the other hand, in recent years, the result that processing efficiency even improves with pulse energy below the ablation threshold of a single pulse when high-repetition processing is performed with laser pulses shorter than the thermal relaxation time of the material [286] has been reported. This indicates that high-efficiency (ablation cooling) processing without thermal damage is possible with GHz high-repetition pulses. Therefore, the development of a fiber laser light source for processing that operates at GHz

repetition has been actively promoted [290,291] In addition, laser processing parameters suitable for various types of materials that have different thermal conductivity, melting points, and specific heats, and whose values dynamically change during processing can be controlled by *in-situ* measurement. There is also a direction to perform excellent pulse laser processing with little damage. Hence, if the high-repetition laser can be dynamically controlled by real-time measurement, adaptive laser processing can be realized. Furthermore, it is possible to monitor GHz processing images for each shot with SF-STAMP. These images can be processed in real-time, and parameters such as laser intensity, pulse width, and repetition frequency of the processing laser can be adaptively controlled. In the sub-nanosecond time region, there are interesting phenomena, such as the interaction between cells and shock waves that have not yet been elucidated, and laser-induced crystal nucleation.

5.2 STAMP in THz wave region

In Chapter 3, a THz pulse was only used for a pump source. In general, however, ultrafast imaging in THz wave region is attractive because there are no high-speed imaging sensors. As chirped-EO sampling in 1D [35], 2D-EO chirped sampling will be possible by employing an SF-STAMP imaging system [292]. **Figure 1.7** shows the example of THz 2D-EO chirped sampling measured by SF-STAMP in the experiment of Chapter 3. In this case, only the THz modulation beam profile was measured for confirming THz overlapping time, but when 2D-spatial information with enough SNR is imaged to STAMP multispectral imaging system, ultrafast 2D-EO imaging of THz wave region with an optical chirped readout pulse can be realized.

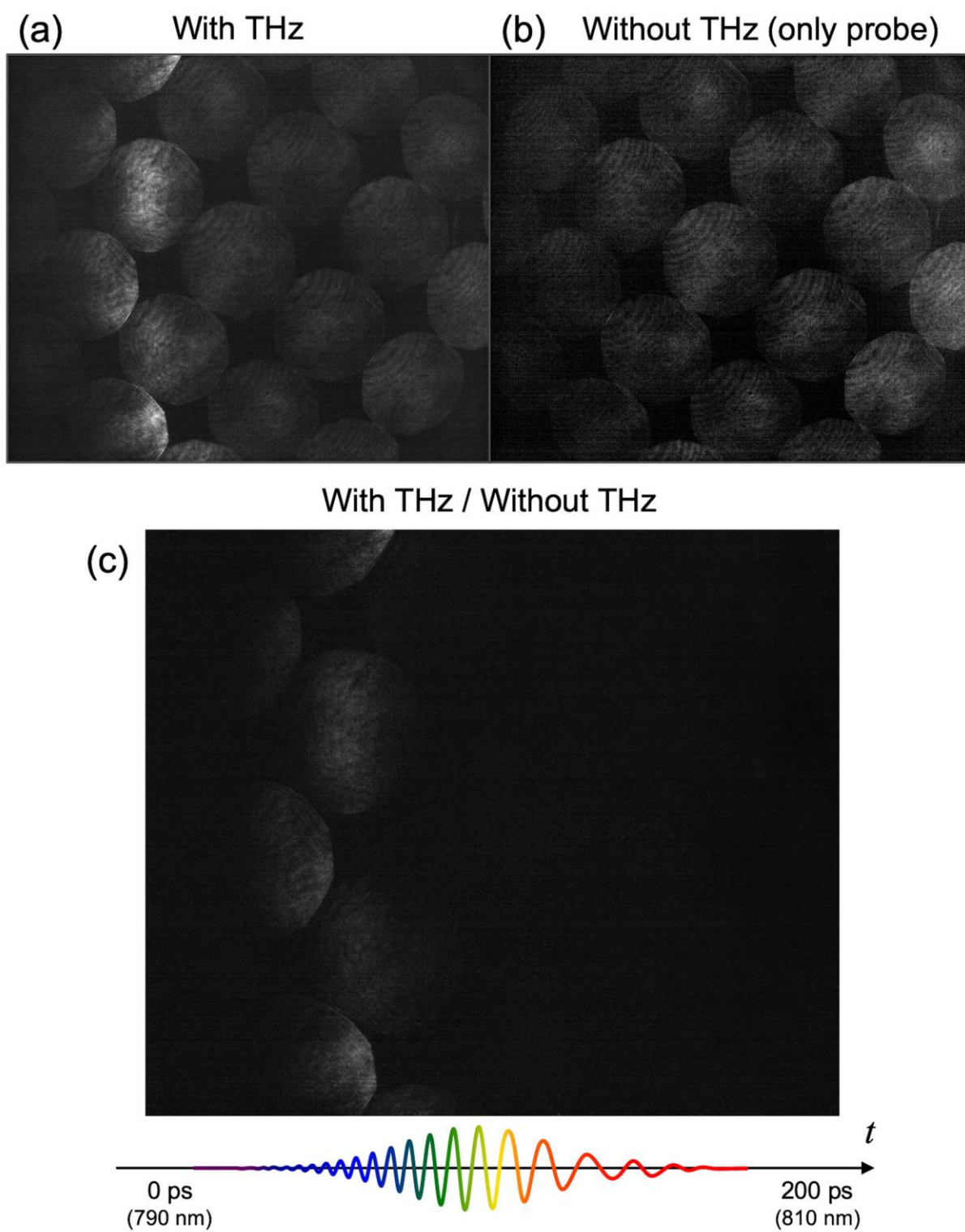


Figure 5.1 Results of 2D-EO chirped sampling obtained by SF-STAMP

Chapter 6

Conclusion

Chapter 6 summarizes the experimental results and knowledge obtained in each chapter.

A frequency-to-time encoding single-shot imaging of STAMP leverages an observation window ranging from sub-picoseconds to nanoseconds, which is impossible to access by the conventional ways. Therefore, STAMP is a highly attractive imaging technique, addressing observations of ultrafast irreversible phenomena. For performing the myriad applications of STAMP to single-shot ultrafast 2D-imaging, however, there are demands to solve the problem of freedom in the number of burst snapshots and expansion of the time window to the nanoseconds region that has been unachieved by both conventional high-speed and state-of-the-art ultrafast imaging technique. In this study, thus, developing the spectral filtering (SF-) STAMP method (SF-STAMP) and establishing a comprehensive SF-STAMP methodology that is simple but widely applicable when single-shot ultrafast 2D-burst imaging is being conducted. Then, applying the SF-STAMP with additional functionality to ultrafast single-shot measurements revealed nonrepetitive phenomena in real-time. These results emphasize the STAMP method is a superb tool over other single-shot ultrafast imaging methods. Moreover, STAMP is the tool for identifying the universality and peculiarity of phenomena that can only be clarified by observing a single event repeatedly.

In Chapter 2, to overcome the original STAMP restriction, we simplified the setup and increased the number of burst frames from 6 up to 25 by developing a modified SF-STAMP. In an SF-STAMP snapshot multispectral imaging system, a diffractive optical element (DOE) duplicates spatially resolved replicas of the probe pulse. These replicas are incident to a tilted bandpass filter (BPF), which selects different narrow-band wavelengths depending on the angle of incidents. The 25-frame SF-STAMP system with a frequency-chirped probe succeeded in capturing real-time 2D-images of a femtosecond laser-induced crystalline-to-amorphous phase change in $\text{Ge}_2\text{Sb}_2\text{Te}_5$ with an exposure time of 465 fs and frame interval of 133 fs (corresponding to frame rates of 7.52 Tfps) inside an entire time window of 3.2 ps. The optimum temporal resolution of SF-STAMP was also discussed. In addition, as an extension approach to the nanoseconds time window, spectrally sweeping burst probes with a ~ 100 -ps interval generated by a 4f-FACED system were applied to the SF-STAMP scheme. Employing six multi-wavelength delayed pulses demonstrated sub-nanosecond temporal snapshots of a femtosecond laser processing of glass. These images in Chapter 2 were obtained with a transmission optical microscopy.

In Chapter 3, the SF-STAMP addressed ultrafast dynamics in THz light-matter interactions. The dynamics of recently discovered high-field intensity THz-induced irreversible phase transition in 2D-TMDs is still unrevealed, since the nonreversible nature of this phenomenon precludes conventional time-resolved techniques. Thus, we applied the SF-STAMP and 1D-optical streak imaging (1D-OSI) spectroscopy to a single-shot measurement of THz-driven irreversible phase transition in multilayer MoTe₂ by observing transient reflectivity change of a chirped probe within ~300 ps. We observed the disappearance of the initial phase and discovered a metastable phase during the irreversible phase transition around 30–40 ps after a THz pulse excitation. This result can be measured for the first time by SF-STAMP's powerful features of a single shot and ps-temporal and μm-spatial resolution. In this case, we employed a reflection optical microscopic layout. Moreover, from the experiment, the combination of both frequency-to-time encoding of 1D-OSI (consecutive) and 2D-STAMP (burst) complementary works and bring much temporal information in single event.

In Chapter 4, a real-time *in-situ* measurement application in multiple femtosecond laser pulses processing has been demonstrated by combining a conventional high-speed (HS) camera and SF-STAMP. Since STAMP's temporal resolution is not controlled by imaging sensors, introducing an HS-camera as a detector in STAMP stored real-time ultrafast 2D-burst images of pulse-by-pulse femtosecond laser ablation of glass driven by a 1-kHz femtosecond laser. Precursor process of each pulse and its effect on femtosecond laser processing of glass under multiple pulses accumulated conditions were monitored with sub-nanosecond time resolution using a chirped pulse probe or spectrally sweeping burst probes. Such *in-situ* ultrafast imaging method is attractive and suitable for collecting transient data in irreversible ultrafast phenomena to increase our understanding of the ultrafast physics in interactions between laser pulses and such procedures as ablation.

In Chapter 5, current limitations in SF-STAMP are discussed, and the outlook for the future applications of SF-STAMP, especially laser processing and THz wave region are explained.

Finally, I conclude this thesis. Rapid advances in the ultrafast laser technology have enabled various new techniques, day by day. The STAMP method is one of the cutting-edge methods in ultrafast optics fields and is expected to clarify unrevealed dynamics in ultrafast timescale both in material science and biological applications. I hope the research on SF-STAMP will contribute to the advent and development of other types of STAMP.

References

1. T. H. Maiman, "Stimulated Optical Radiation in Ruby," *Nature* **187**, 493–494 (1960).
2. P. F. Moulton, "Spectroscopic and laser characteristics of Ti:Al₂O₃," *J. Opt. Soc. Am. B* **3**, 125 (1986).
3. D. E. Spence, P. N. Kean, and W. Sibbett, "60-fsec pulse generation from a self-mode-locked Ti:sapphire laser," *Opt. Lett.* **16**, 42 (1991).
4. D. Strickland and G. Mourou, "Compression of amplified chirped optical pulses," *Opt. Commun.* **56**, 219–221 (1985).
5. M. C. Downer, R. L. Fork, and C. V. Shank, "Femtosecond imaging of melting and evaporation at a photoexcited silicon surface," *J. Opt. Soc. Am. B* **2**, 595 (1985).
6. M. C. Fischer, J. W. Wilson, F. E. Robles, and W. S. Warren, "Invited Review Article: Pump-probe microscopy," *Rev. Sci. Instrum.* **87**, 031101 (2016).
7. B. Guo, J. Sun, Y. Lu, and L. Jiang, "Ultrafast dynamics observation during femtosecond laser-material interaction," *Int. J. Extrem. Manuf.* **1**, 032004 (2019).
8. T. Yasui, K. Minoshima, E. Abraham, and H. Matsumoto, "Microscopic time-resolved two-dimensional imaging with a femtosecond amplifying optical Kerr gate," *Appl. Opt.* **41**, 5191 (2002).
9. A. Barty, S. Boutet, M. J. Bogan, S. Hau-Riege, S. Marchesini, K. Sokolowski-Tinten, N. Stojanovic, R. Tobey, H. Ehrke, A. Cavalleri, S. Düsterer, M. Frank, S. Bajt, B. W. Woods, M. M. Seibert, J. Hajdu, R. Treusch, and H. N. Chapman, "Ultrafast single-shot diffraction imaging of nanoscale dynamics," *Nat. Photon.* **2**, 415–419 (2008).
10. T. Pezeril, G. Saini, D. Veysset, S. Kooi, P. Fidkowski, R. Radovitzky, and K. A. Nelson, "Direct Visualization of Laser-Driven Focusing Shock Waves," *Phys. Rev. Lett.* **106**, 214503 (2011).
11. M. Domke, S. Rapp, M. Schmidt, and H. P. Huber, "Ultrafast pump-probe microscopy with high temporal dynamic range," *Opt. Express* **20**, 10330 (2012).
12. T. Pezeril, C. Klieber, V. Shalagatskyi, G. Vaudel, V. Temnov, O. G. Schmidt, and D. Makarov, "Femtosecond imaging of nonlinear acoustics in gold," *Opt. Express* **22**, 4590 (2014).
13. Z. Wang, F. Su, and F. A. Hegmann, "Ultrafast imaging of terahertz Cherenkov waves and transition-like radiation in LiNbO₃," *Opt. Express* **23**, 8073 (2015).
14. D. Veysset, A. A. Maznev, T. Pezeril, S. Kooi, and K. A. Nelson, "Interferometric analysis of laser-driven cylindrically focusing shock waves in a thin liquid layer," *Sci. Rep.* **6**, 24 (2016).
15. D. Veysset, A. A. Maznev, I. A. Veres, T. Pezeril, S. E. Kooi, A. M. Lomonosov, and K. A. Nelson,

- "Acoustical breakdown of materials by focusing of laser-generated Rayleigh surface waves," *Appl. Phys. Lett.* **111**, 031901 (2017).
16. Y.-C. Lin, C.-J. Cheng, and L.-C. Lin, "Tunable time-resolved tick-tock pulsed digital holographic microscopy for ultrafast events," *Opt. Lett.* **42**, 2082 (2017).
 17. D. Veysset, S. E. Kooi, R. Haferssas, M. Hassani-Gangaraj, M. Islam, A. A. Maznev, Y. Chernukha, X. Zhao, K. Nakagawa, D. Martynowych, X. Zhang, A. M. Lomonosov, C. A. Schuh, R. Radovitzky, T. Pezeril, and K. A. Nelson, "Glass fracture by focusing of laser-generated nanosecond surface acoustic waves," *Scr. Mater.* **158**, 42–45 (2019).
 18. T. G. Etoh, C. Vo Le, Y. Hashishin, N. Otsuka, K. Takehara, H. Ohtake, T. Hayashida, and H. Maruyama, "Evolution of Ultra-High-Speed CCD Imagers," *Plasma Fusion Res.* **2**, S1021 (2007).
 19. P. R. Poulin and K. A. Nelson, "Irreversible Organic Crystalline Chemistry Monitored in Real Time," *Science* **313**, 1756–1760 (2006).
 20. D. R. Solli, C. Ropers, P. Koonath, and B. Jalali, "Optical rogue waves," *Nature* **450**, 1054–1057 (2007).
 21. J. M. Dudley, F. Dias, M. Erkintalo, and G. Genty, "Instabilities, breathers and rogue waves in optics," *Nat. Photon.* **8**, 755–764 (2014).
 22. T. C. Wong, M. Rhodes, and R. Trebino, "Single-shot measurement of the complete temporal intensity and phase of supercontinuum," *Optica* **1**, 119 (2014).
 23. R. Kodama, P. A. Norreys, K. Mima, A. E. Dangor, R. G. Evans, H. Fujita, Y. Kitagawa, K. Krushelnick, T. Miyakoshi, N. Miyanaga, T. Norimatsu, S. J. Rose, T. Shozaki, K. Shigemori, A. Sunahara, M. Tampo, K. A. Tanaka, Y. Toyama, T. Yamanaka, and M. Zepf, "Fast heating of ultrahigh-density plasma as a step towards laser fusion ignition," *Nature* **412**, 798–802 (2001).
 24. H. Iwasaki, Y. Ide, M. Harigaya, Y. Kageyama, and I. Fujimura, "Completely Erasable Phase Change Optical Disk," *Jpn. J. Appl. Phys.* **31**, 461–465 (1992).
 25. M. Konishi, H. Santo, Y. Hongo, K. Tajima, M. Hosoi, and T. Saiki, "Ultrafast amorphization in Ge₁₀Sb₂Te₁₃ thin film induced by single femtosecond laser pulse," *Appl. Opt.* **49**, 3470 (2010).
 26. J. Takeda, W. Oba, Y. Minami, T. Saiki, and I. Katayama, "Ultrafast crystalline-to-amorphous phase transition in Ge₂Sb₂Te₅ chalcogenide alloy thin film using single-shot imaging spectroscopy," *Appl. Phys. Lett.* **104**, 261903 (2014).
 27. Y. Katsumata, T. Morita, Y. Morimoto, T. Shintani, and T. Saiki, "Self-organization of a periodic structure between amorphous and crystalline phases in a GeTe thin film induced by femtosecond laser pulse amorphization," *Appl. Phys. Lett.* **105**, 031907 (2014).
 28. R. Akimoto, H. Handa, S. Shindo, Y. Sutou, M. Kuwahara, M. Naruse, and T. Saiki,

- "Implementation of pulse timing discriminator functionality into a GeSbTe/GeCuTe double layer structure," *Opt. Express* **25**, 26825 (2017).
29. H. Yamakawa, T. Miyamoto, T. Morimoto, T. Terashige, H. Yada, N. Kida, M. Suda, H. M. Yamamoto, R. Kato, K. Miyagawa, K. Kanoda, and H. Okamoto, "Mott transition by an impulsive dielectric breakdown," *Nat. Mater.* **16**, 1100–1105 (2017).
 30. Y. Sanari, T. Tachizaki, Y. Saito, K. Makino, P. Fons, A. V. Kolobov, J. Tominaga, K. Tanaka, Y. Kanemitsu, M. Hase, and H. Hirori, "Zener Tunneling Breakdown in Phase-Change Materials Revealed by Intense Terahertz Pulses," *Phys. Rev. Lett.* **121**, 165702 (2018).
 31. R. R. Gattass and E. Mazur, "Femtosecond laser micromachining in transparent materials," *Nat. Photon.* **2**, 219–225 (2008).
 32. M. Sakakura and M. Terazima, "Initial temporal and spatial changes of the refractive index induced by focused femtosecond pulsed laser irradiation inside a glass," *Phys. Rev. B* (2005).
 33. N. Šiaulyš, A. Melninkaitis, and A. Dubietis, "In situ study of two interacting femtosecond filaments in sapphire," *Opt. Lett.* **40**, 2285–2288 (2015).
 34. H. Mikami, C. Lei, N. Nitta, T. Sugimura, T. Ito, Y. Ozeki, and K. Goda, "High-Speed Imaging Meets Single-Cell Analysis," *Chem* **4**, 2278–2300 (2018).
 35. Z. Jiang and X.-C. Zhang, "Electro-optic measurement of THz field pulses with a chirped optical beam," *Appl. Phys. Lett.* **72**, 1945–1947 (1998).
 36. Z. Jiang and X.-C. Zhang, "Single-shot spatiotemporal terahertz field imaging," *Opt. Lett.* **23**, 1114–1116 (1998).
 37. J. Shan, A. S. Weling, E. Knoesel, L. Bartels, M. Bonn, A. Nahata, G. A. Reider, and T. F. Heinz, "Single-shot measurement of terahertz electromagnetic pulses by use of electro-optic sampling," *Opt. Lett.* **25**, 426 (2000).
 38. G. P. Wakeham and K. A. Nelson, "Dual-echelon single-shot femtosecond spectroscopy," *Opt. Lett.* **25**, 505 (2000).
 39. T. Shin, J. W. Wolfson, S. W. Teitelbaum, M. Kandyla, and K. A. Nelson, "Dual echelon femtosecond single-shot spectroscopy," *Rev. Sci. Instrum.* **85**, 083115 (2014).
 40. C. Y. Chien, B. La Fontaine, A. Desparois, Z. Jiang, T. W. Johnston, J. C. Kieffer, H. Pépin, F. Vidal, and H. P. Mercure, "Single-shot chirped-pulse spectral interferometry used to measure the femtosecond ionization dynamics of air," *Opt. Lett.* **25**, 578 (2000).
 41. S. P. Le Blanc, E. W. Gaul, N. H. Matlis, A. Rundquist, and M. C. Downer, "Single-shot measurement of temporal phase shifts by frequency-domain holography," *Opt. Lett.* **25**, 764 (2000).
 42. Y.-H. Cheng, F. Y. Gao, S. W. Teitelbaum, and K. A. Nelson, "Coherent control of optical phonons

- in bismuth," *Phys. Rev. B* **96**, 134302 (2017).
43. Y.-H. Cheng, S. W. Teitelbaum, F. Y. Gao, and K. A. Nelson, "Femtosecond laser amorphization of tellurium," *Phys. Rev. B* **98**, 134112 (2018).
 44. A. Tikan, S. Bielawski, C. Szwaj, S. Randoux, and P. Suret, "Single-shot measurement of phase and amplitude by using a heterodyne time-lens system and ultrafast digital time-holography," *Nat. Photon.* **12**, 228–234 (2018).
 45. M. Kobayashi, Y. Arashida, G. Yamashita, E. Matsubara, M. Ashida, J. A. Johnson, and I. Katayama, "Fast-frame single-shot pump-probe spectroscopy with chirped-fiber Bragg gratings," *Opt. Lett.* **44**, 163 (2019).
 46. G. Mead, I. Katayama, J. Takeda, and G. A. Blake, "An echelon-based single shot optical and terahertz Kerr effect spectrometer," *Rev. Sci. Instrum.* **90**, 053107 (2019).
 47. J.-P. Geindre, P. Audebert, S. Rebibo, and J.-C. Gauthier, "Single-shot spectral interferometry with chirped pulses," *Opt. Lett.* **26**, 1612 (2001).
 48. J. Itatani, F. Quéré, G. L. Yudin, M. Y. Ivanov, F. Krausz, and P. B. Corkum, "Attosecond Streak Camera," *Phys. Rev. Lett.* **88**, 173903 (2002).
 49. N. H. Matlis, S. Reed, S. S. Bulanov, V. Chvykov, G. Kalintchenko, T. Matsuoka, P. Rousseau, V. Yanovsky, A. Maksimchuk, S. Kalmykov, G. Shvets, and M. C. Downer, "Snapshots of laser wakefields," *Nat. Phys.* **2**, 749–753 (2006).
 50. U. Fröhling, M. Wieland, M. Gensch, T. Gebert, B. Schütte, M. Krikunova, R. Kalms, F. Budzyn, O. Grimm, J. Rossbach, E. Plönjes, and M. Drescher, "Single-shot terahertz-field-driven X-ray streak camera," *Nat. Photon.* **3**, 523–528 (2009).
 51. Y. Minami, K. Horiuchi, K. Masuda, J. Takeda, and I. Katayama, "Terahertz dielectric response of photoexcited carriers in Si revealed via single-shot optical-pump and terahertz-probe spectroscopy," *Appl. Phys. Lett.* **107**, 171104 (2015).
 52. J. Zhang, S. Liu, T. Yi, X. Wu, Y. Song, B. Zhang, and Q. Zhong, "Ultrafast single-shot measurement of optical Kerr effect based on supercontinuum pulse," *Rev. Sci. Instrum.* **87**, 043114 (2016).
 53. M. Kobayashi, Y. Minami, C. L. Johnson, P. D. Salmans, N. R. Ellsworth, J. Takeda, J. A. Johnson, and I. Katayama, "High-Acquisition-Rate Single-Shot Pump-Probe Measurements Using Time-Stretching Method," *Sci. Rep.* **6**, 37614 (2016).
 54. M. Buzzi, M. Makita, L. Howald, A. Kleibert, B. Vodungbo, P. Maldonado, J. Raabe, N. Jaouen, H. Redlin, K. Tiedtke, P. M. Oppeneer, C. David, F. Nolting, and J. Lüning, "Single-shot Monitoring of Ultrafast Processes via X-ray Streaking at a Free Electron Laser," *Sci. Rep.* **7**, 7253 (2017).

55. H. Mikami, L. Gao, and K. Goda, "Ultrafast optical imaging technology: principles and applications of emerging methods," *Nanophotonics* **5**, 98–110 (2016).
56. J. Liang and L. V. Wang, "Single-shot ultrafast optical imaging," *Optica* **5**, 1113–1127 (2018).
57. K. Goda, K. K. Tsia, and B. Jalali, "Serial time-encoded amplified imaging for real-time observation of fast dynamic phenomena," *Nature* **458**, 1145–1149 (2009).
58. K. Nakagawa, A. Iwasaki, Y. Oishi, R. Horisaki, A. Tsukamoto, A. Nakamura, K. Hirosawa, H. Liao, T. Ushida, K. Goda, F. Kannari, and I. Sakuma, "Sequentially timed all-optical mapping photography (STAMP)," *Nat. Photon.* **8**, 695–700 (2014).
59. K. Nakagawa, T. Suzuki, and F. Kannari, "Sequentially Timed All-Optical Mapping Photography for Real- Time Monitoring of Laser Ablation: Breakdown and Filamentation in Picosecond and Femtosecond Regimes," in *Laser Ablation - From Fundamentals to Applications*, T. Itina, ed. (InTech, 2017), p. 105–121.
60. T. Suzuki, F. Isa, L. Fujii, K. Hirosawa, K. Nakagawa, K. Goda, I. Sakuma, and F. Kannari, "Sequentially timed all-optical mapping photography (STAMP) utilizing spectral filtering," *Opt. Express* **23**, 30512–30522 (2015).
61. T. Suzuki, R. Hida, Y. Yamaguchi, K. Nakagawa, T. Saiki, and F. Kannari, "Single-shot 25-frame burst imaging of ultrafast phase transition of $\text{Ge}_2\text{Sb}_2\text{Te}_5$ with a sub-picosecond resolution," *Appl. Phys. Express* **10**, 092502 (2017).
62. T. Suzuki, H. Nemoto, K. Takasawa, and F. Kannari, "1000-fps consecutive ultrafast 2D-burst imaging with a sub-nanosecond temporal resolution by a frequency - time encoding of SF-STAMP," *Appl. Phys. A* **126**, 135 (2020).
63. L. Gao, J. Liang, C. Li, and L. V. Wang, "Single-shot compressed ultrafast photography at one hundred billion frames per second," *Nature* **516**, 74–77 (2014).
64. J. Liang, L. Gao, P. Hai, C. Li, and L. V. Wang, "Encrypted Three-dimensional Dynamic Imaging using Snapshot Time-of-flight Compressed Ultrafast Photography," *Sci. Rep.* **5**, 15504 (2015).
65. L. Zhu, Y. Chen, J. Liang, Q. Xu, L. Gao, C. Ma, and L. V. Wang, "Space- and intensity-constrained reconstruction for compressed ultrafast photography," *Optica* **3**, 694 (2016).
66. J. Liang, C. Ma, L. Zhu, Y. Chen, L. Gao, and L. V. Wang, "Single-shot real-time video recording of a photonic Mach cone induced by a scattered light pulse," *Sci. Adv.* **3**, e1601814 (2017).
67. J. Liang, L. Zhu, and L. V. Wang, "Single-shot real-time femtosecond imaging of temporal focusing," *Light Sci. Appl.* **7**, 42 (2018).
68. X. Liu, J. Liu, C. Jiang, F. Vetrone, and J. Liang, "Single-shot compressed optical-streaking ultra-high-speed photography," *Opt. Lett.* **44**, 1387 (2019).

69. T. Kim, J. Liang, L. Zhu, and L. V Wang, "Picosecond-resolution phase-sensitive imaging of transparent objects in a single shot," *Sci. Adv.* **6**, eaay6200 (2020).
70. A. Ehn, J. Bood, Z. Li, E. Berrocal, M. Aldén, and E. Kristensson, "FRAME: femtosecond videography for atomic and molecular dynamics," *Light Sci. Appl.* **6**, e17045 (2017).
71. M. Fujimoto, S. Aoshima, and Y. Tsuchiya, "Multiframe observation of an intense femtosecond optical pulse propagating in air," *Opt. Lett.* **27**, 309 (2002).
72. N. H. Matlis, A. Axley, and W. P. Leemans, "Single-shot ultrafast tomographic imaging by spectral multiplexing," *Nat. Commun.* **3**, 1111 (2012).
73. Z. Li, C.-H. Pai, Y.-Y. Chang, R. Zgadzaj, X. Wang, and M. C. Downer, "Single-shot visualization of evolving, light-speed structures by multiobject-plane phase-contrast imaging," *Opt. Lett.* **38**, 5157 (2013).
74. T. Kakue, J. Yuasa, M. Fujii, P. Xia, T. Tahara, Y. Awatsuji, K. Nishio, S. Ura, T. Kubota, and O. Matoba, "Light-in-Flight Recording by Parallel Phase-Shifting Digital Holography," *Appl. Phys. Express* **6**, 092501 (2013).
75. B. Heshmat, G. Satat, C. Barsi, and R. Raskar, "Single-shot ultrafast imaging using parallax-free alignment with a tilted lenslet array," in *CLEO: 2014* (OSA, 2014), p. STu3E.7.
76. Z. Li, R. Zgadzaj, X. Wang, Y.-Y. Chang, and M. C. Downer, "Single-shot tomographic movies of evolving light-velocity objects," *Nat. Commun.* **5**, 3085 (2014).
77. X. Wang, L. Yan, J. Si, S. Matsuo, H. Xu, and X. Hou, "High-frame-rate observation of single femtosecond laser pulse propagation in fused silica using an echelon and optical polarigraphy technique," *Appl. Opt.* **53**, 8395–8399 (2014).
78. Q.-Y. Yue, Z.-J. Cheng, L. Han, Y. Yang, and C.-S. Guo, "One-shot time-resolved holographic polarization microscopy for imaging laser-induced ultrafast phenomena," *Opt. Express* **25**, 14182 (2017).
79. G. Gao, K. He, J. Tian, C. Zhang, J. Zhang, T. Wang, S. Chen, H. Jia, F. Yuan, L. Liang, X. Yan, S. Li, C. Wang, and F. Yin, "Ultrafast all-optical solid-state framing camera with picosecond temporal resolution," *Opt. Express* **25**, 8721 (2017).
80. G. Gao, J. Tian, T. Wang, K. He, C. Zhang, J. Zhang, S. Chen, H. Jia, F. Yuan, L. Liang, X. Yan, S. Li, C. Wang, and F. Yin, "Ultrafast all-optical imaging technique using low-temperature grown GaAs/Al_xGa_{1-x}As multiple-quantum-well semiconductor," *Phys. Lett. A* **381**, 3594–3598 (2017).
81. C. Guanghua, L. Jianfeng, P. Qixian, L. Shouxian, and L. Jun, "All-optical coaxial framing photography using parallel coherence shutters," *Opt. Lett.* **42**, 415 (2017).
82. P. Sidorenko, O. Lahav, and O. Cohen, "Ptychographic ultrahigh-speed imaging," *Opt. Express* **25**,

- 10997 (2017).
83. B. K. Chen, P. Sidorenko, O. Lahav, O. Peleg, and O. Cohen, "Multiplexed single-shot ptychography," *Opt. Lett.* **43**, 5379 (2018).
 84. D. Veysset, U. Gutiérrez-Hernández, L. Dresselhaus-Cooper, F. De Colle, S. Kooi, K. A. Nelson, P. A. Quinto-Su, and T. Pezeril, "Single-bubble and multibubble cavitation in water triggered by laser-driven focusing shock waves," *Phys. Rev. E* **97**, 053112 (2018).
 85. S. Yeola, D. Kuk, and K.-Y. Kim, "Single-shot ultrafast imaging via spatiotemporal division of femtosecond laser pulses," *J. Opt. Soc. Am. B* **35**, 2822 (2018).
 86. B. Heshmat, M. Tancik, G. Satat, and R. Raskar, "Photography optics in the time dimension," *Nat. Photon.* **12**, 560–566 (2018).
 87. N. Karasawa, "Chirped pulse digital holography for measuring the sequence of ultrafast optical wavefronts," *Opt. Commun.* **413**, 19–23 (2018).
 88. M. Gragston, C. Smith, D. Kartashov, M. N. Shneider, and Z. Zhang, "Single-shot nanosecond-resolution multiframe passive imaging by multiplexed structured image capture," *Opt. Express* **26**, 28441 (2018).
 89. O. Wengrowicz, O. Peleg, B. Loevsky, B. K. Chen, G. I. Haham, U. S. Sainadh, and O. Cohen, "Experimental time-resolved imaging by multiplexed ptychography," *Opt. Express* **27**, 24568 (2019).
 90. L. Dresselhaus-Cooper, J. E. Gorfain, C. T. Key, B. K. Ofori-Okai, S. J. Ali, D. J. Martynowich, A. Gleason, S. Kooi, and K. A. Nelson, "Single-Shot Multi-Frame Imaging of Cylindrical Shock Waves in a Multi-Layered Assembly," *Sci. Rep.* **9**, 1–12 (2019).
 91. Y. Lu, T. T. W. Wong, F. Chen, and L. Wang, "Compressed Ultrafast Spectral-Temporal Photography," *Phys. Rev. Lett.* **122**, 193904 (2019).
 92. Z. E. Davidson, B. Gonzalez-Izquierdo, A. Higginson, K. L. Lancaster, S. D. R. Williamson, M. King, D. Farley, D. Neely, P. McKenna, and R. J. Gray, "An optically multiplexed single-shot time-resolved probe of laser–plasma dynamics," *Opt. Express* **27**, 4416 (2019).
 93. C. Hu, Z. Du, M. Chen, S. Yang, and H. Chen, "Single-shot ultrafast phase retrieval photography," *Opt. Lett.* **44**, 4419 (2019).
 94. H.-Y. Huang, Z.-J. Cheng, Y. Yang, Q.-Y. Yue, and C.-S. Guo, "Single-shot ultrafast sequential holographic imaging with high temporal resolution and a large field of view," *Opt. Lett.* **44**, 4885 (2019).
 95. D. Haffa, J. Bin, M. Speicher, K. Allinger, J. Hartmann, C. Kreuzer, E. Ridente, T. M. Ostermayr, and J. Schreiber, "Temporally Resolved Intensity Contouring (TRIC) for characterization of the

- absolute spatio-temporal intensity distribution of a relativistic, femtosecond laser pulse," *Sci. Rep.* **9**, 7697 (2019).
96. X. Zeng, S. Zheng, Y. Cai, Q. Lin, H. Wang, X. Lu, J. Li, W. Xie, and S. Xu, "Ultrafast Framing Imaging utilizing Multiple Optical-parametric-amplification with High Spatial Resolution and Imaging Rate," arXiv:1907.00518 (2019).
 97. J. Moon, S. Yoon, Y. Lim, and W. Choi, "Single-shot imaging of microscopic dynamic scenes at 5 THz frame rates by time and spatial frequency multiplexing," *Opt. Express* **28**, 4463 (2020).
 98. C. Yang, F. Cao, D. Qi, Y. He, P. Ding, J. Yao, T. Jia, Z. Sun, and S. Zhang, "Hyperspectrally Compressed Ultrafast Photography," *Phys. Rev. Lett.* **124**, 023902 (2020).
 99. "The Edgerton Digital Collections projectle," <http://edgerton-digital-collections.org/>.
 100. C. Lei, B. Guo, Z. Cheng, and K. Goda, "Optical time-stretch imaging: Principles and applications," *Appl. Phys. Rev.* **3**, 011102 (2016).
 101. M. A. Foster, R. Salem, D. F. Geraghty, A. C. Turner-Foster, M. Lipson, and A. L. Gaeta, "Silicon-chip-based ultrafast optical oscilloscope," *Nature* **456**, 81–84 (2008).
 102. K. Goda and B. Jalali, "Dispersive Fourier transformation for fast continuous single-shot measurements," *Nat. Photon.* **7**, 102–112 (2013).
 103. A. Mahjoubfar, D. V. Churkin, S. Barland, N. Broderick, S. K. Turitsyn, and B. Jalali, "Time stretch and its applications," *Nat. Photon.* **11**, 341–351 (2017).
 104. F. Mochizuki, K. Kagawa, S. Okihara, M. Seo, B. Zhang, T. Takasawa, K. Yasutomi, and S. Kawahito, "Single-event transient imaging with an ultra-high-speed temporally compressive multi-aperture CMOS image sensor," *Opt. Express* **24**, 4155 (2016).
 105. T. Etoh, A. Nguyen, Y. Kamakura, K. Shimonomura, T. Le, and N. Mori, "The Theoretical Highest Frame Rate of Silicon Image Sensors," *Sensors* **17**, 483 (2017).
 106. R. Kuroda, S. Sugawa, and M. Suzuki, "Over 100 million frames per second high speed global shutter CMOS image sensor," in *32nd International Congress on High-Speed Imaging and Photonics*, M. Versluis and E. Stride, eds. (SPIE, 2019), Vol. 11051, p. 12.
 107. S. Dillavou, S. M. Rubinstein, and J. M. Kolinski, "Virtual frame technique: ultrafast imaging with any camera," *Opt. Express* **27**, 8112 (2019).
 108. A. Farina, A. Candeo, A. Dalla Mora, A. Bassi, R. Lussana, F. Villa, G. Valentini, S. Arridge, and C. D'Andrea, "Novel time-resolved camera based on compressed sensing," *Opt. Express* **27**, 31889 (2019).
 109. L. Cester, A. Lyons, M. Braidotti, and D. Faccio, "Time-of-Flight Imaging at 10 ps Resolution with an ICCD Camera," *Sensors* **19**, 180 (2019).

110. T. K. Cheng, S. D. Brorson, A. S. Kazeroonian, J. S. Moodera, G. Dresselhaus, M. S. Dresselhaus, and E. P. Ippen, "Impulsive excitation of coherent phonons observed in reflection in bismuth and antimony," *Appl. Phys. Lett.* **57**, 1004–1006 (1990).
111. H. J. Zeiger, J. Vidal, T. K. Cheng, E. P. Ippen, G. Dresselhaus, and M. S. Dresselhaus, "Theory for displacive excitation of coherent phonons," *Phys. Rev. B* **45**, 768–778 (1992).
112. C. Lefebvre, T. T. Nguyen-Dang, F. Dion, M. J. J. Vrakking, V. N. Serov, and O. Atabek, "Attosecond pump-probe transition-state spectroscopy of laser-induced molecular dissociative ionization: Adiabatic versus nonadiabatic dressed-state dynamics," *Phys. Rev. A* **88**, 053416 (2013).
113. M. Lara-Astiaso, M. Galli, A. Trabattoni, A. Palacios, D. Ayuso, F. Frassetto, L. Poletto, S. De Camillis, J. Greenwood, P. Decleva, I. Tavernelli, F. Calegari, M. Nisoli, and F. Martín, "Attosecond Pump–Probe Spectroscopy of Charge Dynamics in Tryptophan," *J. Phys. Chem. Lett.* **9**, 4570–4577 (2018).
114. Y. Yamaguchi, R. Hida, T. Suzuki, F. Isa, K. Yoshikiyo, L. Fujii, H. Nemoto, and F. Kannari, "Shaping and amplification of wavelength-tunable mid-infrared femtosecond pulses generated by intra-pulse difference-frequency mixing with spectral focusing," *J. Opt. Soc. Am. B* **35**, C1–C7 (2018).
115. M. Rini, R. Tobey, N. Dean, J. Itatani, Y. Tomioka, Y. Tokura, R. W. Schoenlein, and A. Cavalleri, "Control of the electronic phase of a manganite by mode-selective vibrational excitation," *Nature* **449**, 72–74 (2007).
116. A. J. DeMaria, D. A. Stetser, and H. Heynau, "SELF MODE-LOCKING OF LASERS WITH SATURABLE ABSORBERS," *Appl. Phys. Lett.* **8**, 174–176 (1966).
117. F. O’Neill, "Picosecond pulses from a passively mode-locked cw dye laser," *Opt. Commun.* **6**, 360–363 (1972).
118. H. P. Weber, "Generation and Measurement of Ultrashort Light Pulses," *J. Appl. Phys.* **39**, 6041–6044 (1968).
119. E. P. Ippen and C. V. Shank, "Dynamic spectroscopy and subpicosecond pulse compression," *Appl. Phys. Lett.* **27**, 488–490 (1975).
120. M. A. Duguay and J. W. Hansen, "AN ULTRAFast LIGHT GATE," *Appl. Phys. Lett.* **15**, 192–194 (1969).
121. C. V. Shank and E. P. Ippen, "Anisotropic absorption saturation with picosecond pulses," *Appl. Phys. Lett.* **26**, 62–63 (1975).
122. P. P. Ho and R. R. Alfano, "Optical Kerr effect in liquids," *Phys. Rev. A* **20**, 2170–2187 (1979).

123. Hamamatsu Photonics K.K., "Guide to Streak Cameras," https://www.hamamatsu.com/resources/pdf/sys/SHSS0006E_STREAK.pdf.
124. Hamamatsu Photonics K.K., "FESCA-100 femtosecond streak camera C11853-01," https://www.hamamatsu.com/resources/pdf/sys/SHSS0022E_FESCA-100.pdf.
125. H. Fattahi, H. G. Barros, M. Gorjan, T. Nubbemeyer, B. Alsaif, C. Y. Teisset, M. Schultze, S. Prinz, M. Haefner, M. Ueffing, A. Alismail, L. Vamos, A. Schwarz, O. Pronin, J. Brons, X. T. Geng, G. Arisholm, M. Ciappina, V. S. Yakovlev, D.-E. Kim, A. M. Azzeer, N. Karpowicz, D. Sutter, Z. Major, T. Metzger, and F. Krausz, "Third-generation femtosecond technology," *Optica* **1**, 45–63 (2014).
126. C. Manzoni, O. D. Mücke, G. Cirmi, S. Fang, J. Moses, S.-W. Huang, K.-H. Hong, G. Cerullo, and F. X. Kärtner, "Coherent pulse synthesis: towards sub-cycle optical waveforms," *Laser Photon. Rev.* **9**, 129–171 (2015).
127. D. L. Donoho, "Compressed sensing," *IEEE Trans. Inf. Theory* **52**, 1289–1306 (2006).
128. G. Satat, M. Tancik, and R. Raskar, "Lensless Imaging With Compressive Ultrafast Sensing," *IEEE Trans. Comput. Imaging* **3**, 398–407 (2017).
129. M. P. Edgar, G. M. Gibson, and M. J. Padgett, "Principles and prospects for single-pixel imaging," *Nat. Photon.* **13**, 13–20 (2019).
130. W. Zhao, H. Chen, Y. Yuan, H. Zheng, J. Liu, Z. Xu, and Y. Zhou, "Ultrahigh-Speed Color Imaging with Single-Pixel Detectors at Low Light Level," *Phys. Rev. Appl.* **12**, 034049 (2019).
131. Y. Ohki, "News from Japan," *IEEE Electr. Insul. Mag.* **35**, 41–43 (2019).
132. F. Xing, H. Chen, C. Lei, M. Chen, S. Yang, and S. Xie, "A 2-GHz discrete-spectrum waveband-division microscopic imaging system," *Opt. Commun.* **338**, 22–26 (2015).
133. T. T. W. Wong, A. K. S. Lau, K. K. Y. Ho, M. Y. H. Tang, J. D. F. Robles, X. Wei, A. C. S. Chan, A. H. L. Tang, E. Y. Lam, K. K. Y. Wong, G. C. F. Chan, H. C. Shum, and K. K. Tsia, "Asymmetric-detection time-stretch optical microscopy (ATOM) for ultrafast high-contrast cellular imaging in flow," *Sci. Rep.* **4**, 3656 (2015).
134. C. L. Chen, A. Mahjoubfar, and B. Jalali, "Optical data compression in time stretch imaging," *PLoS One* **10**, 1–11 (2015).
135. C. Lei, Y. Wu, A. C. Sankaranarayanan, S.-M. Chang, B. Guo, N. Sasaki, H. Kobayashi, C.-W. Sun, Y. Ozeki, and K. Goda, "GHz Optical Time-Stretch Microscopy by Compressive Sensing," *IEEE Photonics J.* **9**, 1–8 (2017).
136. C. Kim, A. Mahjoubfar, J. C. K. Chan, A. Yazaki, Y.-C. Noh, and B. Jalali, "Matrix Analysis of Warped Stretch Imaging," *Sci. Rep.* **7**, 11150 (2017).

137. S. Tan, X. Wei, B. Li, Q. T. K. Lai, K. K. Tsia, and K. K. Y. Wong, "Ultrafast optical imaging at 2.0 μm through second-harmonic-generation-based time-stretch at 1.0 μm ," *Opt. Lett.* **43**, 3822 (2018).
138. C. Kong, X. Wei, J. Kang, S. Tan, K. Tsia, and K. K. Y. Wong, "Ultra-broadband spatiotemporal sweeping device for high-speed optical imaging," *Opt. Lett.* **43**, 3546 (2018).
139. C. Lei, H. Kobayashi, Y. Wu, M. Li, A. Isozaki, A. Yasumoto, H. Mikami, T. Ito, N. Nitta, T. Sugimura, M. Yamada, Y. Yatomi, D. Di Carlo, Y. Ozeki, and K. Goda, "High-throughput imaging flow cytometry by optofluidic time-stretch microscopy," *Nat. Protoc.* **13**, 1603–1631 (2018).
140. Y. Duan, X. Dong, N. Yang, C. Zhang, K. K. Y. Wong, and X. Zhang, "Temporally structured illumination for ultrafast time-stretch microscopy," *Opt. Lett.* **44**, 4634 (2019).
141. E. D. Diebold, B. W. Buckley, D. R. Gossett, and B. Jalali, "Digitally synthesized beat frequency multiplexing for sub-millisecond fluorescence microscopy," *Nat. Photon.* **7**, 806–810 (2013).
142. H. Mikami, J. Harmon, H. Kobayashi, S. Hamad, Y. Wang, O. Iwata, K. Suzuki, T. Ito, Y. Aisaka, N. Kutsuna, K. Nagasawa, H. Watarai, Y. Ozeki, and K. Goda, "Ultrafast confocal fluorescence microscopy beyond the fluorescence lifetime limit," *Optica* **5**, 117 (2018).
143. H. Kanno, H. Mikami, Y. Kaya, Y. Ozeki, and K. Goda, "Simple, stable, compact implementation of frequency-division-multiplexed microscopy by inline interferometry," *Opt. Lett.* **44**, 467 (2019).
144. J. Wu, Y.-Q. Xu, J. Xu, X. Wei, A. C. Chan, A. H. Tang, A. K. Lau, B. M. Chung, H. Cheung Shum, E. Y. Lam, K. K. Wong, and K. K. Tsia, "Ultrafast laser-scanning time-stretch imaging at visible wavelengths," *Light Sci. Appl.* **6**, e16196 (2017).
145. J. Wu, A. H. L. Tang, A. T. Y. Mok, W. Yan, G. C. F. Chan, K. K. Y. Wong, and K. K. Tsia, "Multi-MHz laser-scanning single-cell fluorescence microscopy by spatiotemporally encoded virtual source array," *Biomed. Opt. Express* **8**, 4160 (2017).
146. W. Yan, J. Wu, K. K. Y. Wong, and K. K. Tsia, "A high-throughput all-optical laser-scanning imaging flow cytometer with biomolecular specificity and subcellular resolution," *J. Biophotonics* **11**, e201700178 (2018).
147. S. Tan, X. Wei, J. Wu, L. Yang, K. K. Tsia, and K. K. Y. Wong, "Flexible pulse-stretching for a swept source at 2.0 μm using free-space angular-chirp-enhanced delay," *Opt. Lett.* **43**, 102–105 (2018).
148. Y. Xu and S. G. Murdoch, "Real-time spectral analysis of ultrafast pulses using a free-space angular chirp-enhanced delay," *Opt. Lett.* **44**, 3697 (2019).
149. Y. Ren, J. Wu, Q. T. K. Lai, H. M. Lai, D. M. D. Siu, W. Wu, K. K. Y. Wong, and K. K. Tsia, "Parallelized volumetric fluorescence microscopy with a reconfigurable coded incoherent

- light-sheet array," *Light Sci. Appl.* **9**, 8 (2020).
150. C. Deeney and P. Choi, "Novel time and two-dimensional space-resolved x-ray imaging technique," *Rev. Sci. Instrum.* **60**, 3558–3559 (1989).
 151. H. Shiraga, N. Miyanaga, M. Heya, M. Nakasuji, Y. Aoki, H. Azechi, T. Yamanaka, and K. Mima, "Ultrafast two-dimensional x-ray imaging with x-ray streak cameras for laser fusion research (invited)," *Rev. Sci. Instrum.* **68**, 745–749 (1997).
 152. H. Shiraga, M. Nakasuji, M. Heya, and N. Miyanaga, "Two-dimensional sampling-image x-ray streak camera for ultrafast imaging of inertial confinement fusion plasmas," *Rev. Sci. Instrum.* **70**, 620–623 (1999).
 153. A. Velten, D. Wu, A. Jarabo, B. Masia, C. Barsi, C. Joshi, E. Lawson, M. Bawendi, D. Gutierrez, and R. Raskar, "Femto-photography: capturing and visualizing the propagation of light," *ACM Trans. Graph.* **32**, 44 (2013).
 154. N. Abramson, "Light-in-flight recording by holography," *Opt. Lett.* **3**, 121 (1978).
 155. T. Kubota, K. Komai, M. Yamagiwa, and Y. Awatsuji, "Moving picture recording and observation of three-dimensional image of femtosecond light pulse propagation," *Opt. Express* **15**, 14348 (2007).
 156. G. Gariepy, N. Krstajić, R. Henderson, C. Li, R. R. Thomson, G. S. Buller, B. Heshmat, R. Raskar, J. Leach, and D. Faccio, "Single-photon sensitive light-in-flight imaging," *Nat. Commun.* **6**, 6021 (2015).
 157. T. Inoue, A. Matsunaka, A. Funahashi, T. Okuda, K. Nishio, and Y. Awatsuji, "Spatiotemporal observations of light propagation in multiple polarization states," *Opt. Lett.* **44**, 2069 (2019).
 158. H. Nemoto, T. Suzuki, Y. Yamaguchi, and F. Kannari, "Single-shot Ultrafast Burst Imaging by Spectrally Sweeping Pulse Train with 100-ps Interval," in *CLEO Pacific Rim Conference (OSA, 2018)*, p. Th1B.3.
 159. N. Yokota and H. Yasaka, "Multi-wavelength discrete pulse train generation using chromatic aberration of time lens for ultrafast single-shot optical imaging," *Opt. Rev.* **26**, 713–718 (2019).
 160. K. Hashimoto, H. Mizuno, K. Nakagawa, R. Horisaki, A. Iwasaki, F. Kannari, I. Sakuma, and K. Goda, "High-speed multispectral videography with a periscope array in a spectral shaper," *Opt. Lett.* **39**, 6942–6945 (2014).
 161. M. Tamamitsu, Y. Kitagawa, K. Nakagawa, R. Horisaki, Y. Oishi, S. Morita, Y. Yamagata, K. Motohara, and K. Goda, "Spectrum slicer for snapshot spectral imaging," *Opt. Eng.* **54**, 123115 (2015).
 162. J. P. Gordon, H. J. Zeiger, and C. H. Townes, "Molecular Microwave Oscillator and New Hyperfine

- Structure in the Microwave Spectrum of NH_3 ," *Phys. Rev.* **95**, 282–284 (1954).
163. J. P. Gordon, H. J. Zeiger, and C. H. Townes, "The Maser—New Type of Microwave Amplifier, Frequency Standard, and Spectrometer," *Phys. Rev.* **99**, 1264–1274 (1955).
 164. A. L. Schawlow and C. H. Townes, "Infrared and Optical Masers," *Phys. Rev.* **112**, 1940–1949 (1958).
 165. T. H. Maiman, "Optical and Microwave-Optical Experiments in Ruby," *Phys. Rev. Lett.* **4**, 564–566 (1960).
 166. A. Javan, W. R. Bennett, and D. R. Herriott, "Population Inversion and Continuous Optical Maser Oscillation in a Gas Discharge Containing a He-Ne Mixture," *Phys. Rev. Lett.* **6**, 106–110 (1961).
 167. R. N. Hall, G. E. Fenner, J. D. Kingsley, T. J. Soltys, and R. O. Carlson, "Coherent Light Emission From GaAs Junctions," *Phys. Rev. Lett.* **9**, 366–368 (1962).
 168. N. Holonyak and S. F. Bevacqua, "COHERENT (VISIBLE) LIGHT EMISSION FROM $\text{Ga}(\text{As}_{1-x}\text{P}_x)$ JUNCTIONS," *Appl. Phys. Lett.* **1**, 82–83 (1962).
 169. C. K. N. Patel, "Continuous-Wave Laser Action on Vibrational-Rotational Transitions of CO_2 ," *Phys. Rev.* **136**, A1187–A1193 (1964).
 170. J. E. Geusic, H. M. Marcos, and L. G. Van Uitert, "Laser oscillations in Nd-doped yttrium aluminum, yttrium gallium and gadolinium garnets," *Appl. Phys. Lett.* **4**, 182–184 (1964).
 171. P. P. Sorokin and J. R. Lankard, "Stimulated Emission Observed from an Organic Dye, Chloro-aluminum Phthalocyanine," *IBM J. Res. Dev.* **10**, 162–163 (1966).
 172. N. G. Basov, E. M. Balashov, O. V. Bogdankevitch, V. A. Danilychev, G. N. Kashnikov, N. P. Lantsov, and D. D. Khodkevitch, "Luminescence of condensed Xe, Kr, Ar and their mixtures in vacuum region of spectrum under excitation by fast electrons," *J. Lumin.* **1–2**, 834–841 (1970).
 173. G. Bret and F. Gires, "Giant-pulse laser and light amplifier using variable transmission coefficient glasses as light switches," *Appl. Phys. Lett.* **4**, 175–176 (1964).
 174. H. W. Mocker and R. J. Collins, "Mode Competition and Self-Locking Effects in a Q-Switched Ruby Laser," *Appl. Phys. Lett.* **7**, 270–273 (1965).
 175. W. Schmidt and F. P. Schafer, "Self-mode-locking of dye-lasers with saturable absorbers," *Phys. Lett.* **26A**, 558–559 (1968).
 176. E. P. Ippen, C. V. Shank, and A. Dienes, "Passive mode locking of the cw dye laser," *Appl. Phys. Lett.* **21**, 348–350 (1972).
 177. C. V. Shank and E. P. Ippen, "Subpicosecond kilowatt pulses from a mode-locked cw dye laser," *Appl. Phys. Lett.* **24**, 373–375 (1974).
 178. R. L. Fork, B. I. Greene, and C. V. Shank, "Generation of optical pulses shorter than 0.1 psec by

- colliding pulse mode locking," *Appl. Phys. Lett.* **38**, 671–672 (1981).
179. D. E. Spence, J. M. Evans, W. E. Sleat, and W. Sibbett, "Regeneratively initiated self-mode-locked Ti:sapphire laser," *Opt. Lett.* **16**, 1762 (1991).
180. H. A. Haus, "Mode-locking of lasers," *IEEE J. Sel. Top. Quantum Electron.* **6**, 1173–1185 (2000).
181. P. W. Roth, A. J. Maclean, D. Burns, and A. J. Kemp, "Directly diode-laser-pumped Ti:sapphire laser," *Opt. Lett.* **34**, 3334–3336 (2009).
182. S. Sawai, A. Hosaka, H. Kawauchi, K. Hirosawa, and F. Kannari, "Demonstration of a Ti:sapphire mode-locked laser pumped directly with a green diode laser," *Appl. Phys. Express* **7**, 022702 (2014).
183. K. Gürel, V. J. Wittwer, M. Hoffmann, C. J. Saraceno, S. Hakobyan, B. Resan, A. Rohrbacher, K. Weingarten, S. Schilt, and T. Südmeyer, "Green-diode-pumped femtosecond Ti:Sapphire laser with up to 450 mW average power," *Opt. Express* **23**, 30043–30048 (2015).
184. R. Sawada, H. Tanaka, N. Sugiyama, and F. Kannari, "Wavelength-multiplexed pumping with 478- and 520-nm indium gallium nitride laser diodes for Ti:sapphire laser," *Appl. Opt.* **56**, 1654 (2017).
185. A. M. Weiner, *Ultrafast Optics* (John Wiley & Sons, Inc., 2009).
186. A. M. Weiner, "Ultrafast optical pulse shaping: A tutorial review," *Opt. Commun.* **284**, 3669–3692 (2011).
187. A. Monmayrant, S. Weber, and B. Chatel, "A newcomer's guide to ultrashort pulse shaping and characterization," *J. Phys. B At. Mol. Opt. Phys.* **43**, 103001 (2010).
188. I. A. Walmsley and C. Dorrer, "Characterization of ultrashort electromagnetic pulses," *Adv. Opt. Photonics* **1**, 308 (2009).
189. J. A. Armstrong, "MEASUREMENT OF PICOSECOND LASER PULSE WIDTHS," *Appl. Phys. Lett.* **10**, 16–18 (1967).
190. J.-C. M. Diels, J. J. Fontaine, I. C. McMichael, and F. Simoni, "Control and measurement of ultrashort pulse shapes (in amplitude and phase) with femtosecond accuracy," *Appl. Opt.* **24**, 1270 (1985).
191. K. Naganuma, K. Mogi, and H. Yamada, "General method for ultrashort light pulse chirp measurement," *IEEE J. Quantum Electron.* **25**, 1225–1233 (1989).
192. L. Lepetit, G. Chériaux, and M. Joffre, "Linear techniques of phase measurement by femtosecond spectral interferometry for applications in spectroscopy," *J. Opt. Soc. Am. B* **12**, 2467 (1995).
193. D. Meshulach, D. Yelin, and Y. Silberberg, "Real-time spatial–spectral interference measurements of ultrashort optical pulses," *J. Opt. Soc. Am. B* **14**, 2095 (1997).
194. T. Tanabe, H. Tanabe, Y. Teramura, and F. Kannari, "Spatiotemporal measurements based on

- spatial spectral interferometry for ultrashort optical pulses shaped by a Fourier pulse shaper," *J. Opt. Soc. Am. B* **19**, 2795–2802 (2002).
195. R. Trebino and D. J. Kane, "Using phase retrieval to measure the intensity and phase of ultrashort pulses: frequency-resolved optical gating," *J. Opt. Soc. Am. A* **10**, 1101–1111 (1993).
 196. R. Trebino, P. Bowlan, P. Gabolde, X. Gu, S. Akturk, and M. Kimmel, "Simple devices for measuring complex ultrashort pulses," *Laser Photonics Rev.* **3**, 314–342 (2009).
 197. R. Trebino, "Measuring the seemingly immeasurable," *Nat. Photon.* **5**, 189–192 (2011).
 198. C. Iaconis and I. a Walmsley, "Spectral phase interferometry for direct electric-field reconstruction of ultrashort optical pulses," *Opt. Lett.* **23**, 792 (1998).
 199. M. E. Anderson, A. Monmayrant, S.-P. Gorza, P. Wasylczyk, and I. A. Walmsley, "SPIDER: A decade of measuring ultrashort pulses," *Laser Phys. Lett.* **5**, 259–266 (2008).
 200. P. Maine, D. Strickland, P. Bado, M. Pessot, and G. Mourou, "Generation of Ultrahigh Peak Power Pulses by Chirped Pulse Amplification," *IEEE J. Quantum Electron.* **24**, 398–403 (1988).
 201. O. E. Martinez, "3000 Times Grating Compressor with Positive Group Velocity Dispersion : Application to Fiber Compensation in 1.3-1.6 μm Region," *IEEE J. Quantum Electron.* **QE-23**, 59–64 (1987).
 202. B. E. Lemoff and C. P. J. Barty, "Quintic-phase-limited, spatially uniform expansion and recompression of ultrashort optical pulses," *Opt. Lett.* **18**, 1651–1653 (1993).
 203. G. Cheriaux, P. Rousseau, F. Salin, J. P. Chambaret, B. Walker, and L. F. Dimauro, "Aberration-free stretcher design for ultrashort-pulse amplification," *Opt. Lett.* **21**, 414–416 (1996).
 204. J. Jiang, Z. Zhang, and T. Hasama, "Evaluation of chirped-pulse-amplification systems with Offner triplet telescope stretchers," *J. Opt. Soc. Am. B* **19**, 678–683 (2002).
 205. S. D. Brorson and H. A. Haus, "Diffraction gratings and geometrical optics," *J. Opt. Soc. Am. B* **5**, 247 (1988).
 206. G. Vaillancourt, T. B. Norris, J. S. Coe, P. Bado, and G. A. Mourou, "Operation of a 1-kHz pulse-pumped Ti:sapphire regenerative amplifier," *Opt. Lett.* **15**, 317 (1990).
 207. W. H. Lowdermilk and J. E. Murray, "The multipass amplifier: Theory and numerical analysis," *J. Appl. Phys.* **51**, 2436 (1980).
 208. C. Le Blanc, G. Grillon, J. P. Chambaret, A. Migus, and A. Antonetti, "Compact and efficient multipass Ti: sapphire system for femtosecond chirped-pulse amplification at the terawatt level," *Opt. Lett.* **18**, 140–142 (1993).
 209. E. B. Treacy, "Optical Pulse Comprssion With Diffraction Gratings," *IEEE J. Quantum Electron.* **QE-5**, 454–458 (1969).

210. P. Gabolde and R. Trebino, "Single-shot measurement of the full spatio-temporal field of ultrashort pulses with multi-spectral digital holography," *Opt. Express* **14**, 11460–11467 (2006).
211. P. Gabolde and R. Trebino, "Single-frame measurement of the complete spatiotemporal intensity and phase of ultrashort laser pulses using wavelength-multiplexed digital holography," *J. Opt. Soc. Am. B* **25**, A25–A33 (2008).
212. Z. Guang, M. Rhodes, M. Davis, and R. Trebino, "Complete characterization of a spatiotemporally complex pulse by an improved single-frame pulse-measurement technique," *J. Opt. Soc. Am. B* **31**, 2736–2743 (2014).
213. Z. Guang, M. Rhodes, and R. Trebino, "Measurement of the ultrafast lighthouse effect using a complete spatiotemporal pulse-characterization technique," *J. Opt. Soc. Am. B* **33**, 1955–1962 (2016).
214. P. Zhu, R. Jafari, T. Jones, and R. Trebino, "Complete measurement of spatiotemporally complex multi-spatial-mode ultrashort pulses from multimode optical fibers using delay-scanned wavelength-multiplexed holography," *Opt. Express* **25**, 24015 (2017).
215. Z. Guang, M. Rhodes, and R. Trebino, "Measuring spatiotemporal ultrafast field structures of pulses from multimode optical fibers," *Appl. Opt.* **56**, 3319 (2017).
216. S. Akturk, M. Kimmel, P. O'Shea, and R. Trebino, "Measuring spatial chirp in ultrashort pulses using single-shot Frequency-Resolved Optical Gating," *Opt. Express* **11**, 68–78 (2003).
217. S. Akturk, M. Kimmel, P. O'Shea, and R. Trebino, "Measuring pulse-front tilt in ultrashort pulses using GRENOUILLE," *Opt. Express* **11**, 491–501 (2003).
218. P. H. Lissberger and W. L. Wilcock, "Properties of All-Dielectric Interference Filters II Filters in Parallel Beams of Light Incident Obliquely and in Convergent Beams," *J. Opt. Soc. Am.* **49**, 126 (1959).
219. T. Suzuki, R. Hida, F. Isa, R. Ueda, and F. Kannari, "Single-shot Multispectral Imaging and Ultrafast 2D-imaging by Sequentially Timed All-optical Mapping Photography utilizing Spectral Filtering (SF-STAMP) system," in *Imaging and Applied Optics 2016* (OSA, 2016), p. IW1E.3.
220. M. Tamamitsu, K. Nakagawa, R. Horisaki, A. Iwasaki, Y. Oishi, A. Tsukamoto, F. Kannari, I. Sakuma, and K. Goda, "Design for sequentially timed all-optical mapping photography with optimum temporal performance," *Opt. Lett.* **40**, 633–636 (2015).
221. X. Mao, S. S. Mao, and R. E. Russo, "Imaging femtosecond laser-induced electronic excitation in glass," *Appl. Phys. Lett.* **82**, 697–699 (2003).
222. X.-L. Liu, X. Lu, X. Liu, T.-T. Xi, F. Liu, J.-L. Ma, and J. Zhang, "Tightly focused femtosecond laser pulse in air: from filamentation to breakdown," *Opt. Express* **18**, 26007 (2010).

223. W. Hu, Y. C. Shin, and G. King, "Early-stage plasma dynamics with air ionization during ultrashort laser ablation of metal," *Phys. Plasmas* **18**, 093302 (2011).
224. H. Zhang, F. Zhang, X. Du, G. Dong, and J. Qiu, "Influence of laser-induced air breakdown on femtosecond laser ablation of aluminum," *Opt. Express* **23**, 1370–1376 (2015).
225. A. V. Kolobov, P. Fons, A. I. Frenkel, A. L. Ankudinov, J. Tominaga, and T. Uruga, "Understanding the phase-change mechanism of rewritable optical media," *Nat. Mater.* **3**, 703–708 (2004).
226. A. V. Kolobov, A. S. Mishchenko, P. Fons, S. M. Yakubenya, and J. Tominaga, "A possible mechanism of ultrafast amorphization in phase-change memory alloys: an ion slingshot from the crystalline to amorphous position," *J. Phys. Condens. Matter* **19**, 455209 (2007).
227. M. Hase, P. Fons, K. Mitrofanov, A. V. Kolobov, and J. Tominaga, "Femtosecond structural transformation of phase-change materials far from equilibrium monitored by coherent phonons," *Nat. Commun.* **6**, 8367 (2015).
228. M. Hada, W. Oba, M. Kuwahara, I. Katayama, T. Saiki, J. Takeda, and K. G. Nakamura, "Ultrafast time-resolved electron diffraction revealing the nonthermal dynamics of near-UV photoexcitation-induced amorphization in $\text{Ge}_2\text{Sb}_2\text{Te}_5$," *Sci. Rep.* **5**, 13530 (2015).
229. E. Matsubara, S. Okada, T. Ichitsubo, T. Kawaguchi, A. Hirata, P. F. Guan, K. Tokuda, K. Tanimura, T. Matsunaga, M. W. Chen, and N. Yamada, "Initial Atomic Motion Immediately Following Femtosecond-Laser Excitation in Phase-Change Materials," *Phys. Rev. Lett.* **117**, 135501 (2016).
230. S. Raoux, "Phase Change Materials," *Annu. Rev. Mater. Res.* **39**, 25–48 (2009).
231. S.-Y. Kim, S. J. Kim, H. Seo, and M. R. Kim, "Variation of the complex refractive indices with Sb-addition in Ge-Sb-Te alloy and their wavelength dependence," in *Proc. SPIE*, S. R. Kubota, T. D. Milster, and P. J. Wehrenberg, eds. (1998), Vol. 3401, pp. 112–115.
232. N. Hagen and M. W. Kudenov, "Review of snapshot spectral imaging technologies," *Opt. Eng.* **52**, 090901 (2013).
233. L. Gao and L. V. Wang, "A review of snapshot multidimensional optical imaging: Measuring photon tags in parallel," *Phys. Rep.* **616**, 1–37 (2016).
234. J. Shi, Y. Bie, W. Chen, S. Fang, J. Han, Z. Cao, T. Taniguchi, K. Watanabe, V. Bulović, E. Kaxiras, P. Jarillo-Herrero, and K. A. Nelson, "Terahertz-driven irreversible topological phase transition in two-dimensional MoTe_2 ," arXiv:1910.13609 (2019).
235. A. V. Kolobov, P. Fons, and J. Tominaga, "Electronic excitation-induced semiconductor-to-metal transition in monolayer MoTe_2 ," *Phys. Rev. B* **94**, 094114 (2016).

236. S. Manzeli, D. Ovchinnikov, D. Pasquier, O. V. Yazyev, and A. Kis, "2D transition metal dichalcogenides," *Nat. Rev. Mater.* **2**, 17033 (2017).
237. J. A. Wilson and A. D. Yoffe, "The transition metal dichalcogenides discussion and interpretation of the observed optical, electrical and structural properties," *Adv. Phys.* **18**, 193–335 (1969).
238. D. N. Basov, R. D. Averitt, and D. Hsieh, "Towards properties on demand in quantum materials," *Nat. Mater.* **16**, 1077–1088 (2017).
239. X. Qian, J. Liu, L. Fu, and J. Li, "Quantum spin Hall effect in two-dimensional transition metal dichalcogenides," *Science* **346**, 1344–1347 (2014).
240. S. Cho, S. Kim, J. H. Kim, J. Zhao, J. Seok, D. H. Keum, J. Baik, D.-H. Choe, K. J. Chang, K. Suenaga, S. W. Kim, Y. H. Lee, and H. Yang, "Phase patterning for ohmic homojunction contact in MoTe_2 ," *Science* **349**, 625–628 (2015).
241. D. H. Keum, S. Cho, J. H. Kim, D.-H. Choe, H.-J. Sung, M. Kan, H. Kang, J.-Y. Hwang, S. W. Kim, H. Yang, K. J. Chang, and Y. H. Lee, "Bandgap opening in few-layered monoclinic MoTe_2 ," *Nat. Phys.* **11**, 482–486 (2015).
242. L. Zhou, A. Zubair, Z. Wang, X. Zhang, F. Ouyang, K. Xu, W. Fang, K. Ueno, J. Li, T. Palacios, J. Kong, and M. S. Dresselhaus, "Synthesis of High-Quality Large-Area Homogenous 1T' MoTe_2 from Chemical Vapor Deposition," *Adv. Mater.* **28**, 9526–9531 (2016).
243. S.-Y. Chen, C. H. Naylor, T. Goldstein, A. T. C. Johnson, and J. Yan, "Intrinsic Phonon Bands in High-Quality Monolayer T' Molybdenum Ditelluride," *ACS Nano* **11**, 814–820 (2017).
244. Y. Wang, J. Xiao, H. Zhu, Y. Li, Y. Alsaied, K. Y. Fong, Y. Zhou, S. Wang, W. Shi, Y. Wang, A. Zettl, E. J. Reed, and X. Zhang, "Structural phase transition in monolayer MoTe_2 driven by electrostatic doping," *Nature* **550**, 487–491 (2017).
245. J. Hebling, G. Almasi, I. Kozma, and J. Kuhl, "Velocity matching by pulse front tilting for large area THz-pulse generation," *Opt. Express* **10**, 1161 (2002).
246. K.-L. Yeh, M. C. Hoffmann, J. Hebling, and K. A. Nelson, "Generation of 10 μJ ultrashort terahertz pulses by optical rectification," *Appl. Phys. Lett.* **90**, 171121 (2007).
247. J. Hebling, K.-L. Yeh, M. C. Hoffmann, B. Bartal, and K. A. Nelson, "Generation of high-power terahertz pulses by tilted-pulse-front excitation and their application possibilities," *J. Opt. Soc. Am. B* **25**, B6–B19 (2008).
248. H. Hirori, A. Doi, F. Blanchard, and K. Tanaka, "Single-cycle terahertz pulses with amplitudes exceeding 1 MV/cm generated by optical rectification in LiNbO_3 ," *Appl. Phys. Lett.* **98**, 091106 (2011).
249. M. Liu, H. Y. Hwang, H. Tao, A. C. Strikwerda, K. Fan, G. R. Keiser, A. J. Sternbach, K. G. West,

- S. Kittiwatanakul, J. Lu, S. A. Wolf, F. G. Omenetto, X. Zhang, K. A. Nelson, and R. D. Averitt, "Terahertz-field-induced insulator-to-metal transition in vanadium dioxide metamaterial," *Nature* **487**, 345–348 (2012).
250. T. Kampfrath, K. Tanaka, and K. A. Nelson, "Resonant and nonresonant control over matter and light by intense terahertz transients," *Nat. Photon.* **7**, 680–690 (2013).
251. S. Ohkoshi, K. Imoto, A. Namai, M. Yoshikiyo, S. Miyashita, H. Qiu, S. Kimoto, K. Kato, and M. Nakajima, "Rapid Faraday Rotation on ϵ -Iron Oxide Magnetic Nanoparticles by Visible and Terahertz Pulsed Light," *J. Am. Chem. Soc.* **141**, 1775–1780 (2019).
252. S. Schlauderer, C. Lange, S. Baierl, T. Ebnet, C. P. Schmid, D. C. Valovcin, A. K. Zvezdin, A. V. Kimel, R. V. Mikhaylovskiy, and R. Huber, "Temporal and spectral fingerprints of ultrafast all-coherent spin switching," *Nature* **569**, 383–387 (2019).
253. E. J. Sie, C. M. Nyby, C. D. Pemmaraju, S. J. Park, X. Shen, J. Yang, M. C. Hoffmann, B. K. Ofori-Okai, R. Li, A. H. Reid, S. Weathersby, E. Mannebach, N. Finney, D. Rhodes, D. Chenet, A. Antony, L. Balicas, J. Hone, T. P. Devereaux, T. F. Heinz, X. Wang, and A. M. Lindenberg, "An ultrafast symmetry switch in a Weyl semimetal," *Nature* **565**, 61–66 (2019).
254. X. Li, T. Qiu, J. Zhang, E. Baldini, J. Lu, A. M. Rappe, and K. A. Nelson, "Terahertz field-induced ferroelectricity in quantum paraelectric SrTiO₃," *Science* **364**, 1079–1082 (2019).
255. B. C. Pein, W. Chang, H. Y. Hwang, J. Scherer, I. Coropceanu, X. Zhao, X. Zhang, V. Bulović, M. Bawendi, and K. A. Nelson, "Terahertz-Driven Luminescence and Colossal Stark Effect in CdSe–CdS Colloidal Quantum Dots," *Nano Lett.* **17**, 5375–5380 (2017).
256. B. C. Pein, C. K. Lee, L. Shi, J. Shi, W. Chang, H. Y. Hwang, J. Scherer, I. Coropceanu, X. Zhao, X. Zhang, V. Bulović, M. G. Bawendi, A. P. Willard, and K. A. Nelson, "Terahertz-Driven Stark Spectroscopy of CdSe and CdSe–CdS Core–Shell Quantum Dots," *Nano Lett.* **19**, 8125–8131 (2019).
257. F. Zhang, H. Zhang, S. Krylyuk, C. A. Milligan, Y. Zhu, D. Y. Zemlyanov, L. A. Bendersky, B. P. Burton, A. V. Davydov, and J. Appenzeller, "Electric-field induced structural transition in vertical MoTe₂- and Mo_{1-x}W_xTe₂-based resistive memories," *Nat. Mater.* **18**, 55–61 (2019).
258. S. M. Teo, B. K. Ofori-Okai, C. A. Werley, and K. A. Nelson, "Invited Article: Single-shot THz detection techniques optimized for multidimensional THz spectroscopy," *Rev. Sci. Instrum.* **86**, 051301 (2015).
259. A. Krishnamoorthy, M.-F. Lin, X. Zhang, C. Weninger, R. Ma, A. Britz, C. S. Tiwary, V. Kochat, A. Apte, J. Yang, S. Park, R. Li, X. Shen, X. Wang, R. Kalia, A. Nakano, F. Shimojo, D. Fritz, U. Bergmann, P. Ajayan, and P. Vashishta, "Optical Control of Non-Equilibrium Phonon Dynamics,"

- Nano Lett. **19**, 4981–4989 (2019).
260. M. Y. Zhang, Z. X. Wang, Y. N. Li, L. Y. Shi, D. Wu, T. Lin, S. J. Zhang, Y. Q. Liu, Q. M. Liu, J. Wang, T. Dong, and N. L. Wang, "Light-Induced Subpicosecond Lattice Symmetry Switch in MoTe₂," Phys. Rev. X **9**, 021036 (2019).
261. Z. Jiang and X.-C. Zhang, "Measurement of spatio-temporal terahertz field distribution by using chirped pulse technology," IEEE J. Quantum Electron. **36**, 1214–1222 (2000).
262. F. G. Sun, Z. Jiang, and X. C. Zhang, "Analysis of terahertz pulse measurement with a chirped probe beam," Appl. Phys. Lett. **73**, 2233–2235 (1998).
263. C. Ruppert, O. B. Aslan, and T. F. Heinz, "Optical Properties and Band Gap of Single- and Few-Layer MoTe₂ Crystals," Nano Lett. **14**, 6231–6236 (2014).
264. J. Shi, B. C. Pein, Y. Zhang, P.-C. Shen, E. J. Sie, J. Siegel, K.-C. Chiu, C.-A. Chen, Y.-H. Lee, J. Kong, and K. A. Nelson, "Observation of Defect-Induced Exciton Polarization in Monolayer MoS₂," Arxiv (2018).
265. G. Froehlicher, E. Lorchat, F. Fernique, C. Joshi, A. Molina-Sánchez, L. Wirtz, and S. Berciaud, "Unified Description of the Optical Phonon Modes in N-Layer MoTe₂," Nano Lett. **15**, 6481–6489 (2015).
266. K. Chen, A. Roy, A. Rai, H. C. P. Movva, X. Meng, F. He, S. K. Banerjee, and Y. Wang, "Accelerated carrier recombination by grain boundary/edge defects in MBE grown transition metal dichalcogenides," APL Mater. **6**, 056103 (2018).
267. M. Hase, M. Kitajima, S. Nakashima, and K. Mizoguchi, "Dynamics of Coherent Anharmonic Phonons in Bismuth Using High Density Photoexcitation," Phys. Rev. Lett. **88**, 067401 (2002).
268. J. C. Bernède, C. Amory, L. Assmann, and M. Spiesser, "X-ray photoelectron spectroscopy study of MoTe₂ single crystals and thin films," Appl. Surf. Sci. **219**, 238–248 (2003).
269. E. Revolinsky and D. J. Beerntsen, "Electrical properties of α - and β -MoTe₂ as affected by stoichiometry and preparation temperature," J. Phys. Chem. Solids **27**, 523–526 (1966).
270. K. C. Phillips, H. H. Gandhi, E. Mazur, and S. K. Sundaram, "Ultrafast laser processing of materials: a review," Adv. Opt. Photonics **7**, 684–712 (2015).
271. M. Sakakura, T. Tochio, M. Eida, Y. Shimotsuna, S. Kanehira, M. Nishi, K. Miura, and K. Hirao, "Observation of laser-induced stress waves and mechanism of structural changes inside rock-salt crystals," Opt. Express **19**, 17780–17789 (2011).
272. G. Wang, Y. Yu, L. Jiang, X. Li, Q. Xie, and Y. Lu, "Cylindrical shockwave-induced compression mechanism in femtosecond laser Bessel pulse micro-drilling of PMMA," Appl. Phys. Lett. **110**, 161907 (2017).

273. M. Vreugdenhil, D. van Oosten, and J. Hernandez-Rueda, "Dynamics of femtosecond laser-induced shockwaves at a water/air interface using multiple excitation beams," *Opt. Lett.* **43**, 4899 (2018).
274. H. M. van Driel, J. E. Sipe, and J. F. Young, "Laser-Induced Periodic Surface Structure on Solids: A Universal Phenomenon," *Phys. Rev. Lett.* **49**, 1955–1958 (1982).
275. B. Öktem, I. Pavlov, S. Ilday, H. Kalaycıoğlu, A. Rybak, S. Yavaş, M. Erdoğan, and F. Ö. Ilday, "Nonlinear laser lithography for indefinitely large-area nanostructuring with femtosecond pulses," *Nat. Photon.* **7**, 897–901 (2013).
276. J. Bonse, S. Hohm, S. V. Kirner, A. Rosenfeld, and J. Kruger, "Laser-Induced Periodic Surface Structures— A Scientific Evergreen," *IEEE J. Sel. Top. Quantum Electron.* **23**, 9000615 (2017).
277. Q. Wang, L. Jiang, J. Sun, C. Pan, W. Han, G. Wang, F. Wang, K. Zhang, M. Li, and Y. Lu, "Structure-Mediated Excitation of Air Plasma and Silicon Plasma Expansion in Femtosecond Laser Pulses Ablation," *Research* **2018**, 5709748 (2018).
278. Q. Wang, L. Jiang, J. Sun, C. Pan, W. Han, G. Wang, H. Zhang, C. P. Grigoropoulos, and Y. Lu, "Enhancing the expansion of a plasma shockwave by crater-induced laser refocusing in femtosecond laser ablation of fused silica," *Photonics Res.* **5**, 488 (2017).
279. Y. Ito, R. Shinomoto, A. Otsu, K. Nagato, and N. Sugita, "Dynamics of pressure waves during femtosecond laser processing of glass," *Opt. Express* **27**, 29158 (2019).
280. X. Jia, T. Q. Jia, N. N. Peng, D. H. Feng, S. A. Zhang, and Z. R. Sun, "Dynamics of femtosecond laser-induced periodic surface structures on silicon by high spatial and temporal resolution imaging," *J. Appl. Phys.* **115**, 143102 (2014).
281. K. Cheng, J. Liu, K. Cao, L. Chen, Y. Zhang, Q. Jiang, D. Feng, S. Zhang, Z. Sun, and T. Jia, "Ultrafast dynamics of single-pulse femtosecond laser-induced periodic ripples on the surface of a gold film," *Phys. Rev. B* **98**, 184106 (2018).
282. J. Liu, X. Jia, W. Wu, K. Cheng, D. Feng, S. Zhang, Z. Sun, and T. Jia, "Ultrafast imaging on the formation of periodic ripples on a Si surface with a prefabricated nanogroove induced by a single femtosecond laser pulse," *Opt. Express* **26**, 6302 (2018).
283. A. Irizawa, S. Suga, T. Nagashima, A. Higashiya, M. Hashida, and S. Sakabe, "Laser-induced fine structures on silicon exposed to THz-FEL," *Appl. Phys. Lett.* **111**, 251602 (2017).
284. R. R. Gattass, L. R. Cerami, and E. Mazur, "Micromachining of bulk glass with bursts of femtosecond laser pulses at variable repetition rates," *Opt. Express* **14**, 5279 (2006).
285. D. Esser, S. Rezaei, J. Li, P. R. Herman, and J. Gottmann, "Time dynamics of burst-train filamentation assisted femtosecond laser machining in glasses," *Opt. Express* **19**, 25632 (2011).
286. C. Kerse, H. Kalaycıoğlu, P. Elahi, B. Çetin, D. K. Kesim, Ö. Akçaalan, S. Yavaş, M. D. Aşık, B.

- Öktem, H. Hoogland, R. Holzwarth, and F. Ö. Ilday, "Ablation-cooled material removal with ultrafast bursts of pulses," *Nature* **537**, 84–88 (2016).
287. K. Mishchik, G. Bonamis, J. Qiao, J. Lopez, E. Audouard, E. Mottay, C. Hönniger, and I. Manek-Hönniger, "High-efficiency femtosecond ablation of silicon with GHz repetition rate laser source," *Opt. Lett.* **44**, 2193–2196 (2019).
288. D. Metzner, P. Lickschat, and S. Weißmantel, "Laser micromachining of silicon and cemented tungsten carbide using picosecond laser pulses in burst mode: ablation mechanisms and heat accumulation," *Appl. Phys. A* **125**, 462 (2019).
289. A. Žemaitis, P. Gečys, M. Barkauskas, G. Račiukaitis, and M. Gedvilas, "Highly-efficient laser ablation of copper by bursts of ultrashort tuneable (fs-ps) pulses," *Sci. Rep.* **9**, 12280 (2019).
290. C. Kerse, H. Kalaycıoğlu, P. Elahi, Ö. Akcaalan, and F. Ö. Ilday, "3.5-GHz intra-burst repetition rate ultrafast Yb-doped fiber laser," *Opt. Commun.* **366**, 404–409 (2016).
291. H. Kalaycıoğlu, P. Elahi, O. Akcaalan, and F. O. Ilday, "High-Repetition-Rate Ultrafast Fiber Lasers for Material Processing," *IEEE J. Sel. Top. Quantum Electron.* **24**, 8800312 (2018).
292. K. Takasawa, Y. Yamaguchi, H. Nemoto, T. Suzuki, M. Tani, H. Kitahara, D. S. Bulgarevich, and F. Kannari, "Single-shot 2-D burst ultrafast THz imaging utilizing SF-STAMP," in *The European Conference on Lasers and Electro-Optics 2019* (IEEE, 2019), p. cc_3_5.

List of Publications

Journal papers (related to this thesis)

1. **Takakazu Suzuki**, Fumihiko Isa, Leo Fujii, Kenichi Hirose, Keiichi Nakagawa, Keisuke Goda, Ichiro Sakuma, and Fumihiko Kannari, “Sequentially timed all-optical mapping photography (STAMP) utilizing spectral filtering,” *Optics Express* **23**(23), 30512–30522 (2015).
2. **Takakazu Suzuki**, Ryohei Hida, Yuki Yamaguchi, Keiichi Nakagawa, Toshiharu Saiki, and Fumihiko Kannari, “Single-shot 25-frame burst imaging of ultrafast phase transition of Ge₂Sb₂Te₅ with a sub-picosecond resolution,” *Applied Physics Express* **10**(9), 092502 (2017).
3. **Takakazu Suzuki**, Hirofumi Nemoto, Kazuki Takasawa, and Fumihiko Kannari, “1000-fps consecutive ultrafast 2D-burst imaging with a sub-nanosecond temporal resolution by a frequency-time encoding of SF-STAMP,” *Applied Physics A* **126**(2), 135 (2020).

Other journal papers

1. **鈴木敬和**, 肥田遼平, 山口勇輝, 神成文彦, “周波数チャープパルスを用いたスペクトラルイメージングによるシングルショット 25 フレーム超高速撮影”, *レーザー研究* **45**(6), 333–338 (2017).
2. 中川桂一, **鈴木敬和**, 神成文彦, “Sequentially Timed All-optical Mapping Photography -超高速現象の可視化のための光学式イメージング-”, *可視化情報* **37**(145), 26–31 (2017).
3. Keiichi Nakagawa, **Takakazu Suzuki**, and Fumihiko Kannari, “Sequentially Timed All-Optical Mapping Photography for Real-Time Monitoring of Laser Ablation: Breakdown and Filamentation in Picosecond and Femtosecond Regimes,” in *Laser Ablation -From Fundamentals to Applications* T. Itina, ed. (InTech, 2017), pp. 105–121.
4. Yuki Yamaguchi, Ryohei Hida, **Takakazu Suzuki**, Fumihiko Isa, Kenta Yoshikiyo, Leo Fujii, Hirofumi Nemoto, and F. Kannari, “Shaping and amplification of wavelength-tunable mid-infrared femtosecond pulses generated by intra-pulse difference-frequency mixing with spectral focusing,” *Journal of the Optical Society of America B* **35**(12), C1–C7 (2018).
5. **鈴木敬和**, 河端瑞貴, “農林業センサスを用いた耕作放棄地の地理的加重回帰分析”, *GIS-理論と応用* **27**(1), 13–23 (2019).

International conferences

1. Fumihiro Isa, Leo Fujii, **Takakazu Suzuki**, Kenichi Hirosawa, and Fumihiko Kannari, “Versatile Generation of Mid Infrared Pulses through Difference Frequency Mixing in Super-Continuum Pulses,” The 4th Advanced Lasers and Photon Sources (ALPS’15), ALPS7-2, Yokohama, Japan, April 22–24 (2015).
2. **Takakazu Suzuki**, Fumihiro Isa, Leo Fujii, Kenichi Hirosawa, and Fumihiko Kannari, “All-optical Ultrafast Burst Imaging using Broadband Frequency Chirped Pulse,” The 4th Advanced Lasers and Photon Sources (ALPS’15), ALPS11-2, Yokohama, Japan, April 22–24 (2015).
3. **Takakazu Suzuki**, Fumihiro Isa, Leo Fujii, Kenichi Hirosawa, and Fumihiko Kannari, “Ultrafast Imaging using Simultaneous Spatially and Temporally Resolved Wavelength-Multiplexed Photography (SSTWP),” The 35th Conference on Lasers and Electro-Optics (CLEO: 2015), STu4N.2, San Jose, USA, May 10–15 (2015).
4. Fumihiro Isa, Leo Fujii, **Takakazu Suzuki**, Kenichi Hirosawa, and Fumihiko Kannari, “Versatile Generation of Mid Infrared Pulses through Difference Frequency Mixing in Super-Continuum Pulses,” The Conference on Lasers and Electro-Optics/Europe and the European Quantum Electronics Conference (CLEO/Europe-EQEC 2015), CF_P_16, Munich, Germany, June 21–25 (2015).
5. **Takakazu Suzuki**, Fumihiro Isa, Leo Fujii, Kenichi Hirosawa, and Fumihiko Kannari, “All-optical Single-shot Ultrafast 2D-burst Imaging using a Linearly Frequency Chirped Pulse,” The 11th Conference on Lasers and Electro-Optics Pacific Rim (CLEO-PR 2015), 27C2-3, Busan, Korea, August 24–28 (2015).
6. **Takakazu Suzuki**, Ryohei Hida, Ryuta Ueda, Fumihiro Isa, and Fumihiko Kannari, “Scaling in Frame Number of Single-shot Ultrafast 2D-burst Imaging by STAMP utilizing Spectral Filtering,” The 5th Advanced Lasers and Photon Sources (ALPS’16), ALPS11-3, Yokohama, Japan, May 17–20 (2016).
7. Ryohei Hida, **Takakazu Suzuki**, Ryuta Ueda, Fumihiro Isa, and Fumihiko Kannari, “Single-Shot Multispectral Imaging by SF-STAMP System Using a Supercontinuum Pulse,” The 5th Advanced Lasers and Photon Sources (ALPS’16), ALPS11-4, Yokohama, Japan, May 17–20 (2016).
8. Ryohei Hida, **Takakazu Suzuki**, Ryuta Ueda, Fumihiro Isa, and Fumihiko Kannari, “Multispectral Imaging using Sequentially Timed All-optical Mapping Photography utilizing Spectral Filtering (SF-STAMP) system,” The 36th Conference on Lasers and Electro-Optics (CLEO: 2016), SM2I.4, San Jose, USA, June 5–10 (2016).

9. **Takakazu Suzuki**, Ryohei Hida, Ryuta Ueda, Fumihiro Isa, Keiichi Nakagawa, and Fumihiko Kannari, “Single-shot Ultrafast 2D-burst Imaging by STAMP utilizing Spectral Filtering (SF-STAMP),” The 20th International Conference on Ultrafast Phenomena (UP2016), UTh4A.18, Santa Fe, USA, UTh4A.18, July 17–22 (2016).
10. **Takakazu Suzuki**, Ryohei Hida, Fumihiro Isa, Ryuta Ueda, and Fumihiko Kannari, “Single-shot Multispectral Imaging and Ultrafast 2D-imaging by Sequentially Timed All-optical Mapping Photography utilizing Spectral Filtering (SF-STAMP) system,” Imaging Systems and Applications (IS2016), IW1E.3, Heidelberg, Germany, July 25–28 (2016).
11. **Takakazu Suzuki**, Ryohei Hida, Yuki Yamaguchi, Fumihiro Isa, and Fumihiko Kannari, “Ultrafast single-shot 25-frame burst imaging with SF-STAMP system,” The 31st International Congress on High-Speed Imaging and Photonics (ICHSIP-31), 3B-A04, Osaka, Japan, November 7–10 (2016).
12. Ryohei Hida, **Takakazu Suzuki**, Yuki Yamaguchi and Fumihiko Kannari, “Mid Infrared Pulse Generation, Shaping and Amplification from a Supercontinuum Pulse,” The 6th Advanced Lasers and Photon Sources (ALPS’17), ALPS7-4, Yokohama, Japan, April 18–21 (2017).
13. Yuki Yamaguchi, **Takakazu Suzuki**, Ryohei Hida and Fumihiko Kannari, “Generation of Supercontinuum using Self-phase Modulation and Induced Phase Modulation in Fused Silica Plates Array,” The 6th Advanced Lasers and Photon Sources (ALPS’17), ALPSp14-02, Yokohama, Japan, April 18–21 (2017).
14. **Takakazu Suzuki**, Takuya Sato, Ryohei Hida, Yuki Yamaguchi and Fumihiko Kannari, “Ultrafast 2D-burst Imaging and 1D-optical Streak Imaging using a linearly frequency-chirped laser pulse,” The 6th Advanced Lasers and Photon Sources (ALPS’17), ALPSp14-36, Yokohama, Japan, April 18–21 (2017).
15. Yuki Yamaguchi, Ryohei Hida, **Takakazu Suzuki** and Fumihiko Kannari, “Supercontinuum Generation by Self-phase Modulation and Induced Phase Modulation at Fused Silica Thin Plate Array,” The 12th Conference on Lasers and Electro-Optics Pacific Rim (CLEO-PR 2017), P1-027, Singapore, July 31–August 4 (2017).
16. **Takakazu Suzuki**, Ryohei Hida, Yuki Yamaguchi, and Fumihiko Kannari, “Single-shot Burst Imaging of Ultrafast Phenomena with Sub-picosecond Resolution and Sub-nanosecond Time Window,” The 12th Conference on Lasers and Electro-Optics Pacific Rim (CLEO-PR 2017), P1-083, Singapore, July 31–August 4 (2017).
17. Ryohei Hida, **Takakazu Suzuki**, Yuki Yamaguchi, and Fumihiko Kannari, “Generation and Amplification of Versatile Ultrafast Laser Pulses around 2 μm ,” The 24th General Congress of International Commission for Optics (ICO-24), M1G-03, Tokyo, Japan, August 21–25 (2017).

18. Yuki Yamaguchi, **Takakazu Suzuki**, Ryohei Hida, and Fumihiko Kannari, “Single-shot Ultrafast 2D-burst Imaging with a Frequency-chirped Supercontinuum Laser Pulse,” The 24th General Congress of International Commission for Optics (ICO-24), Th2D-04, Tokyo, Japan, August 21–25 (2017).
19. Hirofumi Nemoto, **Takakazu Suzuki**, Yuki Yamaguchi, Ryohei Hida, and Fumihiko Kannari, “Single-shot Ultrafast Imaging with Burst Pulses of 100-ps Interval,” The 7th Advanced Lasers and Photon Sources (ALPS’18), ALPSp-36, Yokohama, Japan, April 23–27 (2018).
20. Hirofumi Nemoto, **Takakazu Suzuki**, Yuki Yamaguchi, and Fumihiko Kannari, “Single-shot Ultrafast Burst Imaging by Spectrally Sweeping Pulse Train with 100-ps Interval,” The 13th Conference on Lasers and Electro-Optics Pacific Rim (CLEO-PR 2018), , Hong Kong, China, July 29 –August 3 (2018).
21. Hirofumi Nemoto, **Takakazu Suzuki**, Yuki Yamaguchi, Kazuki Takasawa, Kazuki Matsushita, and Fumihiko Kannari, “Single-shot 2-D burst imaging in sub-nanosecond region with spectrally sweeping ultrafast laser pulses,” The 8th Advanced Lasers and Photon Sources (ALPS’19), ALPS-P1-22, Yokohama, Japan, April 22–25 (2019).
22. Kazuki Takasawa, **Takakazu Suzuki**, Yuki Yamaguchi, Hirofumi Nemoto, Masahiko Tani, Hideaki Kitahara, Dmitry S. Bulgarevich, and Fumihiko Kannari, “Single-shot 2D burst ultrafast imaging in terahertz region utilizing SF-STAMP,” The 8th Advanced Lasers and Photon Sources (ALPS’19), ALPS- P2-15, Yokohama, Japan, April 22–25 (2019).
23. **Takakazu Suzuki**, Hirofumi Nemoto, Kazuki Takasawa, Kazuki Matsushita, Yuki Yamaguchi, and Fumihiko Kannari, “Real-time ultrafast 2D-imaging of femtosecond laser processing by a temporal wavelength division scheme,” The 8th International Congress on Laser Advanced Materials Processing (LAMP2019), Fr1-L5, Hiroshima, Japan, May 21–24 (2019).
24. Kazuki Takasawa, Yuki Yamaguchi, Hirofumi Nemoto, **Takakazu Suzuki**, Masahiko Tani, Hideaki Kitahara, Dmitry S. Bulgarevich, and Fumihiko Kannari, “Single-shot 2-D burst ultrafast THz imaging utilizing SF-STAMP,” The Conference on Lasers and Electro-Optics/Europe and the European Quantum Electronics Conference (CLEO/Europe-EQEC 2019), CC-3.5, Munich, Germany, June 23–27 (2019).
25. Hirofumi Nemoto, **Takakazu Suzuki**, Kazuki Matsushita, Kazuki Takasawa, and Fumihiko Kannari, “Ultrafast single-shot burst imaging in a few-nanosecond window using a spectrally sweeping laser pulse train,” The Conference on Lasers and Electro-Optics/Europe and the European Quantum Electronics Conference (CLEO/Europe-EQEC 2019), CF-12.4, Munich, Germany, June 23–27 (2019).

26. **Takakazu Suzuki**, Hirofumi Nemoto, Kazuki Takasawa, and Fumihiko Kannari, “1000-fps consecutive ultrafast 2D-burst imaging with a sub-nanosecond temporal resolution by a frequency-time encoding of SF-STAMP,” The 15th International Conference on Laser Ablation (COLA2019), Thu13-1, Maui-Hawaii, USA, September 8–13 (2019).

Domestic conferences

1. 伊佐文宏, **鈴木敬和**, 藤井令央, 廣澤賢一, 神成文彦, “広帯域フェムト秒レーザーの偏光波形整形を用いた Type-I 差周波混合中赤外パルス発生”, レーザー学会学術講演会第 35 回年次大会, A311pIII03, 東海大学 高輪校舎, 東京, 2015 年 1 月 11–12 日.
2. 伊佐文宏, 藤井令央, **鈴木敬和**, 廣澤賢一, 神成文彦, “広帯域フェムト秒レーザーを用いた Type-I 差周波混合中赤外パルス波形整形”, 第 62 回応用物理学会春季学術講演会, 12a-A15-7, 東海大学 湘南キャンパス, 神奈川, 2015 年 3 月 11–14 日.
3. **鈴木敬和**, 藤井令央, 伊佐文宏, 廣澤賢一, 神成文彦, “広帯域線形周波数チャープパルスを用いた全光学超高速イメージング”, 第 62 回応用物理学会春季学術講演会, 14a-A15-9, 東海大学 湘南キャンパス, 神奈川, 2015 年 3 月 11–14 日.
4. **鈴木敬和**, 藤井令央, 伊佐文宏, 廣澤賢一, 神成文彦, “広帯域線形周波数チャープパルスを用いた全光学超高速イメージング”, 第 26 回先端光量子科学アライアンスシンポジウム, 慶應義塾大学 日吉キャンパス, 神奈川, 2015 年 3 月 19 日.
5. 伊佐文宏, 藤井令央, **鈴木敬和**, 廣澤賢一, 神成文彦, “広帯域フェムト秒レーザーパルス内差周波発生を用いた帯域・中心波長・波形可変中赤外パルス発生”, 第 26 回先端光量子科学アライアンスシンポジウム, 慶應義塾大学 日吉キャンパス, 神奈川, 2015 年 3 月 19 日.
6. **鈴木敬和**, 伊佐文宏, 中川桂一, 肥田遼平, 植田隆太, 廣澤賢一, 神成文彦, “線形周波数チャープパルスを用いた全光学超高速 2 次元バーストイメージング”, レーザー学会学術講演会第 36 回年次大会, E310aV05, 名城大学 天白キャンパス, 愛知, 2016 年 1 月 9–11 日.
7. **鈴木敬和**, 伊佐文宏, 肥田遼平, 植田隆太, 神成文彦, “フェムト秒レーザーによる超広帯域パルス発生と超高速イメージングおよびマルチスペクトラルイメージング”, 第 8 回文部科学省「最先端の光の創成を目指したネットワーク研究拠点プログラム」シンポジウム, 大阪大学 吹田キャンパス, 大阪, 2016 年 1 月 28 日.
8. 肥田遼平, **鈴木敬和**, 伊佐文宏, 植田隆太, 神成文彦, “SF-STAMP 光学系を用いたマルチスペクトラルイメージング”, 第 63 回応用物理学会春季学術講演会, 21a-H116-1, 東京工業大学 大岡山キャンパス, 東京, 2016 年 3 月 19–22 日.

9. 植田隆太, 肥田遼平, **鈴木敬和**, 伊佐文宏, 神成文彦, “希ガス封入中空ファイバ及び石英薄板を用いた超広帯域フェムト秒光パルスの発生”, 第 63 回応用物理学会春季学術講演会, 21p-S622-18, 東京工業大学 大岡山キャンパス, 東京, 2016 年 3 月 19–22 日.
10. **鈴木敬和**, 肥田遼平, 山口勇輝, 神成文彦, “線形周波数チャープパルスを用いた全光学超高速 2 次元バーストイメージングの性能拡張”, レーザー学会学術講演会第 37 回年次大会, E207pI03, 徳島大学 常三島キャンパス, 徳島, 2017 年 1 月 7–9 日.
11. **鈴木敬和**, 肥田遼平, 山口勇輝, 神成文彦, “スペクトラルフィルタリングを用いた STAMP, 第 9 回文部科学省「最先端の光の創成を目指したネットワーク研究拠点プログラム」シンポジウム, E62, 弘済会館, 東京, 2017 年 1 月 24 日.
12. **鈴木敬和**, 肥田遼平, 山口勇輝, 神成文彦, “周波数チャープパルスとスペクトラルフィルタリングを用いた全光学超高速 25 枚連写イメージング”, 第 64 回応用物理学会春季学術講演会, 16p-418-7, パシフィコ横浜, 神奈川, 2017 年 3 月 14–17 日.
13. 山口勇輝, **鈴木敬和**, 肥田遼平, 神成文彦, “石英薄板アレイにおける自己位相変調, 誘起位相変調を用いた超広帯域フェムト秒光パルスの発生”, 第 64 回応用物理学会春季学術講演会, 16p-311-9, パシフィコ横浜, 神奈川, 2017 年 3 月 14–17 日.
14. 佐藤琢哉, **鈴木敬和**, 神成文彦, “光ストリークイメージングによるフェムト秒レーザー誘起屈折率変化の観測”, 第 64 回応用物理学会春季学術講演会, 16p-418-13, パシフィコ横浜, 神奈川, 2017 年 3 月 14–17 日.
15. **鈴木敬和**, “リーディングプログラムでの経験をキャリア形成へ活かす”, 博士課程教育リーディングプログラムフォーラム 2017, B-A03-3, 名古屋マリオットアソシアホテル, 愛知, 2017 年 10 月 20–21 日.
16. **鈴木敬和**, 河端瑞貴, “農林業センサスを用いた耕作放棄地の空間計量経済分析”, 第 26 回地理情報システム学会研究発表大会, P-06, 宮城大学 大和キャンパス, 宮城, 2017 年 10 月 28–29 日.
17. 肥田遼平, **鈴木敬和**, 山口勇輝, 根本寛史, 神成文彦, “高機能波長可変中赤外フェムト秒レーザーとそのポンプ・プローブ分光応用”, 第 10 回文部科学省「最先端の光の創成を目指したネットワーク研究拠点プログラム」シンポジウム, E31, 京都大学, 京都, 2018 年 1 月 23 日.
18. 山口勇輝, 根本寛史, **鈴木敬和**, 神成文彦, “周波数チャープパルスとスペクトラルフィルタリングを用いた全光学超高速 25 枚連写イメージング”, 第 38 回先端光量子科学アライアンスシンポジウム, 慶應義塾大学 日吉キャンパス, 神奈川, 2018 年 3 月 2 日.
19. 根本寛史, **鈴木敬和**, 山口勇輝, 肥田遼平, 神成文彦, “異波長パルス列を用いたサブナノ秒間隔での時空間バーストイメージング”, 第 65 回応用物理学会春季学術講演会, 19p-B301-19, 早稲田大学 西早稲田キャンパス, 東京, 2018 年 3 月 17–20 日.
20. 山口勇輝, **鈴木敬和**, 根本寛史, 高澤一輝, 松下一輝, 神成文彦, “SF-STAMP を用いたテラヘル

- ツ領域シングルショット2次元超高速バーストイメージング”, レーザー学会学術講演会第39回年次大会, 13pIV-2, 東海大学 高輪キャンパス, 東京, 2019年1月12-14日.
21. 根本寛史, 鈴木敬和, 山口勇輝, 神成文彦, “波長掃引超高速レーザーパルス列を用いたサブナノ秒領域シングルショット2次元バーストイメージング”, レーザー学会学術講演会第39回年次大会, 13pIV-3, 東海大学 高輪キャンパス, 東京, 2019年1月12-14日.
 22. Qiyuan Song, Yuki Yamaguchi, Hirofumi Nemoto, Takakazu Suzuki, Kazuki Takasawa, Kazuki Matsushita, and Fumihiko Kannari, “Structured 2D temporal focusing microscopy for background free fluorescence imaging and enhanced sectioning ability”, レーザー学会学術講演会第39回年次大会, 13pIV-4, 東海大学 高輪キャンパス, 東京, 2019年1月12-14日.
 23. 根本寛史, 鈴木敬和, 松下一輝, 山口勇輝, 神成文彦, “波長掃引超高速レーザーパルス列を用いた透明固体材料中のレーザー誘起応力波ダイナミクスのシングルショット2次元バーストイメージング”, 第66回応用物理学会春季学術講演会, 9a-M135-7, 東京工業大学 大岡山キャンパス, 東京, 2019年3月9-12日.
 24. 高澤一輝, 鈴木敬和, 山口勇輝, 根本寛史, 北原英明, 谷正彦, 松浦裕司, 神成文彦, “SF-STAMP を用いた超高速シングルショットテラヘルツイメージング”, 第66回応用物理学会春季学術講演会, 11p-S421-4, 東京工業大学 大岡山キャンパス, 東京, 2019年3月9-12日.
 25. 鈴木敬和, Jiaojian Shi, Keith Nelson, 神成文彦, “2次元 MoTe₂ の高強度 THz パルス誘起不可逆相転移における準安定相のシングルショット観測”, レーザー学会学術講演会第40回年次大会, F03-21a-XI-02, 仙台国際センター, 宮城, 2020年1月20-22日.
 26. 根本寛史, 鈴木敬和, 高澤一輝, 渡瀬陸, 神成文彦, マイクロレンズアレイによる面分光を用いたサブナノ秒領域シングルショット2次元バーストイメージング, レーザー学会学術講演会第40回年次大会, E03-21p-VI-06, 仙台国際センター, 宮城, 2020年1月20-22日.

Others

1. 受賞 2015年: *The 11th Conference on Lasers and Electro-Optics Pacific Rim (CLEO-PR 2015)*, Best Student Paper Award
2. 受賞 2015年: 2015年度コニカミノルタ光みらい奨励金
3. 受賞 2016年: *The 5th Advanced Lasers and Photon Sources (ALPS'16)*, Best Student Oral Paper Award
4. 受賞 2017年: 電子情報通信学会エレクトロニクスソサイエティ, 平成28年度(第3回)エレクトロニクスソサイエティ優秀学生修了表彰

5. 受賞 2017 年: *The 6th Advanced Lasers and Photon Sources (ALPS'17)*,
Best Student Poster Paper Award
6. 受賞 2017 年: レーザー学会学術講演会第 37 回年次大会,
優秀論文発表賞
7. 受賞 2017 年: 名古屋大学リーディングフォーラム 2017,
Industrial Future Leader Award
8. 受賞 2018 年: 公益財団法人電気電子情報学術振興財団,
平成 30 年度原島博学術奨励賞

Acknowledgements

The work presented in this thesis was carried out in the ultrafast laser group of Prof. Dr. Fumihiko Kannari at the Graduate school of Science and Technology at Keio University. I joined his group in 2014 when I was an undergraduate student at the Department of Electronics and Electrical Engineering. Since then, I learned many things not only research topics but also the way of thinking from his enthusiastic and insightful advice. I am proud of being a member of the Kannari group.

I would like to thank Prof. Dr. Toshiharu Saiki, Prof. Dr. Takasumi Tanabe, Prof. Dr. Shinichi Watanabe, and Prof. Dr. Keith A. Nelson for being the vice-chairs in my dissertation committee, and for reviewing and advice and corrections to sophisticate this thesis.

A part of the work presented in Chapter 3 was conducted as collaborative research from October 2018 to March 2019 in the Nelson group at MIT in Cambridge, MA, USA. I would like to appreciate to Prof. Keith A. Nelson for accepting me as a visiting student and giving me this great opportunity. I also thank Jiaojian (Tristan) Shi, a Ph.D. student in the Nelson group, for helping me during my stay at MIT.

I also thank Dr. Keiichi Nakagawa at the University of Tokyo, who invented the original STAMP, for giving me technical tips of STAMP experiment, many advice and discussions.

I would like to acknowledge all the members of the Kannari group. Especially, Dr. Hiroki Tanaka and Dr. Aruto Hosaka gave me a lot of advice to proceed with my research. Thanks to the Femtosecond technology (Pulse shaping) team, I could spend fulfilling days. I would like to thank Leo Fujii, Fumihiro Isa, Ryohei Hida, Yuki Yamaguchi, Hirofumi Nemoto, Kazuki Takasawa, Riku Watase, Shota Itoyama. I also thank Kodai Iijima Yasuhiro Kojima, Takuya Sato and Ryota Sawada, who are my colleagues joined in the same year.

For its financial and educational support during my research assistant (RA) period, I also would like to appreciate all the relative members of the Program of Leading Graduate Schools (PLGS) at Keio University for “Science for Development of Super Mature Society”.

Finally, I would like to express my sincere gratitude to my family member for supporting the entire my student life. It is time to embark on the next stage in my journey, and I will continue my best for the future.